INFORMATION TO USERS

This material was produced from a microfilm copy of the original document. While the most advanced technological means to photograph and reproduce this document have been used, the quality is heavily dependent upon the quality of the original submitted.

The following explanation of techniques is provided to help you understand markings or patterns which may appear on this reproduction.

1. The sign or "target" for pages apparently lacking from the document photographed is "Missing Page(s)". If it was possible to obtain the missing page(s) or section, they are spliced into the film along with adjacent pages. This may have necessitated cutting thru an image and duplicating adjacent pages to insure you complete continuity.

2. When an image on the film is obliterated with a large round black mark, it is an indication that the photographer suspected that the copy may have moved during exposure and thus cause a blurred image. You will find a good image of the page in the adjacent frame.

3. When a map, drawing or chart, etc., was part of the material being photographed the photographer followed a definite method in "sectioning" the material. It is customary to begin photoing at the upper left hand corner of a large sheet and to continue photoing from left to right in equal sections with a small overlap. If necessary, sectioning is continued again — beginning below the first row and continuing on until complete.

4. The majority of users indicate that the textual content is of greatest value, however, a somewhat higher quality reproduction could be made from "photographs" if essential to the understanding of the dissertation. Silver prints of "photographs" may be ordered at additional charge by writing the Order Department, giving the catalog number, title, author and specific pages you wish reproduced.

5. PLEASE NOTE: Some pages may have indistinct print. Filmed as received.

Xerox University Microfilms
300 North Zeeb Road
Ann Arbor, Michigan 48106

PLEASE NOTE:

Page 76 is not available
for photography.

UNIVERSITY MICROFILMS

THE UNIVERSITY OF OKLAHOMA

GRADUATE COLLEGE

FLUID DYNAMICS OF A TORNADO-LIKE VORTEX FLOW

A DISSERTATION

SUBMITTED TO THE GRADUATE FACULTY

in partial fulfillment of the requirements for the

degree of

DOCTOR OF PHILOSOPHY

BY

MASOOD PARANG

Norman, Oklahoma

1975

FLUID DYNAMICS OF A TORNADO-LIKE VORTEX FLOW

APPROVED BY

Martin C. Fischbe

Edward A. Blair

William N. Hughes

John E. Francis

DISSERTATION COMMITTEE

ACKNOWLEDGMENT

My deepest and most sincere gratitude goes to Dr. Martin C. Jischke, who served as the Chairman of my doctoral advisory committee. I have been extremely fortunate to have had the opportunity to be a student of his and work under his guidance for both my Master's and Doctor's degree. His encouragements and advice during past years and throughout my graduate study have always been a source of motivation and inspiration. It is extremely difficult to fully express my appreciation for his many contributions to my education, both as a teacher and a friend of which the completion of this dissertation is only a small part.

The author is grateful for the financial support of the National Severe Storms Laboratory of the National Oceanic and Atmospheric Administration which made this work possible.

I also wish to thank my parents and brother, Manouchehr, who have a great share in making my education possible. I am grateful to my brother, Morteza, whose help in the experimental portion of this work made its completion possible. His encouraging attitude in difficult times deserves a special thanks.

ABSTRACT

A swirling, converging vortex flow is studied both experimentally and theoretically as a model of tornado flowfields. Laboratory measurements of this vortex flowfield are obtained using Ward's apparatus and such unique features as the multiple-vortex phenomenon are studied. The turbulent boundary-layer due to this swirling converging vortex flowfield is investigated theoretically by means of Von Karman's integral momentum method. In addition, a recirculating vortex core model is studied. Using a nonequilibrium condensation process as a basis, distinctions between the observed tornado funnel and other aspects of the core flow are discussed.

It is found that the swirling, converging vortex flow is a more realistic model of tornadoes. The laboratory measurements show an outer inviscid region similar to a Rott-Burgers' vortex with core dimensions primarily determined by inviscid dynamics and the pressure boundary condition aloft. Theoretical estimates of the core diameter are in agreement with Hoecker's measurements of the 1957 Dallas tornado. Convergence in the inviscid flow region is shown to be responsible for such experimentally observed features as boundary-layer separation and reattachment. Also, the shallow convergence region of the tornado simulation apparatus is shown to be important in the production and advection of vorticity in the ground boundary layer which is believed to lead to the multiple vortex phenomenon observed in naturally-occurring tornadoes. Consideration of the water vapor condensation process near the core and comparison with measurements suggests that, because of nonequilibrium behavior, the funnel cloud is spatially distinct from the recirculating core and condensation pressure isobar.

TABLE OF CONTENTS

TABLE OF CONTENTS (Cont'd.)

LIST OF TABLES

LIST OF PLATES

LIST OF ILLUSTRATIONS

LIST OF ILLUSTRATIONS (Cont'd.)

LIST OF ILLUSTRATIONS (Cont'd.)

LIST OF ILLUSTRATIONS (Cont'd.)

NOMENCLATURE

a	constant in Rott-Burgers vortex flow (See Eq. 2.14a-c)
$\bar{a}(z)$	inner core constant (See Eq. 4.4a)
b	constant disturbed pressure in upper atmospheric layer (See Eq. 4.12)
c	constant (See Eq. 3.26)
D	diffusion coefficient
$\hat{e}_r, \hat{e}_\theta, \hat{e}_z$	unit vectors in cylindrical coordinate system (r,θ,z)
$\hat{e}_s, \hat{e}_n, \hat{e}_z$	unit vectors in inviscid streamline coordinate system (s,n,z)
E	cross-flow function (See Eq. 3.20)
$f(\eta)$	velocity profile function (See Eq. 3.22)
$f_1(n), f_2(s)$	general coordinate function (See Eqs. 3.48 and 3.49)
$g(\eta)$	velocity profile function (See Eq. 3.22)
g	gravitational constant
h	height of the shallow convergence zone in Ward's apparatus
h_s, h_n, h_z	metric coefficients in (s,n,z) coordinate system (See Eq. 3.33)
I	inflow rate of radial component of vorticity (See Eq. 3.116)
K	$= 2b/\rho W_a^{*2}$
m	$= \mathrm{Tan}\phi$, tangent of the swirl parameter (See also Eq. 1.1)
m_o	$= m(r=R)$, constant.
M	angular momentum inflow in Ward's apparatus (See Eq. 2.3)
M_w	molecular weight of water
n	coordinate in inviscid streamline coordinate system (s,n,z)
p	fluid static pressure

$p_a(z)$	static pressure on the axis of the vortex
$p_a(\infty)$	static pressure on the axis as $z \to \infty$
p_c	water vapor equilibrium condensation pressure
p_m	static pressure at the maximum tangential velocity core boundary
p_v	water vapor pressure
$p_{v\infty}, p_{vd}$	vapor pressure for away and on the drop, respectively.
p_1	static pressure at the tornado funnel surface (See Eqs. 4-21 a-b)
p_∞	hydrostatic environmental equilibrium pressure
$\hat{p}$	disturbed static pressure (See Eq. 4.10)
$\hat{p}_s$	disturbed stagnation pressure
P	inviscid pressure at the edge of the boundary layer
Q	volumetric inflow rate
r	radial coordinate in cylindrical coordinate system (r,θ,z)
r_c	the radius of the observed core in Ward's simulated tornado flow.
$r_m(z)$	radius of the maximum tangential velocity core
r_s	the radius at the screen in Ward's apparatus
r_u	the radius of the updraft chamber in Ward's apparatus
$\bar{r}$	the radius of a vapor drop (See Eq. 4.29)
r_o, r_F	the initial and final radius of a vapor drop (See Eq. 4.25)
$r_1(z)$	the radius of the funnel surface
R	the radius of the disk in boundary-layer calculations
$\bar{R}$	the universal gas constant
s	coordinate in inviscid streamline coordinate system (s,n,z)
t_c	characteristic flow time of air particles
T	total torque exerted on the fluid by the boundary

T_1	See Eq. 2.4
$\bar{T}$	$= \bar{T}_{env}$, environmental ambient temperature
$\tilde{T}$	period of rotation of a fluid particle in the core flow
u	velocity component in s direction in the boundary-layer
u^*	radial velocity component in the boundary-layer
U	inviscid streamline velocity (s direction)
U_o	inviscid streamline velocity in s direction at the edge of the disk, r=R
U^*	radial inviscid velocity component in cylindrical coordinate system (r,θ,z)
U_s^*	radial inviscid velocity component at the screen in Ward's apparatus
v	velocity component in n direction in the boundary-layer
v^*	tangential velocity component in the boundary-layer
V	inviscid velocity in the n direction
V_s	screen velocity in Ward's apparatus
V^*	inviscid tangential velocity component in cylindrical coordinate system (r,θ,z)
V_s^*	inviscid tangential velocity component at the screen in Ward's apparatus
V_m^*	maximum inviscid tangential velocity
$\vec{V}_i$	inviscid total velocity vector
w	vertical velocity in the boundary-layer
W, W^*	inviscid vertical velocity [same in both (s,n,z) and (r,θ,z) coordinate system]
$\bar{W}$	average inviscid vertical component of velocity
W_a	inviscid vertical velocity on the axis
W_a^*	inviscid vertical velocity on the axis
$W(\delta)$	vertical velocity at the edge of the boundary-layer
z	vertical coordinate in (s,n,z) and (r,θ,z) coordinate systems

GREEK LETTERS

α	parameter in the expansion at the edge of the disk (See page 61)
β	parameter in the expansion at the edge of the disk (See page 61)
Γ	circulation of velocity (See Eq. 2.2)
δ	normalized boundary-layer thickness
δ_o	characteristic boundary-layer thickness, $= (\frac{\nu R^4 C^4}{U_o})^{1/5}$
Δ	see Eq. 3.40
$\Delta p_1, \Delta p_2$	pressure difference (See Eqs. 4.1 and 4.2)
η	$= \frac{z}{\delta}$, normalized height in the boundary layer
θ	tangential coordinate in cylindrical coordinate system (r,θ,z)
κ	ratio of characteristic condensation time to flowtime of air particles, $= \tau_c/\bar{\tau}$
ν	molecular kinematic viscosity of air
$\tilde{\nu}$	eddy viscosity of air
ρ	density of air
ρ_L	density of liquid water
$\tau_{r,z}, \tau_{\theta,z}$	shear stress components in cylindrical coordinate system (r,θ,z)
$\tau_{r,z}(0), \tau_{\theta,z}(0)$	shear stress components in cylindrical coordinate system at the ground
τ_{sz}, τ_{nz}	shear stress components in inviscid streamline coordinate system (s,n,z)
$\tau_{sz}(0), \tau_{nz}(0)$	shear stress components in inviscid streamline coordinate system at the ground
$\bar{\tau}$	characteristic time for condensation of water vapor
ϕ	swirl parameter defined in Eq. 1.1
ϕ_i	swirl parameter in the inviscid flow
ϕ_{io}	inviscid swirl parameter at the edge of the disk, $r = R$

ϕ_w	swirl parameters at the ground boundary
ϕ_{cr}	critical swirl parameter for double vortex formation
$\vec{\omega}$	vorticity vector
ω_r	radial component of vorticity

CHAPTER I

INTRODUCTION

Tornadoes are among the most violent and unpredictable vortex-like flows in nature. Their occurrence in the spring and summer seasons in the United States, especially in the Midwest and central areas of the country, takes a considerable toll in life and property damage.

Although tornadoes, hurricanes, waterspouts, and dust devils all are naturally occurring vortex-like flows, there are considerable differences among these natural vortices. Tornadoes are much more violent than dust devils and, as opposed to waterspouts, occur more often in populated areas. Their intensity has placed tornadoes in a distinctly more dangerous category of flows as compared with dust devils and waterspouts. Tornadoes also differ from hurricanes in several major respects. In contrast to hurricanes which have a horizontal extent of thousands of kilometers and a lifetime of weeks, tornadoes have a horizontal scale of the order of several kilometers, and a lifetime of the order of less than an hour. Hurricanes can be detected at sea by satellites long before they seriously endanger people and their property whereas tornadoes remain relatively unpredictable and hence more dangerous.

The inability to correctly predict tornado occurrence as well as their intensity is the main reason for the substantial lack of data

and observation on naturally-occurring tornadoes as compared with hurricanes and other natural vortices. Therefore, tornadoes remain unique because of their unpredictability, damage and destruction as well as their unknown nature.

Tornado flows are studied with the ultimate hope of resolving several important questions. The origin and conditions necessary for the creation of tornadoes, the structure and dynamics of tornado flows and the reasons for their disappearance and annihilation are the primary goals of the research in this area. These long-range goals cannot be accomplished, however, unless considerable progress is made in observations of naturally-occurring tornadoes and substantial data is gathered on them. In the meantime, research efforts, such as the present one, have been directed toward the more modest goal of achieving a correct dynamic model of tornado flows consistent with the sketchy and scattered available observations.

There has been a long history of engineering interest in vortex-like flows since they occur in many situations of scientific interest. The fluid dynamicist has been able to help provide the meteorologist with a better understanding of tornadoes, hurricanes, waterspouts, and dust devils by applying his knowledge and research tools in this important area. This is done both in construction of better models for tornado flows as well as providing a more practical basis for the prediction of tornado occurrence. Engineering interest in tornadoes also results from the need to correctly and consistently estimate the maximum wind velocity and pressure drop in tornadoes so as to be able to design vital structures such as those housing nuclear reactors. Finally, a

comprehensive and thorough understanding of this atmospheric phenomenon might suggest ways to alter atmospheric conditions to prevent tornado occurrence or even cause their destruction after they have formed.

Much research has recently been directed toward the achievement of these goals. Many efforts have centered around problems associated with tornado dynamics and the characteristics of tornado-like vortices. Even though there remains much to be accomplished and further research is needed for a better understanding of this remarkable atmospheric phenomenon, significant advances have been made in both experimental and theoretical fronts.

On the experimental front, efforts have been made in two directions. One direction is the creation of better methods of collection of data from naturally-occurring tornadoes. Although progress has been impressive, much remains to be done. The lack of data on velocity and pressure fields associated with tornadoes occurring in nature is probably the greatest single obstacle in the further development and verification of a comprehensive tornado model. This lack of observational data is especially true of the core region of the tornadoes and the region aloft in the clouds from which they are spawned. With the exception of the pressure data accidentally obtained by the Lewis Flight Propulsion Laboratory[1] from a tornado on June 8, 1953 and the velocity data reported by Hoecker[2] from the Dallas tornado of April 2, 1957 as

as well as partially available velocity data of a tornado on May 24, 1973 in Union City, Oklahoma reported by Golden,[3] detailed data on the distribution of velocity and/or pressure in naturally-occurring tornadoes are unavailable.

Tornado observations seem to suggest the need for at least two essential factors in order for the formation of this intense atmospheric vortex to occur. First, there must exist a large upward convection of air, sustained for some period of time. This upward convection is probably due to an instability of the atmospheric layers prior to the formation of tornado-producing storms. This upward flow is then responsible for a converging flow in the ground layers of the atmosphere.

Second, there should also be a circulation in the lower portion of the atmosphere. The source of this circulation as well as the updraft is in the large thunderstorm from which tornadoes are produced. It is believed that the development of severe thunderstorms (which may produce tornadoes) involves essentially two currents. Warm moist air flows into the storm (from the south) and is uplifted. A second current enters the storm from the rear and is cooled by evaporation of precipitation (becoming negatively buoyant) and produces an outflow (from the north west). The two currents, then, meeting at an angle produce the large scale circulation necessary for tornado formation. Observations indicate that indeed tornadoes show a tendency to occur under a connective cell along the shear line between the moist inflow and the rain-cooled outflow.[4] The large scale circulation and the updraft then create

a swirling-converging streamline pattern. This swirling-converging flow seems to be always present in the formation of a tornado funnel and the two factors mentioned are the essential ingredients in any simulation of tornado flows in the laboratory. It is, however, important to note that the tornado flow is a much more complicated flowfield than the above simple picture indicates. This becomes evident if one notes that the presence of low-level convergence and circulation seems to be much more common than observations of tornadoes. The complex nature of tornado flows is further evident in the various shapes and configurations that are observed for tornadoes as well as in such seemingly unusual characteristics of tornado funnels as "core splitting."[5]

Among the observations and measurements of tornado flowfields, Hoecker's observations of the 1957 Dallas tornado remain, up to now, the most complete and extensive. His observations, however, were limited to the lower portions of the funnel cloud and do not exceed horizontally more than 1400 ft. away from the axis. The tangential velocity field as well as the derived distribution of pressure by Hoecker are shown in Figs. 1.1 and 1.2, respectively. These observations suggest certain features of the flow which are believed to be of general importance. First, it is observed that far away from the axis of the tornado the tangential velocity varies approximately inversely with radius. That is the tangential velocity behaves roughly like that of a potential vortex. Furthermore the tangential velocity varies with height close to the ground. Second, a relatively large radial velocity (of the same order of magnitude as the tangential velocity) exists in the lower levels of the atmosphere. This is significant in modeling the impressed

flow over the boundary layer close to the ground if a realistic boundary layer calculation is to be carried out. This is discussed in more detail later. Third, a large conically-shaped core with tangential velocity varying linearly with radius is observed below the funnel cloud. This section of the flowfield seems to extend into the tornado cloud enveloping the lower portions of the funnel itself. The core size seems to be relatively large (of the order of 150 feet) indicating that the dimensions of this core are not determined by viscosity as certain flow models in the literature (see *e.g.* Rott,[6] 1958) suggest. Fourth, there exists a downflow on the axis of the funnel cloud. Although because of the obstruction of sight by the funnel no velocity measurements are available in the funnel, the rapid deceleration of the updraft on the axis near the tip of the funnel clearly suggests a stagnation point. This implies that the observed core should be distinguished from the funnel aloft. The funnel, as suggested by many authors, is probably a two-cell structure with a recirculating flow consisting of downward flow along the axis and upward along the boundary of the funnel. This will be discussed in more detail in Chapter III of this work.

While the observation of naturally-occurring tornadoes remain few and insufficient, the features observed -- particularly those of Hoecker -- serve as a good guide for any laboratory simulation of tornado flows as well as for mathematical models and calculations of tornado-like vortices. It is in this light that the second direction of the experimental research is evaluated.

The second direction of experimental efforts have been the laboratory simulation of tornadoes. Although the accuracy of the various

simulations is often difficult to estimate and only the scattered observations of naturally-occurring tornadoes are available for the comparison and evaluation of the simulation, the efforts in this direction remain important and fruitful. The construction of tornado-like vortices in the laboratory and attempts to produce different features of tornado flows has greatly advanced the understanding of this remarkable vortex flow. Many laboratory experiments on tornado-like vortices have been made. Among the more careful experiments in which some of the apparently central elements of tornado dynamics are simulated are those of Ying and Chang,[7] Wan and Chang,[8] and Ward.[9]

The experiments of Ying and Chang and later of Wan and Chang were conducted in air with the circulation being produced by a rotating cylindrical screen and the updraft by an exhaust fan affixed on the top. The latter is to simulate the convection of air and the former the circulation present in the atmosphere during the formation of tornadoes. It should be emphasized, however, that a vortex can always be produced with relative ease when these two central ingradients of vortex simulation are present. We shall see, however, that the other "details" of the experimental apparatus do seem to be important in an accurate simulation of tornadoes. A vortex core with descending flow along the axis

and a surrounding inviscid flow region were observed by Wan and Chang. Due to the geometry of the apparatus, boundary layers at the top and bottom are also present. Outside these boundary layers and the vortex core, the flow is observed to be similar to a potential vortex flow with very small radial and vertical velocities. Although Wan and Chang produced tangential velocity distributions similar to Hoecker's[2] observations of the 1957 Dallas tornado, there are significant differences between the laboratory simulation and the observations of the latter. For example, the radial and vertical velocities observed by Hoecker in the Dallas tornado were, relatively, much larger than those observed in the experiments of Wan and Chang. Furthermore the rotation of fan is undoubtedly responsible for a direct fan-induced vorticity unlikely to be present in the atmosphere. Also, due to the geometry of the apparatus, there exists an imposed vertical velocity at the screen which cannot be accounted for in a real tornado. Finally, a no-slip condition imposed by the top boundary is also in variance with the conditions aloft outside the vortex core in a real atmospheric situation.

Ward, on the other hand, has developed a tornado simulation apparatus which appears to model tornado flow more realistically as well as exhibit several observed properties of natural tornado vortices. Among these features there is specifically at least one that has not been observed by any other apparatus -- namely the "core splitting" phenomenon to be discussed in more detail shortly.

A schematic of the Ward tornado simulation apparatus is shown in Fig. 1.3. The apparatus consists of a cylindrical container eight feet in diameter in combination with a rotating mesh wire on the side

and a fan affixed on the top of the cylinder. As in the Wan and Chang apparatus, the fan power regulates the volumetric flow rate simulating the strength of the updraft. Likewise, the rotation of the mesh wire is intended to provide the ambient circulation in the atmosphere. The fan power as well as the rotation of the mesh wire can be independently controlled in the experiments. An important feature of Ward's apparatus is the existence of a relatively fine mesh honeycomb at the top of the apparatus. The air is passed through this honeycomb mesh which effectively removes the tangential component of velocity from the flow. This is believed to be a significant feature since the vortex is decoupled from the rotation of the fan and hence a more realistic simulation of the conditions at the top of the atmospheric vortex is achieved. The height of the convergent zone is adjustable with the convergent zone aspect ratio (height-to-radius ratio) varying from 1/8 to 1/4. Another unique feature of the Ward's apparatus is that the diameter of the convection zone of updraft is larger than the depth of the convergent zone and the ratio is adjustable (varying from 4 to 2).

Although similar to Ying and Chang and Wan and Chang, Ward's apparatus appears to have several significant differences. First, honeycomb baffle which eliminates the direct effect of the fan-induced vorticity is unique to the Ward apparatus. Thus the exhaust fan simply creates an updraft and, by mass conservation, a radial inflow at the screen. Second, the extent of the circular updraft region which comprises half of the entire radius of the apparatus is much larger than that in other experiments. This is also believed to be a realistic feature of Ward's apparatus in that a small restricted region of updraft is

unlikely to exist in a tornado-producing storm cloud. Third, the aspect ratio of the convergent zone (typically about 1/8) is smaller than that in other experiments. Finally, the large convection zone, above the convergent zone, eliminates teacup-like secondary flows observed in other experiments such as Ying and Chang[7] and Turner[10] (1963). These unique features of the apparatus are believed to result in a more realistic tornado simulation.

Although Ward did not make detailed measurements of the velocity field, several specific features common to natural tornadoes were qualitatively observed in the original experiments performed in the laboratory. Among these observations were vortex breakdown, surface pressure distributions and the "core splitting" phenomenon. Other features such as a recirculating core flow were also observed by Ward using this apparatus.

Among the above observations, there is a great interest in the "core splitting" feature which is observed in natural tornadoes such as the May 24, 1962 tornado at Newton, Kansas;[11] the Palm Sunday tornado of 1965 in Elkhart, Indiana[12] as well as the Fredrick, Oklahoma tornado of June 18, 1973. (See Plates 1.1 and 1.2). Although a relatively common feature of intense tornado vortices, the "core splitting" phenomenon has been observed in the laboratory only in the Ward apparatus (See Plate 1.3). It is believed that the specific geometrical characteristics of Ward's apparatus are responsible for this unique feature.

The usual single line vortex configurations is observed at low values of the swirl angle, ϕ, defined by

$$\tan\phi = \left(\frac{V^*}{U^*}\right)_{screen} \qquad (1.1)$$

where U*, V* are the radial and tangential components of velocity, respectively. However, as the swirl angle increases the observed vortex diameter increases until, at a critical value of the swirl angle, ($= \phi_{cr}$), the single vortex "splits" into two line vortices, symmetrically displaced from the center of the apparatus. The two vortices revolve about the center with constant angular velocity. A sketch of the two configurations is shown in Fig. 1.4. Further increases in the swirl lead to a second critical value with three symmetrically displaced vortices resulting. Occasionally a third critical value of ϕ is observed resulting in four symmetrically displaced vortices.

In the original experiments of Ward, the study of "core splitting" phenomenon, however was rather qualitative and incomplete. Development and verification of any theoretical calculations on this phenomenon required detailed experiments and measurements of the variation of the critical swirl parameter with circulation, height of the convergent zone and the volumetric flow rate.

Previous calculations (Jischke, 1974) had shown that $\tan\phi_{cr}$ varied linearly with the height of the convergent zone, in agreement with the observations of Ward. However, these theoretical calculations were based on a potential vortex model of the flow and ignored some effects of the imposed radial inflow. The verification of the calculations as well as an investigation of the effects of an imposed radial velocity had not been completed. Furthermore, although Ward's apparatus exhibits many of the features of naturally-occuring tornadoes, no detailed information was available as to the nature of the flow. Specifically, no velocity measurements were available to enable a comparison between the

flow field obtained by this apparatus with that of other investigators. In addition, the variation of the radial distribution profile of surface pressure with volumetric flow rate was of interest if a basis for estimating the pressure drop near the core was to be obtained for this flow. The core flow was also completely unknown and no measurements of flow in the core were available. Finally, suggestions for possible improvements of the apparatus for better simulation of tornado flowfield remained unknown. These improvements could be significant for further advances in the laboratory simulation of tornadoes.

There has been many efforts on the theoretical front in the study of concentrated vortices. Most of these studies, however, involve untested simplifying assumptions due to the complicated nature of the governing fluid dynamic equations. Comprehensive reviews can be found by Lilly,[13] Davies-Jones and Kessler[4] and Morton.[14]

Among the studies, for example, leading to exact solutions of simplified equations are those of Burgers[15] and Rott.[6] An exact solution to incompressible, steady state Navier-Stokes equations are developed there for a constant density swirling fluid with uniform horizontal convergence and vertical convection. This solution (which is discussed in more detail in Chapter II and III) exhibits an essentially inviscid outer flow with an inner viscous core in solid body rotation. Simplifications introduced in the governing equations -- specifically that of ignoring the viscous drag by the lower boundary -- seem to limit the application of this model to atmospheric vortices. Furthermore, the dimensions of the core in this solution do not seem to agree with the observations of real tornado cores. We will discuss this in more detail

in Chapter III. Another example is the similarity solution developed by Long[16] for a vortex in an infinite viscous fluid. This solution is also not very useful in the application to atmospheric vortices due to the overriding importance of viscous effects, even in regions far above the ground. The solution also exhibits a singularity on the axis which cannot exist in a real physical situation.

An example of an approximate solution to the flow equations is that of Einstein and Liu[17] for a single vortex configuration in an infinite inviscid fluid. The lack of a vertical component of velocity in the solution for the region outside of the core is not in agreement, however, with observations of tornado flows. As generalization of the solution obtained by Einstein and Liu was developed by Lewellen[18] using an asymptotic expansion involving a small parameter characterizing vortices with large circulation. However, the solution was found not to satisfy all the boundary conditions corresponding to a desired geometry. Assuming only two dependent parameters, Γ (circulation of velocity) and ν (kinematic viscosity), Serrin[19] developed an exact similarity solution of the Navier-Stokes equations for a line vortex in a semi-infinite fluid above the plane $z = 0$. The resulting numerical solution showed three distinct streamline patterns, one of which seems to pertain to tornado-like flows. This streamline pattern-involves a downward-outward flow near the axis with inward-upward outer flow. The inner and outer streamlines merge on a conical surface with half angle α given as a function of tangential Reynolds number, $R_t=\frac{\Gamma}{\nu}$. The similarity solution obtained however, does not show a boundary layer flow. While the solution obtained by Serrin may be valid locally near the vortex-ground intersection, it does not appear to be uniformly valid throughout the

flowfield. The flowfield measurements of the Dallas tornado of April 2, 1957 as well as photographic evidence of other tornado vortices suggest a cylindrical symmetry unlike the similarity solution obtained by Serrin. Furthermore, Serrin's solution neglects the viscous core along the axis resulting in a singular solution with infinite tangential velocity on the axis.

The boundary-layer region of a vortex flow adjacent to a surface has also been subject of numerous studies. However, in almost all of the studies pertaining to a tornado-like flow, the inviscid impressed flow has been assumed to be that of a non-converging flow with zero vertical velocity. Hence the boundary-layer studies are primarily limited to potential vortex flows or similar purely swirling flows. For example, Kuo[20] obtained a similarity solution for the boundary layer produced by a potential vortex near a boundary, assuming the ratio of boundary-layer thickness to a radial length scale to be small everywhere. Barcilon[21] in a study related to dust devils, obtained a boundary-layer solution for vortices driven by buoyancy. Assuming a potential vortex outer flow, the unbalanced radial pressure gradient near the lower plate drives the boundary layer flow toward the core where it is uplifted by byouancy maintaining the updraft necessary for the maintenance of the vortex. Burgraff, *et al.*[22] obtained the solution of the laminar boundary-layer equations associated with a potential vortex over a finite disk. The results, obtained by means of numerical integration of the partial differential equations of boundary-layer theory, suggest a boundary-layer eruption at the vortex axis and show the strong secondary flow induced in the boundary layer by the inviscid pressure gradient. Also the

momentum integral method was used to analyze the turbulent boundary-layer induced by a potential vortex by Weber[23] and Rott, *et al.*,[24] and later modified and compared with experimental results by Chang, *et al.*[25]

Although the variation of tangential component of velocity seems to be accurately described by a potential vortex in the inviscid swirling flow region as Hoecker's observations of Dallas tornado suggests, no such agreement seems to exist for the other components of velocity field in this region. Furthermore, it is believed that boundary-layer calculations for a potential vortex inviscid flow is probably not appropriate to a swirling-converging inviscid flow which seems to be better model of a tornado flowfield. However, no investigation of the structure of the boundary-layer flow due to a turbulent axisymmetric swirling converging flow has yet been made. Such a study could show the effect of both swirl and convergence on the boundary-layer structure. Furthermore, observations in Ward's tornado simulation apparatus indicate a complicated boundary-layer flow structure involving separation in the convection zone of the apparatus. The flow separation in the boundary layer in Ward's apparatus has been observed through smoke visualization of the flow near the lower boundary. It is observed that the streamlines near the ground plane are uplifted from the boundary as they converge toward the core. These streamlines, which presumably form a shear surface separating the converging flow from the back flow in the boundary layer, quickly become unsteady showing small wave-like behavior and turbulence. However, smoke visualization of the flow on the ground closer to the core shows a boundary-layer flow with no separation. Thus,

it is believed that flow separation occurs near the edge of the updraft chamber followed by a reattached boundary-layer flow region near the core. Furthermore, measurements of the radial pressure distribution on the lower boundary in Ward's flow simulation clearly indicate an unfavorable radial pressure gradient near the edge of the updraft chamber. Closer to the axis, however, the pressure gradient becomes extremely favorable as shown by results to be presented in Chapter II. Hence, the measurements of pressure gradient impressed upon the boundary-layer flow also confirm the existence of a separated flow region followed by a reattached boundary layer near the core. Although a full understanding of the separated flows involves a rather complicated task, a study of boundary-layer would shed some light on the flow observed in Ward's apparatus.

The core region of tornado-like vortices has also been subject to observation and study. As stated previously, Hoecker's observations of the Dallas tornado show a single-cell structure of a vortex in solid body rotation with updraft along the axis. Furthermore, it was suggested that the funnel aloft pendant from the cloud possess a double-cell structure consisting of a recirculating flow with downdraft along the axis and updraft along the boundary of the core funnel. The existence of the stagnation point on the tip of the funnel suggests vortex "break down". Many authors such as Soo,[26] Kuo,[20] Glaser[27] and others have assumed a simplified model of a laminar viscous core in solid body rotation in conjunction with an outer inviscid potential vortex flow or similar purely swirling flow. The solution by Rott[6] also exhibits a viscous core with, however, a uniform updraft everywhere including

along the axis. The existence of a downdraft in the central portion of the core associated with an updraft along the boundary of the core is suggested by experiments of Turner,[10] Ying and Chang[7] as well as the observations of Ward[9] as mentioned earlier. An exact double-cell structure solution to the steady-state, incompressible Navier-Stokes equations were developed for an axisymmetric vortex by Sullivan[28] and later a similar recirculatory structure was also suggested by a solution developed by Kuo.[29] Assuming a recirculating flow and using observable features of tornado funnels Dergarabedian and Fendall[30,31] were able to derive a rough estimate of the maximum wind speeds in the proximity of the core in fair agreement with observations. Although the understanding of the details of the core region is essential for a correct modeling of tornado flows, there remains much confusion with regard to the relationship of the tornado flow, the viscous core of solid body rotation and a recirculating core. For example, the spatial relationship between the tornado funnel, the condensation pressure isobar, and the recirculating core flow remain unknown.

The present study is divided into four main parts. The first part, given in Chapter II, comprises the results of a series of experimental observations which were conducted on Ward's apparatus. Section 2.2 is devoted to results obtained in the investigation of the "core-splitting" phenomenon. Using smoke visualization, the variation of critical swirl parameter with aspect ratio was determined for various values of volumetric inflow rate and was compared with previous calculations conducted by Parang. The results proved to be in good agreement with the calculations in which $\tan\phi_{cr}$ was shown to vary linearly with the aspect ratio. Furthermore, a

second series of experiments were performed to determine the effect of the inflow rate on ϕ_{cr} at fixed aspect ratio. An empirical relationship was then developed expressing the dependency of ϕ_{cr} on the volumetric inflow rate in the form of a Reynolds number. In Section 2.3, the results of experiments conducted to measure the velocity field are presented. A three-dimensional probe designed for this purpose was constructed and measurements of the velocity components at different radii and height in both the convergent and the convection zones were carried out. However, the bottom boundary layer as well as the core were excluded in these experiments. The measurements were all carried out for a stable single-cell vortex flow for different values of screen swirl parameters corresponding to different volumetric flow rates. Specifically, three experiments were conducted for three values of volumetric flow rate (including zero inflow corresponding to a pure radial flow), and fixed aspect ratio to compare the effect of the updraft strength on the distribution of velocities. Furthermore, a set of measurement for a small aspect ratio were also obtained to show the effect of comparatively shallower convergence zone on the velocity field. It is observed that the velocity field exhibits certain similarities with those of other experimental simulations of tornadoes as well as certain unique features due to the unique geometry of Ward's apparatus. Also, a series of measurements of surface pressure were obtained, utilizing a static pressure probe, for the convergent and the convection zones of the apparatus. Measurements were made for two different values of inflow rate and these results are presented in this section. The unsteady character of the flow as well as the dimensions of the core flow, however, made

any accurate flow measurements of the vortex impossible. Extensive modifications of the apparatus would be necessary before complete core flow measurements could be carried out. Nonetheless, through the placement of a small propeller in the center of the core flow and the use of a strobe light the angular velocity of the propeller was measured for different values of the swirl parameter. Assuming a linear variation of tangential velocity in the core with the radius, a relationship was developed between the core angular velocity and the swirl parameter. Comparison of these calculations with the measurements showed good agreement. Finally the results of a set of measurements of the independence of the swirl and exhaust controls are given in Appendix A for the sake of completeness.

Chapter III of this work describes a theoretical study of the turbulent boundary-layer region of a tornado-like vortex. Specifically, the momentum integral method is used to obtain the structure of the turbulent boundary layer associated with a more general and, presumably, more realistic inviscid impressed flow. The outer inviscid flow is assumed to be that of a converging swirling vortex flow. The potential vortex, dealt with previously by other authors then corresponds to the special case of zero convergence of the inviscid flow. This swirling, converging inviscid flow allows for the existence of radial and axial velocities outside the boundary layer with these velocities components not necessarily being small compared with the tangential component of velocity. Results are presented for various ratios of the swirl to the flow convergence. As discussed previously, the existence of a nonzero

inviscid radial component of velocity at the boundary layer edge is thought to be of importance in the modeling of tornado dynamics as suggested by Hoecker's observations of Dallas tornado as well as the experimental results obtained using Ward's apparatus. The integrated boundary-layer equations, for reasons to be discussed later in detail, had to be derived in the inviscid streamline coordinate system and, hence, apply to a general impressed flow. Three special cases corresponding to a decelerating, accelerating and a combined decelerating-accelerating converging flow were considered. The latter case is believed to be a good approximation to the flow observed in the Ward's apparatus as suggested in the flow measurements in Chapter II. The equations were numerically integrated for each particular case and the results for different values of the swirl parameter were obtained. The results contain the solution of Chang, *et al.*[25] as a special case and appear to exhibit "separation" for certain ranges of the swirl parameters values.

Chapter IV includes a study of the core region of tornado flows. In particular, certain characteristics of tornado core are discussed based on the Hoecker's observation of Dallas tornado. A four "funnel" inner structure is proposed for tornado core flows and an investigation of condensation of water vapor in the vicinity of core using Hoecker's measurements are included to substantiate the distinction between two different "funnels" in the core region. Although the calculations are based on order of magnitude analysis and hence are only crude estimates, the distinctions proposed appear justified.

Finally, in Chapter V concluding remarks are presented based on the experimental evidence obtained in Ward's apparatus as well as the

boundary-layer calculations. A dynamic model of a tornado flow is proposed and suggestions are made for further experimental investigations as well as possible improvements of Ward's apparatus. A discussion on further future theoretical studies are also presented in this concluding part of the work.

CHAPTER II

EXPERIMENTAL OBSERVATIONS

2.1. Introductory Remarks

The experimental observations of Ward's tornado simulation apparatus were motivated by the observation of features similar to those observed by naturally-occurring tornadoes. The most unique feature of Ward's simulated tornado was the multiple vortex formation or "core splitting" phenomenon. Thus, along with the complete measurements of a single vortex flowfield, observations of the transition to multiple vortex flows were also conducted. The flow measurements, however, excluded the core flow region and the boundary layer produced on the bottom boundary. The small dimensions of these regions and extreme sensitivity of the core flow to small disturbances made the measurements with a conventional pitot tube impossible. However, some general observations of the core flow as well as core angular velocity measurements were possible and were conducted. The results of these observations are also included in this chapter.

Before a description of the experiments is presented, however, some preliminary comments concerning the apparatus and certain problems that had to be overcome in initial phase of experimentations are in order.

The first problem was that of flow visualization. The importance

of a good visualization technique which could reduce the disturbance of the flow to a minimum is clearly obvious. This is especially true of vortex flows where small disturbances tend to be amplified near the center of the vortex flow. Hence in the measurement of the critical swirl parameter necessary for the transition from a single-vortex flow to a two-vortex flow, for example, disturbances of the flow could cause large errors in the measured values of ϕ_{cr}. Furthermore, the visualization of the flow had to be continuous if the transition to a double vortex was to be clearly observed. This is important since the transition occurs suddenly as the flow parameters -- *e.g.* volumetric flow rate -- are changed. The problem was resolved by a continuous slow injection of titanium tetrachloride (T_iCl_4) through a small hole in the center of the lower boundary of the apparatus. When mixed with slightly humid air, T_iCl_4 forms a dense white smoke which is easily visualized. The injection of T_iCl_4 was made possible by means of a gravity feed from a small burette outside of the apparatus. Thus there was a minimum disturbance of the flowfield by this technique.

The second problem was that of calibration. The swirl angle was measured directly by a wind vane located near the screen. The exhaust fan and screen were driven by two identical small motors each connected to a transformer. One of the two identical transformers, then, controlled the volumetric flow rate and the other the swirl given to the flow by means of the screen. Although the screen velocity was fixed for most of the measurements, the volumetric flow rate had to be changed in different experimental measurements. Hence the exhaust fan power had to be calibrated for volumetric flow rate. This was achieved by directly

measuring the velocity at the screen for different values of the fan power setting. The volumetric flow rate was then directly calculated from the measured value of the velocity and the dimensions of the apparatus.

There also were problems relating to the unsteady fluctuations in the vortex flowfield. There are, at least, four causes of these fluctuations. The first cause is due to the fact that the flow is exhausted to the ambient air outside of the room through a discharge tunnel. The variation in wind velocity due to gusting conditions outside the laboratory was clearly seen to effect the volumetric flow rate through the fan. The second cause could be found in the design of the gear system connecting the motor and the rotating meshwire screen. This caused disturbances in the flow which, after amplification in the central part of the apparatus, caused severe fluctuations and created substantial inaccuracies in measurements. The two other possible reasons contributing to the scatter in the data are due to the surges in the power source as well as in the electrical equipments used in operating the fan and the screen.

Although it is impossible to completely eliminate noise and fluctuations, care was taken to reduce the effect of these fluctuations and flow unsteadiness. For example, all experiments were conducted at night when wind gusts were at a minimum. Likewise, within the framework of the existing design of the apparatus, every effort was undertaken to improve the quality of the parts incorporated within the apparatus. However, suggestions for a better design and possible modifications and improvements for a more noise-free experiment can be made and they will be discussed later.

2.2 Multiple Vortex Formation.

The single vortex flow observed in Ward's apparatus is a stable flow only within certain range of the ratio of the swirl to convergence of the flow. This ratio can be expressed in terms of the swirl parameter defined as the ratio of the tangential to the radial components of velocity at the edge of the apparatus. That is, the swirl angle ϕ is defined by

$$\tan\phi = \left(\frac{V^*}{U^*}\right)_{screen} \quad . \tag{2.1}$$

An increase in the swirl parameter corresponding to an increase in ϕ results in a stable single vortex flow configuration only below certain values of ϕ. Increases in ϕ result in increases in the diameter of the vortex core. Ward's observations of the variation of the core diameter with swirl angle ϕ were shown to be proportional to $\tan^2\phi$.

The single vortex is observed to be unstable at a critical value of the swirl angle, ϕ_{cr}. Increasing ϕ beyond ϕ_{cr} results in a sudden replacement of the single vortex configuration by a two-vortex system displaced symmetrically with respect to the center of the apparatus. The vortices were observed to rotate about the center of the apparatus in the direction of the swirling outer flow. This configuration also proved to be unstable for values of ϕ above a second critical swirl angle. An increase in ϕ beyond the first critical value would result in further separation of the two vortices until at a second critical value of ϕ, configuration is suddenly replaced by a three-vortex system. A four-vortex system can also be produced by Ward's apparatus for sufficiently large values of ϕ.

The multiple vortex formation is believed to be related to the advection of vorticity produced at the boundary. Flow convergence results in concentration of the vorticity produced in the boundary layer around the basic vortex. The existence of a downdraft along the axis with an outward radial flow observed through smoke visualization then is responsible for concentrating this vorticity produced in the boundary layer in a ring-shaped region around the basic vortex. The existence of this shear layer ring is believed to be responsible for the "core splitting" observed at even relatively small values of ϕ. That is, the reason for "core splitting" should probably be sought in the instability of the ring-shaped shear layer concentrated around the basic vortex. Increasing the imposed swirl results in a larger downflow (larger diameter of the core) and an increase in the vorticity produced in the boundary layer. Sufficiently close to the critical values of ϕ, the unstable ring-shaped shear layer about the vortex is then reorganized into two concentrated vortices separated by an irrotational flow as observed in the experiments.

Due to the complexity of the flow, a conventional stability calculation in which the effect of small perturbation on the basic vortex flow is investigated, was ruled out. Instead, the application of certain basic concepts of mechanics allows an upper bound for the swirl angle ϕ in a single vortex flow configuration.to be estimated. These calculations are given in detail in Ref. 5 . Briefly, by application of Newton's second law under steady state conditions, it is shown that for a single-vortex configuration the rate at which angular momentum flows into the apparatus could be exceeded by the net torque exerted

by the boundary of the apparatus on the flow at sufficiently large values of ϕ. This is obviously an impossible situation and the single vortex configuration is not dynamically possible at these values of ϕ.

Specifically, the rate at which angular momentum flows into the apparatus, M, is

$$M = \rho h \, r_s \Gamma U_s^* \tag{2.2}$$

where Γ, r_s and U_s^* are the circulation of the velocity at the screen ($2\pi r_s V_s^*$), the radius and the radial velocity at the screen, respectively. Note that M varies linearly with Γ at fixed h, r_s and U_s^*. The torque T exerted by the boundary on the flow is due primarily to viscous forces acting at the boundary of the apparatus. This torque varies nonlinearly with Γ. Assuming a single line vortex configuration, T varies approximately as $\Gamma^{3/2}$ for a laminar flow and $\Gamma^{9/5}$ for a turbulent flow. It can be shown that the contribution of the core region to the total torque is negligible (more detailed calculations verify this assumption[32]). Hence neglecting the region close to the core and assuming an attached turbulent boundary layer, T increases more rapidly with Γ than M. Thus for Γ sufficiently large, T will exceed M and, as mentioned earlier, this situation is dynamically impossible. We can conclude then that when the calculated value of T (determined assuming a single line vortex configuration is greater than N, the assumption of a single line vortex configuration is not valid. It can be shown further that if one assumes the single line vortex of strength Γ undergoes transition to a two-vortex configuration, each vortex being of strength $\Gamma/2$, the resulting torque exerted by the two vortices is less than that of the single vortex of strength Γ. Thus, for situations where the single vortex flow is dynamically impossible, the two-vortex flow is dynamically possible.

The critical condition for transition occurs when the rate at which angular momentum flows into the apparatus M equals the torque exerted by the ground on the single vortex flow T_{cr},

$$T_{cr} = M = (\rho h r_s \Gamma U_s^*) \quad . \tag{2.3}$$

A result for ϕ_{cr} follows once T_{cr} is known. One can estimate T_{cr} from the result for the torque T_1 due to a disk rotating in a fluid at rest. One then obtains

$$T_1 = 0.0093 \rho \nu^{1/5} \Gamma^{9/5} r_s \tag{2.4}$$

for turbulent flow. This result neglects the effect of the volumetric flow rate Q on the torque. Thus from Eqs. (2.3) and (2.4), we have

$$\tan \phi_{cr} = \text{Const.} \frac{h}{r_s} \left(\frac{Q}{r_s \nu}\right)^{\frac{1}{4}} \quad . \tag{2.5}$$

Thus, for a fixed Q, $\tan\phi_{cr}$ varies linearly with h/r_s, a result which agrees to within about 13 per cent with the results obtained by Ward. However, the results obtained by Ward were for various values of Q, not a fixed value. Thus it was necessary to conduct experiments to overcome this limitation of Ward's data as well as determine the effect of the inflow on the torque exerted on the flow by the boundary. Hence experiments were conducted in which the variation of ϕ_{cr} with both the aspect ratio, h/r_s, and the volumetric flow rate, Q, were measured. The results are presented in Table I.

The vortex transition in each observation was made visible through a small continuous injection of $T_iC\ell_4$ through a small hole in the center of the apparatus as discussed before. Measurements were begun by setting the fan power transformer to zero power and then increasing

Table I. Variation of $\tan_{cr}$ with cylindrical height (h) for different volumetric flow rates (Q).

h/r_s \ Q(ft^3/sec)	22	27.9	32.4	35.6	38.8	42.4	44.6	50.8	55.4
.242	.573	.539	.530	.522	.496	.488	.479	.460	.429
.287	.729	.690	.665	.601	.596	.580	.577	.547	.531
.315	.857	.776	.754	.735	.716	.669	.675	.652	.615
.35	.959	.959	.893	.857	.839	.798	.788	.771	.744
.392	1.005	.933	.919	.90	.859	.858	.861	.841	.826
.421	1.084	1.013	1.042	1.021	1.00	.974	.994	.974	.949

the power to the desired value. The screen angular velocity was then gradually increased from zero by means of a separate power transformer until the single vortex configuration was observed to "split" into a two-vortex configuration. A sketch of the two configuration is shown in Fig. 1.4. The swirl parameter at this critical condition was then measured by a wind vane and the critical values of the screen and exhaust fan power were read from the transformers.

After each data point was obtained, the transformers were set to zero and the flow was brought to rest. There are two reasons for bringing the flow to rest and zeroing the transformers. First, single and multiple vortex flows exhibit a hysteresis behavior. That is, after a "forward" transition from the single vortex condition to a two-vortex condition occurred, the flow would not undergo a "backward" transition to a single-vortex condition until the swirl angle was significantly less than the "forward" critical value. Hence, data obtained for ϕ_{cr} might vary if the initial conditions of the flow were different. Second, the transformers were always set at their desired values by increasing from zero in order to avoid hysteresis behavior in the electrical instruments (*e.g.* screen motor, fan motor, and transformers). Measurements were repeated to ensure the absence of any such hysteresis effect.

The variation of $\tan\phi_{cr}$ with volumetric flow rate Q for different aspect ratios h/r_s is presented in Figs. 2.1-2.6. These data show that the critical value of the swirl parameter decreases with increasing volumetric flow rate Q at a given aspect ratio h/r_s. Furthermore, for a given Q, the values of $\tan\phi_{cr}$ increase with h/r_s in an approximately linear way as shown in Fig. 2.7 for Q = 42.4 ft^3/sec. Thus, although

the linear variation of $\tan\phi_{cr}$ with h/r_s for a fixed Q obtained theoretically in Ref. 5 appears to remain valid, the effect of volumetric flow rate Q on $\tan\phi_{cr}$ is not correctly given by Eq. 2.5.

The measured relation between $\tan\phi_{cr}$, h/r_s, and Q can be empirically correlated by

$$\tan\phi_{cr} \propto \frac{h}{r_s}\left(\frac{Q}{r_s\nu}\right)^{-11/30} , \tag{2.6}$$

within the range of experimental values obtained. This relationship implicitly assumes

$$\phi_{cr} \to 0 \quad \text{as} \quad Q\to\infty \tag{2.7a}$$

$$\phi_{cr} \to \pi/2 \quad \text{as} \quad Q\to 0 \quad . \tag{2.7b}$$

We have chosen to write the Q dependence in Eq. (2.6) in terms of $(Q/r_s\nu)$ as this is a nondimensional quantity (a radial Reynolds number) and both r_s and ν did not vary throughout the experiments. Now $\tan\phi$ is defined such that

$$\tan\phi_{cr} \propto \left(\frac{\Gamma}{r_s U_s^*}\right)_{cr} . \tag{2.8}$$

Thus, we conclude from Eqs. (2.6) and (2.8)

$$\Gamma_{cr} \propto \left[r_s U_s^* \frac{h}{r_s}\left(\frac{Q}{\nu r_s}\right)^{-11/30}\right]_{cr} . \tag{2.9}$$

The result for M, the rate at which angular momentum flows into the apparatus, can be written

$$\begin{aligned} M &= \rho h r_s \Gamma U_s^* \\ &= \rho \Gamma^{9/5} r_s \left(\frac{h U_s^*}{\Gamma^{4/5}}\right) . \end{aligned} \tag{2.10}$$

Substituting for Γ from Eq. (2.9) and equating this to T_1 for the

critical condition, we have

$$\frac{T_1}{T_{1_{theor.}}} \simeq \left(\frac{Q}{\nu r_s}\right)^{\frac{1}{2}} \tag{2.11}$$

where $T_{1_{theor.}}$ is the result given by Eq. (2.4). Thus the experimental results indicate that the factor $(Q/\nu r_s)^{\frac{1}{2}}$ should be included in Eq. (2.4) to empirically compensate for the neglected effect of the radial inflow in that result.

The cause of the scatter in data in Figs. 2.1-2.7 is believed to be the fluctuations in volumetric flow rate. The two most important reasons for these fluctuations are the ambient wind gusting and power surges in the electrical system which were discussed previously. It can, however, be safely concluded from the experimental results that the critical swirl parameter necessary for "core splitting" varies linearly with the convergent zone aspect ratio, h/r_s. Furthermore, the variation of the critical swirl parameter with volumetric flow rate, Q, can be correlated by $(Q/r_s\nu)^{-11/30}$. Although the former results were predicted theoretically in Ref. 5 using a single line potential vortex, the latter is not obtained assuming the same model.

2.3 Velocity Measurements.

Velocity measurements were made with a pitot-static tube. The pitot-static tube measures the difference between the static pressure p and total pressure p_o from which the velocity V can be deduced according to the Bernoulli equation

$$p_o = p + \tfrac{1}{2}\rho V^2 \ . \tag{2.12}$$

As the pitot-static tube must be aligned with the flow direction to measure both p and p_o, the tube was mounted on a traverse mechanism (Plate 2.1) which allowed placement and orientation. Briefly, the traverse mechanism consisted of two arms OA and OB of equal length, two graduated circular unislides B and C, and a vertical unislide D. The unislides were manufactured by Velmex, Inc. The arms OA and OB were riveted at one end to the pitot tube and at the other to the circular unislide B. It was then possible to rotate the pitot tube to any desired angle Θ by rotating unislide B as shown in Fig. 2.8. This assembly was attached to the vertical unislide D allowing placement of the pitot tube at any desired height z above the lower boundary. Finally, by placing unislide D and its attachments on the larger circular unislide C as shown in Fig. 2.8, the pitot-static tube could be directed to any desired azimuthal angle ϕ.

Alignment of the pitot-static tube with the flow direction required knowledge of the two spherical polar coordinate angles θ and ϕ that the velocity vector makes with respect to specified axes (in the radial and vertical directions). In principle, the pitot-static tube, itself, could be used for this purpose as the total pressure is maximized when the tube is aligned with the flow. However, the small dynamic pressures along with the unsteadiness in the flow made this method of alignment impractical. While electronic filtering of the pressure signal may have made this method feasible, both funds available and time dictated a simpler and cruder approach. A small wind vane was designed which could be attached directly to the ends of the arms OA and OB of the traverse mechanism. The small vane was set horizontally and

vertically and the angles θ and ϕ were measured. Once the angles were determined, the pitot-static tube was then aligned with the flow through manipulation of the two circular unislides. While this method of alignment was satisfactory for most of the flowfield, the dimensions of the wind vane made measurement of the flow direction near the boundaries impossible by this technique. To overcome this difficulty, $T_iC\ell_4$ smoke was introduced into the flow making it possible to visualize the streamline containing the point of interest. The pitot-static tube was then aligned with the smoke; that is, with the direction of the streamline passing through the point of interest. Thus, the direction of the velocity vector at different points in the flow was measured using a wind vane and the $T_iC\ell_4$ smoke.

The differential pressure output from the pitot-static tube was inputed to a Barocel pressure sensor (type 511) connected to a Barocel electronic manometer (type 1012). The signal from the electronic manometer was then recorded on a strip chart recorder. Thus, by measuring the total velocity V at any point in the flow and the angles θ and ϕ, the three components of velocity V*, V*, W* (referred to as cylindrical polar coordinates) at any point (r,z) could be calculated.

Velocity measurements were made for two values of the volumetric flow rate Q (approximately 47 ft^3/sec and 35 ft^3/sec) with the height h fixed at 12" (corresponding to an aspect ratio of $\frac{1}{4}$). We shall refer to the data obtained with Q equal to 47 ft^3/sec and 35 ft^3/sec as Cases I and II, respectively. A third set of measurements, Case III, were made with Q equal to approximately 47 ft^3sec and h equal to 6" (corresponding to an aspect ratio of $\frac{1}{8}$). The screen velocity v_s was held

constant for all of the measurement. The imposed swirl angles were 5° and 8° for the Cases I and II while ϕ was equal to 2° for Case III. Finally, a fourth and fifth set of measurements, Cases IV and V, were made with Q = 47 ft^3/sec and 35 ft^3/sec and the screen velocity set to zero -- i.e. purely radial flows. The various cases are listed in Table II.

Figures 2.9, 2.10, and 2.11 give the measured variation of the radial, tangential, and vertical components of velocity (that is, U^*, V^*, W^* respectively) with height z at different radii for Case I. Figures 2.12, 2.13, and 2.14 give the same results for Case II while Figures 2.15, 2.16 and 2.17 give the results for Case III. Figures 2.18, 2.19, 2,20 and 2.21 give the radial and vertical velocities for Cases IV and V, respectively.

The data in the outer convergent zone (42">r>24") show that the radial velocity U^* outside the boundary layer does not vary with height z. The flow in this region is similar to radial flow between parallel plates with a variation in the radial direction only. As shown in Figs. 2.9, 2.12 and 2.15, the radial velocity increases with decreasing radius due to conservation of mass. Near the beginning of the convection zone (r = 24"), the flow near the top of the convergent zone is accelerated as it is convected upward. This "edge effect" is most apparent in the rapid increase in the radial velocity U^* at r = 24", especially near z = h. The edge effect diminishes as the radius decreases below 24". However this edge effect is still evident at r = 18" where there is a slight increase of U^* at the larger values of z. Also, near the vortex at the center of the apparatus, there is a slight increase in the radial velocity near the bottom boundary. This increase in U^* grows toward the center.

Table II. Various cases of flowfield used in the experiments.

Case	Q (ft^3/sec)	ϕ (degrees)	h (in)
I	47	5	12
II	35	8	12
III	47	2	6
IV	47	0	12
V	35	0	12

In all cases, the radius r_s of the screen was held fixed at 48" and the radius r_u of the convection zone was held fixed at 24".

Away from the bottom boundary, however, the radial velocity decreases with decreasing radius. Figures 2.22, 2.23, and 2.24 show that U^* decreases with decreasing r in an approximately linear fashion in the inner convergent zone. The behavior of the radial velocity in Case II seems to provide an exception to the linear behavior. Specifically, the values of U^* at r = 12" and r = 8" with z = 6" are almost the same. Examining Fig. 2.12, we note that this is due to the radial acceleration as r tends to zero near the lower boundary. Indeed, if we had plotted U^* versus r for z less than 6", U^* would increase as r approaches zero while for z greater than 6", U^* would decrease as r approaches zero. This seemingly unusual behavior, however, is, to a smaller degree, present in Case I as well as in Case III. A study of the vertical profiles of radial velocity in Cases I and II given in Figs. 2.9 and 2.12 clearly demonstrate this fact. The radial component of velocity at r = 12" in both cases show a distinct increase indicating an accelerating flow near the ground. This acceleration seems to continue and the relative growth of the measured values of the radial component of velocity is clearly visible at r = 8". This phenomenon is believed to be associated with the separation of the boundary layer on the lower boundary. The flow separation seems to occur somewhere between r = 24" and r = 18" with the particular values of swirl parameter in Cases I through III. The separation is due to a slightly adverse pressure gradient imposed on the boundary layer in this region. The resulting flow is probably an attached symmetric recirculatory eddy flow which extends horizontally far into the convection zone near the basic vortex. A sketch of a meridional cross section illustrating this separated flow is shown in

Fig. 2.25. In fact, by means of flow visualization, it can be observed that the flow streamlines near the bottom boundary are clearly curved upward as they extend into the convection zone. Furthermore, smoke introduced near the center indicates a "reattached" turbulent boundary layer at the ground near the center of the apparatus. This reattachment is believed to be due to high swirl in the flow near the core corresponding to a large local swirl parameter. Although a boundary-layer flow measurement should be conducted for a better understanding of the flow structure in this region, a boundary layer calculation based on an approximately similar model of Ward's inviscid flow would be helpful in clarifying some of the ambiguities in this flow regime. Such a calculation along with the discussion of the results is given in Chapter IV.

The tangential velocity V^* is observed to remain relatively constant with height z at any fixed radius r. One exception to this is the small deviation near r = 24" which is due to the "edge effect." The second exception is the increase of V^* near the bottom boundary in Cases I and II which is similar to the variation of the radial velocity U^* and is also believed to be associated with flow separation. The relative lack of variation of V^* with z remains otherwise true throughout the flow.

The vertical velocity W^* is very small in the outer convergent zone (r>24"). However, a rapid increase occurs at r = 24" due to the imposed upward convection. In the inner convergent zone (r<24") the vertical velocity W^* increases almost linearly with height z for any particular value of r. The rate of increase of W^* with z appears to decrease slightly as r decreases.

A comparison of these results with a theoretical model is of

interest. The Rott-Burgers vortex[15] is an exact solution of the Navier-Stokes equations and is often used as a model of natural vortices. This flow is given by

$$U^* = -ar, \quad V^* = \frac{\Gamma_\infty}{2\pi r}\left[1-\exp\left(-\frac{ar^2}{2\nu}\right)\right], \quad W^* = 2az \qquad (2.13a\text{-}c)$$

where a is a positive constant and Γ_∞ is the constant value of the circulation far from the axis r = 0. For values of r sufficiently large relative to the "core" size (the core is a region of solid body rotation with extent of the order of $\sqrt{2\nu/a}$), the Rott-Burgers solution can be approximated by that of a potential vortex with a superimposed meridional flow,

$$U^* = -ar, \quad V^* = \frac{\Gamma_\infty}{2\pi r}, \quad W^* = 2az \quad . \qquad (2.14a\text{-}c)$$

As shown in Figs. 2.22, 2.23, and 2.24 the radial velocity U^* varies approximately linearly with r for r < 24". The vertical velocity W^* is also seen to have a linear variation with z. And sufficiently far from the edge of the convection zone (r = 24"), W^* remains almost independent of r. Finally, the tangential velocity varies roughly like 1/r. This is shown in Fig. 2.26 where depth averaged values of (rV^*) are presented for comparison with the theoretical model (rV^* = constant). The comparison is fair for Cases I and II and rather poor for Case III. This poor comparison with Case III is attributed, in part, to the high level of flow unsteadiness in that case, especially in the inner part of the convergent zone. Thus the present results seem to agree qualitatively with the Rott-Burgers vortex. However, the size of the observed core cannot be made to agree with the Rott-Burgers result for any reasonable value of the viscosity ν. The significant difference in the core size indicates

a difference in the core flow. The observation of Ward's flow as well as naturally-occurring tornadoes suggest a fundamentally different structure for the core than the proposed model of the Rott-Burgers vortex. We shall discuss this question further in Chapter IV.

Among the factors that could be responsible for errors in measurements was the flow sensitivity to ambient wind gusts. Efforts were made to minimize the effects of the ambient winds on the flow. All experiments were performed at night with velocity less than five miles per hour. This greatly limits the number of evenings when experiments can be run. Other factors contributing to the experimental uncertainty were the warping of the meshwire screen and slippage between the screen and the linkage connecting the screen motor and the screen. In general, this unsteady flow behavior is amplified near the core region and, as observed, the data scatter is substantially higher in this region. Also, the unsteadiness was more pronounced for the higher values of the radial velocity U^* at the screen. Finally, there were errors associated with the visual alignment of the pitot-static tube with the flow direction which also contribute to the data scatter. This is especially true near the center of the convergent zone where the unsteadiness in the flow is amplified.

2.4 Surface Pressure Measurements.

The earlier theoretical calculations[5] emphasize the importance of the flow in the viscous boundary layers on the walls of the apparatus. Calculation of the flow in the bottom boundary layer requires knowledge of the pressure gradient impressed on it. This pressure gradient is, to within the order of the error of classical boundary layer theory, the

same as that acting on the bottom boundary. The pressure distribution acting on this surface was obtained for Cases I and II (h = 12", V_{screen} = 0.13 ft/sec, and Q = 47 ft^3/sec and 35 ft^3/sec., respectively). Measurements were made at eleven radial stations. These stations were closer together near the vortex at the center of the apparatus where the pressure changes most rapidly. The pressures were all measured relative to ambient. The results are shown in Fig. 2.27.

The results show that the pressure remains relatively constant in the other convergent zone (r>18") and decreases rapidly in the inner convergent zone (r<18"). The difference between the two sets of data is significant only in the inner regions. For Case I a slight relative minimum is observed in the surface pressure distribution in the region r>24". While this agrees with the results obtained by Ward, the extent of the decrease is not as pronounced as that obtained in Ref. 9. Although the measured decrease is not significant, the pressure "hill" is probably sufficient for boundary layer separation to occur. Furthermore, the minimum is seen to occur in the proximity of the boundary of the convergence and convection zone. Hence these observations seem to be consistent with the behavior of the visualized streamlines near this point.

For r less than about 18", the pressure varies almost as r^{-2}. Thus the pressure in the inner convergent zone can be described to within the order of accuracy of the experimental data, as that of a potential vortex. We shall return to this point later, when a boundary layer calculation corresponding to Ward's flow model is discussed.

Because of the unsteady character of the vortex and possible

flow separation, high frequency, turbulent-like oscillation in the pressure were observed near the center of the flow (especially at r = 0" and r = 1"). This unsteadiness, of course, contributes significantly to the inaccuracies in the data.

2.5 Core Angular Velocity Measurements.

The unsteadiness of the vortex itself and its sensitivity to disturbances by the instruments available made detailed velocity surveys in the vortex core impossible. This does not of course diminish the interest in and importance of data on the core structure. Flow visualization using $T_iC\ell_4$ smoke indicated that the vertical velocity along the axis of the vortex was downward suggesting a recirculating meridional flow in the core.

In order to obtain some understanding of the tangential velocity in the vortex core, measurements of the core angular velocity were conducted. A small propeller, designed for this purpose, was placed inside the vortex core. Provided the propeller is sufficiently small, its angular velocity should be equal to the angular velocity of the fluid at the center of the vortex core (e.g. one-half the vertical component of vorticity). The angular velocity of the propeller was measured by means of a strobe light. Data was first obtained for various values of the volumetric flow rate Q keeping the screen velocity fixed. Three sets of data were obtained for three different values of V_s (approximately 0.13, 0.18, and 0.23 ft/sec). The depth of the convergent zone was held constant at 12" for all measurements. The results are given in Fig. 2.28 where the period of rotation $\tilde{T}$ is plotted as a function of the fourth power of the tangent of the swirl angle, $\tan^4\phi$. The data shows that $\tilde{T}$ varies almost linearly with $\tan^4\phi$.

This result agrees quite well with a calculation based on a modified Rott-Burgers model of the vortex. The angular velocity ω at the center of the vortex core is

$$\omega = \frac{2\pi}{\tilde{T}} = \frac{\Gamma}{2\pi r_c^2} \quad , \tag{2.15}$$

where r_o is the actual radius of the vortex core and Γ_∞ is again the constant circulation far from the axis of the vortex. It has been shown theoretically[5] and experimentally[9] that the core radius r_c varies with the swirl angle ϕ according to

$$r_c = r_s \tan^2\phi \tag{2.16}$$

where r_s is the radius of the convergent zone. Substituting Eq. (2.16) in Eq. (2.15) we obtain

$$\tilde{T} = \frac{4\pi^2 r_s^2}{\Gamma} \tan^4\phi \quad , \tag{2.17}$$

which compares quite favorably with the experimental results. That is, for fixed V_s, corresponding to fixed Γ , $\tilde{T}$ varies linearly with $\tan^4\phi$.

In a related set of experiments the angular velocity of the propeller was measured for different values of the screen velocity at a constant volumetric flow rate Q for three different values of Q (57.8, 50.8, and 38.8 ft^3/sec). The experimental results are given in Fig. 2.29 where the period $\tilde{T}$ is plotted as a function of $\tan^3\phi$. A corresponding theoretical result can also be obtained. The circulation Γ_∞ is given by

$$\Gamma = 2\pi r_s V_s^* \tag{2.18}$$

which can be rewritten

$$\Gamma = 2\pi r_s U_s^* \tan\phi \tag{2.19}$$

or

$$\Gamma = \frac{Q}{h} \tan\phi \quad . \tag{2.20}$$

Substituting this result in Eq. (2.17), we obtain

$$\tilde{T} = \frac{4\pi r_s^2 h}{Q} \tan^3\phi \tag{2.21}$$

Hence with Q and h held fixed, T varies linearly with $\tan^3\phi$. This theoretical result compares favorably with the experimental data in Fig. 2.29 except for small angles (less then 8°). The deviation between theory and experiment at small values of the swirl angle is attributed to the unsteadiness of the flow for small swirl angles (high radial velocity at the screen U_s) as described earlier. The small radius of the observed core relative to the propeller size is also believed to be a factor contributing to the scatter of the data at low swirl angles.

In the measurements of the core angular velocity, care was taken to avoid transition to a two-vortex configuration. It was observed, however, that upon transition to a two-vortex configuration, the propeller (which was positioned in the center of the apparatus) showed no significant rotation. This verifies the assumption made in the theoretical calculation of Jischke and Parang[5] that the two-vortex system can be modeled as two viscous line vortices with an essentially irrotational, potential vortex flow outside the viscous cores of these vortices.

2.6 Summary.

In summary, the main features of the simulated tornado flowfield can be described as follows. First, sufficiently far above the lower boundary, the radial and tangential components of velocity can be assumed to vary only with radius. This is approximately true throughout the convergent and lower updraft flow regions. Furthermore, the radial velocity can be assumed to vary as -1/r in the convergence zone and as -r in the updraft region of the apparatus. The tangential velocity exhibits a behavior similar to a potential vortex flow. That is, $v^* \sim 1/r$ outside the core. The "edge effect" will be ignored. The radial variation of the pressure also behaves as $1/r^2$ in the updraft zone similar to the potential vortex flow. Hence, the pressure field is approximated by the cyclostrophic balance in the radial momentum equation,

$$-\frac{1}{\rho}\frac{\partial p}{\partial r} = \frac{V^{*2}}{r} \quad , \tag{2.22}$$

in this region. Finally, a linear variation of the tangential velocity component in the core is consistent with the experimental results obtained herein.

It is important, however, to note that a more detailed flowfield could be described. This formulation would include the effect of the separation of the boundary layer, especially near the core region. Also, such a description should include details of the interaction of the separated flow with the pressure field imposed on the boundary layer. In spite of this, a more simple and straightforward approach will be taken here. It is believed that the above-mentioned form of the velocity

field as well as the radial variation of the surface pressure are a sufficiently good approximation to the results obtained in the experiments. Furthermore, the simple analytical form of these approximations allow a boundary layer calculation to be conducted. It should be further stated that although such important factors as the interaction of the separated flow and the inviscid flow region is not included, it will be shown that the existence of a flow separation is suggested by the bonndary layer calculations to be described shortly.

Hence, a swirling-converging flow field can be assumed to be a good approximation to the flowfield in Ward's apparatus. This velocity field is given by

$$U^* = U^*(r), \quad V^* = \frac{V_{ref}}{r} \tag{2.23a-b}$$

with the vertical velocity W^* following from mass conservation as

$$W^* = -\frac{z}{r}\frac{d}{dr}[rU^*(r)] \tag{2.24}$$

in agreement with observations.

Furthermore, the radial velocity behaves approximately as

$$U^*(r) \sim -\frac{1}{r} \qquad \text{in the convergent zone} \tag{2.25a}$$

$$U^*(r) \sim -r \qquad \text{in the convection zone .} \tag{2.25b}$$

This swirling converging flow, presumably an accurate model of a tornado flowfield, is utilized in subsequent chapters of this work.

CHAPTER III

BOUNDARY LAYER OF A TORNADO-LIKE VORTEX

3.1 Introductory Remarks.

In this chapter we shall investigate the boundary-layer structure associated with a vortex flow model. This region of the vortex flow is of great interest -- especially in tornadoes -- for several reasons. First, it is in this region that the people and their structures are located. Hence an accurate estimate of wind velocities in this region is of importance. Second, the debris pattern and the damage to trees and grassy fields produced by tornadoes are also principally due to the flowfield in this region. Since the observations of the damage pattern is one of the few available means of investigating naturally-occurring tornadoes, a knowledge of boundary-layer structures could enhance understanding of the overall flowfield of these intense vortices. Third, the boundary-layer region has been suggested as being responsible for the phenomenon of "core splitting" observed in Ward's apparatus as well as in the naturally-occurring tornadoes. An accurate estimation of the torque exerted on the flow by the lower boundary can only be found, however, by a boundary-layer calculation using a realistic model of the inviscid flow.

All of the previous investigations of the boundary layer region of vortex flows over a surface have been limited so far to that of a pure potential vortex [Burgers, Long, and Einstein] as discussed before.

But this flow is not an adequate model of the vortex flows associated with tornadoes in that they ignore the flow convergence imposed on the boundary layer. The existence of a radial component of velocity can be deduced from the measurements of the 1957 Dallas tornado as well as in Ward's apparatus. Furthermore, the potential vortex model of the tornado is a special case of the more general class of swirling converging flows. It is not likely that the complicated flow structure of a tornado can be accurately modeled by the relatively special swirling flow with updraft limited only to a narrow region of the core. A swirling, converging flow model which allows for a wide range of the values of the swirl parameter (swirl to convergence ratio) is more likely to describe the great variety of intensity, shape and wind velocities observed in tornadoes.

Hence the turbulent boundary-layer due to a swirling, converging axisymmetric steady flow with constant density over a finite circular disk of radius R was investigated using Von Karman's [1921] integral momentum method. The boundary layer equations were developed for the inviscid flowfield given by

$$U^* = U^*(r,z) \ , \qquad V^* = \frac{\Gamma}{2\pi r} \ , \qquad W^* = W^*(r,z) \ . \tag{3.1}$$

The tangential component is that of a potential vortex which (except for $V^*=0$) is the only inviscid solution to the constant density axisymmetric flow equations (no body force) for which V^* is a constant at some radius $r = R$. Near the ground ($z = 0$), the meridional flow has the form

$$U^* = U^*(r), \qquad W^* = -\frac{z}{r}\frac{d}{dr}[rU^*(r)] \ . \tag{3.2}$$

While the theory to be developed will be valid for arbitrary $U^*(r)$, there is particular interest in the cases

$$\text{(i)} \quad U^*(r) \sim -\frac{1}{r}$$

$$\text{(ii)} \quad U^*(r) \sim -r \tag{3.3}$$

corresponding to the regions of low-level convergence and updraft, respectively, in the Ward's tornado flow simulation. Also a third case of a converging-convecting flow composed of a mixed solution of the above two cases corresponding to a combination of the flow regions of Ward's apparatus is also included.

The boundary layer equations for this swirling converging,flow have to be developed in a suitable coordinate system and integrated toward the axis, using appropriate initial conditions at the edge of the disk. It is important to note here, that although a solution of integral form of the boundary layer equations can be straightforwardly obtained using cylindrical polar coordinates for the case of pure potential vortex ($U^* = 0$), it is not straightforward for the more general cases associated with nonzero U^*. In particular, the cylindrical polar coordinate system cannot be used for nonzero U^* and a more general coordinate system is necessary. The need for a more general coordinate system appears to arise physically from the nature of the basic force balance in the flowfield. Physically, the fluid outside the boundary layer is accelerated along the inviscid streamlines by the inviscid pressure gradient. Near the wall in the boundary layer this flow is retarded by viscous stresses, the viscous stress being *primarily* directed opposite to the inviscid flow. The pressure gradient normal to the streamlines, which balances the

centripetal acceleration due to streamline curvature in the inviscid streamlines. For turbulent flows, the shear stresses at the boundary which are used in the momentum integral method are only known approximately by means of empirical equations. These empirical shear stress laws are only valid if expressed in the direction of the inviscid flow That is, in the turbulent boundary layer the choice of the coordinate system, is limited to a coordinate system which is aligned with the invisic flow at all times if the empirical shear stress laws are to be used. The cylindrical polar coordinate system is only useful for the special cases of a pure potential vortex inviscid flow ($V^* \neq 0, U^* = 0$) and purely radial inflow ($V^* = 0, U^* \neq 0$) since only in these cases do cylindrical polar coordinates happen to coincide with the inviscid streamline direction and the direction normal to it. Hence in order to employ momentum integral method for turbulent boundary layer in conjunction with the empirical shear stress laws (which are only valid if expressed in a coordinate system aligned with the inviscid impressed flow) one must use the inviscid streamline coordinate system. In fact, only in this coordinate system is one able to obtain a meaningful, physically acceptable and consistent solution at the edge of the disk. More detailed discussion on this point is included in Appendix B. Thus in the general case ($V^* \neq 0, U^* \neq 0$) for a turbulent boundary-layer flow, the use of a coordinate system (s,n,z) aligned with the inviscid flow at the edge of the boundary layer is necessary. The (s,n,z) coordinate system is defined such that the unit vectors in the s and n directions, $\hat{e}_s$ and $\hat{e}_n$, are given by

$$\vec{V}_i \times \hat{e}_s = 0 \qquad \hat{e}_n = \hat{e}_z \times \hat{e}_s \quad . \tag{3.4}$$

Here $\vec{V}_i$ is the inviscid velocity vector on the gound ($z = 0$).

We now proceed to derive the basic boundary-layer equations and their integral form, the general relations governing the metric coefficients for the inviscid streamline coordinates and their specific form for special cases of interest.

3.2 Boundary-Layer Equations.

The inviscid streamline coordinate system (s,n,z) is chosen with $(U,0,W)$ as the components of velocity in the outer inviscid flow. (A sketch of the swirling converging streamline is shown in Fig. 3.1) Conservation of mass and momentum equations for the inviscid, incompressible outer flow (flowfield variables in the inviscid streamline coordinate system denoted by capital letters)

$$\frac{\partial}{\partial s}(Uh_n) + \frac{\partial}{\partial z}(Wh_n h_s) = 0 \tag{3.5}$$

$$\frac{U}{h_s}\frac{U}{\partial s} = -\frac{1}{\rho h_s}\frac{\partial P}{\partial s} \tag{3.6}$$

$$-\frac{U^2}{h_s h_n}\frac{\partial h_s}{\partial n} = -\frac{1}{h_n}\frac{\partial P}{\partial n} \tag{3.7}$$

$$P = P(s,n) \tag{3.8}$$

where h_s, h_n are metric coefficients associated with (s,n,z) coordinate system. Furthermore, $h_z = 1$ and h_s and h_n can be taken to be independent of z in the boundary layer. From Eqs. (3.5) and (3.6) we have

$$-\frac{1}{\rho h_s}\frac{\partial P}{\partial s} = \frac{1}{h_s h_n}\frac{\partial}{\partial s}(U^2 h_n) + U\frac{\partial W}{\partial z} \quad . \tag{3.9}$$

The boundary-layer continuity and momentum equations for incompressible flow expressed in the inviscid streamline coordinate system

with (u,v,w) as the components of velocity is (s,n.z) coordinates [not to be confused with the cylindrical coordinate components of velocity which are denoted by a supercript ()*] are

Continuity:

$$\frac{\partial}{\partial s}(uh_n) + \frac{\partial}{\partial n}(vh_s) + h_s h_n \frac{\partial w}{\partial z} = 0 \tag{3.10}$$

Momentum(s):

$$\frac{u}{h_s}\frac{\partial u}{\partial s} + \frac{v}{h_n}\frac{\partial u}{\partial n} + w\frac{\partial u}{\partial z} + \frac{uv}{h_s h_n}\frac{\partial h_s}{\partial n} - \frac{v^2}{h_s h_n}\frac{\partial h_n}{\partial s} = -\frac{1}{\rho h_s}\frac{\partial p}{\partial s} + \frac{1}{\rho}\frac{\partial}{\partial z}(\tau_{sz}) \tag{3.11}$$

Momentum(n)

$$\frac{u}{h_s}\frac{\partial v}{\partial s} + \frac{v}{h_n}\frac{\partial v}{\partial n} + w\frac{\partial v}{\partial z} + \frac{uv}{h_s h_n}\frac{\partial h_n}{\partial s} - \frac{u^2}{h_s h_n}\frac{\partial h_s}{\partial n} = -\frac{1}{\rho h_n}\frac{\partial p}{\partial n} + \frac{1}{\rho}\frac{\partial}{\partial z}(\tau_{nz}) \tag{3.12}$$

Momentum(z):

$$p = p(s,n) = P(s,n) \quad , \tag{3.13}$$

where P is the impressed pressure as calculated from the inviscid outer flow (Eq. 3.8).

Rewriting the continuity equation, Eq. (3.10), in the following form

$$\frac{1}{h_s}\frac{\partial u}{\partial s} + \frac{1}{h_n}\frac{\partial v}{\partial n} + \frac{\partial w}{\partial z} + \frac{u}{h_s h_n}\frac{\partial h_n}{\partial s} + \frac{v}{h_s h_n}\frac{\partial h_s}{\partial n} = 0 \tag{3.14}$$

and adding its product with u to Eq. (3.11) we have

$$\frac{1}{h_s}\frac{\partial u^2}{\partial s} + \frac{1}{h_n}\frac{\partial}{\partial n}(uv) + \frac{\partial}{\partial z}(uw) + \frac{2uv}{h_s h_n}\frac{\partial h_s}{\partial n} + \frac{u^2 - v^2}{h_s h_n}\frac{\partial h_n}{\partial s} = -\frac{1}{\rho h_s}\frac{\partial p}{\partial s} + \frac{1}{\rho}\frac{\partial}{\partial z}\tau_{sz} \tag{3.15}$$

Algebraic manipulation and substitution of the pressure term from Eq. (3.12) allows us to rewrite the s-momentum equation as

$$\frac{1}{h_s h_n}\frac{\partial}{\partial s}(h_n u^2) + \frac{1}{h_n h_s^2}(h_s^2 uv) + \frac{\partial}{\partial z}(uw) - \frac{v^2}{h_s h_n}\frac{\partial h_n}{\partial s} = -\frac{1}{\rho h_s}\frac{\partial P}{\partial s} + \frac{1}{\rho}\frac{\partial}{\partial z}\tau_{sz} \tag{3.16}$$

The pressure force can be eliminated by making use of Eq. (3.9). There results

$$- \frac{\partial}{\partial s}[(U^2-u^2)h_n] + \frac{1}{h_s}\frac{\partial}{\partial n}[uvh_s^2] + h_s h_n[\frac{\partial}{\partial z}(uw) - U\frac{\partial w}{\partial z}] - v^2\frac{\partial h_n}{\partial s}$$

$$= \frac{h_s h_n}{\rho}\frac{\partial}{\partial z}\tau_{sz} \quad . \tag{3.17}$$

The n-momentum equation, Eq. (3.11), can similarly be manipulated by the addition v times the continuity equation to give

$$\frac{1}{h_s}\frac{\partial}{\partial s}(uv) + \frac{1}{h_n}\frac{\partial}{\partial n}(v^2) + \frac{\partial}{\partial z}(vw) + \frac{2uv}{h_n h_s}\frac{\partial h_n}{\partial s} + \frac{v^2-u^2}{h_s h_n}\frac{\partial h_s}{\partial n}$$

$$= -\frac{1}{\rho h_n}\frac{\partial P}{\partial n} + \frac{1}{\rho}\frac{\partial}{\partial z}\tau_{nz} \, . \tag{3.18}$$

The pressure term can be eliminated using Eq. (3.7). With minor manipulation, there results

$$\frac{1}{h_s h_n^2}\frac{\partial}{\partial s}(h_n^2 uv) + \frac{1}{h_s h_n}\frac{\partial}{\partial n}(h_s v^2) + \frac{\partial}{\partial z}(vw) + \frac{U^2-u^2}{h_s h_n}\frac{\partial h_s}{\partial n}$$

$$= \frac{1}{\rho}\frac{\partial}{\partial z}\tau_{nz} \quad . \tag{3.19}$$

We now wish to develop the integral form of these boundary-layer equations by formally integrating them with respect to z. In the spirit of the integral methods we assume the following velocity profiles after Taylor [1950]

$$u = Uf(\eta) \, , \qquad v = UE(s,n)g(\eta) \tag{3.20}$$

where η is a normalized boundary layer coordinate defined as

$$\eta = \frac{z}{\delta} \quad . \tag{3.21}$$

The functions f and g are assumed known. Here δ is the boundary-layer

thickness. Thus η varies from 0 to 1 across the boundary layer. The unknowns are now δ and E, the cross-flow function. We assume, following Weber [1956], the following forms for f and g, the profile functions,

$$f(\eta) = \eta^{1/7} \quad , \qquad g(\eta) = \eta^{1/7} - \eta \quad . \tag{3.21}$$

Integrating Eqs. (3.17) and (3.19) with respect to z from $z = 0(\eta = 0)$ to $z = \delta(\eta = 1)$, we immediately obtain, noting that $u \to U$, $u \to 0$ and $w \to w(\delta)$ as $\eta \to 1$ and $W \to 0$ as $z \to 0$,

$$- \frac{\partial}{\partial s} \left[U^2 \delta h_n \int_0^1 (1-f^2)\,d\eta\right] + \frac{1}{h_s} \frac{\partial}{\partial n} \left[U^2 E h_s^2 \delta \int_0^1 fg\,d\eta\right] + h_s h_n [Uw(\delta)] - U^2 E^2 \delta \frac{\partial h_s}{\partial n} \cdot \int_0^1 g^2 d\eta = - \frac{h_s h_n}{\rho} \tau_{sz}(0) \tag{3.23}$$

$$\frac{1}{h_n} \frac{\partial}{\partial s} \left(h_n^2 U^2 E \delta \int_0^1 fg\,d\eta\right) + \frac{\partial}{\partial n} \left(h_s U^2 E^2 \delta \int_0^1 g^2 d\eta\right) + U^2 \frac{\partial h_s}{\partial n} \delta \int_0^1 (1-f^2)\,d\eta = - \frac{h_s h_n}{\rho} \tau_{nz}(0) \quad . \tag{3.24}$$

Integration of boundary-layer continuity equation with respect to z can be shown to give

$$w(\delta) = - \frac{1}{h_s h_n} \left[\frac{\partial}{\partial s} \left(\delta h_n U \int_0^1 f\,d\eta\right) - h_n U \frac{\partial \delta}{\partial s} + \frac{\partial}{\partial n} \left(U h_s \delta E \int_0^1 g\,d\eta\right)\right] \tag{3.25}$$

For the ground shear stress components we assume the well-known forms after Karman [1921]

$$\tau_{sz}(s,n,o) = c\rho U^2 \sqrt{1+E^2(s,n)} \left(\frac{\nu}{U\delta\sqrt{1+E^2(s,n)}}\right)^{\frac{1}{4}}$$

$$\tau_{nz}(s,n,o) = c\rho U^2 E(s,n) \sqrt{1+E^2(s,n)} \left(\frac{\nu}{U\delta\sqrt{1+E^2(s,n)}}\right)^{\frac{1}{4}} \tag{3.26}$$

where c is a constant (with value approximately 0.0225). Making use of these shear stress forms as well as Eqs. (3.22), we obtain

$$-\frac{2}{9}\frac{\partial}{\partial s}(\delta U^2 h_n)+\frac{14}{45}\frac{1}{h_s}\frac{\partial}{\partial n}(U^2 E h_s^2\delta)-\frac{7}{8}U\frac{\partial}{\partial s}(h_n\delta U)+h_n U^2\frac{\partial\delta}{\partial s}$$

$$-\frac{3}{8}U\frac{\partial}{\partial n}(\delta h_s UE)-\frac{8}{45}U^2E^2\delta\frac{\partial h_n}{\partial s}=-ch_sh_nU^{7/4}(1+E^2)^{3/8}\left(\frac{\nu}{\delta}\right)^{1/4} \tag{3.27}$$

$$\frac{14}{45}\frac{1}{h_n}\frac{\partial}{\partial s}(h_n^2U^2E\delta)+\frac{8}{45}\frac{\partial}{\partial n}(h_sU^2E^2\delta)+\frac{2}{9}U^2\delta\frac{\partial h_s}{\partial n}=$$

$$-ch_sh_nU^{7/4}E(1+E^2)^{3/8}\left(\frac{\nu}{\delta}\right)^{1/4}\ . \tag{3.28}$$

Arranging these in a form suitable for numerical integration for $\delta(s,n)$ and $E(s,n)$, we have

$$\left(\frac{23}{360}h_s\delta\right)\frac{\partial E}{\partial n}+\left(\frac{7}{72}h_n\right)\frac{\partial\delta}{\partial s}+\left(\frac{23}{360}h_sE\right)\frac{\partial\delta}{\partial n}=-\left(\frac{79}{72}+\frac{8}{45}E^2\right)\delta\frac{\partial h_n}{\partial s}$$

$$+\frac{89}{360}E\delta\frac{\partial h_s}{\partial n}-\frac{95}{72}\frac{h_n\delta}{U}\frac{\partial U}{\partial s}+\left(\frac{89}{360}h_sE\frac{\delta}{U}\right)\frac{\partial U}{\partial n}+ch_sh_nU^{-1/4}(1+E^2)^{3/8}\left(\frac{\nu}{\delta}\right)^{1/4} \tag{3.29}$$

$$\left(\frac{14}{45}h_n\delta\right)\frac{\partial E}{\partial s}+\left(\frac{16}{45}h_sE\delta\right)\frac{\partial E}{\partial n}+\left(\frac{14}{45}h_nE\right)\frac{\partial\delta}{\partial s}+\left(\frac{8}{45}h_sE^2\right)\frac{\partial\delta}{\partial n}=-\left(\frac{28}{45}E\delta\right)\frac{\partial h_n}{\partial s}$$

$$-\left(\frac{2}{9}+\frac{8}{45}E^2\right)\delta\frac{\partial h_s}{\partial n}-\left(\frac{28}{45}h_n\frac{\partial U}{\partial s}+\frac{16}{45}h_sE\frac{\partial U}{\partial n}\right)\frac{E\delta}{U}-ch_sh_nU^{-1/4}E(1+E^2)^{3/8}\left(\frac{\nu}{\delta}\right)^{1/4}\ . \tag{3.30}$$

We now non-dimensionalize h_s and n with R and all velocities with the characteristic inviscid velocity $U(r=R)=U_o$. The boundary layer thickness δ is nondimensionalized by the length scale $(\nu R^4c^4/U_o)^{1/5}$. The non-dimensional form of the equations is then

$$\left(\frac{23}{360}\,h_s\delta\right)\frac{\partial E}{\partial n}+\left(\frac{7}{72}\,h_n\right)\frac{\partial \delta}{\partial s}+\left(\frac{23}{360}\,h_sE\right)\frac{\partial \delta}{\partial n}=-\left(\frac{79}{72}+\frac{8}{45}\,E^2\right)\delta\,\frac{\partial h_n}{\partial s}$$

$$+\frac{89}{360}\,E\delta\,\frac{\partial h_s}{\partial n}-\left(\frac{95}{72}\,\frac{h_n\delta}{U}\right)\frac{\partial U}{\partial s}+\left(\frac{89}{360}\,h_sE\,\frac{\delta}{U}\right)\frac{\partial U}{\partial n}+h_sh_nU^{-\frac{1}{4}}(1+E^2)^{3/8}\delta^{-\frac{1}{4}} \tag{3.31}$$

$$\left(\frac{14}{45}\,h_n\delta\right)\frac{\partial E}{\partial s}+\left(\frac{16}{45}\,h_sE\delta\right)\frac{\partial E}{\partial n}+\left(\frac{14}{45}\,h_nE\right)\frac{\partial \delta}{\partial s}+\left(\frac{8}{45}\,h_sE^2\right)\frac{\partial \delta}{\partial n}=-\left(\frac{28}{45}\,E\delta\right)\frac{\partial h_n}{\partial s}$$

$$-\left(\frac{2}{9}+\frac{8}{45}\,E^2\right)\delta\,\frac{\partial h_s}{\partial n}-\left(\frac{28}{45}\,h_n\,\frac{\partial U}{\partial s}+\frac{16}{45}\,h_sE\,\frac{\partial U}{\partial n}\right)\frac{E\delta}{U}-h_sh_nU^{-\frac{1}{4}}E(1+E^2)^{3/8}\delta^{-\frac{1}{4}}\ . \tag{3.32}$$

Equations (3.31) and (3.32) are two first-order, coupled partial differential equations to be solved for the two unknowns $\delta(s,n)$ and $E(s,n)$. The boundary conditions corresponding to the boundary-layer at the edge of the disk are $E(s_o,n_o) = o$, $\delta(s_o,n_o) = o$ where s_o and n_o values of the streamline coordinates at the edge of the disk, $r = 1$. Because of the axisymmetry of the flow, these equations can be reduced to two first-order, ordinary differential equations and this will be done later.

3.3 Derivation of Metric Coefficients.

The differential vector $d\vec{r}$ can be expressed in the streamline coordinate system (s,n,z) as well as the cylindrical coordinate system (r,θ,z) as

$$d\vec{r} = h_s ds\ \hat{e}_s + h_n dn\ \hat{e}_n = dr\ \hat{e}_r + rd\theta\ \hat{e}_\theta \tag{3.33}$$

and since, in general,

$$ds(r,\theta) = \left(\frac{\partial s}{\partial r}\right)_\theta dr + \left(\frac{\partial s}{\partial \theta}\right)_r d\theta \tag{3.34}$$

$$dn(r,\theta) = \left(\frac{\partial n}{\partial r}\right)_\theta dr + \left(\frac{\partial n}{\partial \theta}\right)_r d\theta \tag{3.35}$$

we have by substitution of above in Eq. (3.33)

$$d\vec{r} = h_s\left(\frac{\partial s}{\partial r}\,dr + \frac{\partial s}{\partial \theta}\,d\theta\right)\hat{e}_s + h_n\left(\frac{\partial n}{\partial r}\,dr + \frac{\partial n}{\partial \theta}\,d\theta\right)\hat{e}_n \quad . \tag{3.36}$$

By comparison of the above different expressions for the differential vector $d\vec{r}$, we have

$$h_s^2\left(\frac{\partial s}{\partial r}\right)^2 + h_n\left(\frac{\partial n}{\partial r}\right)^2 = 1 \quad , \qquad d\theta = 0 \tag{3.37}$$

$$h_s^2\left(\frac{\partial s}{\partial \theta}\right)^2 + h_n^2\left(\frac{\partial n}{\partial \theta}\right)^2 = r^2 \quad , \qquad dr = 0 \tag{3.38}$$

Hence, the metric coefficients follow as

$$h_s^2 = \frac{1}{\Delta}\begin{vmatrix} 1 & \left(\frac{\partial n}{\partial r}\right)^2 \\ r^2 & \left(\frac{\partial n}{\partial \theta}\right)^2 \end{vmatrix} \quad , \qquad h_n^2 = \frac{1}{\Delta}\begin{vmatrix} \left(\frac{\partial s}{\partial r}\right)^2 & 1 \\ \left(\frac{\partial s}{\partial \theta}\right)^2 & r^2 \end{vmatrix} \tag{3.39}$$

where

$$\Delta = \begin{vmatrix} \left(\frac{\partial s}{\partial r}\right)^2 & \left(\frac{\partial n}{\partial r}\right)^2 \\ \left(\frac{\partial s}{\partial \theta}\right)^2 & \left(\frac{\partial n}{\partial \theta}\right)^2 \end{vmatrix} \tag{3.40}$$

The metric coefficients thus depend on the relations between the coordinates of the two systems. From the definition of a streamline, we have for a converging flow

$$\hat{e}_s = -\frac{|U^*|}{U}\,\hat{e}_r + \frac{V^*}{U}\,\hat{e}_\theta \tag{3.41a}$$

where the starred quantities are inviscid velocity components in the cylindrical coordinate system. Since

$$\hat{e}_n = \hat{e}_z \times \hat{e}_s$$

hence

$$\hat{e}_n = -\frac{V^*}{U}\hat{e}_r - \frac{|U^*|}{U}\hat{e}_\theta \ . \qquad (3.41b)$$

Hence Eq. (3.33) can be rewritten as

$$d\vec{r} = (-h_s \frac{|U^*|}{U} ds - h_n \frac{V^*}{U} dn)\hat{e}_r + (h_s \frac{V^*}{U} ds - h_n \frac{|U^*|}{U} dn)\hat{e}_\theta \ . \qquad (3.42)$$

Comparing Eqs. (3.33) and (3.42), we obtain

$$- h_s \frac{|U^*|}{U} ds - h_n \frac{V^*}{U} dn = dr \qquad (3.43)$$

$$h_s \frac{V^*}{U} ds - h_n \frac{|U^*|}{U} dn = r d\theta \ . \qquad (3.44)$$

We define the inviscid swirl angle ϕ_i as

$$\tan\phi_i(r) = \frac{V^*}{|U^*|} = m(r), \qquad \tan\phi_i(r=1) = \tan\phi_{i0} \ . \qquad (3.45)$$

We then infer from Eqs. (3.43) and (3.44)

$$d\theta = -m\frac{dr}{r}, \qquad dn = 0 \qquad (3.45)$$

$$d\theta = \frac{1}{m}\frac{dr}{r}, \qquad ds = 0 \ . \qquad (3.47)$$

Upon integration of Eqs. (3.46) and (3.47), we obtain

$$f_1(n) = \theta + \int m \frac{dr}{r} \qquad (3.48)$$

$$f_2(s) = \theta - \int \frac{1}{m}\frac{dr}{r} \ . \qquad (3.49)$$

To proceed further we must specify m(r) explicitly. We shall do so for two specific cases of interest.

Case (i)

The non-dimensionalized components of velocities for this case

are, in cylindrical coordinates,

$$U^* \sim \frac{-1}{r} \quad , \qquad V^* \sim \frac{1}{r} \quad , \qquad W^* \sim 0 \tag{3.50}$$

This corresponds to the inviscid flow between two parallel plates due to a sink and a potential vortex along the axis at $r = 0$. The flow in the outer converging zone in the Ward apparatus is modeled closely by these forms for U*, V*, and W*. It follows that

$$\tan\phi_i(r) = m(r) = m_o \tag{3.51}$$

where m_o is a constant corresponding to the ratio of the components of velocity at the edge of the disk.

Hence the integrations in Eqs. (3.48) and (3.49) can be completed to yield

$$f_1(n) = \theta + m_o \ln r + \text{const.} \tag{3.52}$$

$$f_2(s) = \theta - \frac{1}{m_o} \ln r + \text{const.} \tag{3.53}$$

Useful choices of the functions f_1 and f_2 are

$$f_2(s) = s \quad , \qquad f_1(n) = - \ln n \tag{3.54}$$

and the coordinates s and n are given by

$$s = \theta - \frac{1}{m_o} \ln r \quad , \qquad n = \frac{e^{-\theta}}{r^{m_o}} \tag{3.55}$$

where the constants of integrations are chosen such that at $r = 1$, $\theta = 0$ the corresponding streamline coordinates are $s = 0$, $n = 1$.

It is easily seen from Eq. (3.55) that, in this case,

$$\frac{\partial s}{\partial r} = - \frac{1}{m_o r} \quad , \qquad \frac{\partial s}{\partial \theta} = 1, \qquad \frac{\partial n}{\partial r} = - m_o \frac{n}{r} \quad , \qquad \frac{\partial n}{\partial \theta} = - n \ . \tag{3.56}$$

Substitution of above in Eqs. (3.40) yields the following expressions for the metric coefficients

$$h_s = r \sin\phi_{io} \quad , \qquad h_n = \frac{r}{n} \cos\phi_{io} \tag{3.57}$$

Solving Eqs. (3.55) for r(s,n), we obtain

$$r = n^{-(m_o/1+m_o^2)} \exp[(-m_o/1+m_o^2)s] \quad . \tag{3.58}$$

Thus

$$\frac{\partial r}{\partial n} = -(\frac{m_o}{1+m_o^2}) \frac{r}{n} \quad , \qquad \frac{\partial r}{\partial s} = -(\frac{m_o}{1+m_o^2}) r \quad . \tag{3.59}$$

This result, along with Eqs. (3.57), then gives

$$(\frac{\partial h_s}{\partial n})_s = -\frac{r}{n} \sin^2\phi_{io} \cos\phi_{io} \quad , \qquad (\frac{\partial h_n}{\partial s})_n = -\frac{r}{n} \sin\phi_{io} \cos^2\phi_{io} \tag{3.60}$$

Case (ii)

The second case of interest is the flow regime with the inviscid non-dimensional components of velocity expressed in the cylindrical coordinate system as

$$U^* \sim -r \quad , \qquad V^* \sim \frac{1}{r} \quad , \qquad W^* \sim 2z \quad . \tag{3.61}$$

This corresponds to the inviscid region of the Rott-Burgers vortex and gives a converging, uprising, swirling flow. The source strength along the axis is zero. This flow appears to be a reasonable approximation to the inviscid flow in the updraft region of Ward's apparatus. In this flow the ratio of the components of velocity depends on radial position;

$$\tan\phi_i = \tan\phi_i(r) = m(r) \quad . \tag{3.62}$$

It can easily be shown that

$$m = \frac{m_o}{r^2} \tag{3.63}$$

where

$$m_o = m(r = 1) \ . \tag{3.64}$$

A convenient choice of the functions $f_1(n)$ and $f_2(s)$ for this case is

$$f_2(s) = s \ , \qquad f_1(n) = - n \ . \tag{3.65}$$

Hence from Eqs. (3.48) and (3.49) we have

$$s = \theta - \int \frac{1}{m} \frac{dr}{r} \tag{3.66}$$

$$n = - \theta - \int m \frac{dr}{r} \ . \tag{3.67}$$

Substitution of the value of m and integration of above equations (taking $r = 1$, $\theta = 0$ as corresponding to $s = 0$, $n = 1$), we obtain

$$s = \theta - \frac{1}{2m_o} (r^2 - 1) \tag{3.68}$$

$$n = - \theta + \frac{m_o}{2} \left(\frac{1}{r^2} - 1\right) + 1 \ . \tag{3.69}$$

We then have in this case

$$\frac{\partial s}{\partial r} = - \frac{1}{mr} \ , \quad \frac{\partial s}{\partial \theta} = 1 \ , \quad \frac{\partial n}{\partial r} = - \frac{m}{r} \ , \quad \frac{\partial n}{\partial \theta} = - 1 \tag{3.70}$$

and hence from Eqs. (3.39) and (3.40), the metric coefficients are

$$h_s = r \sin\phi_i \ , \qquad h_n = r \cos\phi_i \ . \tag{3.71}$$

Simultaneous solution of Eqs. (3.68) and (3.69) for $r = r(s,n)$ gives

$$r = \left[\tfrac{1}{2}\left\{ - \left(2m_o(n-1) + m_o^2 - 1 + 2m_o s\right) + \left\{ \left(2m_o(n-1) + m_o^2 - 1 + 2m_o s\right)^2 + 4m_o^2 \right\}^{\frac{1}{2}} \right\}\right]^{\frac{1}{2}} . \tag{3.72}$$

It can then be shown that

$$\left(\frac{\partial r}{\partial n}\right)_s = \left(\frac{\partial r}{\partial s}\right)_n = - m_o r\left[\left(2m_o(n-1)+m_o^2-1+2m_o s\right)^2+4m_o^2\right]^{-\frac{1}{2}} \tag{3.73}$$

Also,

$$U = \frac{1}{r}\left(\frac{m_o^2+r^4}{m_o^2+1}\right)^{\frac{1}{2}}, \qquad \left(\frac{\partial U}{\partial n}\right)_s = \frac{r^4-m_o^2}{\sqrt{1+m_o^2}}\frac{1}{r^2\sqrt{m_o^2+r^4}}\left(\frac{\partial r}{\partial n}\right)_s \tag{3.74}$$

From Eqs. (3.71) we obtain

$$\left(\frac{\partial h_s}{\partial n}\right)_s = \frac{m_o(m_o^2-r^4)}{(m_o^2+r^4)^{3/2}}\left(\frac{\partial r}{\partial n}\right)_s, \qquad \left(\frac{\partial h_n}{\partial s}\right)_n = \frac{r^2(r^4+3m_o^2)}{(r^4+m_o^2)^{3/2}}\left(\frac{\partial r}{\partial s}\right)_n . \tag{3.75}$$

Since the velocity components in cylindrical coordinates are only functions of radius, the flow is axisymmetric. This axisymmetry of the flow can be used to simplify the equations of motion in the (s,n,z) coordinate system. It is important to realize that only physical quantities are axisymmetric (such as velocity and pressure; not the metric coefficients). The axisymmetry condition enables one to express all derivatives with respect to s in terms of those with respect to n or vice versa. That is, axisymmetry implies

$$\left(\frac{\partial}{\partial\theta}\right)_r = \left(\frac{\partial s}{\partial\theta}\right)_r\left(\frac{\partial}{\partial s}\right)_n + \left(\frac{\partial n}{\partial\theta}\right)_r\left(\frac{\partial}{\partial n}\right)_s = 0 . \tag{3.76}$$

Thus, solving for $(\partial/\partial s)_n$, we have

$$\left(\frac{\partial}{\partial s}\right)_n = \left[-\frac{(\partial n/\partial\theta)_r}{(\partial s/\partial\theta)_r}\right]\left(\frac{\partial}{\partial n}\right)_s . \tag{3.77}$$

Evaluating $(\partial n/\partial\theta)_r$ and $(\partial s/\partial\theta)_r$, we have

$$\left(\frac{\partial}{\partial s}\right)_n = \begin{cases} n\left(\frac{\partial}{\partial n}\right)_s & \text{for case (i)} \\ \left(\frac{\partial}{\partial n}\right)_s & \text{for case (ii)} \end{cases} \tag{3.78}$$

Substitution of the above results in Eqs. (3.31) and (3.32) yields the final integral form of the equations of motion

Case (i)

$$\left(\frac{23}{360} h_s\delta\right) \frac{\partial E}{\partial n} + \left(\frac{7}{72} h_n n + \frac{23}{360} h_s E\right) \frac{\partial \delta}{\partial n} = -\left(\frac{79}{72} + \frac{8}{45} E^2\right)\delta \frac{\partial h_n}{\partial s} + \frac{89}{360} E\delta \frac{\partial h_s}{\partial n}$$

$$-\left(\frac{95}{72} h_n n - \frac{89}{360} h_s E\right) \frac{\delta}{U} \frac{\partial U}{\partial n} + h_s h_n U^{-\frac{1}{4}} (1+E^2)^{3/8} \delta^{-\frac{1}{4}} \tag{3.79}$$

$$\left(\frac{14}{45} h_n n\delta + \frac{16}{45} h_s E\delta\right) \frac{\partial E}{\partial n} + \left(\frac{14}{45} h_n n E + \frac{8}{45} h_s E^2\right) \frac{\partial \delta}{\partial n} = -\frac{28}{45} E\delta \frac{\partial h_n}{\partial s}$$

$$-\left(\frac{2}{9} + \frac{8}{45} E^2\right)\delta \frac{\partial h_s}{\partial n} - \left(\frac{28}{45} h_n n + \frac{16}{45} h_s E\right) \frac{E\delta}{U} \frac{\partial U}{\partial n} - h_s h_n U^{-\frac{1}{4}} E (1+E^2)^{3/8} \delta^{-\frac{1}{4}} \tag{3.80}$$

Case (ii)

$$\left(\frac{23}{360} h_s\delta\right) \frac{\partial E}{\partial n} + \left(\frac{7}{72} h_n + \frac{23}{360} h_s E\right) \frac{\partial \delta}{\partial n} = -\left(\frac{79}{72} + \frac{8}{45} E^2\right)\delta \frac{\partial h_n}{\partial n} + \frac{89}{360} E\delta \frac{\partial h_s}{\partial n}$$

$$-\left(\frac{95}{72} h_n - \frac{89}{360} h_s E\right) \frac{\delta}{U} \frac{\partial U}{\partial n} + h_s h_n U^{-\frac{1}{4}} (1+E^2)^{3/8} \delta^{-\frac{1}{4}} \tag{3.81}$$

$$\left(\frac{14}{45} h_n\delta + \frac{16}{45} h_s E\delta\right) \frac{\partial E}{\partial n} + \left(\frac{14}{45} h_n E + \frac{8}{45} h_s E^2\right) \frac{\partial \delta}{\partial n} = -\frac{28}{45} E\delta \frac{\partial h_n}{\partial s}$$

$$-\left(\frac{2}{9} + \frac{8}{45} E^2\right) \delta \frac{\partial h_s}{\partial n} - \left(\frac{28}{45} h_n + \frac{16}{45} h_s E\right) \frac{E\delta}{U} \frac{\partial U}{\partial n} - h_s h_n U^{-\frac{1}{4}} E (1+E^2)^{3/8} \delta^{-\frac{1}{4}} \tag{3.82}$$

These equations were numerically integrated and solutions for the boundary-layer thickness δ and the cross flow function E were obtained.

3.4 Numerical Results.

Equations (3.79) and (3.80) for case (i) and Eqs. (3.81) and (3.82) for case (ii) were integrated numerically using a fourth-order Runge-Kutta numerical scheme. A varying step size was imposed on r and the resulting change in coordinate n was then used to calculate and E for each step. The integration was carried out from r = 1 down to the region close to the center (typically to r 0.01) for both cases (i) and (ii).

The choice of coordinate n as the independent variable in the integration process proved to be more convenient for the range of m_o considered. Also, the choice of n as the independent variable rather than coordinate s reduced the numerical error for values of m_o exceeding unity.

The numerical scheme could not be used at the edge of the disk (r = 1) as the solutions are singular there. Thus an analytical solution valid near r = 1 was obtained by assuming the boundary-layer thickness δ and the cross-flow function E behave as $\delta = c_1(n-1)^{\alpha}$ and $E = c_2(n-1)^{\beta}$, respectively. Substitution of these forms in the equations of motion in each case imply a balance of the shear stress and inertial forces at the edge of the disk such that $\alpha = 4/5$ and $\beta = 1$. The existence of a non-zero radial velocity U* at the edge of the disk always implies $\alpha = 4/5$ and $\beta = 1$ so that near the edge

$$\delta \sim (n-1)^{4/5} , \qquad E \sim (n-1) . \tag{3.83}$$

However, in the special case of U* = 0, corresponding to a pure potential vortex inviscid flow, an entirely new force balance is obtained near the edge with $\alpha = 2/5$ and $\beta = 1/2$. As illustrated in the Appendix,

B, the choice of any coordinate system other than the inviscid streamline (s,n,z) coordinate system -- for example, cylindrical coordinates -- for a non-zero U* makes it impossible for one to obtain a unique solution for the values of δ and E at the edge of the disk. As explained earlier, this is due to the use of the empirical shear stress laws in the integral momentum method.

Substitution of Eqs. (3.83) into Eqs. (3.79) and (3.80) as well as (3.81) and (3.82) yields the solutions near the edge for case (i) as

$$\delta = [\frac{90}{7} \sin\phi_{io}(n-1)]^{4/5} \quad , \quad E = \frac{100}{287} \sin^2\phi_{io}(n-1) \quad . \tag{3.84}$$

The same powers for δ and E can be used for case (ii). The resulting solution near the edge is

$$\delta = [\frac{90}{7} \sin\phi_{io}(n-1)]^{4/5} \quad , \quad E = \frac{100}{287} \sin^2\phi_{io}\cos^2\phi_{io}(m_o^2-1)(n-1) \quad . \tag{3.85}$$

The numerical results for δ and E are presented in Figs. 3.2 -3.5. Although the numerical results were obtained in the (s,n,z) coordinate system, these results have been transformed to cylindrical coordinates for ease of presentation and understanding. The variation of E with radius for different values of $m(r=1) = m_o$ are presented in Figs. 3.2 and 3.3 for cases (i) and (ii), respectively. The change in the values of m_o is four and two order of magnitudes for cases (i) and (ii), respectively.

It is noted that for large values of m_o -- that is, for a flow approaching that of a pure potential vortex -- the solutions presented tend to the solutions obtained by Chang, *et al.* for the special case of potential vortex [1969]. Furthermore the same result is obtained

for a fixed value of m_o and sufficiently small radii where the tangential components of velocity become relatively very large.

We also note that for the limit of $m_o \to 0$ (pure radial flow) the solution for the cross-flow function E tend to the solution of the pure radial flow, $E \to 0$, as expected.

The solutions are significantly different, however, for values of m_o of order unity or smaller; that is where U* and V* are of the same order and neither is zero. This situation should be more applicable to tornado velocity fields as inferred from experimental measurements. [Hoecker, 1960]

The variation of the boundary layer thickness δ with radius for different values of m_o is presented in Figs. 3.4 [case (i)] and 3.5 [case (ii)]. For case (i), corresponding to the bounded flow between parallel plates, the boundary layer thickness growth is significantly increased with increasing values of m_o. The variation is shown for values of m_o between 0.1 to 100. For the large values of m_o, the solution tends to that of pure potential vortex as obtained by Chang. For the limit of $m_o \to 0$ we note that Eq. (3.31) expressed in cylindrical coordinate system becomes

$$-\frac{7}{72} r \frac{\partial \delta}{\partial r} = -\frac{16}{72} \delta + r^{5/4} \delta^{-\frac{1}{4}} . \qquad (3.86)$$

The above equation can be solved analytically to give

$$\delta = r[8(1-r^{45/28})]^{4/5} . \qquad (3.87)$$

This analytical result for $m_o = 0$ is also shown in Fig. 3.4. We observe that the analytical solution for the pure radial case is indeed the limit of the numerical solutions of Eqs. (3.31) as $m_o \to 0$. Hence the

pure potential vortex boundary-layer thickness solution [Chang, 1969] and the pure radial flow ($m_o = 0$) are in fact the limiting solutions of the general equations of the flow [Eqs. (3.31) and (3.32)] for $m_o \to \infty$ and $m_o = 0$, respectively, thus adding confidence to the essential correctness of the numerical scheme.

These results do not suggest boundary-layer separation anywhere in case (i). This is anticipated as the pressure gradient is quite favorable, $\frac{\partial P}{\partial r} \sim 1/r^2$. For the case (ii), corresponding to a radially converging flow with an updraft, the boundary layer growth is significantly decreased with increasing values of m_o. That is, the potential vortex solution represents a lower bound for $\delta(r)$ in case (ii) as opposed to the upper bound in case (i). The solutions are presented for the values for m_o ranging from 1.0 to 70.0. It is noted that for smaller values of m_o, typically less than 10, these boundary-layer solutions suggest separation. For example, for $m_o = 1.0$, $\delta = 2.8 \times 10^8$ at $r = 0.09$ while for $m_o = 10$, $\delta = 33.8$ at $r = 0.1$. However, increasing m_o further delays the separation to regions very close to the center where presumably the boundary layer notion is no longer valid. For large values of m_o, the variation of δ with radius approaches the pure potential vortex solution.

The separation of boundary-layer obtained in the calculations for case (ii) and for m_o less than unity is in agreement with experimental observation of Ward's flow. For small swirl parameters (as in cases i and ii in Chapter II of this work) which corresponds to $m_o < 1$, a flow separation is distinctly observed. A potential vortex model corresponding to $m_o = \infty$, however, fails to show this except perhaps on

the axis where the boundary-layer concept is no longer valid. Furthermore, the numerical results indicate an unseparated boundary layer for large values of m_o. Since the flow achieves a large value of this parameter locally close to axis (e.g. $m \sim r^{-2}$), regardless of its initial value, a boundary-layer flow can be assumed to exist in the region very close to the axis. That is, the boundary-layer structure due to a swirling converging vortex flow resembles that of a potential vortex sufficiently close to the axis of the vortex. Observations of the flow in Ward's apparatus is also in agreement with these calculations. Introducing smoke at the gound near the axis indicates a smooth, unseparated boundary-layer flow in this high swirl region. The helical streamlines are observed to converge toward the axis turning upward to form the stream surface which separates the core flow from the inviscid, swirling, converging flow in Ward's apparatus. The core exhibits a narrowing near the ground and forms a tip on the lower boundary (see sketch in Fig. 1.4). This variation of the core diameter with height which extends for approximately one inch above the ground is probably a region of interaction of the boundary layer and the core. An estimate of the boundary-layer thickness near the axis can be found using the results obtained. For $\delta \simeq 10$, $R \simeq 8"$ and $U_o \simeq 2$ ft/sec, one obtains $\delta_{dim} \simeq 0.6"$ which is in agreement with the observations. This agreement further confirms the assumed existence of a 'reattached' turbulent boundary layer near the core. That is, this estimate of the tip length obtained using boundary layer calculations indicates that the boundary layer notion is valid near the core even though the flow is observed to separate at a large radius. Hence the assumption of a 'reattached' boundary layer near the axis seems to be confirmed.

A third regime of interest is a combination of cases (i) and (ii) modeling the combined regions of shallow convergence and an updraft in Ward's simulation of a tornado fieldflow. For this case the equations were integrated for case (i) up to $r = 0.5$ and then the results at that station were used as an initial condition for the integration of the equations for the case (ii) from $r = 0.5$ to near $r = 0$.

The variation of cross-flow function E and the boundary-layer thickness with radius for the case of mixed flow are given in Figs. 3.6 and 3.7, respectively. The values of δ and E adjust rather quickly in the transition zone between the flow regimes (i) and (ii).

A knowledge of the variation of the swirl parameter on the ground for various initial values of the swirl parameter (m_o) is useful in estimating the direction of the flow at the ground. The flow direction of a naturally-occurring tornado near the ground can often be obtained from debris patterns and damaged trees left in the aftermath of a tornado. The observed flow direction might then be used in estimating the flow direction and velocity outside of the boundary layer. By definition, the swirl parameter at the ground is given by

$$\tan\phi_{wall} = \left(\frac{v^*}{|u^*|}\right)_{wall} . \qquad (3.89)$$

In addition,

$$v^* = (u\hat{e}_s + v\hat{e}_n)\cdot\hat{e}_\theta \quad , \qquad u^* = (u\hat{e}_s + v\hat{e}_n)\cdot\hat{e}_r \quad . \qquad (3.90)$$

as well as

$$u = U\eta^{1/7} \quad , \qquad v = UE(\eta^{1/7} - \eta) \quad . \qquad (3.91)$$

Thus, it can be shown that

$$\tan\phi_{wall} = \frac{m_o - E}{1+m_o E} \qquad \text{case (i)} \qquad (3.92$$

and

$$\tan\phi_w = \frac{m_o - Er^2}{m_o E + r^2} \qquad \text{case (ii)} \qquad (3.93)$$

The variation of the ratio of the swirl parameter at the wall to that of the inviscid flow are presented in Figs. 3.8-3.10 for case (i), (ii) and the mixed flow respectively.

These results show that the streamlines turn toward the origin relative to the streamlines of the inviscid flow for all values of m_o as expected. The ratio of swirl parameters decrease more rapidly with decreasing radius for large values of the initial inviscid-flow swirl parameter m_o.

The discontinuity of the parameters at $r = 0.5$ in the mixed flow case observed in the figures are smoothed out by an arbitrarily-drawn dashed line representing schematically a more realistic transitional region.

In the vicinity of the origin the ratio of the swirl parameters vanishes as observed from the figures. The value of the swirl parameter at the wall, however, for case (ii) approaches 1. This is clearly shown by Eq. (3.93)

$$\tan\phi_{wall} = \frac{m_o - Er^2}{m_o E + r^2} \sim \frac{1}{E}, \qquad r \ll 0 . \qquad (3.94)$$

Since the numerical value of E approaches 1 regardless of the value of the initial swirl parameter m_o, $\tan\phi_{wall} \to 1$ for all values of

m_o as $r \to 0$. We note that for a pure potential vortex flow

$$\tan\phi_w = \frac{1}{E} \qquad \text{for any } r \tag{3.95}$$

and hence the swirl parameter at the ground for case (ii) approaches that of a pure potential vortex as a limiting case as $r \to 0$. Photographic evidence of debris and damaged trees of naturally occurring tornadoes suggest the qualitative correctness of this result.

The components of the shear stress at the ground in the cylindrical coordinate system can be obtained in terms of the shear stress components at the wall in the inviscid streamline coordinate system by noting that

$$\tau_{rz} = (\tau_{sz}\hat{e}_s + \tau_{nz}\hat{e}_n)\cdot\hat{e}_r \tag{3.96}$$

$$\tau_{\theta z} = (\tau_{sz}\hat{e}_s + \tau_{nz}\hat{e}_n)\cdot\hat{e}_\theta \tag{3.97}$$

Substituting Eqs. (3.41a) and (3.41b) and

$$m = m_o\,, \quad U = \frac{1}{r}\,, \quad U^* = \frac{1}{r\sqrt{1+m_o^2}} \qquad \text{for case (i)} \tag{3.98}$$

or

$$m = \frac{m_o}{r^2}\,, \quad U = \frac{1}{r}\sqrt{\frac{r^4+m_o^2}{1+m_o^2}}\,, \quad U^* = \frac{r}{\sqrt{1+m_o^2}} \quad \text{for case (ii)} \tag{3.99}$$

into Eqs. (3.92) and (3.93), we obtain

$$\tau_{rz}(0) = \frac{-1}{\sqrt{1+m_o^2}}\left[\tau_{sz}(0)+m_o\tau_{nz}(0)\right] \tag{3.100a}$$

case (i)

$$\tau_{\theta z}(0) = \frac{1}{\sqrt{1+m_o^2}}\left[m_o\tau_{sz}(0)-\tau_{nz}(0)\right] \tag{3.100b}$$

and

$$\tau_{rz}(0) = \frac{r^2}{\sqrt{r^4+m_o^2}} \left[\tau_{sz}(0) + \frac{m_o}{r^2} \tau_{nz}(0)\right] \qquad (3.101a)$$

case (ii)

$$\tau_{\theta z}(0) = \frac{r^2}{\sqrt{r^4+m_o^2}} \left[\frac{m_o}{r} \tau_{sz}(0) - \tau_{nz}(0)\right] \qquad (3.101b)$$

All shear stress components are non-dimensionalized by $\rho U_o^2 \frac{\delta_o}{R}$. The above shear stress components were further normalized with respect to U^2 and their variations with r were calculated. Figures 3.11-3.13 are the results for cases (i), (ii) and the mixed flow of the variation of the normalized radial components of the shear stress at the wall. It can be seen that the radial shear stress components at the wall possess a relative minimum for all values of m_o in the initial phases of the development of the boundary layer. The radial shear stress components also appear to approach zero near $r = 0$ because of the decrease of the radial component of velocity in that region.

Similar results for the normalized tangential components of the shear stress at the ground are presented in Figs. 3.14-3.16 for cases (i), (ii) and the mixed flow case. As expected all shear stress components are singular at the edge of the disk $r = 1$. The tangential components also seem to vanish near $r = 0$ suggesting that the flow near $r = 0$ could be assumed to be essentially inviscid. Also the contribution to the torque of regions close to $r = 0$ is negligible as was suggested elsewhere. [Jischke and Parang, 1974]

The axial flow velocity given by Eq. (3.25) was calculated and its variation with radius for cases (i), (ii) and mixed flow are presented in Figs. 3.17-3.19, respectively. The axial velocity is non-dimensionalized

by $(U_o R_e^{-1/5})$ where $R_e = U_o R/\nu$.

As expected, these results show a singular behavior for the axial velocity at the edge of the disk. It should be recognized, however, that the results for the axial flow at the edge of the disk for a non-zero inviscid radial velocity component is positive (upward) as opposed to a negatively singular behavior of w at the edge of the disk for an inviscid pure potential vortex. [Burgraff, Stewartron, and Belcher, 1971] This is clearly seen by considering the boundary-layer mass continuity equation [Eq. (3.25)]

$$w(\delta) = -\frac{1}{h_s h_n}\left[\frac{\partial}{\partial s}\left(\delta h_n U\int_o^1 f d\eta\right) - h_n U\frac{\partial \delta}{\partial s} + \frac{\partial}{\partial n}\left(U h_s \delta E\int_o^1 g d\eta\right)\right] . \qquad (3.102)$$

For a pure potential vortex flow, the derivative of all physical quantities with respect to s vanish and hence

$$w(\delta) = -\frac{1}{h_s h_n}\frac{\partial}{\partial n}\left(U h_s \delta E\int_o^1 g d\eta\right) , \qquad (3.103)$$

$$w(\delta) = \frac{1}{r}\frac{\partial}{\partial r}\left(U r \delta E\int_o^1 g d\eta\right) , \qquad (3.104)$$

where for $\delta \sim (1-r)^{2/5}$ and $E \sim (1-r)^{1/2}$ gives

$$w(\delta) \sim -(1-r)^{-\frac{1}{2}} \qquad \text{near } r = 1 \qquad (3.105)$$

For case (ii), however, we note that with $\delta \sim (n-1)^{2/5}$ and $E \sim (n-1)$ the dominant terms of Eq. (3.25) near $r = 1$ are

$$w(\delta) \sim -\frac{1}{h_s h_n}\left[\frac{\partial}{\partial s}\left(\delta h_n U\int_o^1 f d\eta\right) - h_n U\frac{d\delta}{ds}\right] , \qquad (3.106)$$

which can be shown to result in

$$w(\delta) \sim (n-1)^{-3/5} \qquad (3.107)$$

Hence the edge conditions are again seen to be fundamentally different for a non-zero inviscid radial velocity component ($U^* \neq 0$) as compared to that of a pure potential vortex ($U^*=0$).

These results also suggest that for small values of m_o and/or very small radii, the boundary-layer notion may not be valid for case (ii) and mixed flow. This can be inferred from the observed large (order of 10 or more) values of the vertical velocity at the edge of the boundary layer for small values of m_o and/or very small radii. This is suggestive of the boundary-layer eruption at the axis noted by Burgraff *et al.*

Finally, the numerical results for the tangential shear stress at the ground were used to calculate the torque T exerted on the ground by the flow,

$$T = \int_o^1 \tau_{\theta z}(2\pi r)dr \quad . \tag{3.108}$$

The results for $(T/2\pi)$ for the mixed flow, applicable to Ward's tornado simulation, are presented in Figs. 3.20 and 3.21. The integration process was carried from the edge of the disk to r = .014. It is observed that the value of the torque applied to the disk by the flow approaches a constant value for large values of m_o which would be the torque applied to the disk by a pure potential vortex.

The above value of torque can be used to obtain a formula for the total torque exerted by a potential vortex flow above a disk in terms of the circulation of the velocity

$$\Gamma = 2\pi r V^* \quad . \tag{3.109}$$

A formula for the torque in the turbulent boundary-layer of a

swirling converging flowfield, based on results for the torque exerted on a rotating disk in a staticnary fluid, was given [Jischke and Parang, 1974] as

$$T \sim \delta \nu^{1/5} Rr^{9/5} \quad . \tag{3.110}$$

The numerical results presented in Fig. (3.20) can be used to obtain a numerical value for the constant of proportionality of (.007) for $m_o \gtrsim 15$. Thus, we have for $m_o \gtrsim 15$,

$$T = .007\, \delta \nu^{1/5} Rr^{9/5} \quad . \tag{3.111}$$

Although the value of the constant suggested [Jischke, Parang, 1974] was approximately correct (.009), the value (.007) is exact within the momentum integral approximation. The approximate equality of the numerical constant obtained here for $m_o \geq 15$ ($\phi \geq 80°$) and that of pure potential vortex $m_o = \infty (\phi = 90°)$ obtained [Jischke,Parang] adds confidence to the accuracy of the present results. However, multiple vortices were experimentally observed to occur at smaller values of ϕ(e.g. $\phi_{cr} \approx 40°$). The numerical constant corresponding to $\phi = 40°$ in the expression for the torque can be obtained using a linear interpolation of the results obtained here numerically (see Fig. 3.21). We obtain a value of approximately 0.0036. This relatively small value of the numerical constant in Eq. (3.111) seems to clarify the reasons for the discrepancy between the experimental results and the theoretical values predicted [Jischke, Parang, 1974] for ϕ_{cr}. The difference between the theory and the experiment is now believed to be due to an instability of the vortex core that occurs at values of swirl angle near 40°. This instability arises because of the inflow of radial

vorticity (produced in the boundary layer) near the ground and its reorientation vertically in a thin layer around the core region. This thin annulus of enchanced vertical vorticity can become unstable if the vorticity is sufficiently intense. Thus a stability analysis accounting for vorticity production and inflow toward the core would seem to offer the possibility of a more accurate estimate of the critical swirl parameter.

An estimate of the vorticity, $\vec{\omega}$, produced in the boundary layer can be obtained using the results of the boundary-layer calculation presented in this chapter. In particular, it is of interest to determine the inflow of the radial component of vorticity produced in the boundary-layer within the approximation of the integral momentum method used here. This component of vorticity is presumably convected inward and tilted upward forming the ring-shaped shear layer which is believed to be responsible for the instability of the core resulting in "core splitting" phenomenon discussed previously. The radial component of vorticity produced in the boundary layer is given by

$$\omega_r = - \frac{\partial v^*}{\partial z} \quad , \tag{3.112}$$

where v* is the tangential component of velocity in the boundary-layer. Furthermore we have

$$v^* = (u\hat{e}_s + v\hat{e}_n)\hat{e}_o \quad , \tag{3.113}$$

and with unit vectors along the s and n coordinates given by Eqs. (3.41a) and (3.41b), we obtain after simplifications

$$\omega_r = |U^*| \frac{\partial}{\partial z} \frac{v}{U} - V^* \frac{\partial}{\partial z} \frac{u}{U} \quad . \tag{3.114}$$

The substitution of velocity profiles given in Eqs. (3.57) in the above equation results in

$$\omega_r = E|U^*|\left\{\frac{1}{7}\left(\frac{1}{\delta z^6}\right)^{1/7} - \frac{1}{\delta}\right\} - \frac{1}{7} V^* \left(\frac{1}{\delta z^6}\right)^{1/7} \qquad (3.115)$$

The rate of inflow of the radial component of vorticity is

$$I = \int_0^\delta u^* \omega_r (2\pi r) dz \qquad (3.116)$$

where with

$$u^* = (ue_s + ve_n)\cdot\hat{e}_r \quad , \qquad (3.117)$$

and with substitution of velocity profiles it can be shown that

$$I = \frac{3\pi r E}{4}(U^{*2}+V^{*2}) + \pi r U^* V^* \quad . \qquad (3.118)$$

For the two limiting cases of pure potential vortex (U*=0) and pure radial flow (V*=0,E=0) the radial vorticity convected inward becomes $\frac{3\pi r}{4} V^{*2} E$ and zero (as expected), respectively.

The substitution of Eqs. (3.98) and (3.99) for U* and V* for cases i and ii, respectively, gives

$$I = \frac{3\pi E}{4r} + \frac{\pi}{r}\frac{m_o}{1+m_o^2} \quad , \quad \text{, case i} \qquad (3.119)$$

$$I = \frac{3\pi E}{4r}\frac{r^4+m_o^2}{1+m_o^2} + \pi r \frac{m_o}{1+m_o^2} \quad , \quad \text{case ii} \qquad (3.120)$$

Numerical results for the radial vorticity inflow rate, I, are presented in Figs. 3.22 and 3.23 for cases i and ii, respectively, for different values of m_o. For small radii, it is observed that $I \sim \frac{1}{r}$ for both cases and for all values of m_o. However, as the boundary layer solution is not valid for r sufficiently small these results

for I are probably not valid near the axis (r=0). Also the results show that for case i the radial vorticity inflow rate at any radius increases with m_o for values of m_o less than unity. Further increases in m_o result in a decrease of vorticity inflow rate until the limiting case of the pure potential vortex flow ($m_o=\infty$) is reached. The results for case ii show a continuous decrease in radial vorticity inflow with increasing m_o for large values of r(r>.8). For $m_o \leq 1$ these results for I are not valid for this case (except possibly for r>.8) due to the boundary-layer separation as suggested in Fig. 3.5. The vorticity inflow rate is seen to be independent of m_o for $m_o \geq 10$.

It is of interest to note that for the values of m_o used in the experiments with Ward's apparatus ($m_o<1$) the shallow convergence contributes most to the total torque exerted on the flow by the lower boundary. The experiments indicated that the critical swirl parameters necessary for the production of multiple vortices in Ward's apparatus lie within the range of $\phi_{cr}<45°$ corresponding to $m_o<1$. Also, the above results indicate that increasing values of m_o result in substantial increases in the radial vorticity inflow rate only for casei-corresponding to the shallow convergence zone of Ward's apparatus -- and only for $m_o<1$. Thus it appears that the existence of the shallow region with an inviscid flow similar to case i is crucial for the production of such features as multiple vortex phenomenon for several reasons. First, the existence of the convergence region is important in that only within this region is considerable torque exerted on the flow due to large values of the radius. Second, it is within this region that an unseparated

boundary-layer exists and therefore considerable torque as well as radial vorticity could be produced. Third, only in this region is it observed that the radial vorticity inflow rate increases with increases in the values of m_o (provided $m_o<1$). Fourth, the fact that the critical values of the swirl parameter for the production of two and even three vortices in Ward's apparatus correspond to $\phi_{cr}<45°$ ($m_o<1$) is consistent with the view that vorticity production in this region is responsible for the observance of this phenomenon. It seems reasonable to conclude that the shallow convergence zone in Ward's apparatus which is absent in all other laboratory tornado simulations plays an essential role in the occurrence of such features as multiple vortices.

3.5. Summary.

The results obtained and presented in Figs. 3.2 through 3.7 give solutions for the boundary-layer flow parameters $\delta(r)$ and $E(r)$ needed for determination of the velocity field in the boundary-layer region in cases of interest pertaining to tornado flowfields. These results contain the previously known limiting case of pure potential vortex flow ($m_o = \infty$) as well as the derived analytical solutions for the limiting case of pure radial flow ($m_o = 0$). The numerical solutions were obtained by integration of the boundary-layer momentum equations which were expressed in the inviscid streamline coordinate system (s,n,z). In Figs. 3.8 through 3.21, results are given for the relative direction change of streamlines at the ground as compared with the impressed inviscid flow, the shear stress components at the ground, the axial velocity at the edge of the boundary layer and the total torque exerted by the fluid on the ground.

The outer inviscid flowfield associated with naturally-occurring tornado vortices was discussed and was used in obtaining the associated solutions of the boundary-layer equations. It is believed that the existence of a non-zero radial velocity component is the more realistic flow model for tornado vortices in contrast to that of a pure potential vortex inviscid flow. This is confirmed by previous observations as well as by laboratory experiments using Ward's apparatus. Specifically, the existence of a separated flow region is confirmed in experiments with Ward's flow. Also, a "reattached" boundary layer in the high swirl region near the core is observed which is in agreement with the calculations of boundary-layer thickness presented here for large m_o.

The numerical results obtained herein could also be used for the evaluation of such boundary-layer phenomena as the streamline direction change in comparison with observed debris pattern to increase understanding of various types of tornado vortices. An estimation of the flow direction and velocity near the ground is also readily obtained by means of the results presented here. It should be emphasized, however, that for small values of radius the flow direction at the ground as obtained by the above calculations is not significantly different from the results obtained using a potential vortex flow model. That is, sufficiently close to the core the flow direction at the ground becomes independent of the inviscid outer flow model chosen for the boundary-layer calculations. This is due to the large local values of the swirl parameter obtained near the axis for both the potential vortex model and the swirling converging flow model. That is, in the latter case the radial component of velocity in the outer flow becomes negligible near

the axis ($U^* \sim r$) yielding an inviscid flowfield near the axis which is quite like that of the potential vortex model which has zero radial velocity. It can thus be concluded that observation of debris patterns very close to the axis of tornadoes would not discriminate any outer flow structure from that of the purely swirling potential vortex flow model.

The results obtained for the radial vorticity inflow, Figs. 3.22 and 3.23, indicate the importance of the convergence zone in Ward's experimental apparatus in the simulation of tornado flow. This is due to the fact that only in this region (corresponding to case i of our calculation) does the vorticity produced in the boundary layer increase with increasing m_o. The experimental range of values of ϕ_{cr} necessary for "core splitting" phenomenon to occur in Ward's apparatus also seems to be in agreement with the calculated range of $m_o (m_o < 1)$ for which vorticity inflow is observed to increase with increasing m_o. These results, therefore, add confidence to the core instability model described herein as well as emphasize the importance of such distinct features of Ward's apparatus as the convergence zone in the laboratory simulation of tornado flows.

CHAPTER IV

TORNADO CORE AND THE FUNNEL

4.1 Introduction

Of all the features of tornadoes, least is known about the tornado funnel. Although important in the overall dynamics of the vortex flow, little is known about the nature of the flow in the funnel. This is the case, primarily, because the cloud particles forming the funnel surface make photographic and visual observations of debris and dust particles, necessary for flowfield measurements, impossible. In the Hoecker's observation of Dallas tornado of April 2, 1957 (the most complete tornado flowfield measurements available), no data could be obtained near the tornado axis except in the region below the pendant funnel.

This lack of experimental measurements on the core flow region has resulted in uncertainty as to the structure of the vortex. There exist disagreements on such basic questions as the direction of the flow on the axis of the funnel and only indirect qualitative observations are available for any realistic evaluation of vortex flow models.

4.2 Radius of Maximum Tangential Velocity.

One of the features of the tornado core which has been, at least relatively, accurately measured by Hoecker is the radius of maximum tangential velocity. In Hoecker's observations, for example, two

important features associated with this radius are observed. First, the radius of maximum tangential velocity varies with height. This variation is shown in Fig. 4.1. The radius is observed to increase rapidly from zero at the ground to a value of about 140 feet at a height of about 200 feet and then remain relatively constant with height in a cylindrical shape up to a height of about 800 feet. A relatively constant moderate increase in the radius of maximum tangential velocity is then observed to occur up to a height of about 1400 feet. Second, the diameter of this core is observed to be larger than most vortex models would predict. The diameter which starts from zero on the ground increases to about 300 feet at 1400 feet above the ground. Most of the theoretical vortex flow models for tornadoes predict values much less than those observed by Hoecker. This is parimarily due to the fact that in these models the core is assumed to be structured by viscosity. For example, the Rott-Burgers solution for an axisymmetric vortex flow discussed previously fails to show a variation of the core radius in the height because of the assumed decoupling of the swirl and the meridional flow. Furthermore, in this model the radius of maximum tangential velocity is determined by the viscosity and is given by $r_m = 1.12\sqrt{2\bar{\nu}/a}$ where $\bar{\nu}$ is the eddy viscosity and a is defined by Eq. (2.14a). Among other similar models of viscous vortices is the two-cell solution of Sullivan which gives a somewhat larger core radius of $2.38\sqrt{2\bar{\nu}/a}$. Likewise, Kuo's solution of a two-cell vortex driven by the release of latent heat in a conditionally unstable atmosphere gives a viscous core radius approximately equal to that of Rott-Burger's vortex. A comparison of these results with the result of observations of tornadoes

is useful. For a ≈.2 (from a radial velocity profile given by Hoecker and $\bar{\nu} \approx 90$ ft^2/sec, (a value assumed by some authors [Davies-Jones,and Kessler, 1973] and probably too large), the radii of maximum tangential velocity obtained by the Rott-Burgers vortex and Sullivan two-cell vortex (which is not applicable to lower single vortex flow of the Dallas tornado) are approximately 35 ft and 75 ft, respectively. The radius of the core in solid body rotation observed by Hoecker, although varying with height, shows corresponding value of approximately 220 feet at the same height. Thus observations of core radius in naturally occurring tornadoes give values for the core radius almost one order of magnitude larger than the calculated values given by viscous vortex models.

There are also several questions concerning the observed funnel and its relationship to the core flow. Specifically, although the funnel is understood to be a condensation pressure surface, the spatial location of this surface with respect to the stream surface representing the boundary of the recirculating core flow is not clear. It is commonly assumed that the two surfaces coincide indicating that the funnel is, at the same time, the boundary of a two-cell core structure. A more common assumption, however, is the coincidence of the funnel surface and the condensation pressure isobar. The observations of Hoecker, however, clearly indicate that the location of the funnel surface and the derived position of the condensation isobar do not coincide at any time during the entire observed life time of the Dallas tornado. Likewise, the radius of the maximum tangential velocity (r_m) profile is not usually distinguished from the observed tornado funnel, especially in

situations where the funnel is located on the ground.

In the following we suggest a possible reason for the large observed radius (as compared with viscous-structured core model results) based on an estimate obtained neglecting viscosity all together. Also, a qualitative model of the tornado vortex is proposed involving a four "funnel" core structure. An order of magnitude calculations relating the water vapor condensation process to the spatial location of the funnel is also given to substantiate the arguments presented. Although the discussion is qualitative and the numerical values obtained are estimates based on order of magnitude analysis, it is believed that the model proposed is more accurate than the simplier ones now extent.

It is known that an exact analysis of the core flow cannot ignore the effects of viscous forces. However, it can be shown that the core radius is not necessarily determined by viscosity. Although a coupling of the meridional and tangential flows by viscosity would seem to be important in describing the observed variation of tangential velocity with height [giving, in turn, a z-dependent radius of maximum tangential velocity, $r_m(z)$], the dimensions of the core could be determined by flow-field dynamics that are essentially inviscid. More specifically, the axial and the lateral pressure changes must be dynamically related so that they match on the axis of the vortex. That is, if the pressure at $r = 0$, $z \to \infty$ and $r \to \infty$, $z = z$ are $p_a(\infty)$ and $p_\infty(z)$, respectively, and if we further define

$$\Delta p_1(Z) = p_a(\infty) - p_a(Z) \tag{4.1}$$

and

$$\Delta p_2(Z) = p_\infty(Z) - p_a(Z) \tag{4.2}$$

where $p_a(Z)$ is the pressure on the axis of the vortex at a height Z, continuity of the pressure requires

$$p_a(\infty) - \Delta p_1(Z) = p_\infty(Z) - \Delta p_2(Z) \quad . \tag{4.3}$$

This matching condition for the pressure as well as initial conditions for swirl imposed by the large scale atmospheric flow can be used to estimate the dimensions observed for the tornado core. In this way, it is assumed that viscous forces do not play a primary role in the determination of the core radius.

To illustrate this in more detail, a cylindrical region of constant density fluid is assumed with an interior axisymmetric vortex given by a modified combined Rankine vortex. The tangential velocity is assumed to vary as

$$V^* = \bar{a}(z)\, r \qquad r \leq r_m \tag{4.4a}$$

$$V^* = \frac{\Gamma(z)}{2\pi r} \qquad r \geq r_m \tag{4.4b}$$

The pressure far away from the radius approaches the ambient pressure p_∞ as the velocity components all go to zero.

We further assume hydrostatic equilibrium in the environment. The vertical momentum equation for the undisturbed environment becomes

$$0 = -\frac{1}{\rho_\infty}\frac{\partial p_\infty}{\partial Z} - g \tag{4.5}$$

where p_∞ and ρ_∞ are environmental pressure and density, respectively. Introducing the disturbance pressure, $\hat{p}$, as

$$\hat{p} = p - p_\infty \tag{4.6}$$

we then obtain the vertical momentum equation along the vortex axis, neglecting viscous effects, as

$$W_a^* \frac{\partial W_a^*}{\partial Z} = -\frac{1}{\rho}\frac{\partial \hat{p}_a}{\partial Z} \quad . \tag{4.7}$$

The boundary condition imposed on the top of the cylindrical region corresponding to the conditions aloft in a real tornado are not clear. To proceed, we assume a constant pressure boundary imposed at the top. That is we assume $\hat{p} \to$ constant as $Z \to \infty$ for any r. This constant pressure corresponds to the disturbed pressure at some large height presumably determined by the thermodynamic state of the upper atmospheric layers (which is different than that in the lower regions of the atmosphere where, as $r \to \infty$, $\hat{p} \to 0$). The assumption of a constant pressure boundary is based on two observations. First, Hoecker's derived pressure field which is based on the cyclostrophic balance in the radial direction indicates an almost linear variation of disturbed ($\hat{p}$) pressure with height in the region near the tornado axis. This disturbed pressure variation with height is shown in Fig. 4.2. Although the observations are limited to a relatively shallow layer near the ground, a straight line extrapolation of the data suggests the pressure returns to ambient at about 3000 feet above the ground. The observed decrease of the disturbed pressure along the axis suggests that $\hat{p}_a$ would approach a constant value (due to the finite extent of the atmosphere) far away ($Z \to \infty$). Thus, with the choice of zero reference disturbed pressure in the lower atmosphere, $\hat{p}_a(Z \to \infty) = -b < 0$. The approximations involved in the derivation of pressure field by

Hoecker and the linear extrapolation are sufficient for the estimates to be made here. The second observation is that of Ward's simulated tornado flow. The honeycomb baffle separating the observed vortex from the exhausting flow above destroys the swirl in the flow and produces an approximately constant radial pressure profile at the top of the vortex flow. The assumption of a constant pressure boundary condition would then imply a downward flow along the axis due to the vertical pressure gradient produced by the swirl in the interior of the cylindrical model. This downward flow along the axis is observed both in naturally-occurring tornadoes as well as laboratory models of the flow. The stagnation point on the ground at the axis and the vertical shear produced by the outer coverging-convecting flow would then create a recirculating flow in the core in order to satisfy conservation of mass. It should be noted that the stagnation point could be located above the ground such as in cases where the tornado funnel does not touch the ground. A case in point is the 1957 Dallas tornado where an upward decelerating flow along the axis near the ground is observed. We will return to this possibility shortly.

To arrive at an estimated value for the radius of maximum tangential velocity we assume, as previously suggested, that the pressure drop along the axis must match the drop in pressure with radius due to the radial pressure gradient. The latter can be obtained from a cyclostrophic balance as an approximation to the radial momentum equation

$$\frac{1}{\rho}\frac{\partial \hat{p}}{\partial r} = \frac{V^{*2}}{r} \quad . \tag{4.8}$$

Integration of above along the radius with the velocity profiles given

by Eqs. (4.4a) and (4.4b) implies

$$- \hat{p}_m \simeq \tfrac{1}{2}\rho \left(\frac{\Gamma(z)}{2\pi r_m}\right)^2 \tag{4.9}$$

and

$$\hat{p}_m - \hat{p}_a(z) \simeq \tfrac{1}{2}\rho (\bar{a}\ r_m)^2 \tag{4.10}$$

where $\hat{p}_m = \hat{p}(r=r_m)$ and $\hat{p}_a(z)$ is the disturbed pressure on the axis. Elimination of $\hat{p}_m$ in above equations yields

$$- \hat{p}_a = \rho \left(\frac{\Gamma}{2\pi r_m}\right)^2 \quad . \tag{4.11}$$

The pressure drop along the axis is obtained by integrating the vertical momentum equation, Eq. (4.7), on the axis with respect to Z. There results

$$- \hat{p}_a(z) = \tfrac{1}{2}\rho W_a^{*2} + b \ . \tag{4.12}$$

Equating (4.11) and (4.12) gives an estimate of r_m as

$$r_m \simeq \sqrt{2}\, \frac{\Gamma/2\pi}{W_a^*} \frac{1}{\sqrt{1+K}} \tag{4.13}$$

where $K = \dfrac{2b}{\rho W_a^{*2}}$ is a ratio of the pressure far above on the axis to the dynamic head at a point on the axis. It should be emphasized that the above estimate for r_m is based on an inviscid analysis. Therefore, Eq. (4.12) is not valid in the region near the lower boundary where, because viscous forces become significant, $W_a^* \to 0$.

To be able to compare this result with observation, we derive the same estimate in a slightly different manner for the single-vortex, 1957 Dallas tornado which had an upward flow along the axis at low

levels. For this purpose, consider a swirling, converging streamline with negligible velocity far away from the axis (see Hoecker, 1960). The radial convergence of the streamline converts potential energy of a fluid element into kinetic energy (assuming negligible dissipation). This "fall" toward the axis produces a kinetic energy per unit volume equal to $\rho(\frac{\Gamma}{2\pi r_m})^2$, assuming the cyclostrophic balance, Eq. (4.8). Furthermore, once on the axis the fluid element is decelerated upward toward the stagnation point aloft. Hence the kinetic energy of the fluid element is spent on overcoming the pressure "hill" along the axis. If the disturbed pressure at the stagnation point ($\hat{p}_s$) is assumed to be determined by the axial streamline descending from far aloft ($Z \to \infty$), then neglecting viscous effects, we have

$$\hat{p}_s = \hat{p}(Z=\infty) = -b \quad . \tag{4.14}$$

Therefore the pressure "hill" to be overcome is given by Eq. (4.7) as $(\frac{1}{2}\rho W_a^{*2} + b)$. A mechanical energy balance then gives an estimate of the radius of maximum winds as

$$r_m \simeq \sqrt{2}\ (\frac{\Gamma/2\pi}{W_a^*})\ \frac{1}{\sqrt{1+K}} \quad . \tag{4.15}$$

the same result as obtained above Eq. (4.13). The above result is also based on an inviscid model. Therefore near the ground where $W_a^* \to 0$ it is not applicable. Also, such factors as the contribution of radial velocity to the kinetic energy of the flow is neglected.

In order to compare above results with Hoecker's data we further assume the simplification $b = 0 (k = 0)$. Although this assumption would result in a higher estimate for radius of tangential velocity the result

is believed to be accurate for the purpose of argument here -- that the radius of maximum tangential velocity, r_m, is determined by an inviscid analysis based on the pressure matching condition given in Eq. (4.3). Choosing a streamline with $\Gamma \simeq 1600$ mph-ft and an axial velocity of 100 mph at $Z \simeq 400$ feet we obtain from the simplified result

$$r_m \simeq \sqrt{2}\ \left(\frac{\Gamma/2\pi}{W_a^*}\right) \quad . \tag{4.16}$$

An estimated value of $r_m \simeq 200$ feet. This is in good agreement with the observed 160 feet, considering the approximate nature of the calculations and that the result obtained is an upper estimate due to the assumption $b = 0$.

We conclude that an inviscid analysis based on the assumption of a matching of the pressure change of the axis gives an estimate of the radius of maximum tangential velocity which is in better agreement with observation than those derived from viscous-structured vortex models.

It should be further noted that a significant feature of the above analysis is that the axial velocity is the same order of magnitude as the tangential velocity near the axis. This can be directly deduced from the governing flow equations for vortex flows with small Rossby number (negligible coriolis forces) and Froud numbers of order one or less (negligible buoyancy forces). In these flows, the vertical momentum equation implies a balance of pressure gradient and inertial terms, $p \sim \rho W^{*2}$, and the tangential momentum equation implies a pressure gradient-centrifugal force balance implying $p \sim \rho V^*$. These two results then give $V^* \sim W^*$. This is believed to be an important

feature of tornado core flows [Morton ,1966]. Hoecker's measurements of axial velocity, given in Fig. 4.3, substantiate this conclusion. Qualitative observations of Ward's core flow are also in agreement. By introducing smoke directly into the core above ground, it is observed that the smoke is swept down rapidly in a thin column toward the ground. Observations suggest that the downward axial velocity above the lower boundary layer is comparable to the tangential velocity component near the core.

4.3 Structure of Tornado Flows Near the Tornado Axis-A Qualitative Description.

We now wish to discuss a qualitative model of tornado flows near the axis based on assumptions that will be elicidated shortly. To begin, it should be noted that laboratory simulations of tornado cores have certain inherent limitations in simulating all of the features associated with this region. For example, the tornado funnel, which is often assumed to be a condensation pressure isobar, cannot be easily simulated in the laboratory. In almost all laboratory simulations of tornadoes, the observed "funnel" (actually the recirculating boundary) core is, in fact, a stream surface. This is true in the simulated tornadoes of Yin and Chang [1970], Wan and Chang [1972], Turner [1966], as well as Ward [1972]. For the latter, for example, this observed stream surface shows the boundary between the recirculating core flow and the outer, inviscid swirling, converging flow. Smoke particles introduced near the ground for visualization purposes are swept inward by the converging, radially decelerating flow in the experiment. The

convergence of these streamlines near the ground is balanced by the diverging flow in the interior of the core, concentrating the smoke particles in the stream surface separating the two regions. Laboratory simulations of tornado flows, then, may not be very useful for examining the relationship between the observed funnels in naturally-occurring tornadoes and the recirculating core flow (if such exists). As a consequence, discussions of the funnel must rely on the available direct, qualitative observations of naturally-occurring tornadoes and approximate calculations based on the dynamic and thermodynamic processes in these vortex flows.

In order to describe certain observed features of tornado funnels, we propose that a clear distinction be made between four different funnel-like profiles. This is important if any realistic estimate of significant parameters of the flow is to be obtained -- especially near the axis of the tornado. Although distinct from each other, these four "funnel" profiles are dynamically and thermodynamically coupled.

The first "funnel" profile is the most obvious feature of natural tornadoes. This is the observed trunk-shaped funnel which is pendant from the cloud deck of the storm. The funnel could end either in mid-air or on the ground. This "funnel" of tornadoes is, of course, the only one that can be easily observed. The size, behavior and the motion of the funnel can be determined by photographic or visual methods. Although this profile is the most easily observed feature of tornadoes, there is, however, uncertainty as to what it represents. The most common assumption is that the tornado funnel is the condensation pressure isobar. This is partly based on the similarity of the pressure

isobar profiles with the funnel [Dergarabedian, Fendell, 1970]. A second assumption is that the funnel is a stream surface [Hoecker, 1961][35]; that is there is no flow normal to the observed surface of the funnel.

The second "funnel" profile is the radius of the maximum tantential velocity in tornadoes. This profile for Dallas tornado is presented in Fig. 4.1 and has been discussed already. It would seem reasonable to assume that this relatively large diameter core always begins from the ground surface regardless of the position of the observed funnel. As shown in Fig. 1.1, the profile $V^*_{max}(r,z)$ while similar to the shape of the observed tornado funnel, is by no means coincident with it.

That this is possible can be clearly demonstrated by the following estimation of the relative position of the funnel cloud and the maximum tangential velocity profile. We assume that the funnel cloud is approximately given by a pressure isobar p_1 (we will discuss this in more detail later) and the tangential component of velocity field is given by a combined Rankine vortex.

$$V^* \sim r \qquad r \leq r_m \tag{4.17}$$

$$V^* \sim \frac{1}{r} \qquad r \geq r_m \tag{4.18}$$

where r_m is here the radius of maximum tangential velocity. If a cyclostrophic balance is assumed

$$-\frac{1}{\rho}\frac{\partial p}{\partial r} = \frac{V^{*2}}{r} \quad . \tag{4.19}$$

Then, with proper nondimensionalization, we have

$$\frac{\partial p}{\partial r} = \begin{cases} -r & r \leq r_m \qquad (4.20a) \\ -\frac{1}{r^3} & r \geq r_m \qquad (4.20b) \end{cases}$$

where all the quantities in above equations are nondimensional. Integration of above equations yields

$$p_\infty - p_1 = \begin{cases} \frac{1}{2}\left(\frac{1}{r_m^2} - r_m^2\right) + \frac{1}{2} r_1^2 & r_1 \le r_m \quad (4.21a) \\ \frac{1}{2}\frac{1}{r_1^2} & r_1 \ge r_m \quad (4.21b) \end{cases}$$

where r_1 and p_1 are the radius and the pressure of the funnel surface. Rewriting the above in the following forms

$$r_1^2 = 2(p_\infty - p_1) + \left(r_m^2 - \frac{1}{r_m^2}\right), \qquad r_1 \le r_m \qquad (4.22)$$

and

$$r_1^2 = \frac{1}{2(p_\infty - p_1)}, \qquad r_1 \ge r_m \qquad (4.23)$$

where r_m is the radius of maximum tangential velocity. We observe that for sufficiently large p_1 (but $\le p_\infty$), the second equation could be satisfied; that is $r_1 > r_m$ corresponding to the funnel lying outside the radius of the maximum tangential velocity. Likewise with $p_1 > p_\infty - \frac{1}{2r_m^2}$ the first equation would imply $r_1 < r_m$ corresponding to the funnel lying inside the radius of the maximum tangential velocity. Since p_1 is determined by independent factors such as water content of the surface layer of atmosphere, the tornado funnel cloud could completely encompass the maximum tangential velocity profile or vice-versa. Hoecker's observational evidence [1961] confirms the existence of at least the latter possibility. In this regard, unusual observations of the Ellsworth, Kansas tornado of June 20, 1926 [Flora, 1959][36], suggests that

for sufficiently low p_1 (very dry air in the lower atmosphere) the vortex could fail to produce a funnel. Photographic evidence of the debris pattern on the gound near the axis for this case, nonetheless, does suggest that the existence of a vortex.

The third "funnel" profile is the condensation pressure isobar as given by the conditions far away from the tornado vortex. Because of strong swirling flow the shape of this profile, which is similar to other pressure isobars, resembles the observed funnel and in fact it is commonly assumed that they are coincident. Hoecker reports that the condensation pressure at the time of the occurrence of the Dallas tornado of April 2, 1957 was about 950 mb. The pressure profile system of this tornado (see Fig. 1.2) indicates a large diameter (e.g. approximately 200 feet) for the isobar corresponding to this value. Also, the diameter of the suggested 950 mb pressure profile is observed to remain larger (at any height) than the diameter of the observed funnel all during the lifetime of the tornado. In fact, the largest observed funnel diameter on the ground (approximately 100 feet) is less than half of the value of the diameter of the 950 mb isobar. This observation is attributed by Hoecker to the change of the water content in the recirculating core flow [Hoecker, 1961]. This, however, is based on the assumption that the observed funnel coincides with the condensation pressure isobar, p_c, and the recirculating core flow boundary. There is no reason, however, why this assumption should be true. The condensation pressure isobar is essentially determined by thermodynamic processes involving water vapor condensation whereas the boundary of the core flow is determined by a dynamic balance involving pressure

and inertial forces near the axis. Therefore, Hoecker's observations of a larger diameter for the condensation pressure isobar than the diameter of the observed funnel might be explanable by considering the details of condensation process in the converging inviscid flow. A nonequilibrium condensation process to be discussed shortly is believed to explain this observed difference in the two diameters.

The fourth "funnel" in tornadoes is the boundary of the recirculating core of the tornado. This is the profile that separates the two regions of the flow -- an outer, upward-converging, swirling flow region and an inner, downward -- diverging core region. The former is that of the swirling converging flow which is turned upward as a consequence of mass conservation and the latter is believed to be a recirculating flow which meets the outer region at the "wall" of the core. The existence of the latter funnel-like profile presupposes the assumption of a downflow along the vortex axis. Although not a certainty, there exists supporting evidence for a downflow in the core of real tornadoes [Hoecker, 1961] as well as in the laboratory simulation models as discussed earlier. The existence of an exact solution to the Navier-Stokes equations of a vortex flow with a double-cell structure, the experimental evidence as well as the assumed nature of the conditions aloft (imposed constant pressure boundary) have led several authors to assume a descending flow on the axis of the core (e.g. [Ward, 1972; Hoecker, 1961]). It should, however, be noted that the existence of downflows would not necessarily imply a closed recirculating core flow. In fact the nature of the closure aloft still remains a difficult question to be resolved.

If one, however, assumes a closed recirculating core, the model would then imply the existence of at least two stagnation points on the axis of the tornado. This follows by the boundary condition imposed on the axial velocity $W_a^* = 0$ at $z = 0,\ h$, where h is the height at which pressure reaches an undisturbed value. Furthermore, if it is assumed that the tornado core is not in contact with the ground, there would be a third stagnation point on the axis where the axial velocity changes sign. In this situation the axial flow has a more complicated structure in which the converging swirling flow near the ground, forming a single-cell vortex, is decelerated axially and diverges outward forcing a two-cell structure to close in mid-air. The swirl-to-updraft-strength ratio as well as the conditions aloft imposed on the flow seems to be important in determining the position of this stagnation point on the axis. It should be of significance that the existence of this stagnation point located along the axis is also observed in Ward's flow [Ward, 1972; Davies-Jones, 1973] for small values of swirl parameter (small swirl to radial convergence ratio). Increasing the swirl, with the low-level convergence kept constant, results in lowering the stagnation point toward the lower boundary. Hence, it seems reasonable to assume that during the observed life of a tornado (from birth to decay) the axial flow exhibits both a two-cell vortex structure (stagnation point on the ground) and a combination of a one-cell vortex on the ground with a two-cell vortex aloft (stagnation point on the axis above the ground) due to the changes in the strength of low-level convergence and/or the imposed circulation, resulting in a variation of their ratio. These two situations are shown in Figs. 4.4 and 4.5,

respectively. The former represents a two-cell vortex on the ground (two stagnation points A and B) and the latter a combination of one and two-cell core structures (three stagnation points A, B and C).

Some investigators have assumed the observed funnels of tornadoes, the core of the tornado and, in some cases, the condensation pressure isobar to be coincident. We now want to show that although the tornado is a condensation surface it may not be coincident with the condensation pressure isobar.

The tornado funnel would coincide with the condensation pressure isobar only if the characteristic time for condensation to occur is much smaller than the characteristic flow time of air particles -- the time required for a fluid particle to traverse a characteristic length. That is, if the former time is $\bar{\tau}$ and the latter is t_c, then a nondimensional parameter κ can be defined as $\kappa = \frac{\bar{\tau}}{t_c}$. If $\kappa << 1$ then the tornado funnel is expected to coincide with the condensation isobar. This limiting case is the equilibrium situation in which the condensation process proceeds much faster than the typical time scale of motion of the particles. If $\kappa >> 1$ then the tornado funnel is expected to coincide with the tornado core. This is the "frozen" situation where water vapor is presumably brought down in the core from the cloud deck above by means of the recirculating flow in the core.

The time required for the equilibrium to be reached in a condensation process is dependent on many factors such as pressure, water vapor content, etc. but the order of magnitude of the characteristic time as 1-10 seconds [McCarthy] even for large (50%) pressure drops. This relatively large value is due to the slow diffusion process which

is the limiting factor in the condensation process. We now want to estimate the order of magnitude of $\bar{\tau}$ for the particular case of the Dallas tornado. The condensation pressure at the time of the tornado was 950 mb as given in [Hoecker, 1961]. The rate of growth of drop radius as a consequence of diffusion can be shown [Fuchs, 1959] to be

$$\bar{r}\,\frac{d\bar{r}}{dt} = \frac{D}{\rho_L}\,\frac{M_w}{R\bar{T}}\,(P_{v\infty}-P_{vd}) \quad , \tag{4.24}$$

where $\bar{r}$, D, ρ_L, M_w, $\bar{R}$, $\bar{T}$, $P_{v\infty}$, P_{vd} are the radius of the drop, diffusion coefficient, liquid water density, molecular weight of water, universal gas constant, ambient temperature, water vapor pressure far away from the drop and the vapor pressure at the surface of the drop, respectively.

In Eq. (4.24) it is assumed that the contribution due to the relative velocity of the drops and the air is negligible. Also, other non-diffusion effects (such as the influence of Stefan flow etc. [Fuchs, 1959] are believed to be small and negligible. However, there are two assumptions made in the above equations that need special attention. First, heat conduction is neglected and the temperature change due to conduction at the drop is not considered. However, the effect of heat conduction and its influence on the growth of condensation particles does not effect the order of magnitude of the results obtained. It will be shown later that although the accuracy of the results obtained will be reduced somewhat, the order of magnitude analysis in the following calculations is essentially correct. The second and more important factor neglected in the above is the presence of soluble nuclei in the atmosphere. That is, we assume that the condensation nuclei present in the atmosphere have radii of the order of

one micron or less. The wind velocity as well as the turbulent nature of the flow in the vicinity of tornado vortices would, in all probability, cause the presence of large ($\bar{r} \geq 1\mu m$) nuclei in the atmosphere. This would considerably influence the rate of condensation of water vapor near saturation conditions. On the other hand, a factor that, could greatly decrease the presence of large size soluble nuclei is the abundant precipitation caused by the tornado producing storm. That is, the decrease in the density of large nuclei could be significant since rain drops are quite efficient in sweeping out precisely these large nuclei. The collection efficiency of rain drops become negligible only for nuclei with $\bar{r} < 0.1\mu m$ [Mason, 1971]. A clear resolution of this question would have to wait for the result of experimental observations on the density of the large nuclei ($\bar{r} \sim 10\mu$) in the atmosphere in conditions considered here. We shall proceed assuming the density of such large nuclei is negligible.

With the above approximations, we now wish to obtain a rough estimate of the time $\bar{\tau}$ required for the growth of a cloud particle. If the initial radius of the drop is assumed to be 1 μm, and the final radius 10 μm (typical of an observable cloud particle) we have from Eq. (4.24) that

$$\int_0^{\bar{\tau}} (p_{v\infty} - p_{vd}) dt = \frac{\rho_L \bar{R} \bar{T}}{D M_w} \left(\frac{r_F^2 - r_o^2}{2}\right) . \tag{4.25}$$

If we take the following as being typical parameter values

$$\rho_L = 1 \frac{g}{cm^3} , \quad M_w = 18.02 \frac{g}{mole} , \quad \bar{T} = T_{env} = 283°K,$$

$$\bar{R} = 8.314 \times 10^7 \frac{erg}{mole\text{-}°K} , \quad r_o = 1\mu = 10^{-4}cm, \quad r_r = 10\mu = 10^{-3}cm$$

$$D = .257 \frac{cm^2}{sec}$$

we would obtain

$$\int_0^{\bar{\tau}} (p_{v\infty} - p_{vd})\,dt = 2675 \ \frac{g}{cm\text{-}sec} \ . \qquad (4.26)$$

We further assume a steady flow where the flow particles would then follow the swirling converging streamlines. The integrand in above equation is estimated from the pressure variation for a fluid particle converging on a typical streamline in the Dallas tornado. For this purpose we chose a streamline passing through a point at approximately 500 feet radius from the tornado axis with a height of 60 feet from the ground (see Hoecker, 1960). Using the pressure profile [Hoecker, 1961], the pressure variation on this streamline is shown in Fig. 4.6. In the regions where streamlines were not available, extrapolation was used. The resulting inaccuracy is thought to be negligible for the purposes of the order of magnitude estimate being developed here.

Assuming dry adiabatic cooling, a temperature history of the air parcels on this streamline is shown in Fig. 4.7. It is important to note that assuming dry adiabatic cooling (as contrasted with a moist adiabatic cooling) results in a lower bound for the temperature and hence a lower bound for the vapor pressure p_{vd}. This in turn will give an upper bound for the integrand and hence a *lower bound* $\bar{\tau}$. For $\bar{T}$ = 283 °K, a maximum temperature change of 10 degrees is obtained. Also, from Fig. 4.7, $p_{v\infty} \simeq 0.17$ psi and $p_{vd} \simeq 0.14$ psi. Hence, an approximate evaluation of Eq. (4.26) yields

$$\bar{\tau} = \frac{2675}{[(.17)-(.14)]\frac{1.01\times 10^6}{14.7}\frac{\text{dyne/cm}^2}{\text{psi}}} \simeq 1.3 \text{ sec} \qquad (4.27)$$

The effect of heat conduction away from the drop, assumed small in the above calculations, can now be estimated. For the particular streamline chosen we note that heat conduction would result in a lower temperature and a corresponding lower p_{vd}. However, even for much larger decreases in temperature (say, 50%), the decrease in p_{vd} (then, 20%) would not cause large errors in the value of $\bar{\tau}$ obtained (less than 50%). Furthermore, the assumption of dry adiabatic cooling process tends to compensate for the errors produced by neglect of heat conduction. Therefore, the order of magnitude obtained for $\bar{\tau}$ is believed to be correct.

With a lower limit of 1.3 seconds for $\bar{\tau}$, the condensation characteristic time is observed to be comparable to the characteristic flow time. That is, for values of t_c between 1-10 seconds, a lower bound value of κ for the typical lower streamline discussed lies between 1.3 and .13. Hence, roughly, κ is expected to be of the order of unity.

It thus appears that, given the velocity fields of typical tornadoes, the condensation process in natural tornadoes is a non-equilibrium one. Thus, once an air parcel's pressure is reduced to the condensation pressure, the parcel may travel as much as 300 feet before visible condensation has occurred. It then follows that the core cannot coincide with the funnel cloud except near the top of the funnel where it blends into the cloud deck -- corresponding to long

flow times. Furthermore it is expected that the core region and, in particular, the stagnation point near the tip of the funnel (point c in Fig. 4.5) should always lie on or within the funnel cloud and never outside of it if the saturation condition are achieved in the outer flow. Thus, we expect that the core flow will always be enclosed by the condensation surface of the tornado funnel cloud in this situation.

A sketch of the proposed relative positions of the four funnel-like profiles -- the recirculating core, the condensation funnel, the condensation pressure isobar surface and the maximum tangential velocity profile -- are shwon in Fig. 4.8. It is of interest to note that the nonequilibrium process described would, presumably, result in a relatively wide region of partial condensation surrounding the funnel. The existence of different sized soluble nuclei in the environment of the vortex would cause partial condensation to occur in the region between the condensation isobar surface, p_c, and the surface of the funnel. Therefore, photographic evidence of the edge of this region of partial condensation may be used as an estimate of the position of condensation pressure isobar. The thickness of this region should be of order of $\bar{U}^*$ where $\bar{U}$ is the average radial component of velocity in the vicinity of the funnel. While there exists photographic evidence [Flora, 1959] of tornado funnels which shows such a wide relatively transparent, fog-like region surrounding the opaque surface of the funnel, the possibility that dust particles cause this partial condensation region must be assessed. Furthermore, our nonequilibrium conden-- sation implies that the position of the tip of the funnel is probably displaced furthest from the corresponding point on the P_c isobar due

to the large vertical velocities on the axis. In this regard, [Dergarabedian and Fendell, 1970] obtain estimates of maximum tangential velocity based on the distance of the funnel tip from the ground assuming that the funnel surface is coincident with the condensation pressure isobar. However, if the assumption of a non-equilibrium condensation process is correct, such estimates could be made more accurate. That is, the nonequilibrium model implies that the "tip" of the P_c isobar is lower in height from the funnel tip by a distance of approximately $\bar{W}_a^*\bar{\tau}$, where $\bar{W}_a^*$ is the average vertical velocity on the axis. For example, for the Dallas tornado [Dergarabedian, Fendell, 1970] obtain estimates of maximum tangential velocity based on the distance of the funnel tip from the ground assuming that the funnel surface is coincident with the condensation pressure isobar. However, if the assumption of a nonequilibrium condensation process is correct, such estimates could be made more accurate. That is, the nonequilibrium model implies that the "tip"of the P_c isobar is lower in height from the funnel tip by a distance of approximately $\bar{W}_a^*\bar{\tau}$, where $\bar{W}_a^*$ is the average vertical velocity on the axis. For example, for the Dallas tornado where the funnel cloud tip was in mid-air for a considerable portion of the observed life of the tornado, if we assume $\bar{W}_a^* \simeq 150$ ft/sec., this difference in height could amount to as much as 300 feet causing considerable under-estimate of V_{max}^* -(more than 50%). Of course, if the actual value of $\bar{\tau}$ tends toward the lower end of our estimates (e.g. $\kappa \sim 0.1$), this error is reduced to less than ten per cent.

In closing this discussion, it should be emphasized once again that the assumptions used in estimating the order of magnitude of the

condensation time scale -- particularly the question of the presence of giant soluble nuclei -- remain to be experimentally investigated. In any event, it should now be apparent that the observed funnel, radius of maximum winds, condensation pressure isobar, and recirculating core boundary do not coincide and their differences may be important in interpreting observational information.

CHAPTER V

SUMMARY, CONCLUSIONS, AND RECOMMENDATIONS FOR FUTURE RESEARCH

5.1 Summary.

Measurement of the critical swirl angle ϕ_{cr} at which the usual single vortex configuration undergoes transition to a two vortex configuration as a function of the aspect ratio h/r_s of the convergent zone and normalized volumetric flow rate $(Q/r_s\nu)$ shows that

$$\tan\phi_{cr} \alpha \frac{h}{r_s} (Q/r_s\nu)^{-11/30} \quad . \tag{5.1}$$

The variation of $\tan\phi_{cr}$ with h/r_s agrees with previous theoretical results [Jischke and Parang, 1974] while the variation with $(Q/r_s\nu)$ does not agree with that theory.

Velocity measurements in the convergent zone shows that outside the edge of the convection zone (r>24"), the vertical velocity is negligibly small, the radial velocity increases with decreasing radius to conserve mass while the tangential velocity increases with decreasing radius to conserve angular momentum. In the inner convergent zone (r<24"), the radial velocity decreases approximately linearly with radius, the vertical velocity increases almost linearly with height, and the tangential velocity increases inversely with decreasing radius much like a potential vortex. The inner and outer convergent zones are separated by a transition region near r = 24" where a pronounced edge

effect is observed. The surface pressure in the inner zone varies as the inverse square of the radius, quite like that of a potential vortex. The angular velocity at the center of the vortex core was shown to vary with the imposed swirl angle ϕ as

$$\omega_{core} \sim \tan^{-4}\phi \qquad (\Gamma, h \text{ constant}) \qquad (5.2)$$

$$\omega_{core} \sim \tan^{-3}\phi \qquad (Q, h \text{ constant}) \qquad (5.3)$$

in agreement with a solid body rotation model of the core provided the correct variation of core radius with imposed swirl angle is employed (e.g. $r_c = r_s \tan^2\phi$).

These experimental results in the inner convergent zone agree qualitatively with the flow due to a potential vortex with superimposed radial velocity,

$$U^* \sim -r, \qquad V^* \sim 1/r, \qquad W^* \sim z \qquad (5.4)$$

quite like a Rott-Burgers vortex outside the core.

Comparison of the results obtained on these experiments [Wan, Chang, 1972] show that the radial and vertical velocities are considerably larger in the present study. This is due to the fact that the volumetric flow rates in the present experiments are from three to twenty-five times those in Wan and Chang's. As a result, the radial momentum associated with these higher volumetric flow rates is a significant factor in the dynamics of the flow.

The results obtained and presented in Chapter III give solutions for the boundary-layer flow parameters $\delta(r)$ and $E(r)$ needed for determination of the velocity field in the boundary-layer region in cases of interest pertaining to tornado flowfields. These results contain the previously known limiting case of pure potential vortex flow ($m_o = 0$)

as well as the derived analytical solutions for the limiting case of pure radial flow ($m_o = \infty$). The numerical solutions were obtained by the integration of the boundary-layer momentum equations which, for reasons discussed in Chapter III and in Appendix B, are expressed in the inviscid streamline coordinate system (s,n,z). Also, the calculated results for other parameters such as the change of streamline direction at the ground as compared with the impressed inviscid flow, the shear stress components at the ground, the axial velocity at the edge of the boundary layer, the total torque calculations and radial vorticity flux are given in Chapter III.

The outer inviscid flowfield associated with naturally occurring tornado vortices were discussed and were used in obtaining the associated solutions of the boundary-layer equations. It is believed that the existence of a non-zero radial velocity component is the more realistic flow model for tornado vortices in contrast to a pure potential vortex inviscid flow. This is confirmed by laboratory experiments using Ward's apparatus given in Chapter II.

The boundary-layer results obtained in this study along with the assumed outer inviscid flow enable one to evaluate several boundary-layer induced features of tornadoes. Such turbulent boundary-layer-induced phenomena as direction change in the streamlines could be used in conjunction with observations of debris patterns to increase understanding of the various types of tornado vortices as well as estimate the flow direction at the ground. However, the results obtained for the swirling converging flow near the core are similar to those obtained for a pure potential vortex flow model. Therefore, we conclude

that observations of debris patterns on the ground near the core would have to be complemented with other observations (such as flow direction in the outer flow) before they can be used to obtain a better understanding of the inviscid vortex flow.

An important boundary-layer produced feature of tornadoes is the vorticity production and its subsequent radial convergence by the outer converging flow to the vicinity of the core. The instabilities associated with the vortex sheet surrounding the core region is believed to give rise to the observed multiple-vortex formation. It appears that the radial distribution of the vorticity near the core boundary is accounted for by the upward convection of radial vorticity produced in the boundary layer. The vorticity calculations in the boundary layer could be used in the determination of the vorticity distribution near the core.

In Chapter IV we discussed qualitatively the core flow of vortices similar to tornadoes. Although the velocity field of the outer inviscid flow was shown to be similar to the Rott-Burgers vortex, the core dimension given by viscous-structured vortex model such as that of Rott and Burgers was shown to be roughly one order of magnitude smaller than the observed radius of maximum tangential velocity in naturally-occurring tornadoes. That is, the core dimension given by viscous vortex models (e.g. $r_m \propto \sqrt{2\nu/a}$) fails to yield core dimension comparable to the radius of maximum tangential velocity observed by Hoecker. This is true even with relatively large assumed value of eddy viscosity ($\tilde{\nu} \simeq 90$ ft^2/sec).

An inviscid analysis of the core flow, however, resulted in an estimation of the radius of the maximum tangential velocity as

$r_m \simeq \sqrt{2}\,\frac{\Gamma/2\pi}{W_\alpha^*}$. This result seems to be in agreement with the values of r_m observed. It can also be concluded that the axial velocity has to be of the same order of magnitude as the maximum tangential velocity. The above analysis was made based on an imposed condition on the pressure. Specifically, the radial and vertical pressure gradients were required to yield a pressure match on the axis for any height z. Furthermore, two possible cases of core structure were discussed. The recirculating core could terminate above the ground or on the ground. In the former case there would be a change in the direction of axial velocity due to a stagnation point above the ground. The estimation of r_m was made for both cases although it could only be verified for the single vortex with upward axial flow where flowfield measurements were available.

A qualitative picture distinguishing different features of the core (which were commonly assumed coincident) was also developed. It is observed that the condensation pressure isobar would always lie outside the funnel cloud due to the non-equilibrium nature of the condensation of water vapor. However, the assumptions leading to the order of magnitude analysis presented -- especially the presence of giant size nuclei -- has to be verified. It is believed however, that the qualitative picture given is correct.

5.2 Conclusions.

A swirling, converging, steady, axisymmetric flow model was assumed with constant density fluid as a tornado flow model in this study. A shallow convergence zone and a constant pressure boundary condition were some of the other features of this flow.

The inviscid swirling converging flow in the shallow convergence region is shown to give an increasing rate of radial vorticity production in the boundary layer with increases in the imposed swirl. This feature is believed to be central to the production of multiple vortices and could not be observed in a pure potential vortex of the tornado flowfield. The constant pressure imposed on the top of this model (produced by the baffle in Ward's apparatus) is also believed to better simulate upper atmospheric conditions. The downflow along the axis and core dimensions typically observed in naturally-occurring tornadoes can be explained using this inviscid swirling converning flow with the pressure boundary condition imposed on the top. The role of viscosity is considered only important in the thin boundary-layer region near the ground and was shown to have no significant effect in the determination of the core dimensions in contrast to many other tornado flow models (e.g. Rott-Burgers vortex). Thus the dynamics of the flow in the core appear to be essentially inviscid.

Another feature of this flow model is a separated flow region in the thin boundary layer. This separated flow is followed by a reattached zone with decreasing radius. This is not observed in potential vortex model of tornado flows. Sufficiently close to the axis the flow is seen to behave as a potential vortex and features observed in that model such as boundary-layer eruption near the axis are also obtrained here. While this model includes the potential vortex flow model as a special case, considerably different results are obtained for this more general vortex flow with various swirl to convergence ratio than the special case of pure potential vortex. For example, the

boundary-layer radial velocity and boundary-layer thickness for the more general situation are seen to be different -- expecially away from the axis -- than the special case of purely swirling flow.

This model however neglects certain important features of a more realistic tornado flow such as density variation in the atmosphere. Such thermodynamic considerations would seem to be important in such features as the position and the flow conditions at the stagnation point observed along the axis above the ground. Also, buoyancy effects due to precipitation and condensation are neglected in this model.

The investigation of a non-equilibrium process of water vapor condensation near the core associated with a swirling converging flow seems to indicate the importance of this process in forming such features as tornado funnel clouds. However, no experimental verification of this process was possible with Ward's apparatus and assumptions used in this study remain to be further investigated experimentally.

5.3 Recommendations for Future Research.

There remains a need for further experimental work using Ward's tornado simulation apparatus. However, modifications of this apparatus are necessary before further experiments can be conducted. Specifically, the apparatus should be redesigned so that the fan discharges into the room as opposed to the ambient environment outside the laboratory. This modification would allow for more accurate measurements by eliminating the interference due to ambient wind gusts. Also, experiments could then be performed more often as the present need to restrict experiments to the night time would be removed. Furthermore,

the gearing system driving the rotating meshwire should be redesigned to reduce fluctuations and noise in the converging air region. This is clearly necessary for more accurate measurements.

Such a redesigned tornado simulation apparatus could then be used for further experiments and flow measurements of three regions of the flow. First, flowfield measurements of the region above the honeycomb baffle could be carried out using conventional pitot-static tubes. Measurements of the static pressure and its radial distribution in this region would provide additional insight into the origin of the downflow observed in the core. The determination of the dependence of statis pressure near the axis in this region with swirl to convergence ratio and the diameter of the core would enhance understanding of the dynamics of the core flow. Also, the effect of lowering the baffle (decreasing the height of the updraft chamber) on the core behavior and dimensions could be useful in determining the significance of the height of the updraft chamber in the overall dynamics of the vortex. Second, flowfield measurements of the core region would be of great benefit for further comparison of Ward's tornado simulation with that of naturally-occurring tornadoes. Due to the unsteadiness and small dimensions of the core as well as the free nature of this vortex, measurements in the core must be conducted with minimum flow disturbances. This seems to be possible only with a laser Doppler velocimeter in which the frequency shift of scattered light is used to infer velocities. Only with this kind of probe can the flowfield measurements be carried out with a sufficiently small disturbance. However, the use of laser Doppler velocimeter for such measurements would require significant finances and a

greater development time than the use of more conventional means of flowfield velocity measurement. Third, the velocity in the boundary-layer region could be measured using a hot wire anemometer. The position of separation and reattachment could be determined and measurements could be used to verify boundary-layer calculations obtained in this work. Comparison of boundary-layer flow measurements with other tornado simulation flows (e.g. Chang, *et al*) would also be useful in defining more accurately the difference between these various simulations.

Measurements of turbulent velocity field could also be carried out in the outer flowfield in Ward's apparatus. These measurements could be conducted by means of conventional hot wire or hot film anemometers to determine the level of turbulence and mixing in this region of the flow. Lilly (private communication) has noted that the turbulent velocity field appears to enhance angular momentum of the fluid near the vortex core. Thus, an understanding of the turbulence in the flowfield may be required before a comprehensive model of the tornado flowfield is possible.

Experimental verification of the nonequilibrium water vapor condensation process near the core discussed in this work would enhance understanding of the photographic data on tornadoes. Using a swirling, converging flow model with water as the fluid, it might be possible to simulate the condensation process by an air bubble growth process introduced into the flow. The location of the "funnel" in this model could then be compared with pressure isobars in the flowfield. The effect of variation in swirl and convergence on the "funnel" shape and

position could also be obtained using this bubble growth process.

Further theoretical studies associated with tornado flows could be carried out in at least two areas. First, there is a need for a study of the core flow associated with the swirling, converging outer flow observed in the present experiments. Such a study should be based on observations and measurements obtained by means of Ward's apparatus as well as Hoecker flow measurement of Dallas tornado of April 2, 1957. As discussed in Chapter IV, observations indicate large axial velocities with radius of maximum tangential velocity being determined by essentially inviscid dynamical considerations. These features should be a part of any theoretical core flow model. Second, a stability analysis of the vortex could be made using the boundary-layer calculations obtained in this work to estimate the enhanced vertical vorticity near the edge of the core. Such a calculation might help clarify the conditions leading to multiple vortex production and determine a more accurate relationship between the critical swirl parameter ϕ_{cr} and the imposed swirl and updraft.

REFERENCES

1. Lewis, William and Perkins, Porter J. "Recorded Pressure Distribution in the Outer Portion of a Tornado Vortex". *Monthly Weather Review 81*, No. 12, December, 1953, pp. 379-385.

2. Hoecker, W. H. "Wind Speed and Air Flow Patterns in the Dallas Tornado of April 2, 1957". *Monthly Weather Review 88*, No. 5, May, 1960, pp. 167-180.

3. Golden, J. H. Private communication of unpublished flowfield measurements of the Union City Tornado of May 24, 1973.

4. Davies-Jones, R. P. and Kessler, E. "Tornadoes", National Severe Storms Laboratory, Technical Publication, 1973.

5. Jischke, M. C. and Parang, M. "Properties of Simulated Tornado-Like Vortices". *J. Atm. Sci. 31*, No. 2, March, 1974, pp. 506-512.

6. Rott, N. "On the Viscous Core of a Line Vortex". *J. Appl. Math. Phys. (ZAMP) 9*, 1958, pp. 543-553.

7. Ying, S. J. and Chang, C. C. "Exploratory Model Study of Tornado-Like Vortex Dynamics". *J. Atm. Sci. 29*, No. 1, January, 1970, pp. 3-14.

8. Wan, C. A. and Chang, C. C. "Measurement of the Velocity Field in a Simulated Tornado-Like Vortex Using a Three-Dimensional Velocity Probe". *J. Atm. Sci. 29*, No. 1, January, 1972, pp. 116-127.

9. Ward, N. B. "The Exploration of Certain Features of Tornado Dynamics Using a Laboratory Model". *J. Atm. Sci. 29*, No. 6, Sept. 1972, pp. 1194-1204.

10. Turner, J. A. "The Constraints Imposed on Tornado-Like Vortices by the Torn and Bottom Boundary Conditions". *J. Fluid Mechanics 25*, Part 2, 1966.

11. Ward, N. B. "The Newton, Kansas Tornado Cyclone of May 24, 1962". Amer. Meteor. Soc., Proceedings Eleventh Weather Radar Conf., pp. 410-415, 1964.

12. Fugita, Tetsuya J., Bradbury, Dorothy L. and Van Thullenar, C. F. "Palm Sunday Tornadoes of April 11, 1965". *Monthly Weather Review 98*, No. 1, January, 1970.

13. Lilly, D. K. "Tornado Dynamics", National Center for Atmosphere Research, Report No. 69-117, Boulder, Colorado.

14. Morton, B. "Geological Vortices". *Progress in Aeronautical Sciences 7*, Pergamon Press, New York, 1966, pp. 145-193.

15. Burgers, J. M. "A Mathematical Model Illustrating the Theory of Turbulence". *Advances in Applied Mechanics 1*, Academic Press, 1948.

16. Long, R. R. "A Vortex in an Infinite Viscous Fluid". *J. Fluid Mech. 11*, pp. 611-624.

17. Einstein, H. A. and Li, H. L. "Steady Vortex Flow in a Real Fluid". *Proc. Heat Transfer and Fluid Mechanic Inst.*, Stanford University, 1951.

18. Lewellen, W. S. "A Solution for Three-Dimensional Vortex Flows with Strong Circulation". *J. Fluid Mech. 14*, Part 3, 1963, pp. 420-433.

19. Serrin, B. "The Swirling Vortex". *Philosophical Transaction of Royal Society of London*, Series A, Vol. 271, pp. 325-369, Jan.1972.

20. Kuo, H. L. "Assymetric Flows in the Boundary Layer of a Maintained Vortex". *J. Atm. Sci. 25*, January 1971, pp. 20-42.

21. Barcilon, A. "A Theoretical and Experimental Model for Dust Devil" *J. Atm. Sci. 24*, September 1967.

22. Burgraff, O. R., Stewartson, K., and Belcher, R. "Boundary-Layer Induced by a Potential Vortex". *Phys. Fluids 14*, 1971, pp. 1821-1833.

23. Weber, H. E. "Boundary-Layer Inside a Conical Surface Due to a Swirl". *J. Applied Mech. 23*, 1956, pp. 587-592.

24. Rott, N. and Lewellen, W. S. "Boundary-Layers in Rotating Flows", Aerospace Corporation, Report No. ATN-64(9227)-6, 1964.

25. Chang, C. C., Chi, S. W. and Ying, S. J. "The Ground Turbulent Boundary-Layer of a Stationary Tornado-Like Vortex". *Tellus 1*, 1969, pp. 693-699.

26. Soo, S. L. "Vortex Flow Adjacent to a Stationary Flow". *Applies Sci. Res. 28*, July, 1973, pp. 20-26.

27. Glaser, A. H. "An Observational Deduction of the Structure of a Tornado Vortex". *Cumulus Dynamics*, pp. 157, Pergamon Press.

28. Sullivan, R. D. "A Two-Cell Vortex Solution of the Navier-Stokes Equations". *J. Aero/Space Sci. 26,* 1959, pp. 767-768.

29. Kuo, H. L. "Note on the Similarity Solutions of the Vortex Equations in an Unstably Stratified Atmosphere". *J. Atm. Sci. 24,* No. 1, 1967, pp. 95-97.

30. Dergarabedian, P. and Fendell, F. "On Estimation of Maximum Wind Speeds in Tornadoes and Hurricans". *J. Aeronautical Sciences 17,* No. 4, January, 1970, pp. 215-236.

31. Dergarabedian, P. and Fendell, F. "Estimation of Maximum Wind Speeds in Tornadoes", *Tellus 22,* 1970, pp. 511-515.

32. Parang, M., Master's Thesis, University of Oklahoma, 1972.

33. Von Karman, T. H. "Uber Laminar Und Turbulente Reibung". *Z.A.M.M. 1,* 1921, pp. 233-247.

34. Taylor, G. I. "The Boundary-Layer in the Converging Nozzle of a Swirl Atomizer". *Quarterly Journal of Mathematics and Applied Mechanics 3,* No. 2, 1950, pp. 120-139.

35. Hoecker, W. H. "Three Dimensional Pressure Pattern of the Dallas Tornado and Some Resultant Implications". *Monthly Weather Review 89,* December 1961, pp. 533-542.

36. Flora, S. D. *Tornadoes of the United States,* University of Oklahoma Press, 1959.

37. Davies-Jones, R. P. "The Dependence of Core Radius on Swirl Ratio in a Simulated Tornado Simulation". *J. Atm. Sci. 30,* No. 7, October, 1973.

38. McCarthy, J., private communication, University of Oklahoma.

39. Fuchs, N. A., *Evaporation and Drop Growth in Gaseous Media,* Pergamon Press, New York, 1959.

40. Mason, B. J. *The Physics of Clouds,* Clarendon Press, Second Edition, Oxford, 1971.

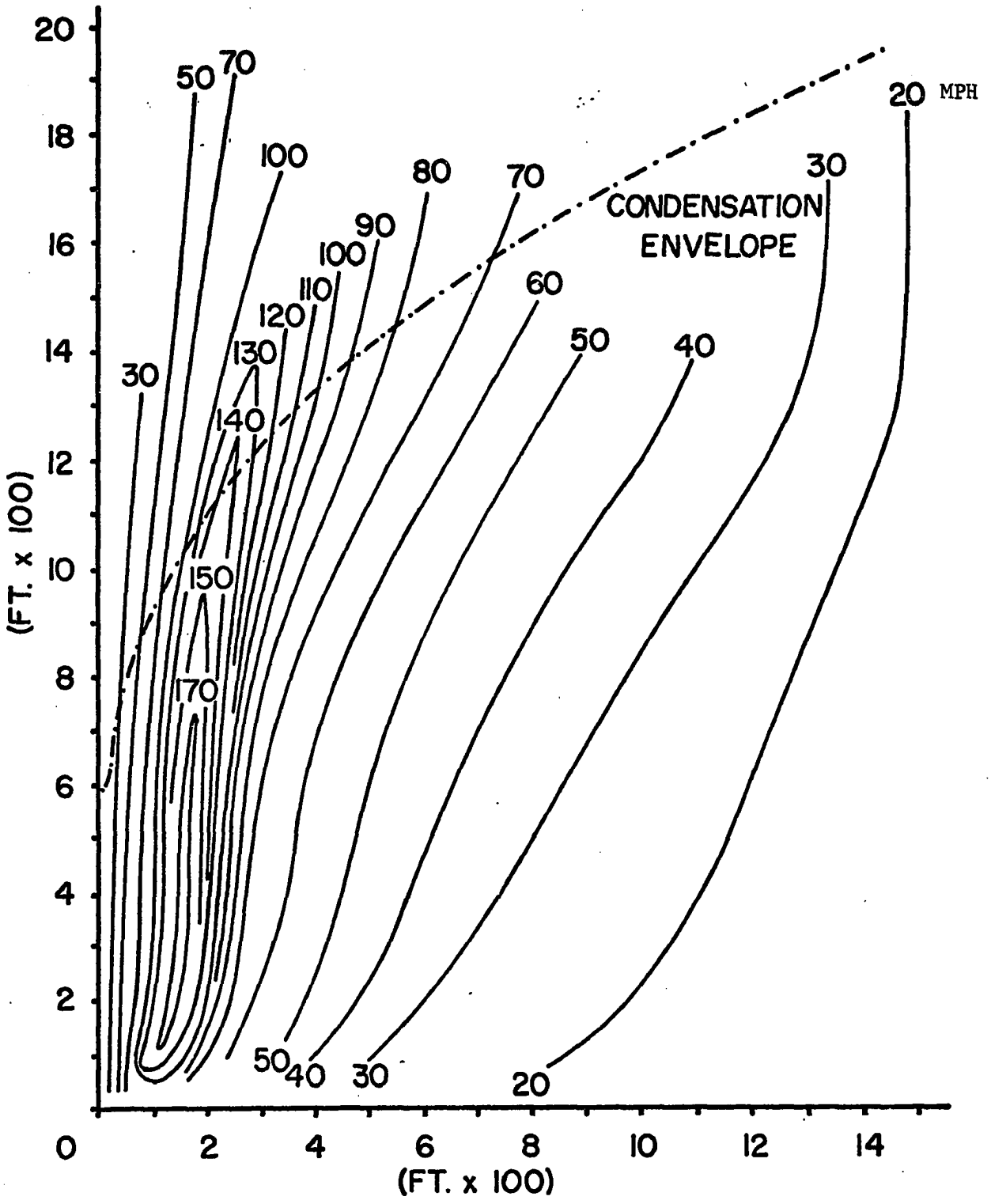

Figure 1.1. Tangential Velocity Distribution of Dallas Tornado of April 2, 1957 (from Ref. 2)

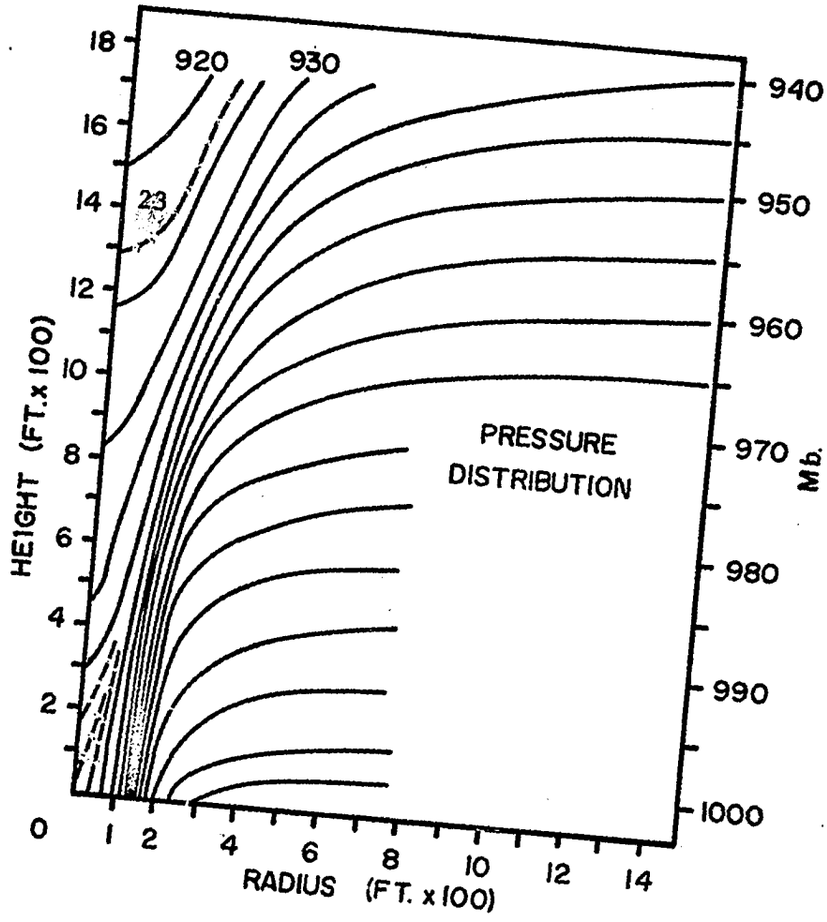

Figure 1.2. Derived Pressure Distribution of Dallas Tornado of April 2, 1957 (from Ref. 2).

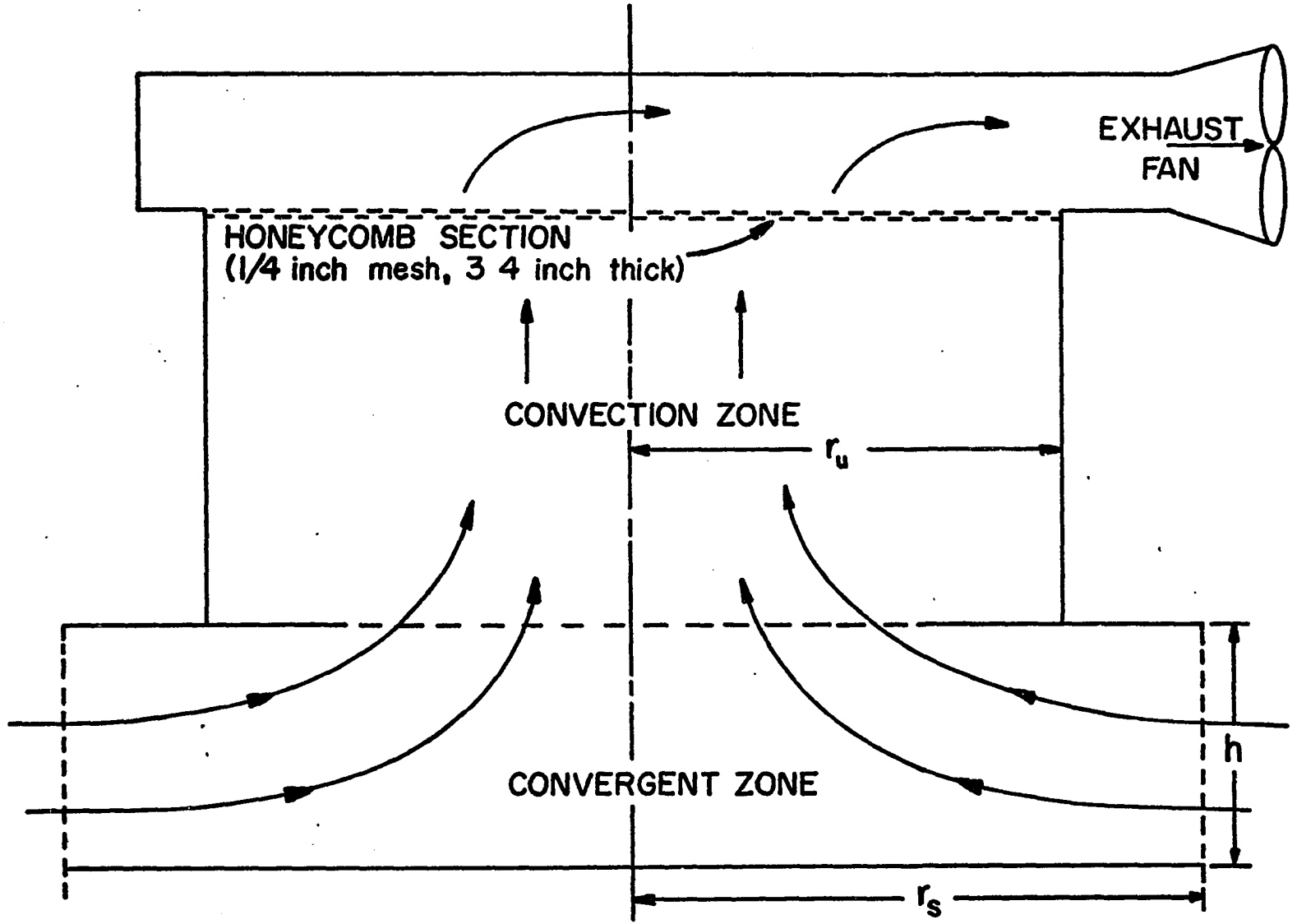

Figure 1.3. Schematic of Ward's Apparatus.

Figure 1.4. Sketch of (a) Single-Vortex Configuration and (b) Double-Vortex Configuration.

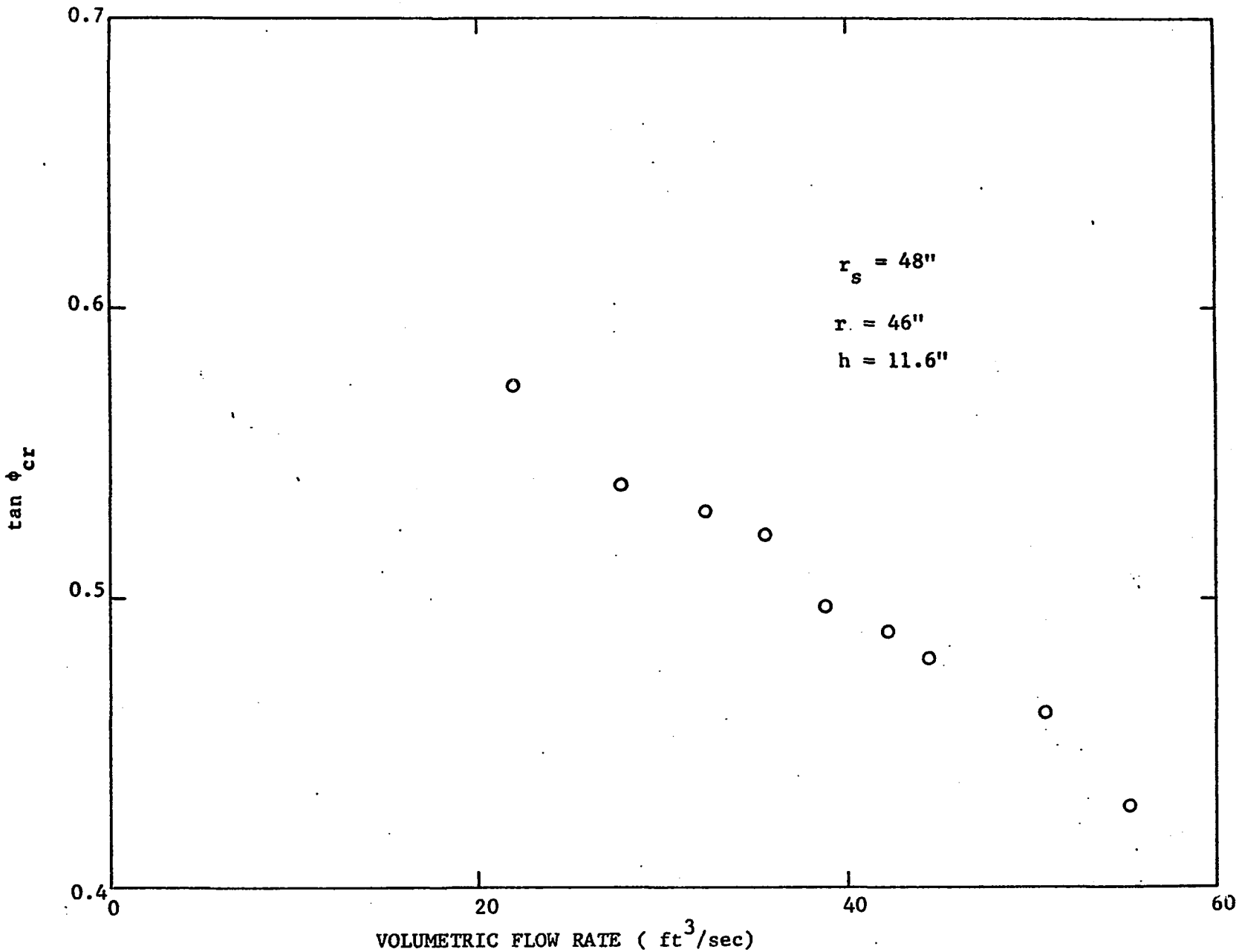

Fig.2.1 Variation of the Critical Swirl Parameter with volumetric flow rate (h = 11.6")

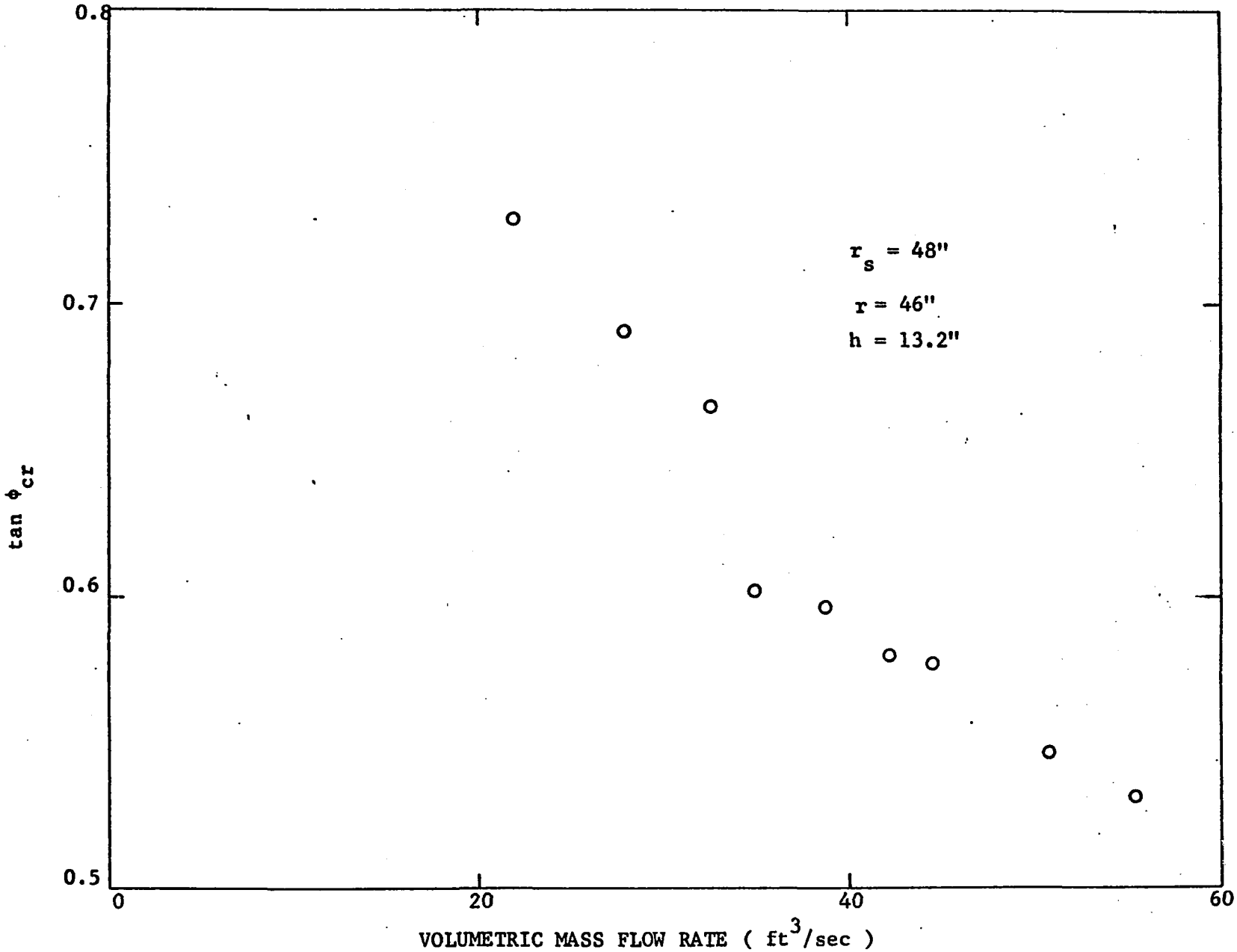

Fig. 2.2 Variation of the Critical Swirl Parameter with Volumetric Flow Rate (h = 13.2")

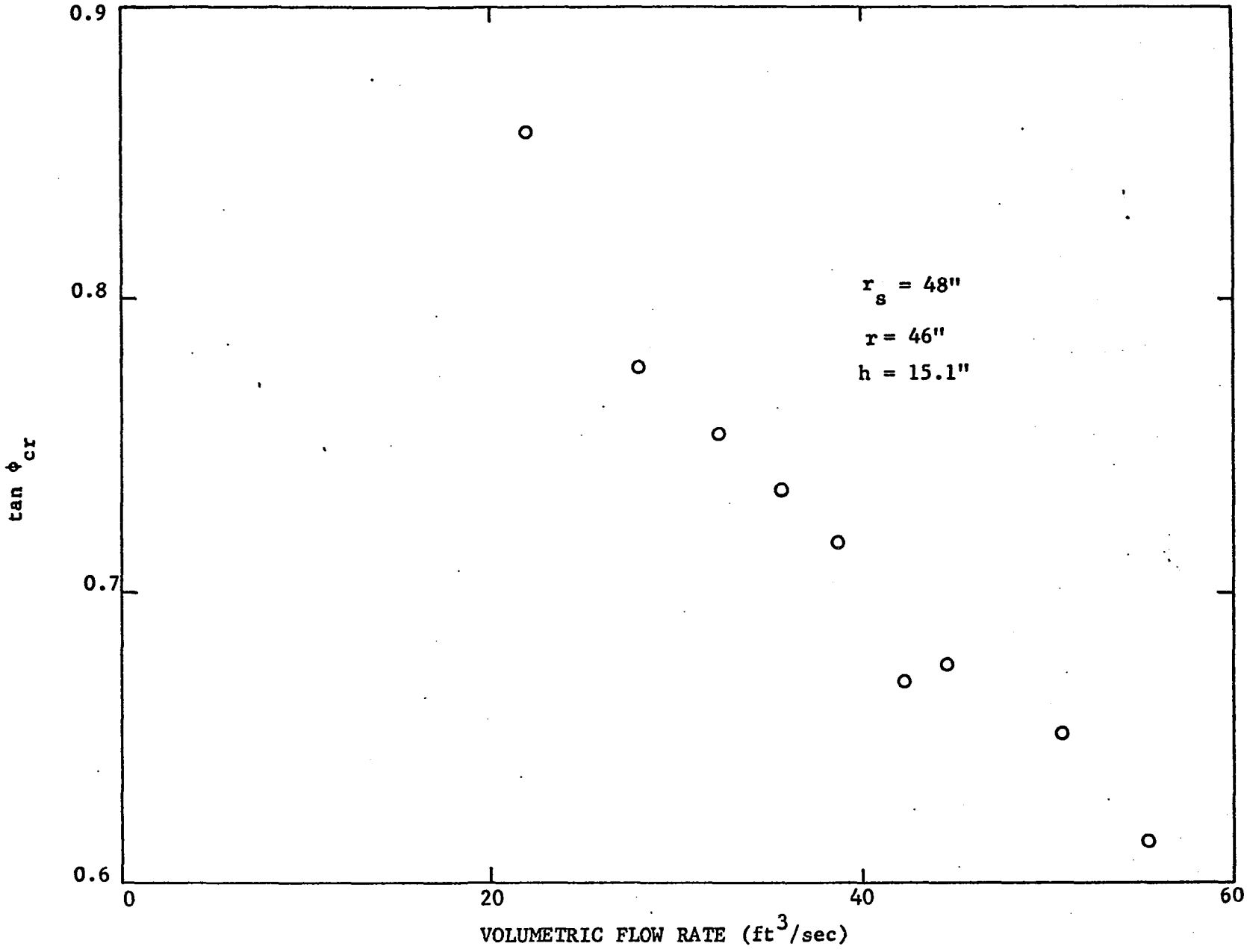

Fig. 2.3 Variation of the Critical Swirl Parameter with Volumetric Flow Rate (h = 15.1")

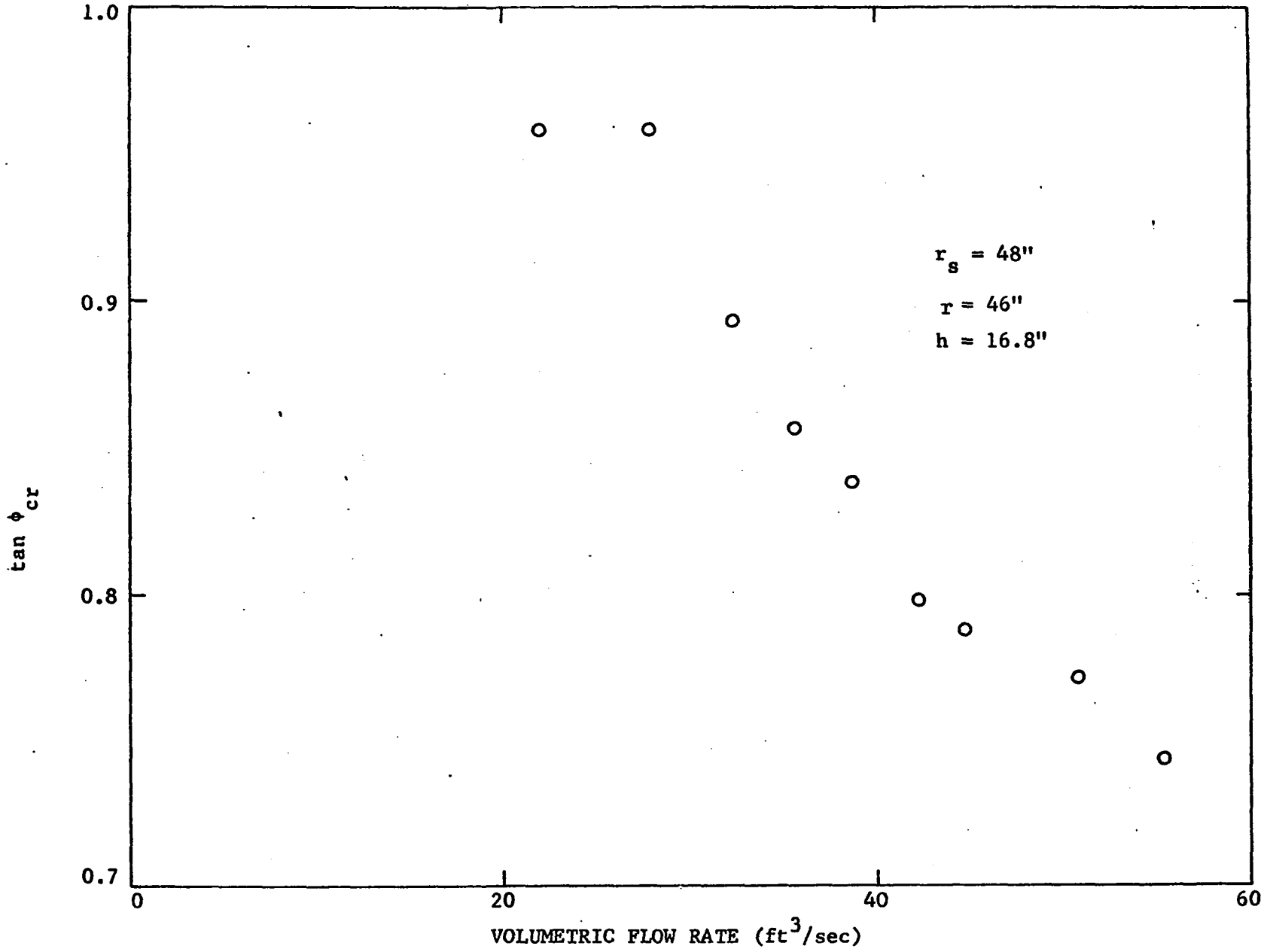

Fig. 2.4 Variation of the Critical Swirl Parameter with Volumetric Flow Rate (h = 16.8")

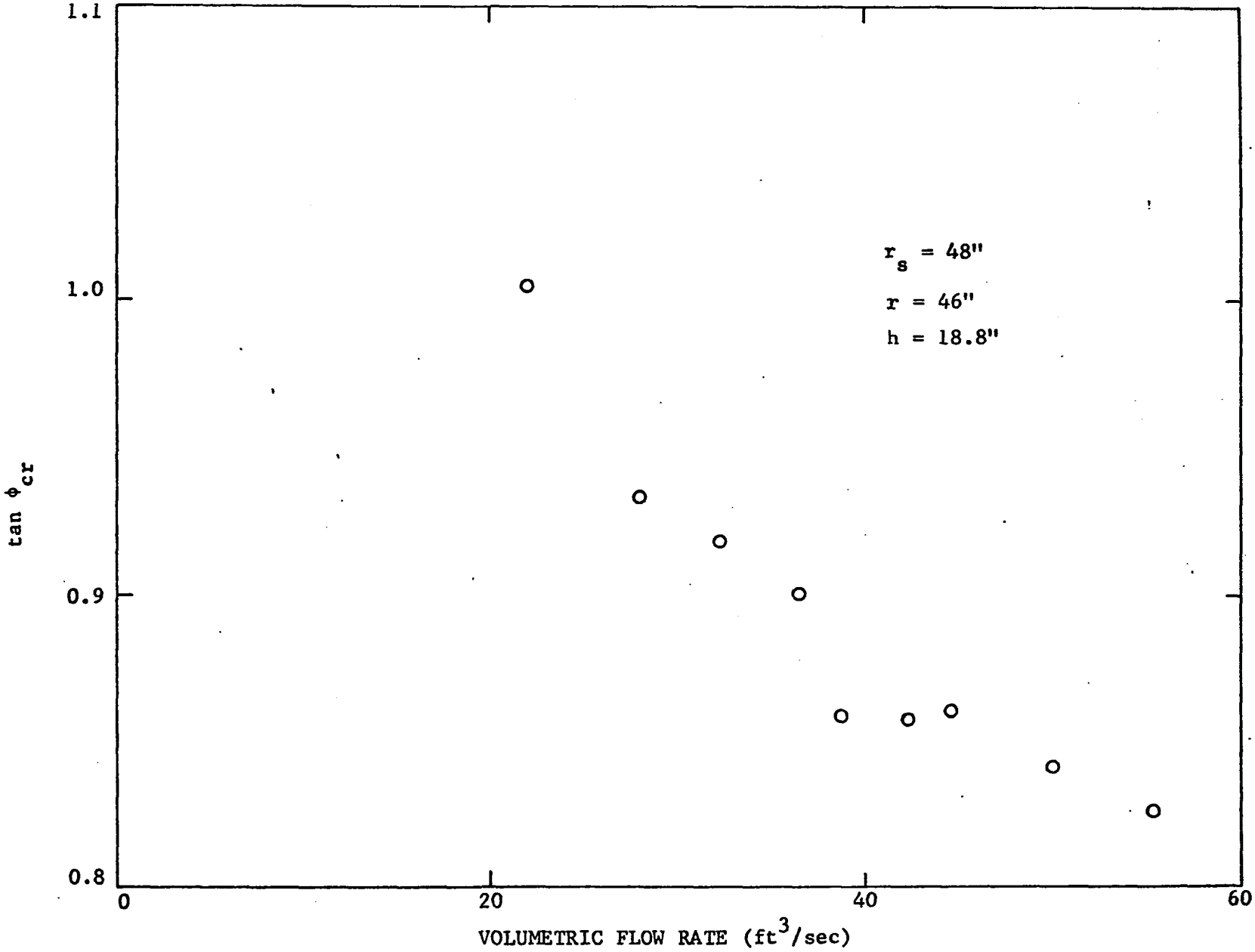

Fig. 2.5 Variation of the Critical Swirl Parameter with Volumetric Flow Rate (h = 18.8")

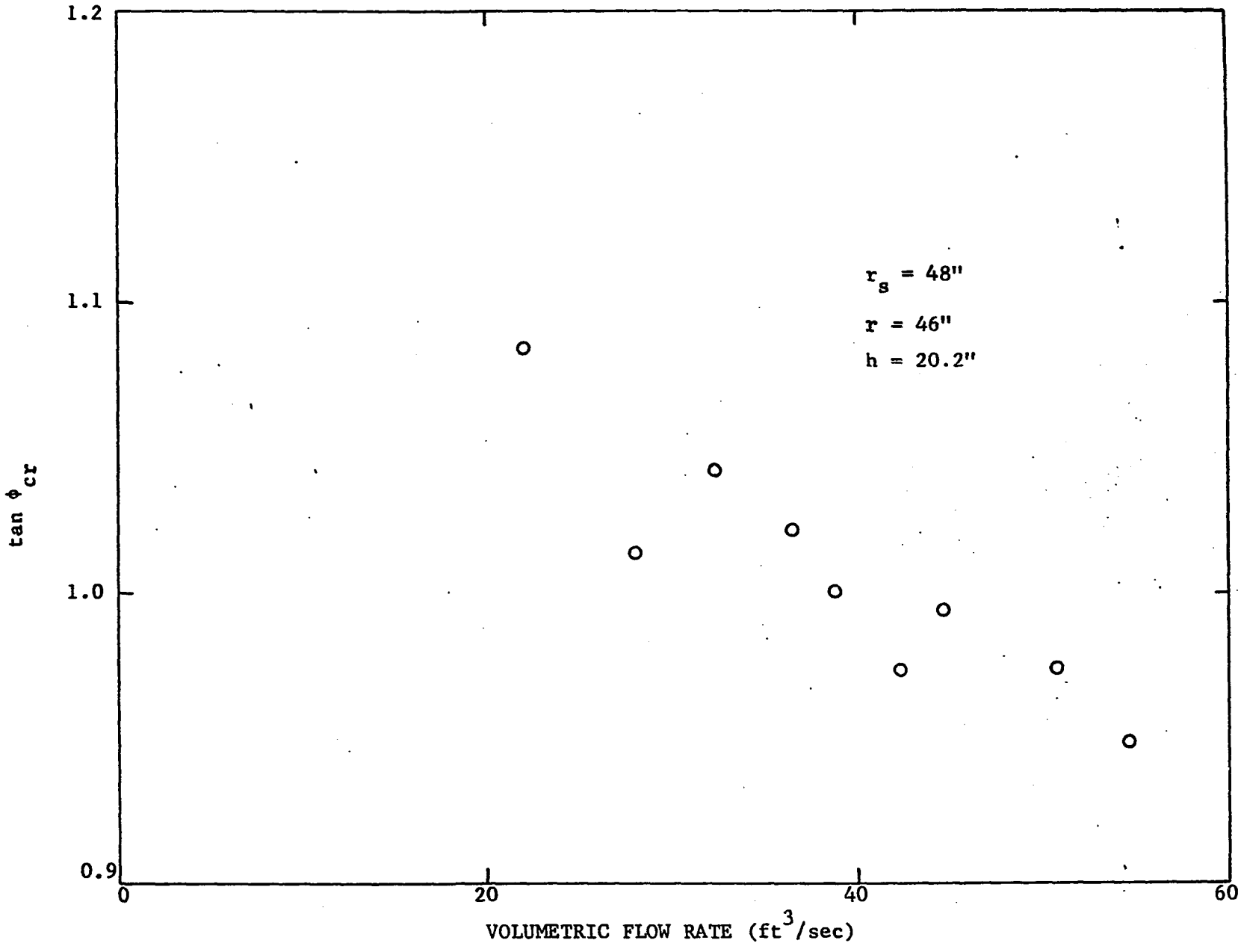

Fig. 2.6 Variation of the Critical Swirl Parameter with Volumetric Flow Rate (h = 20.2")

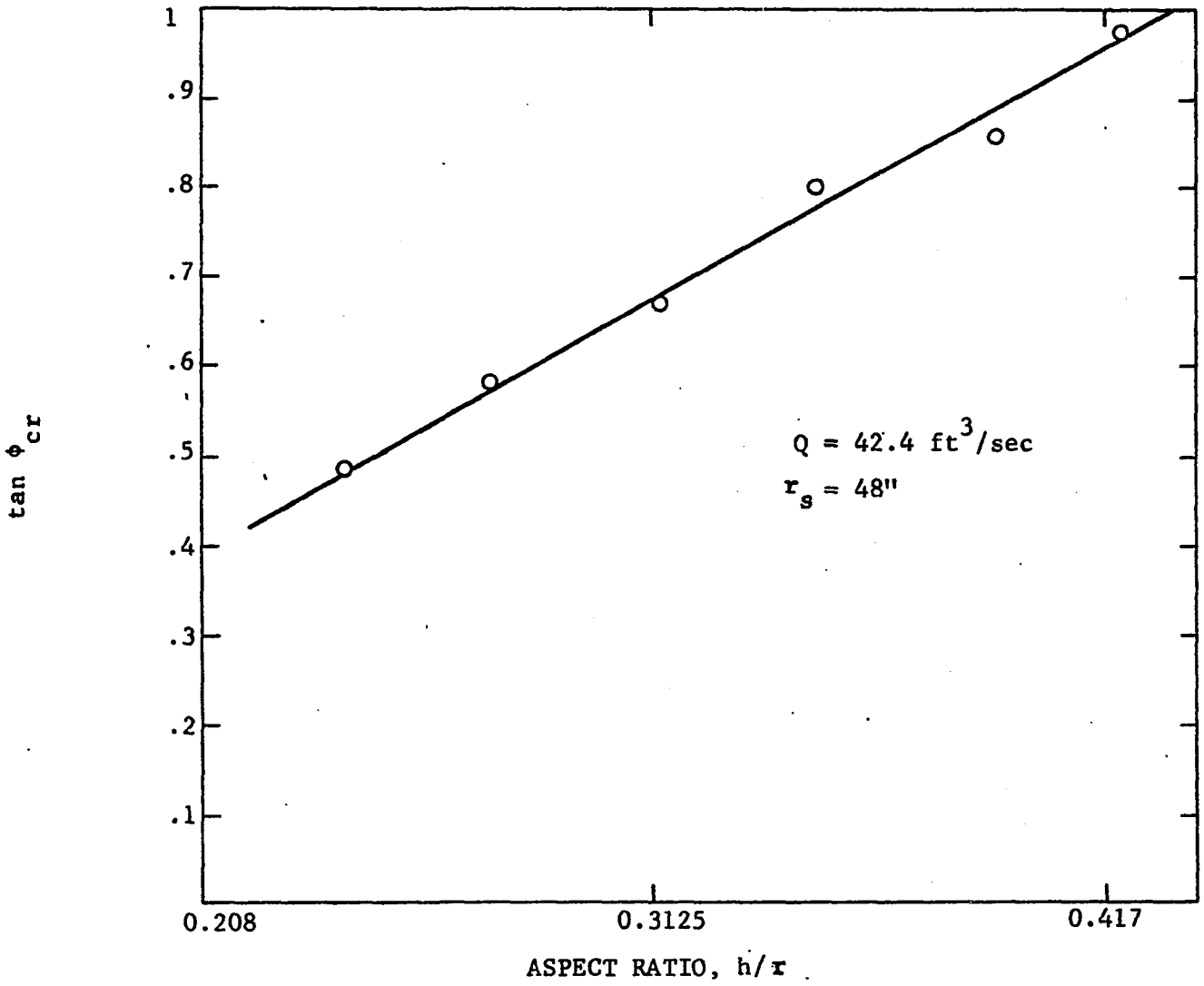

Fig. 2.7 Variation of the Critical Swirl Parameter with the Aspect Ratio (h/r)

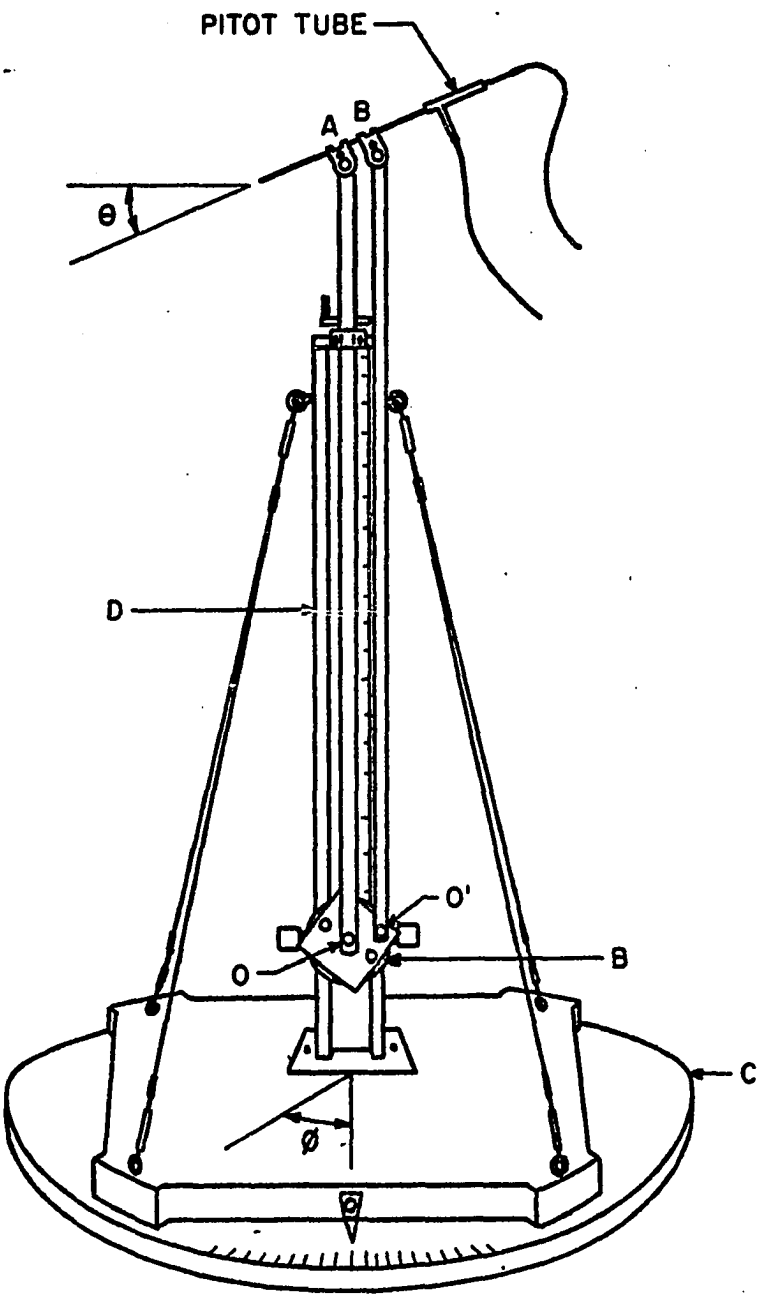

Fig. 2.8 Schematic of the Traverse Mechanism

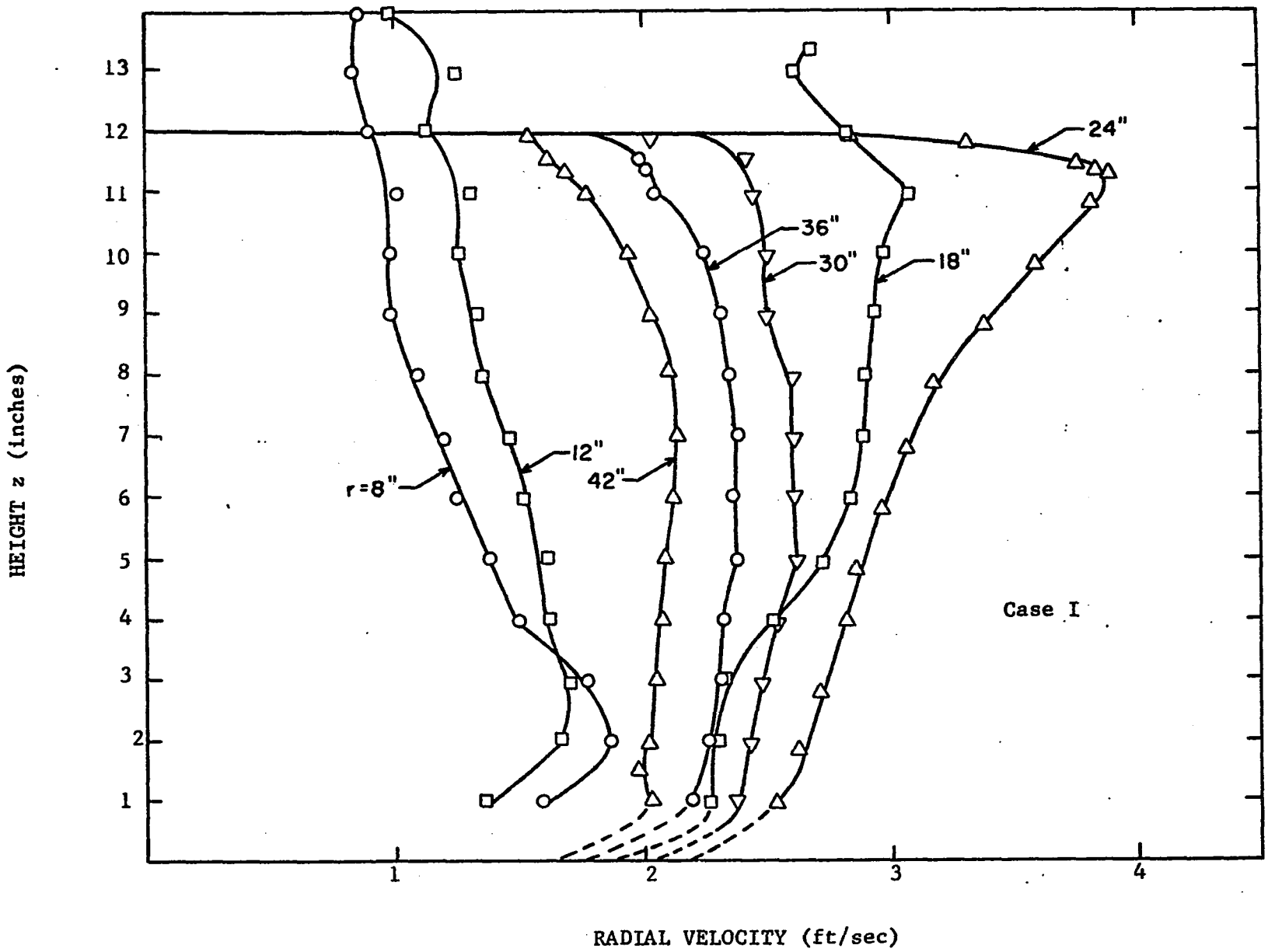

Fig. 2.9 Variation of Radial Velocity with Height

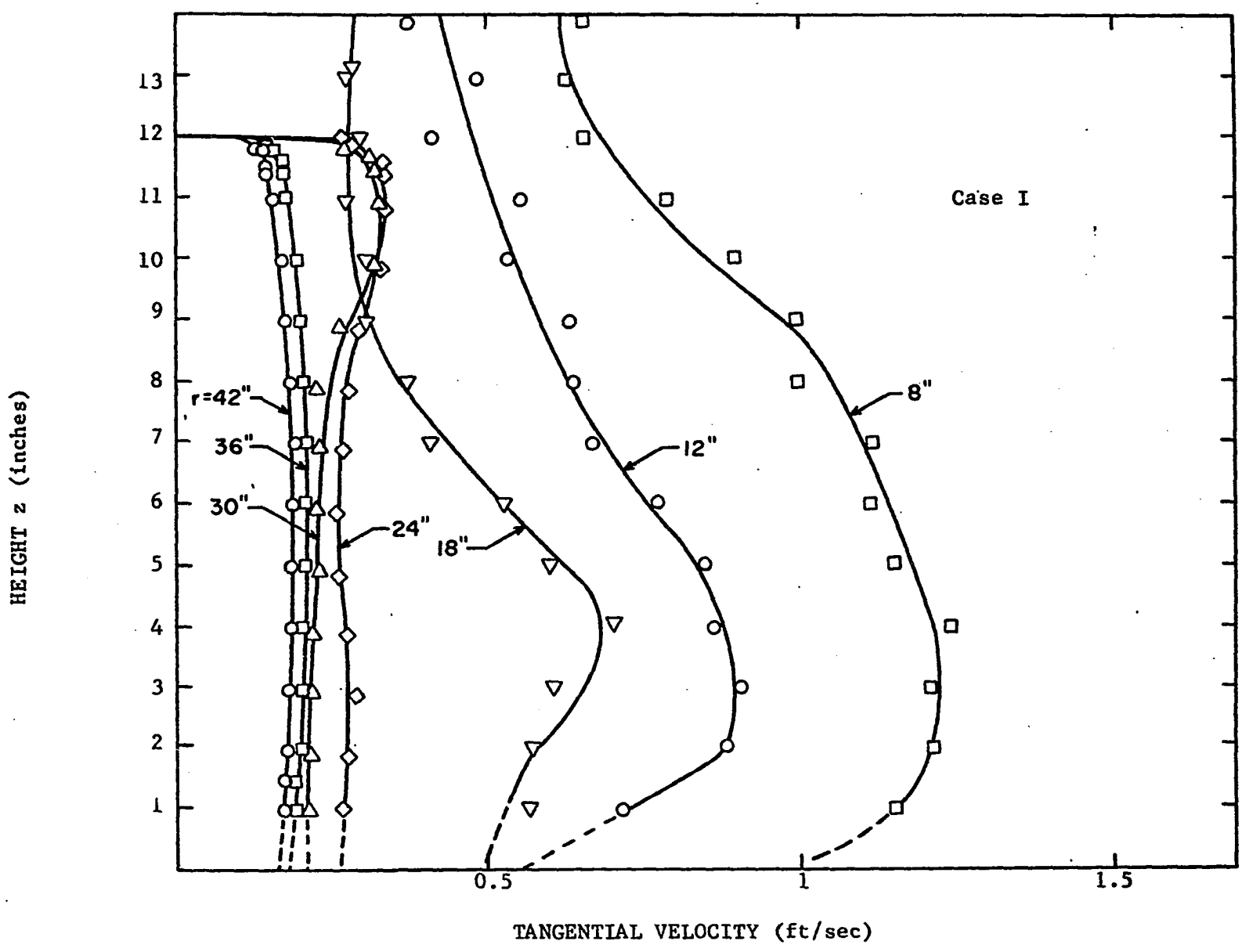

Fig. 2.10 Variation of Tangential Velocity with Height

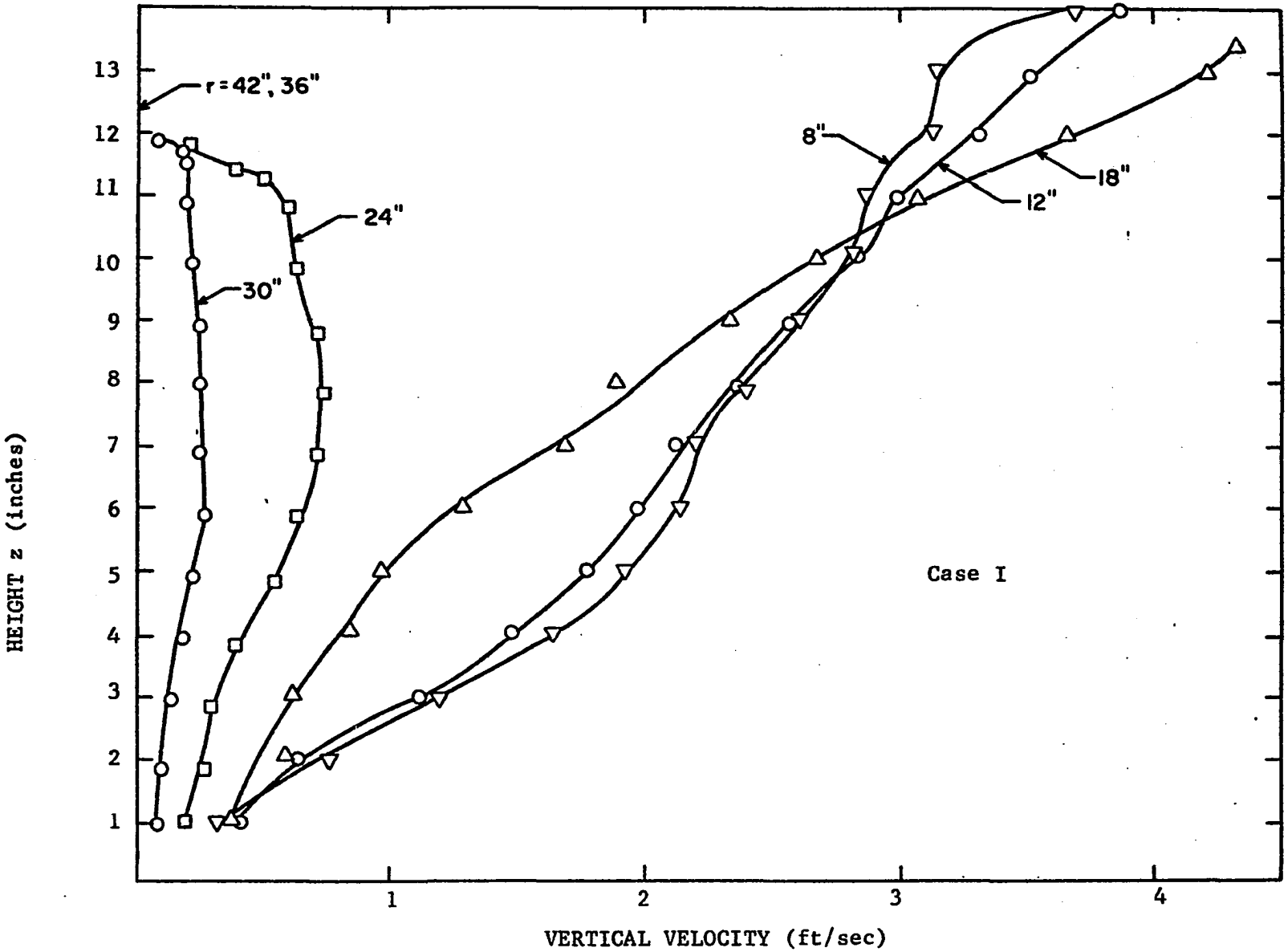

Fig. 2.11 Variation of Vertical Velocity with Height

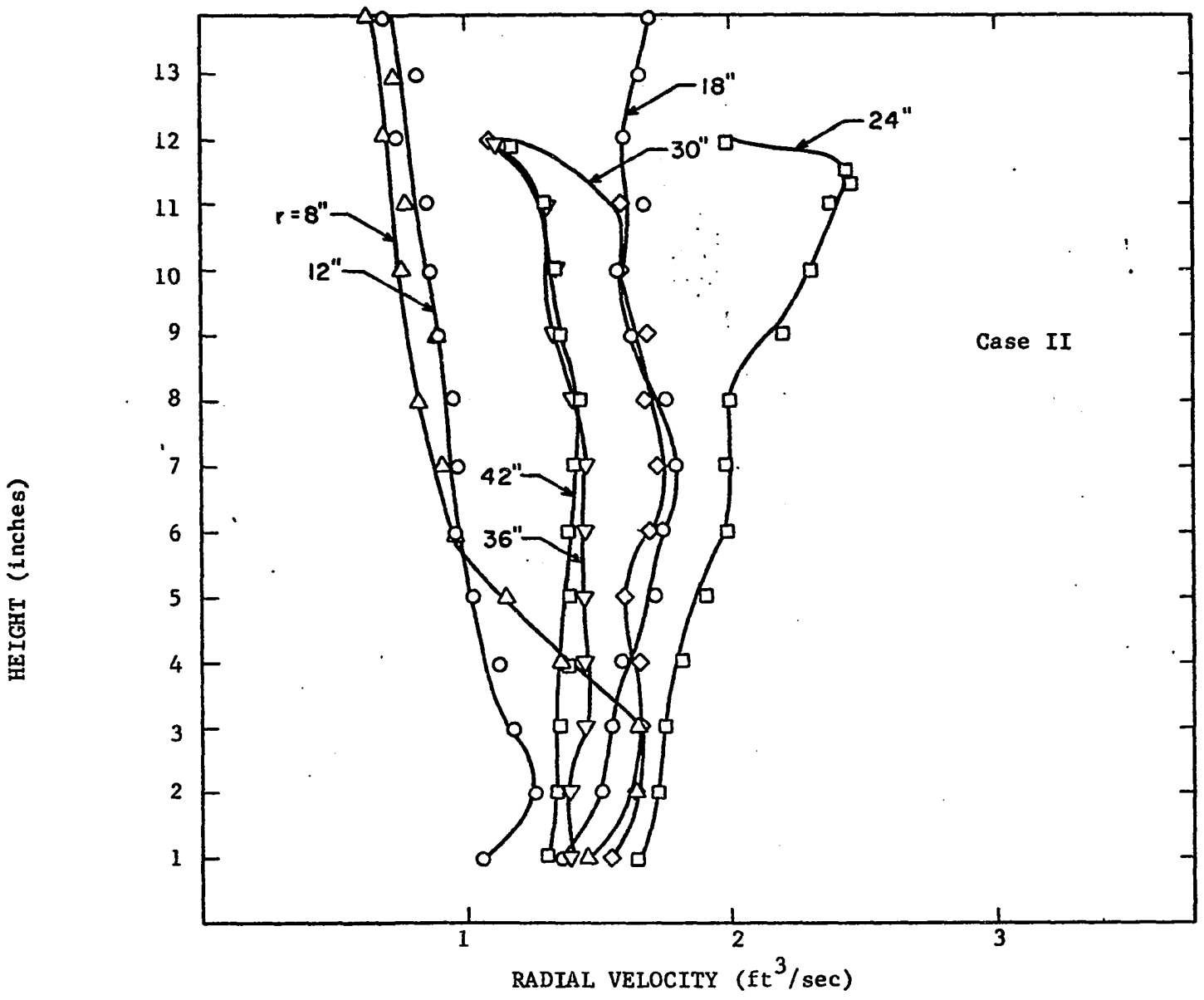

Fig. 2.12 Variation of Radial Velocity with Height

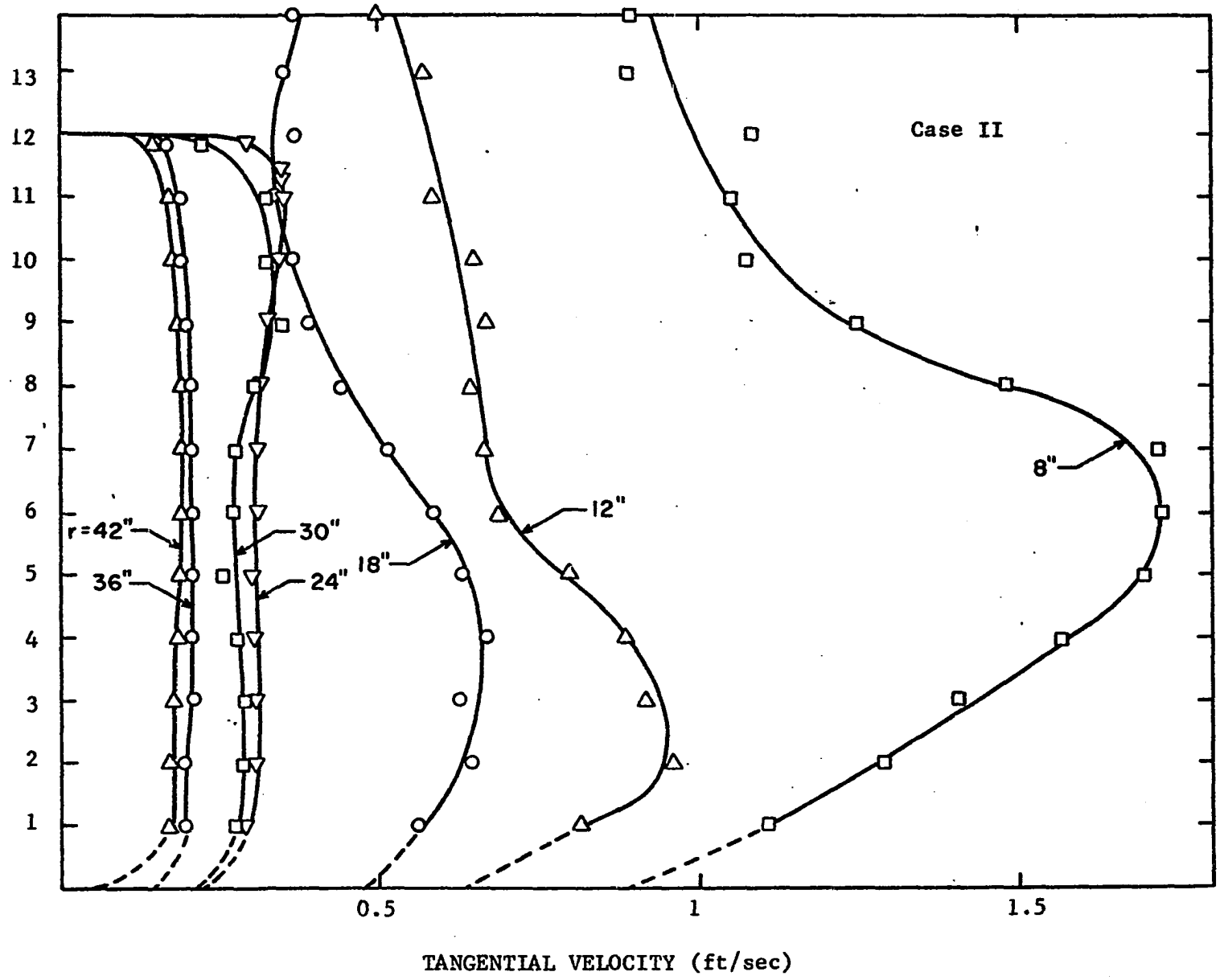

Fig. 2.13 Variation of Tangential Velocity with Height

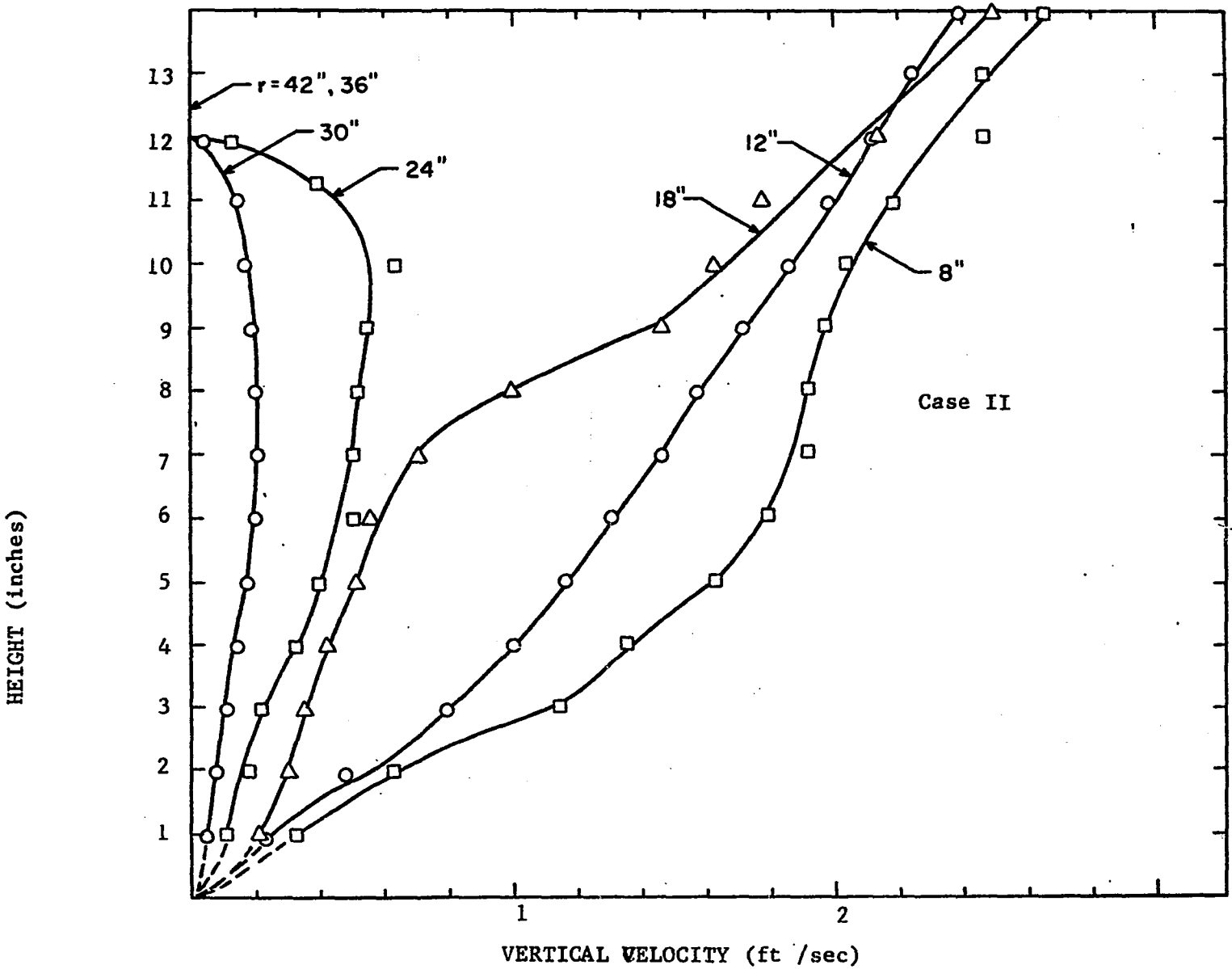

Fig. 2.14 Variation of Vertical Velocity with Height

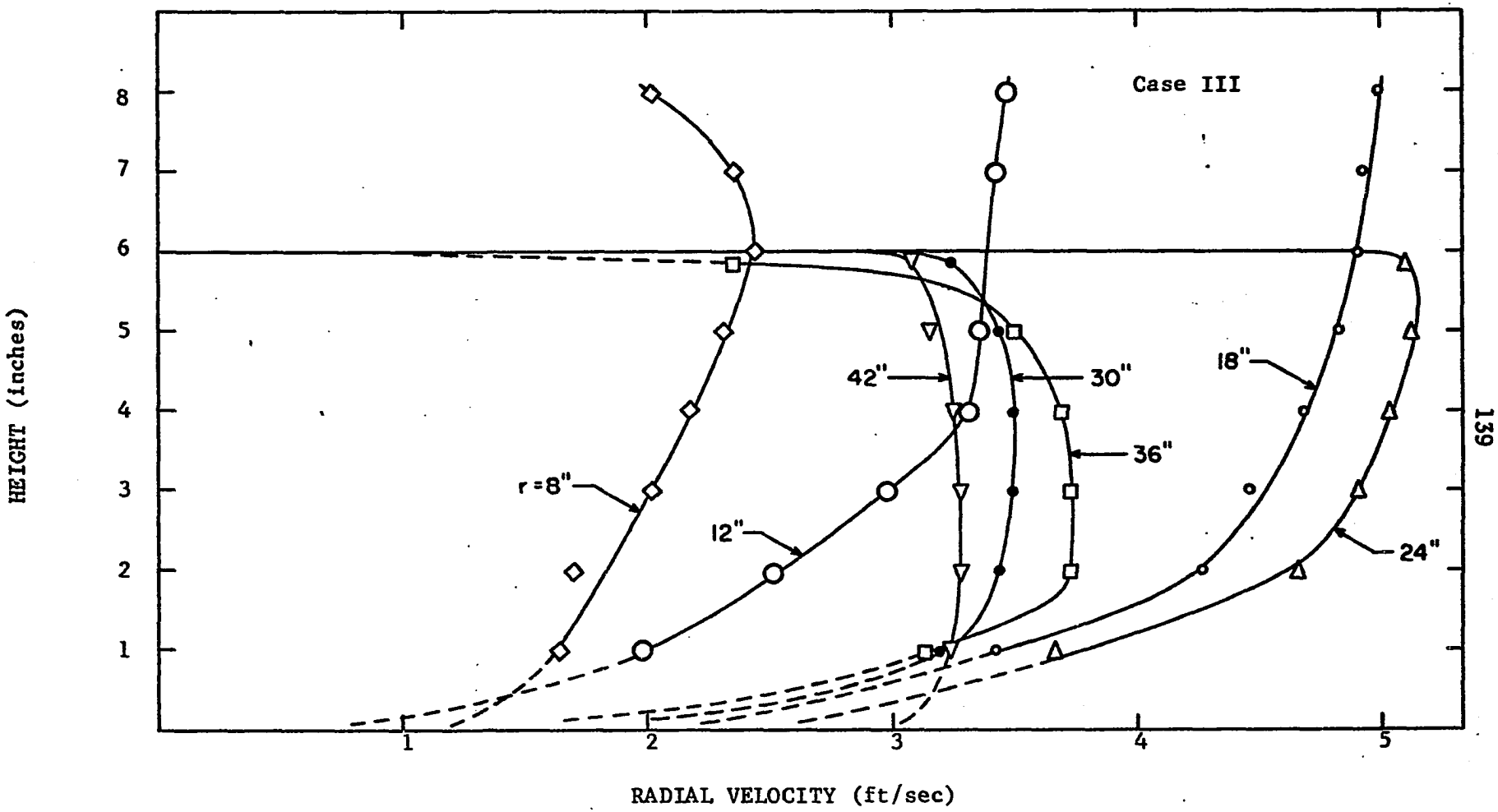

Fig. 2.15 Variation of the Radial Velocity with Height

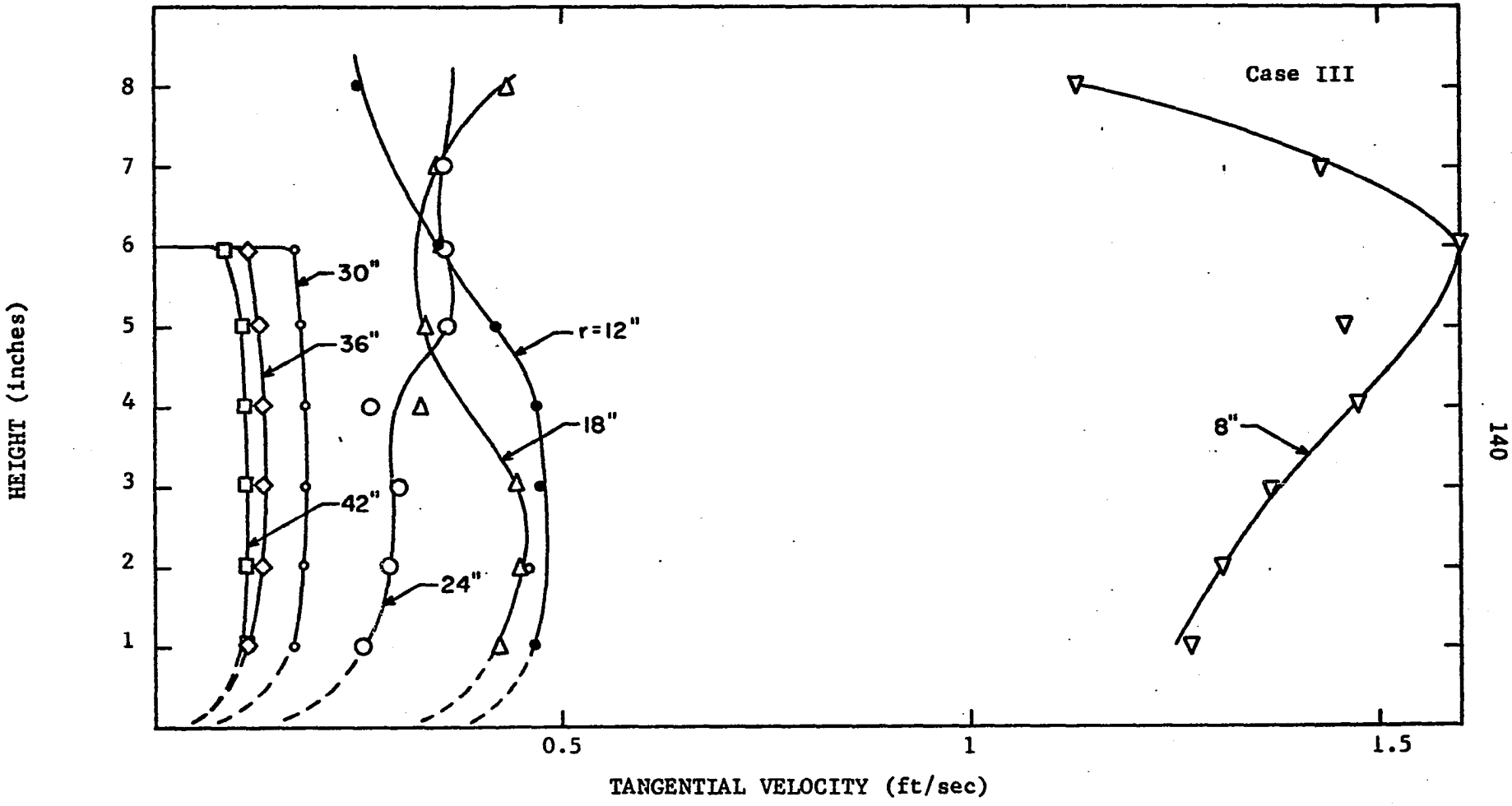

Fig. 2.16 Variation of Tangential Velocity with Height

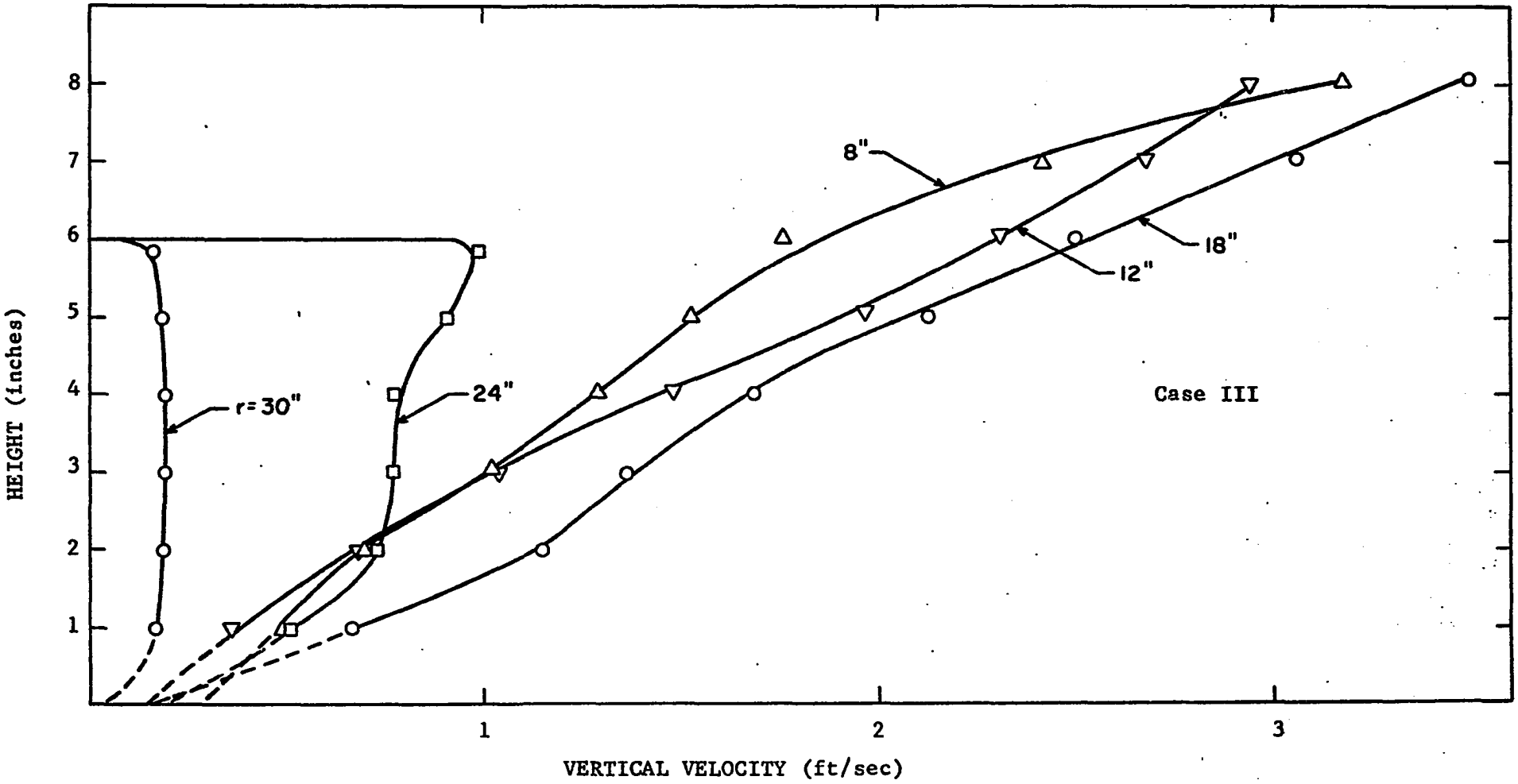

Fig.2.17 Variation of Vertical Velocity with Height

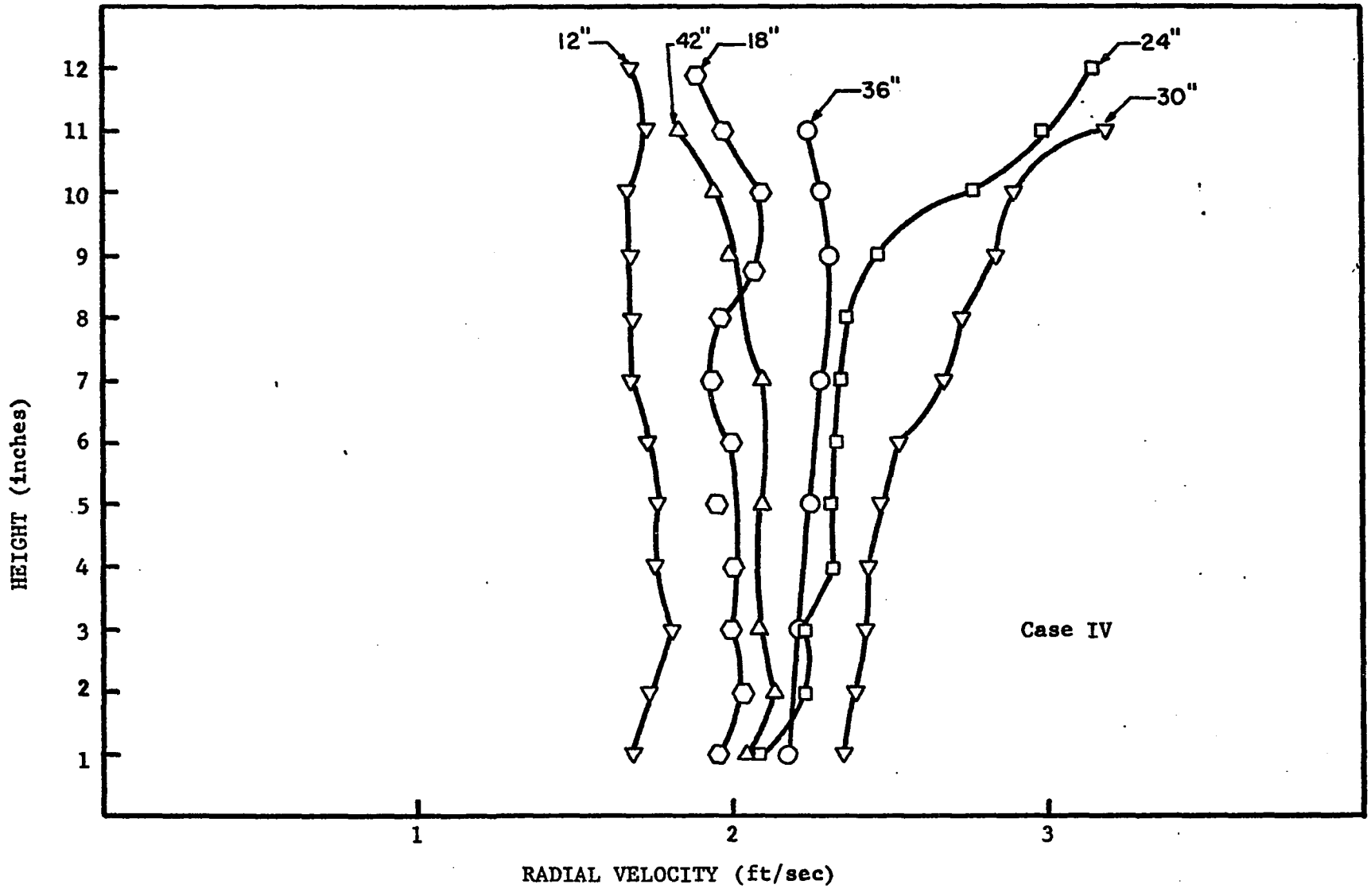

Fig. 2.18 Variation of Radial Velocity with Height

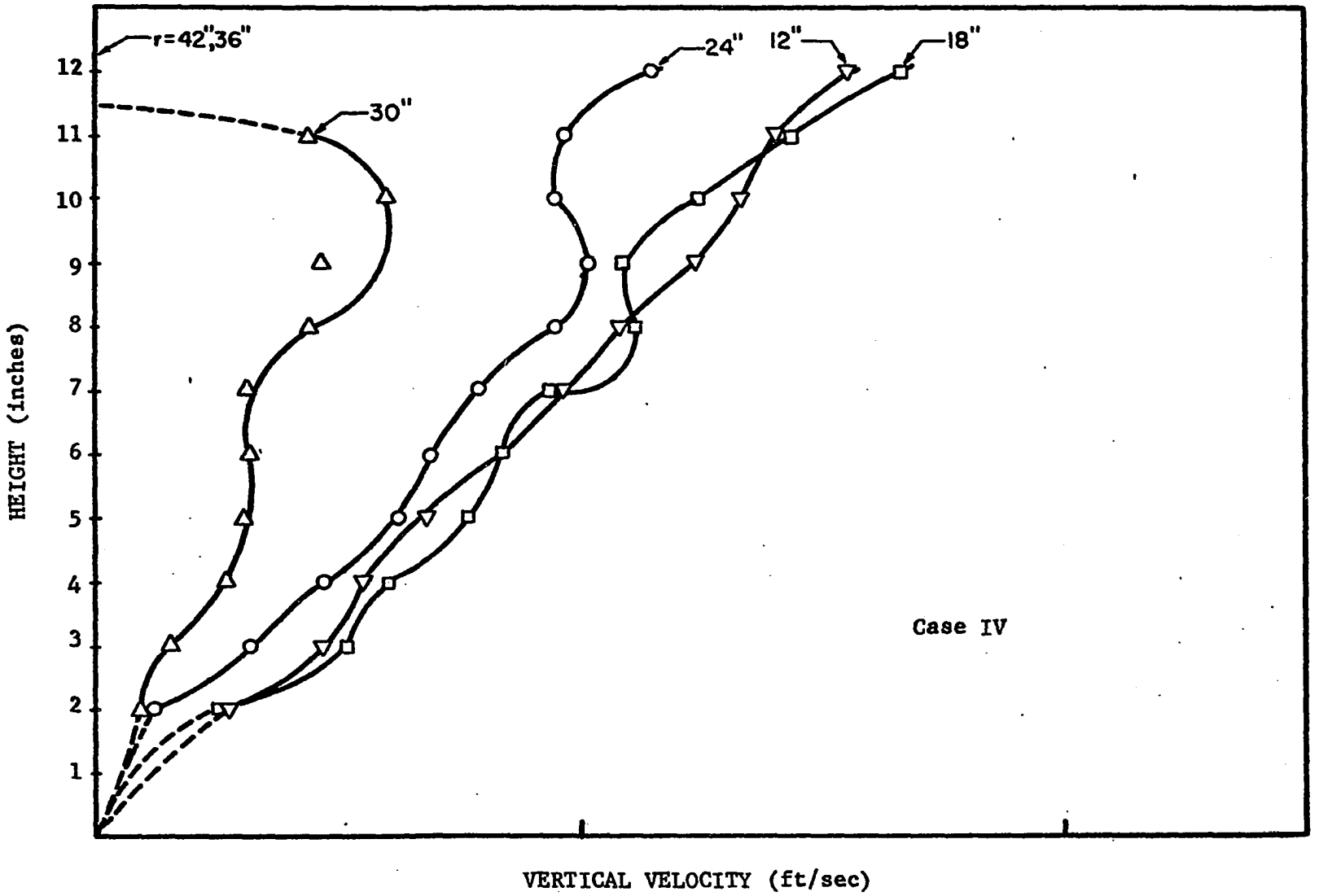

Fig. 2.19 Variation of Vertical Velocity with Height

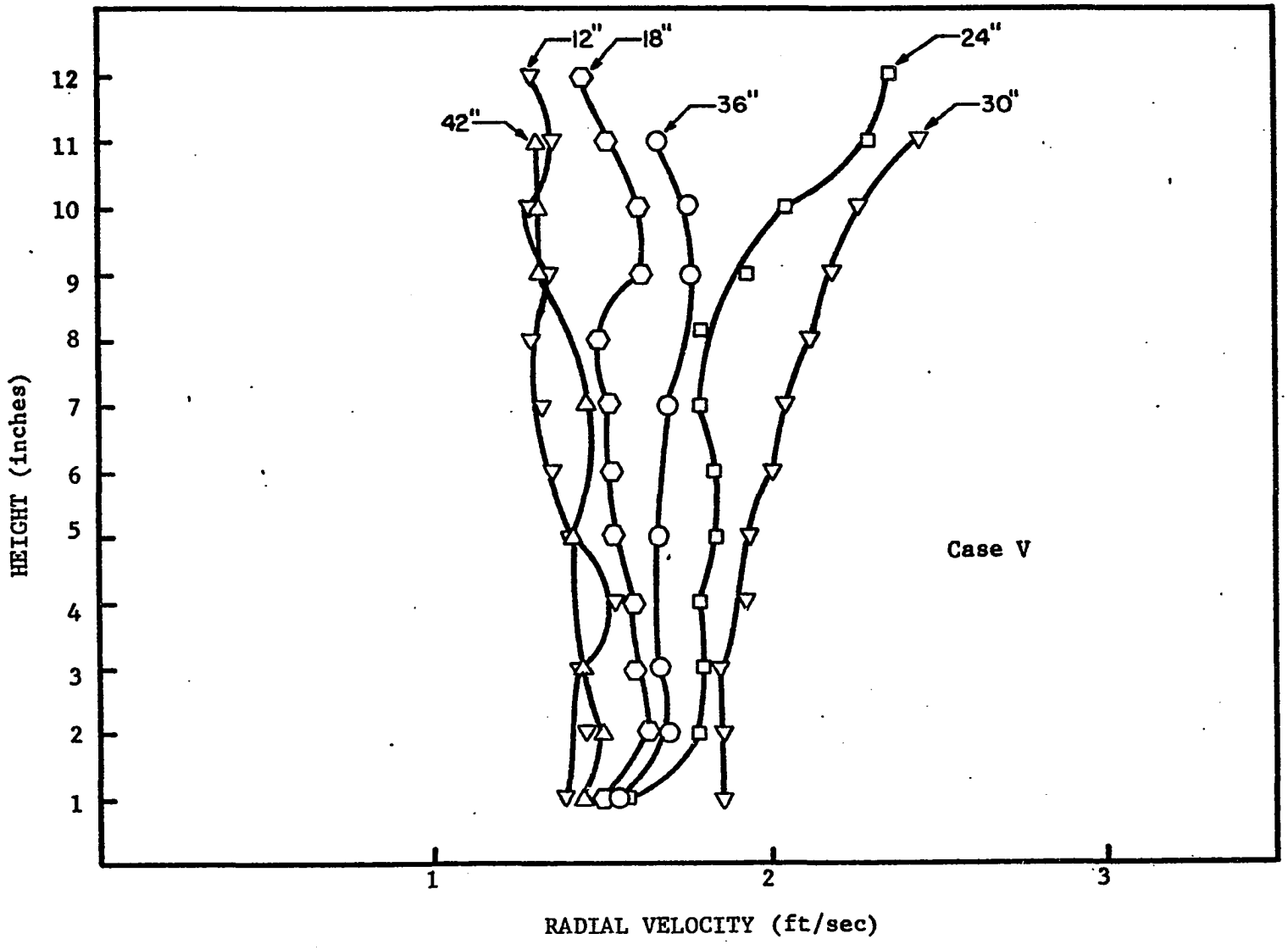

Fig. 2.20Variation of Radial Velocity with Height

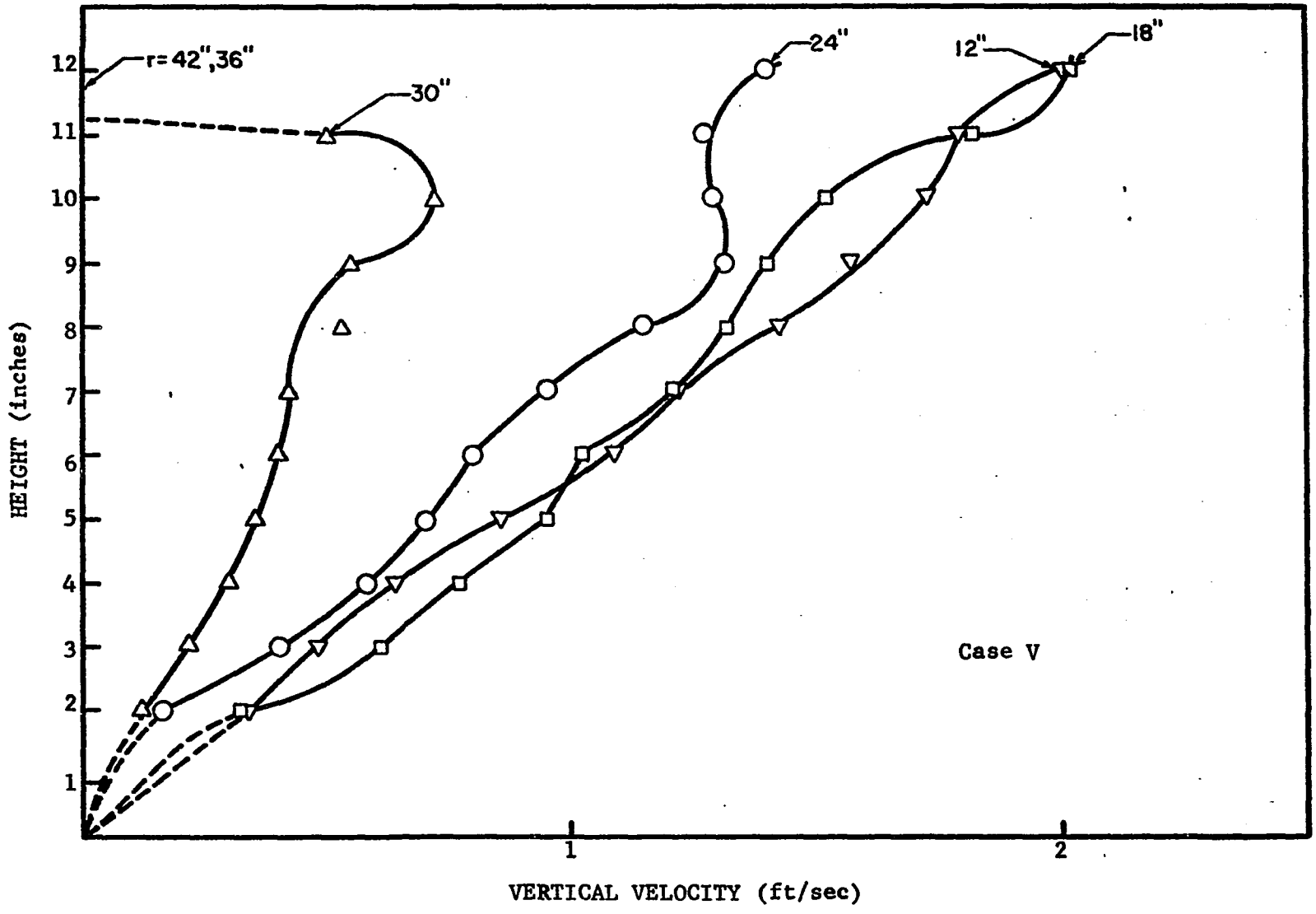

Fig.2.21 Variation of Vertical Velocity with Height

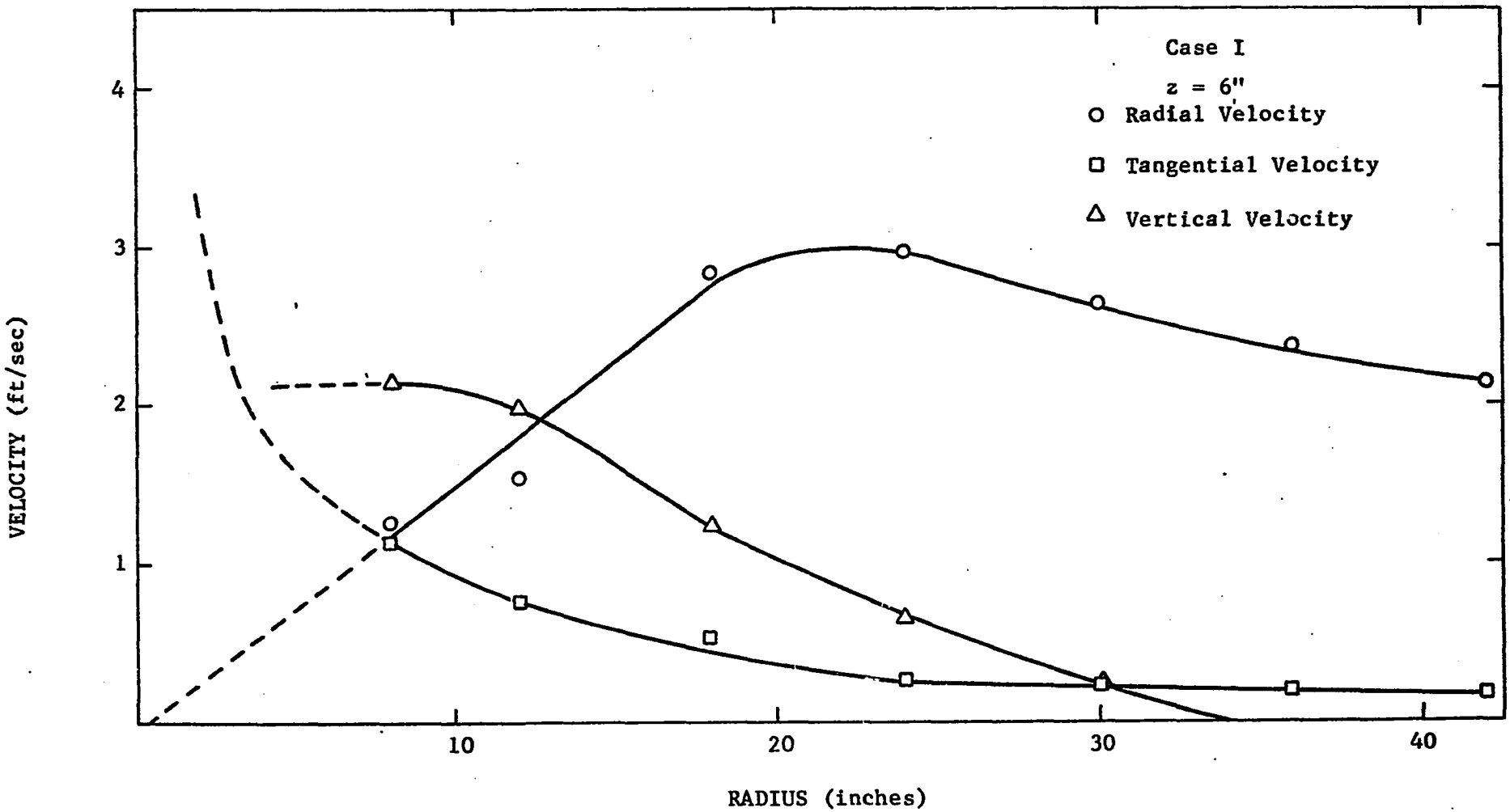

Fig. 2.22 Variation of Velocity Components with Radius (Case I)

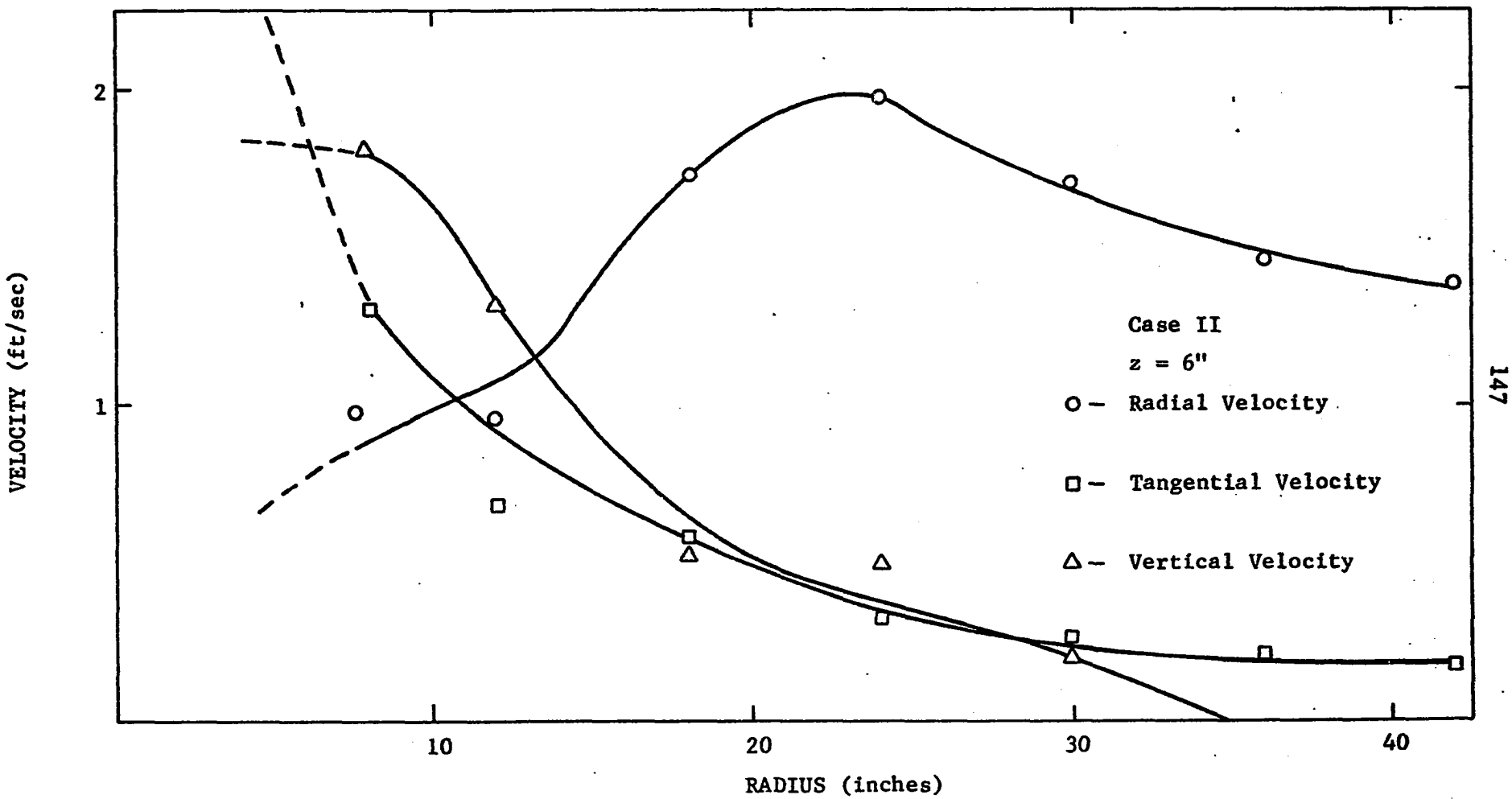

Fig.2.23 Variation of Velocity Components with Radius (Case II)

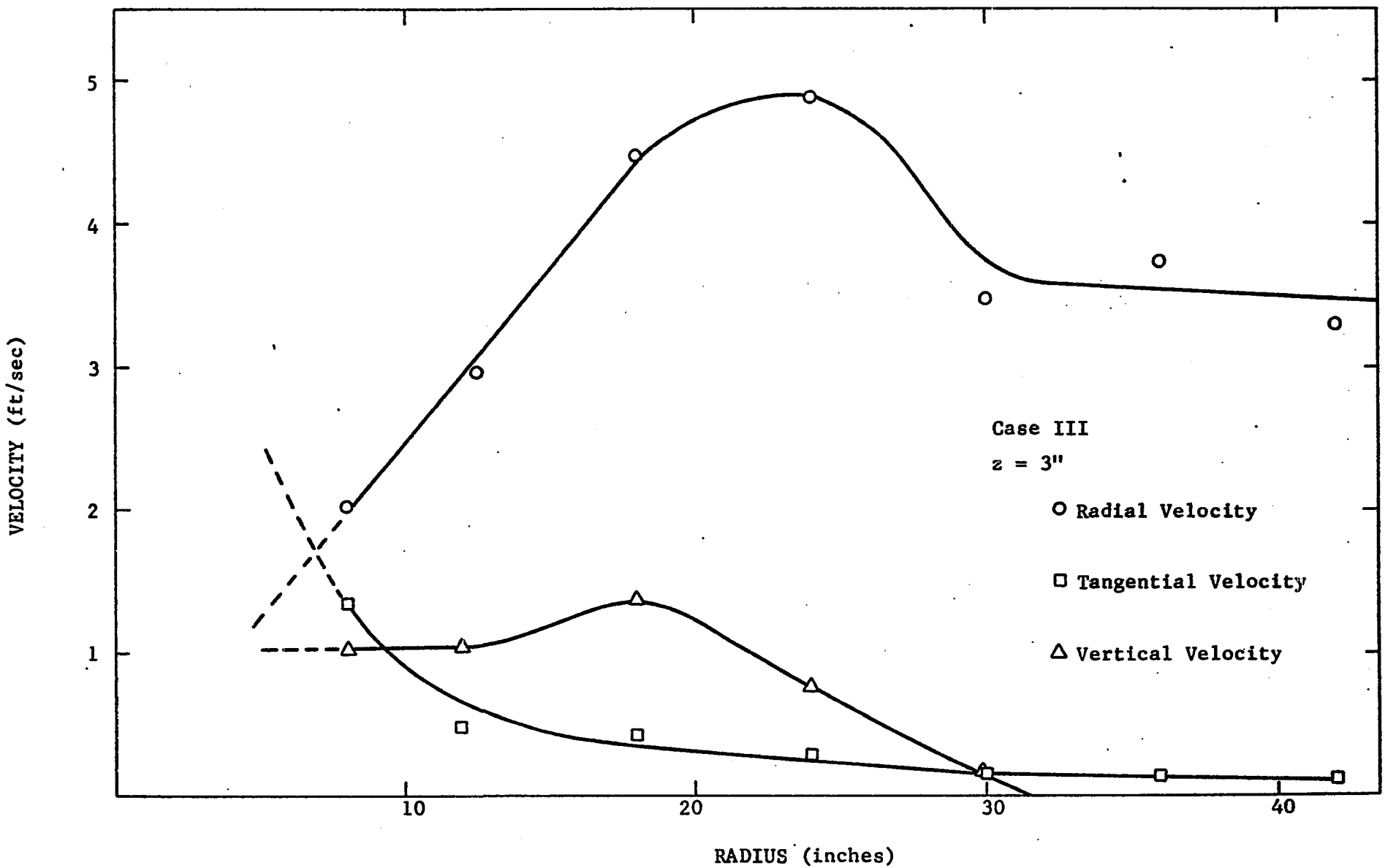

Fig.2.24 Variation of Velocity Components with Radius (Case III)

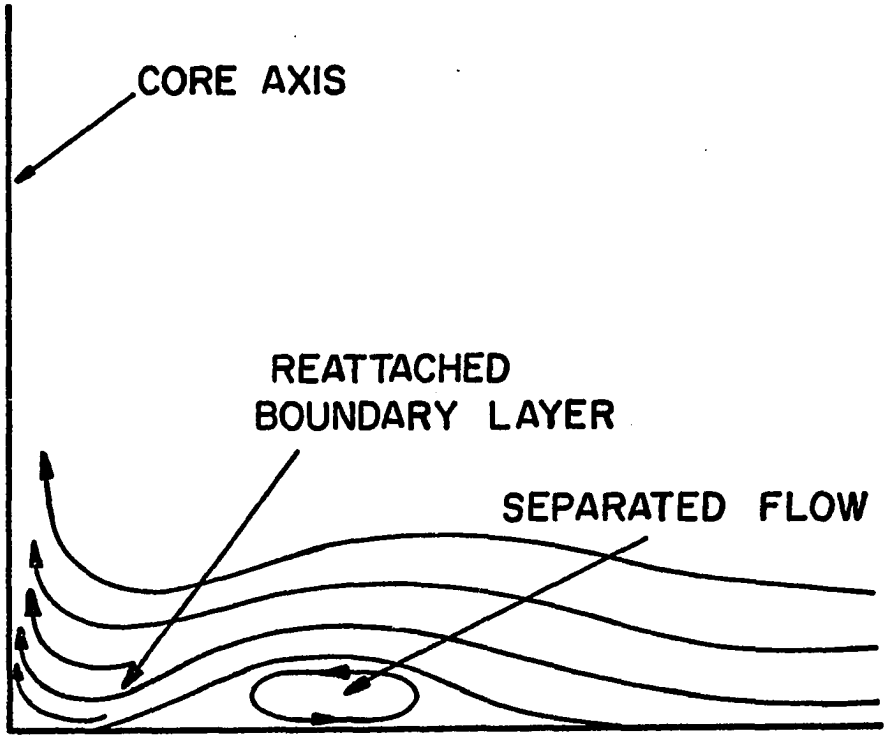

Figure 2.25 Schematic of Separation and Reattachment of the Boundary-Layer.

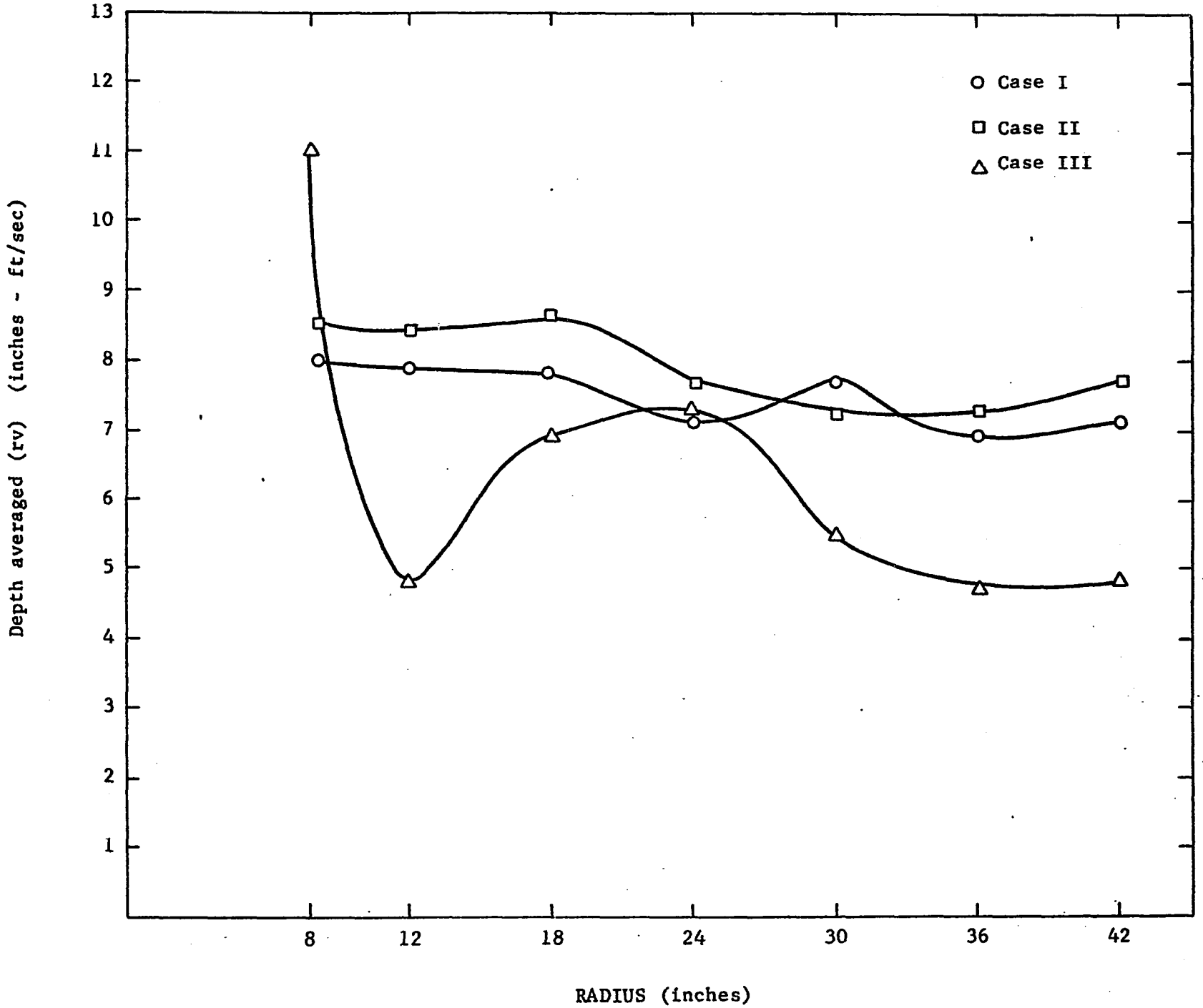

Fig. 2.26 Variation of Depth-averaged (rv) with Radius

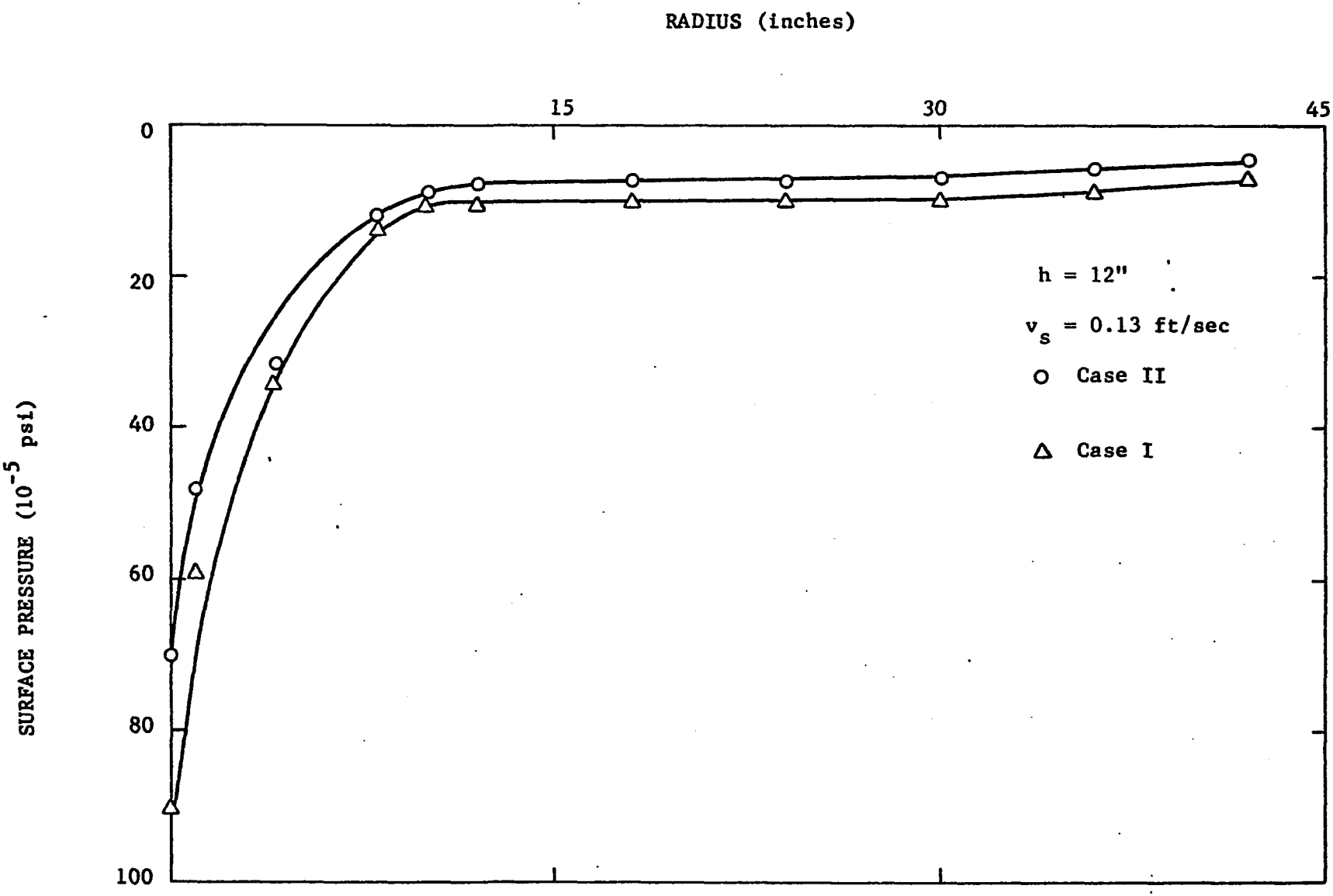

Fig. 2.27 Radial Variation of Surface Pressure

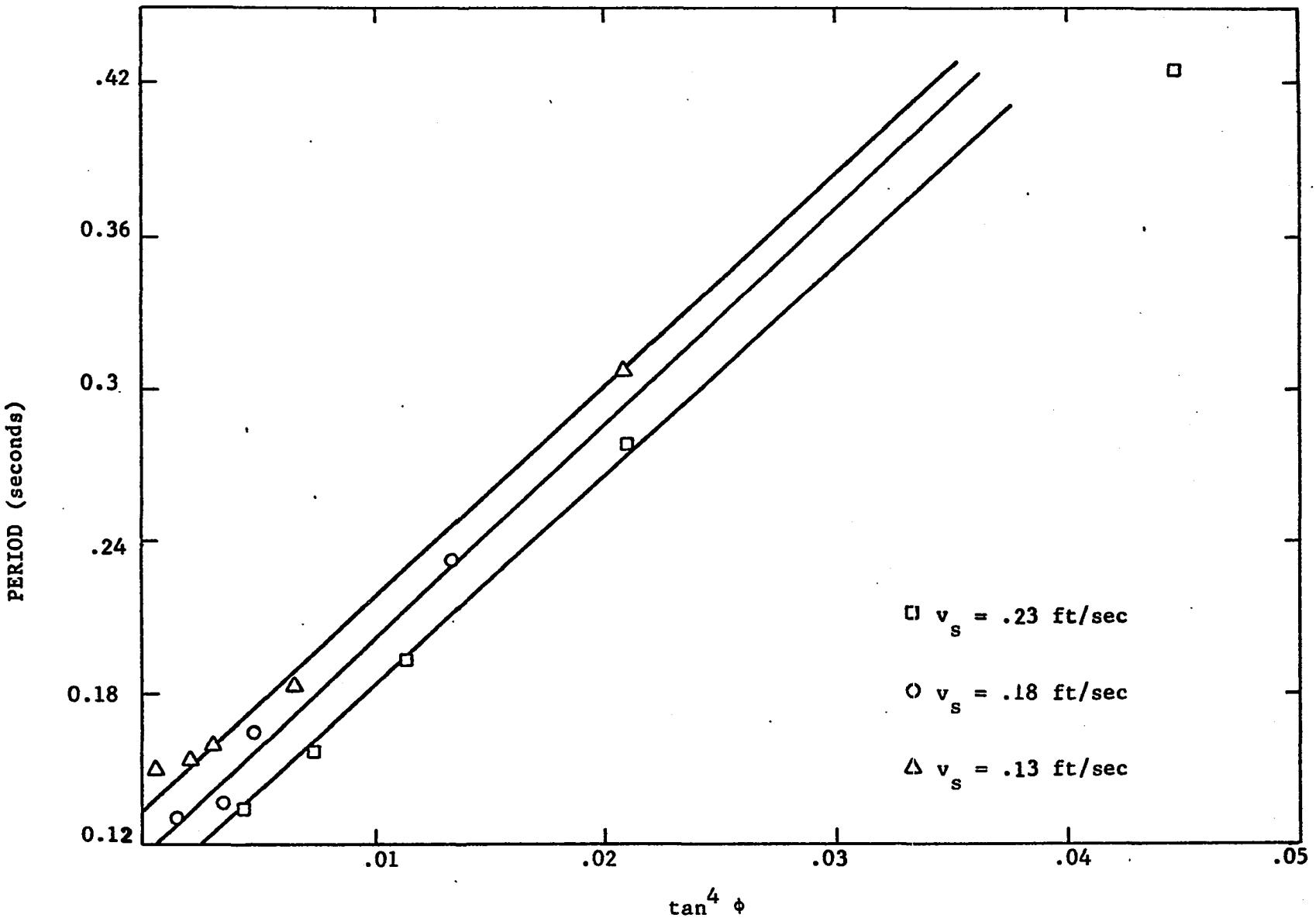

Fig. 2.28 Variation of the Period of the Vortex Core with Swirl Angle for Fixed Screen Angular Velocity

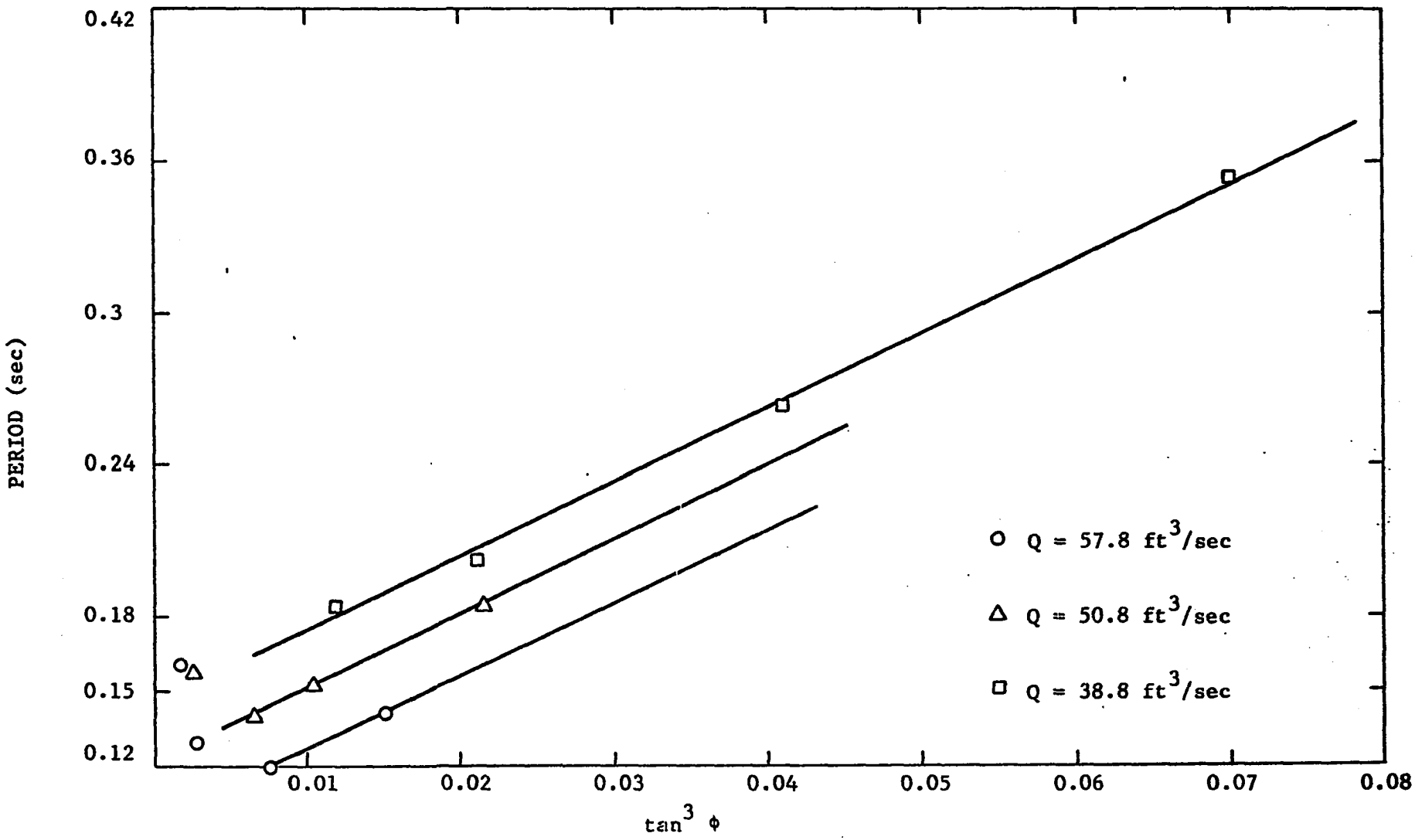

Fig.2.29 Variation of the Period of the Vortex Core with Swirl Angle for fixed Q

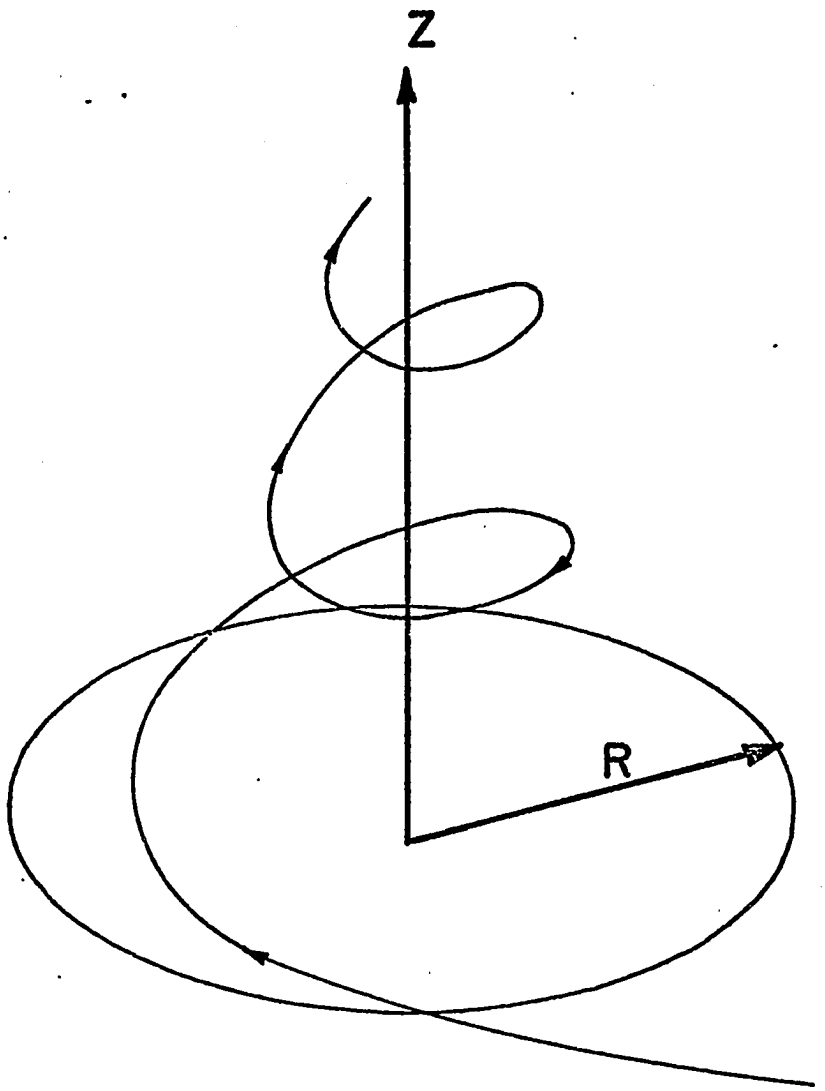

Figure 3.1 Flowfield Schematic

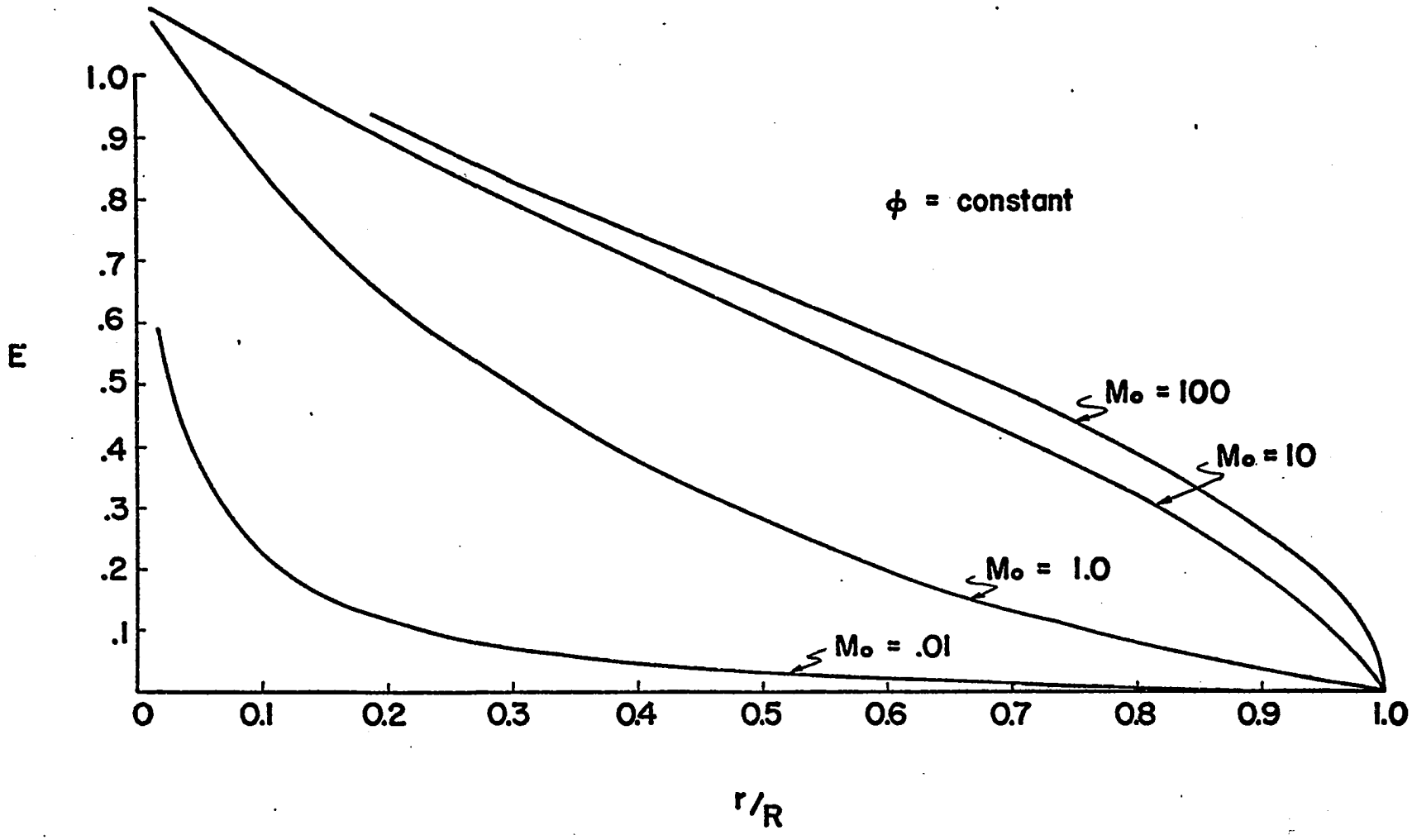

Figure 3.2 Variation of Cross-Flow Function E with Nondimensional Radius (Case i)

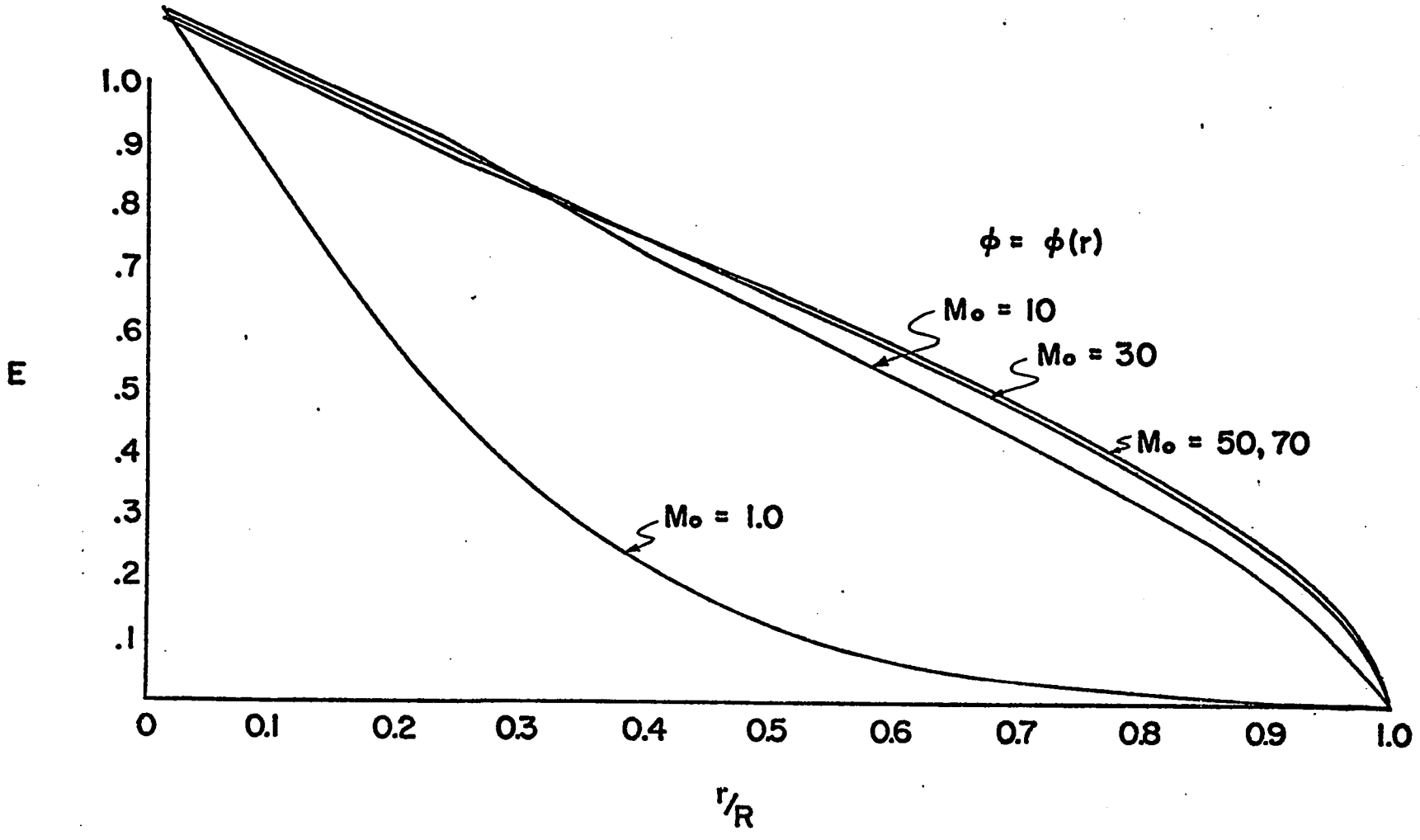

Figure 3.3 Variation of Cross-Flow Function E with Nondimensional Radius (Case ii)

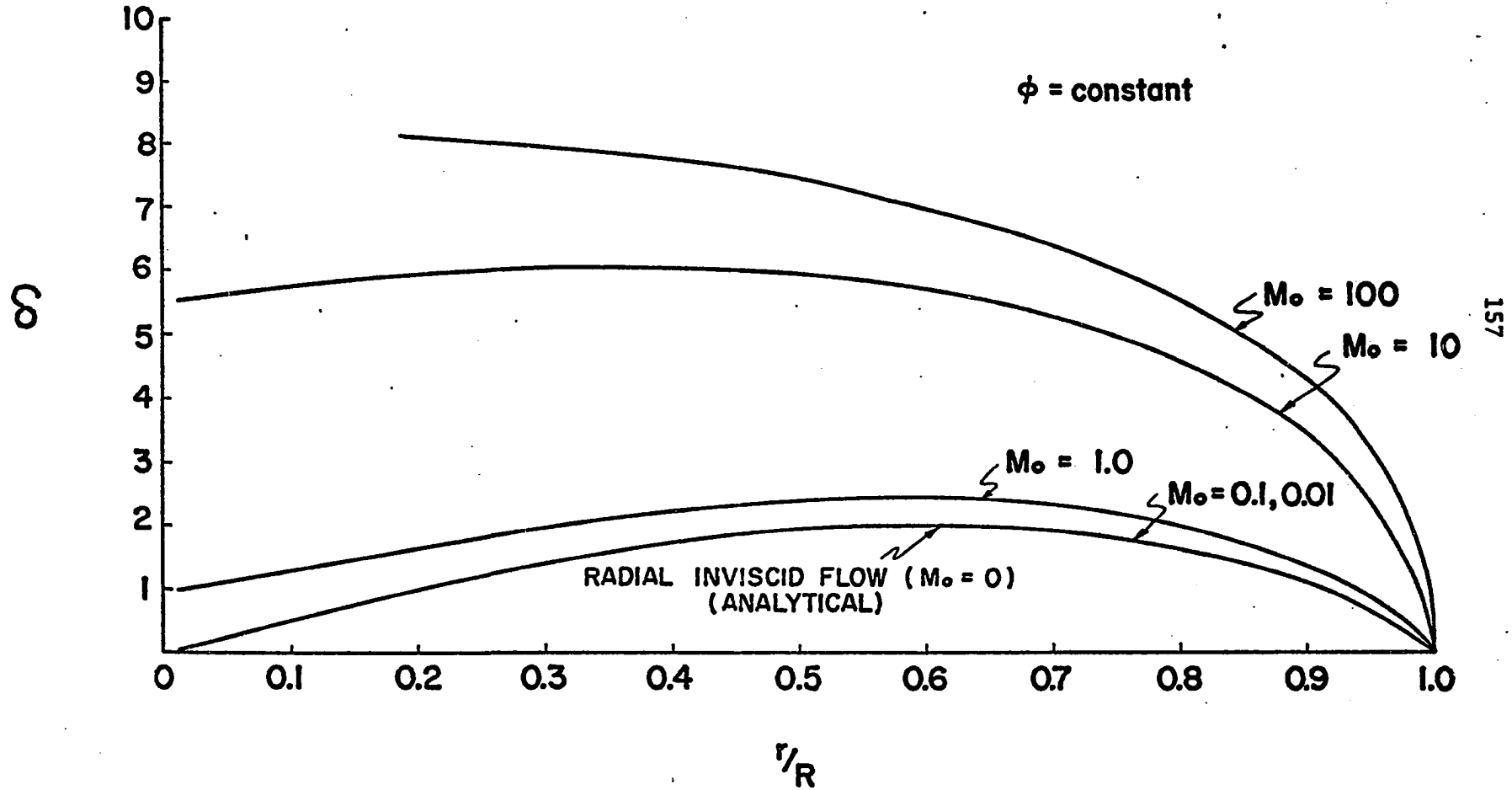

Figure 3.4 Variation of Boundary-Layer Thickness δ with Radius (Case i)

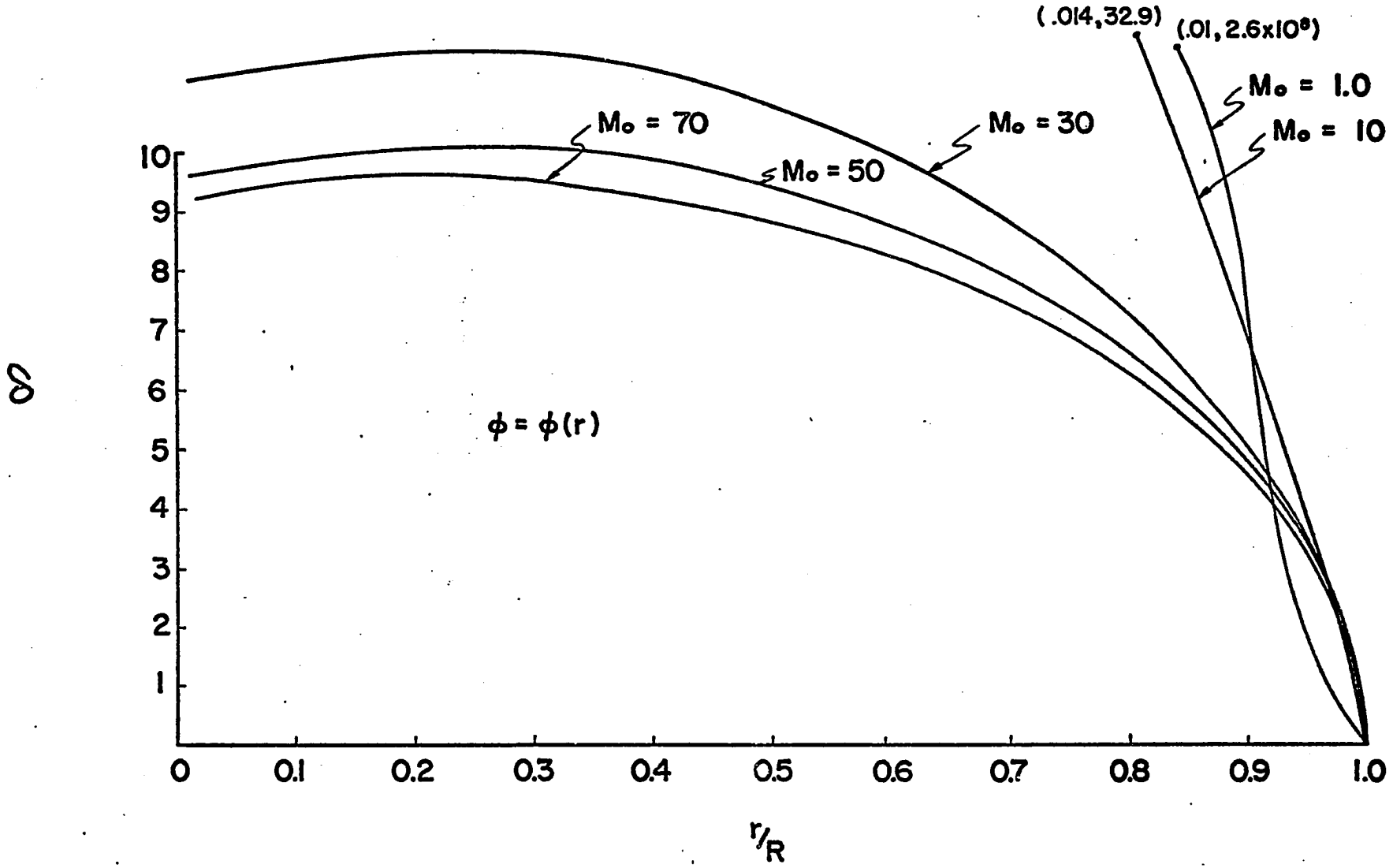

Figure 3.5 Variation of Boundary-Layer Thickness δ with Radius (Case ii)

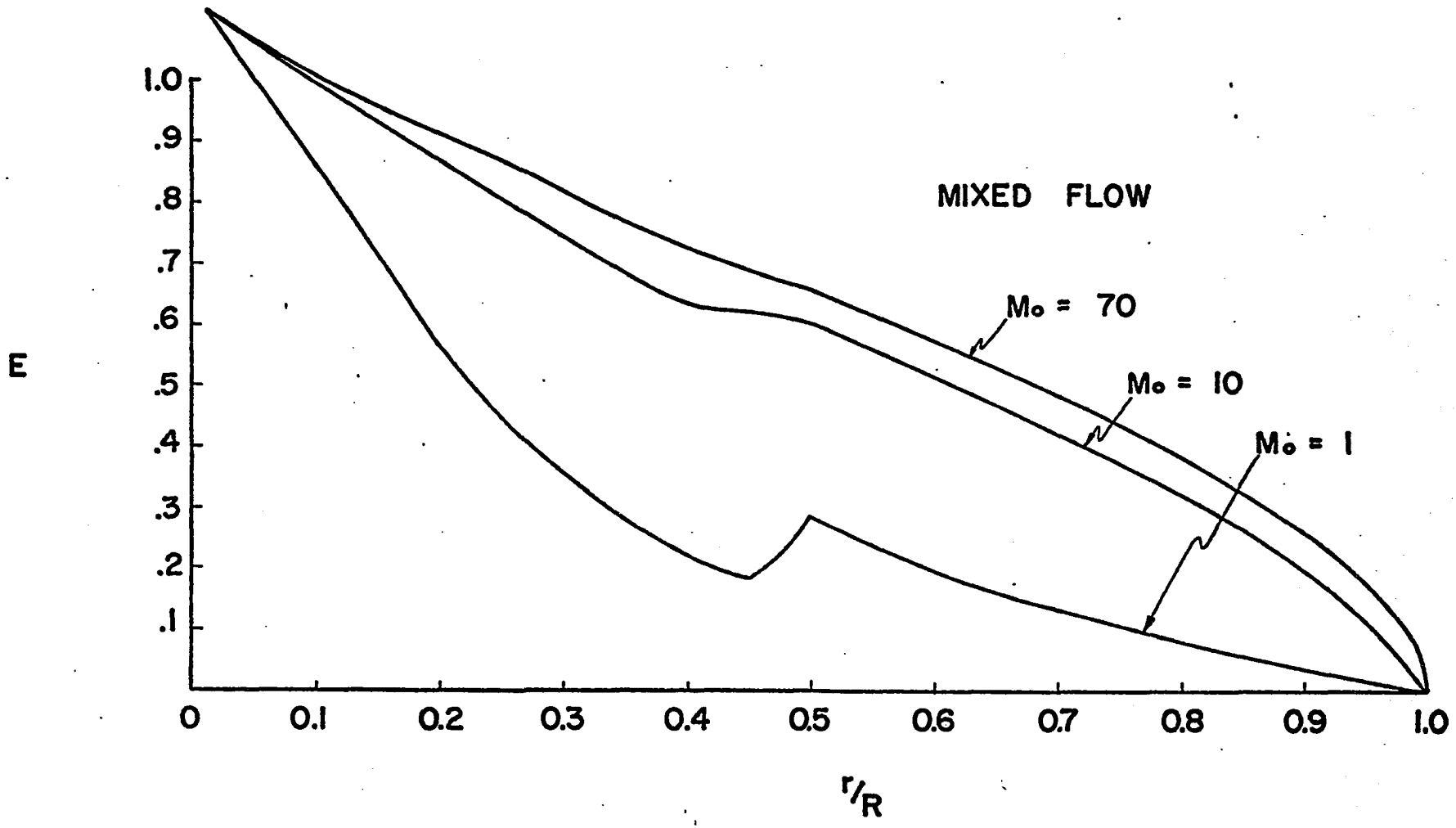

Figure 3.6 Variation of Cross-Flow Function E with Radius (Mixed Case)

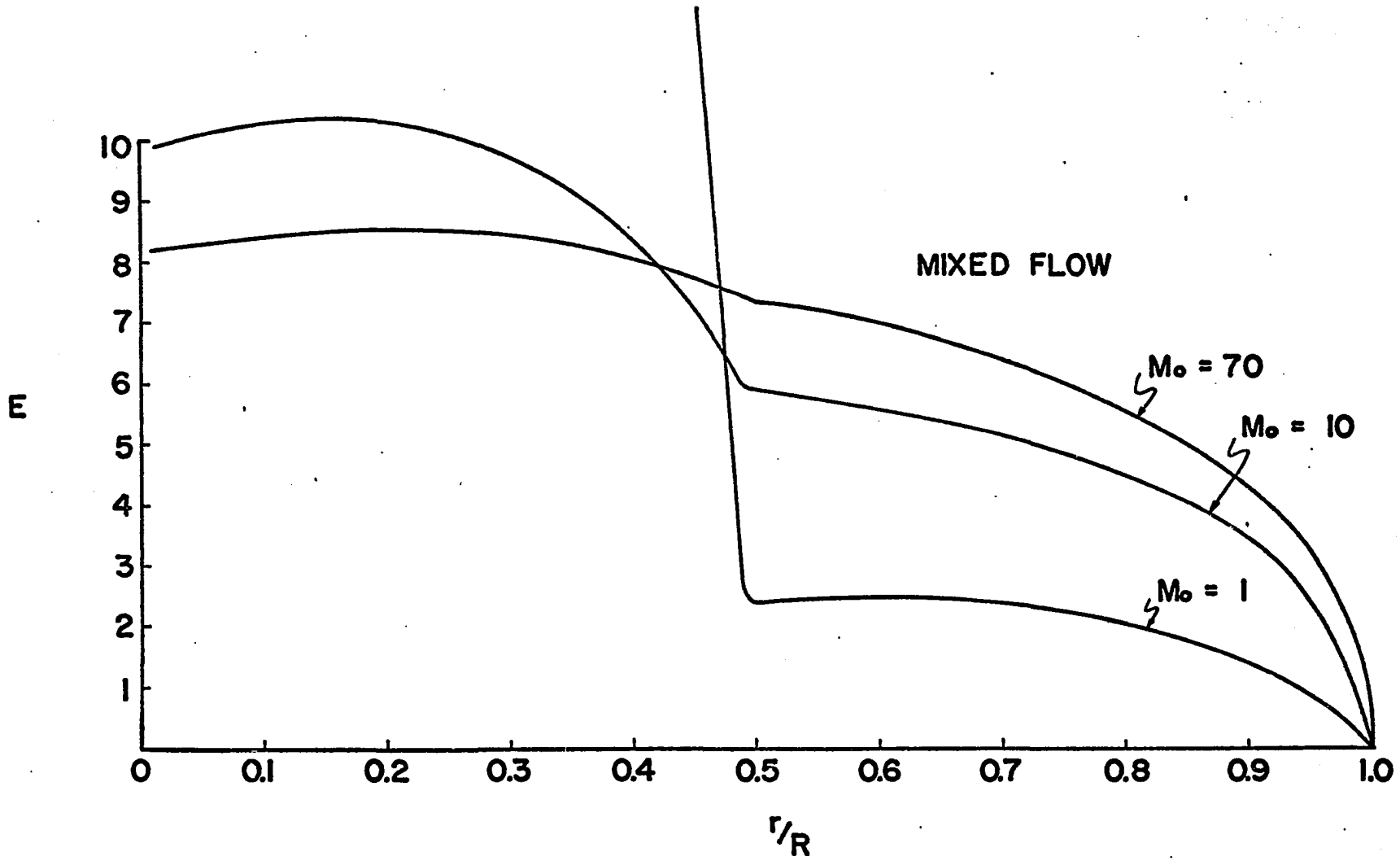

Figure 3.7 Variation of Boundary-Layer Thickness δ with Radius (Mixed Case)

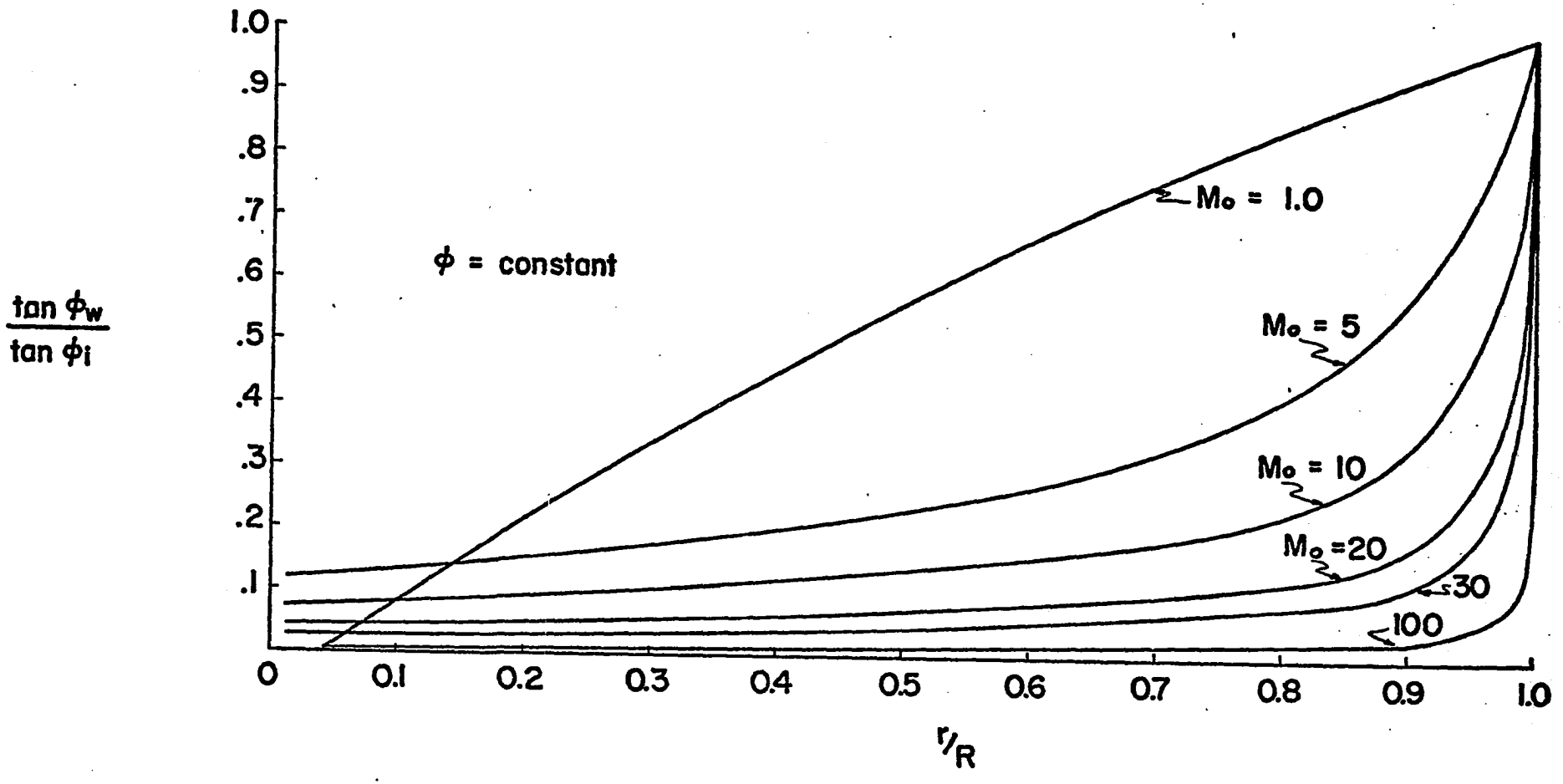

Figure 3.8 Variation of the Ratio of Swirl Parameters at Ground to Inviscid Flow with Radius (Case i)

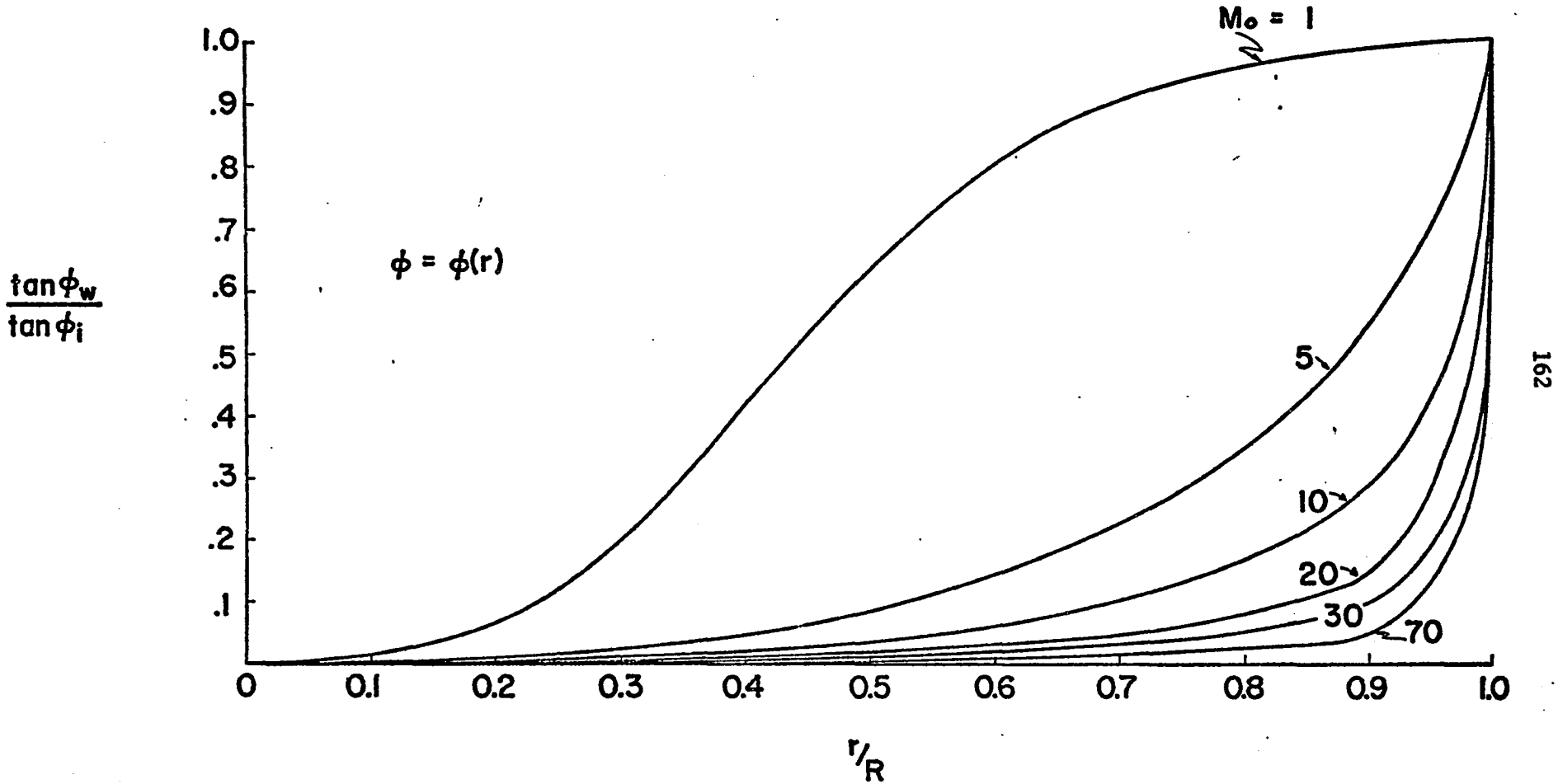

Figure 3.9 Variation of the Ratio of Swirl Parameter at z=0 and z=δ with Radius (Case ii)

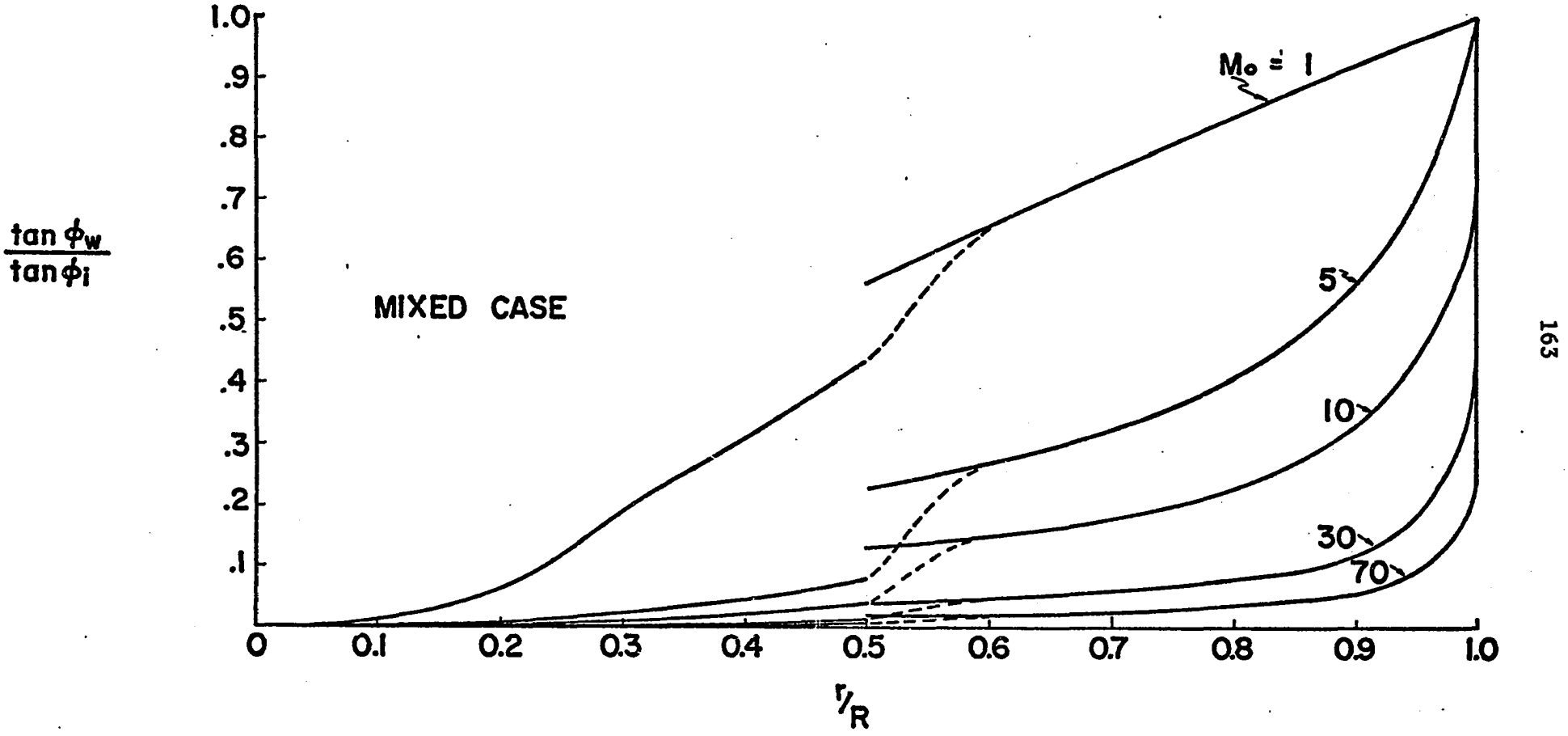

Figure 3.10 Variation of the Ratio of Swirl Parameter at z=0 and z=δ with Radius (Mixed Case)

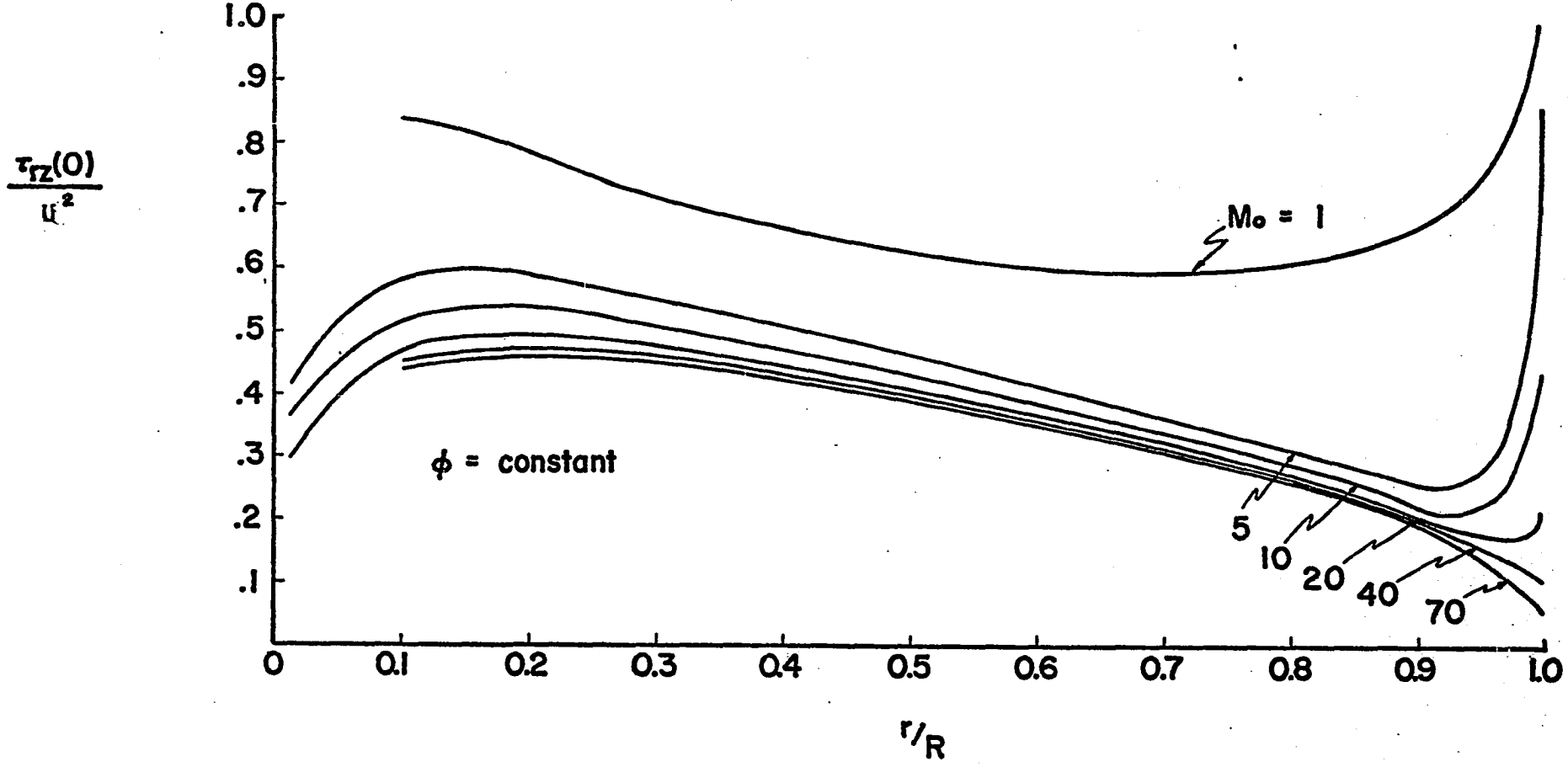

Figure 3.11 Variation of the Normalized Radial Shear Stress Component at the Ground with Radius (Case i)

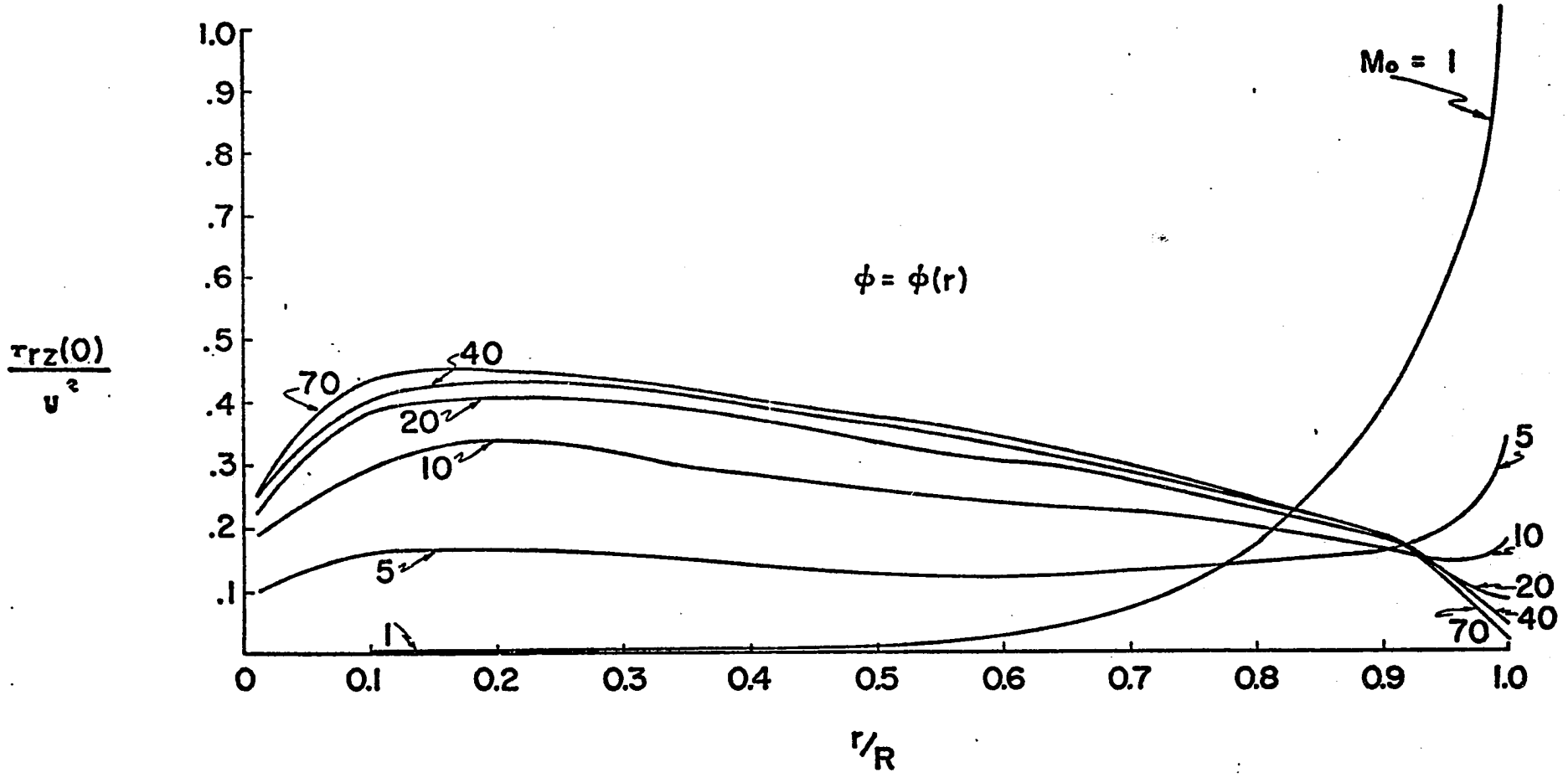

Figure 3.12 Variation of the Normalized Radial Shear Stress Component at the Ground with Radius (Case ii)

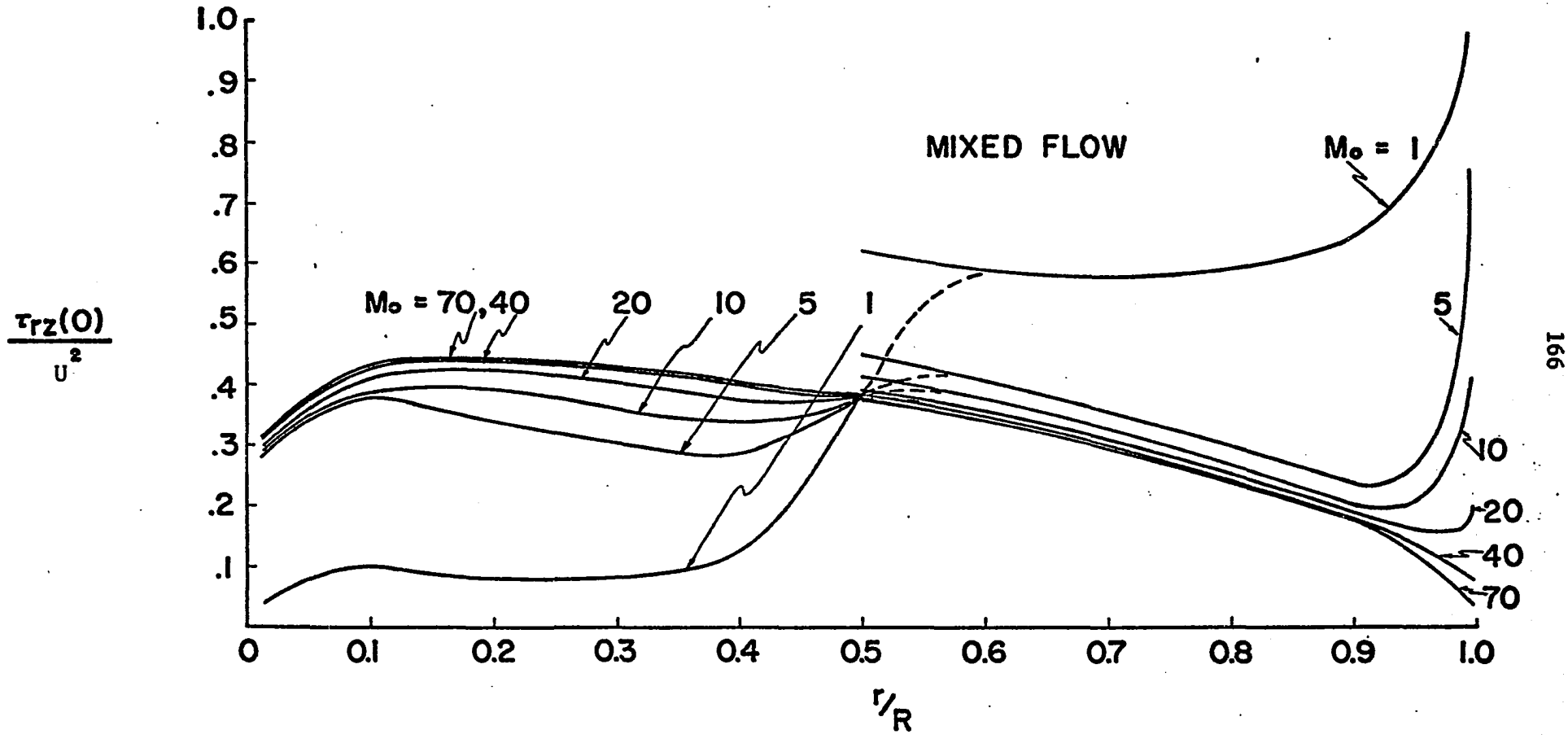

Figure 3.13 Variation of the Normalized Radial Shear Stress Component at the Ground with Radius (Mixed Case)

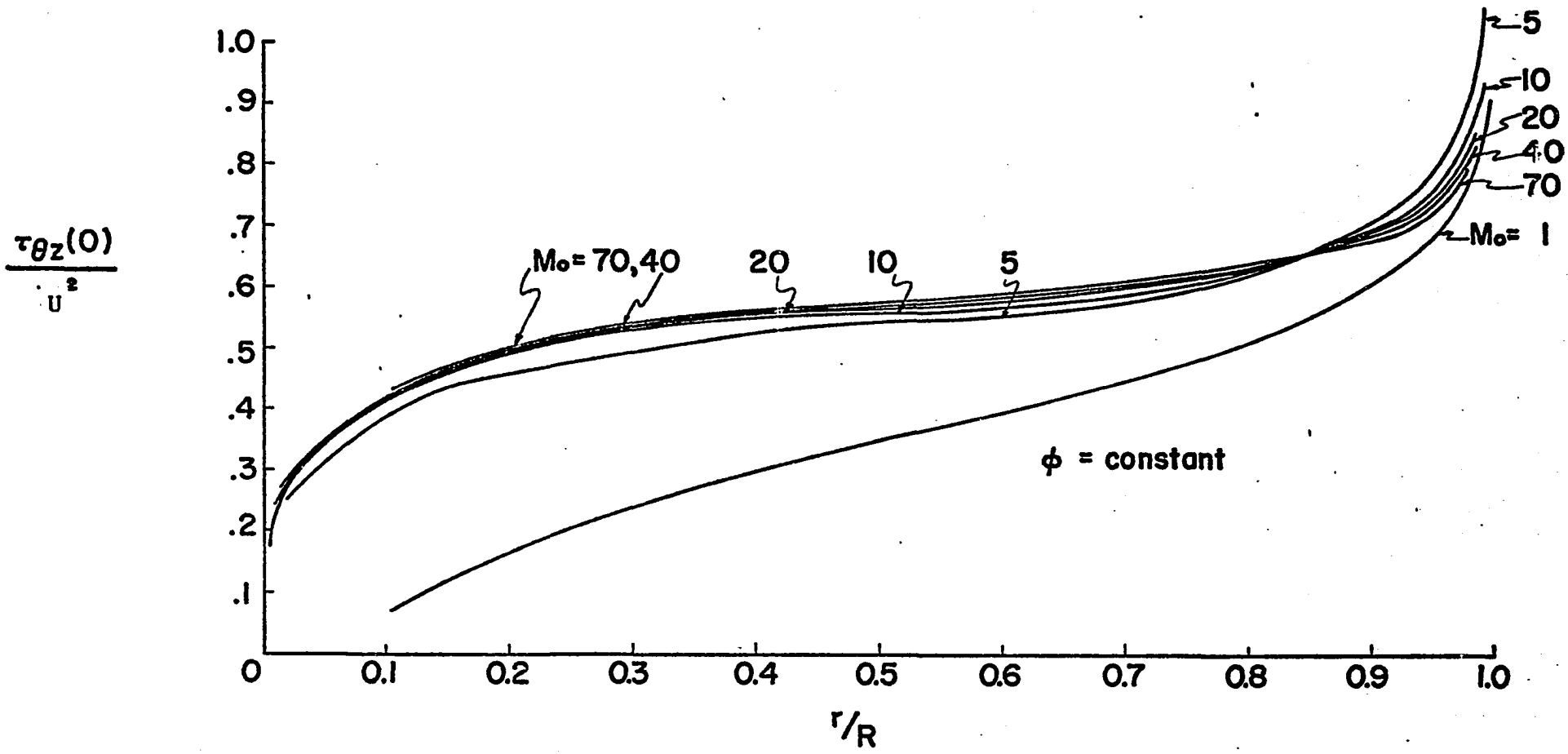

Figure 3.14 Variation of the Normalized Tangential Shear Stress Component at the Ground with Radius (Case i)

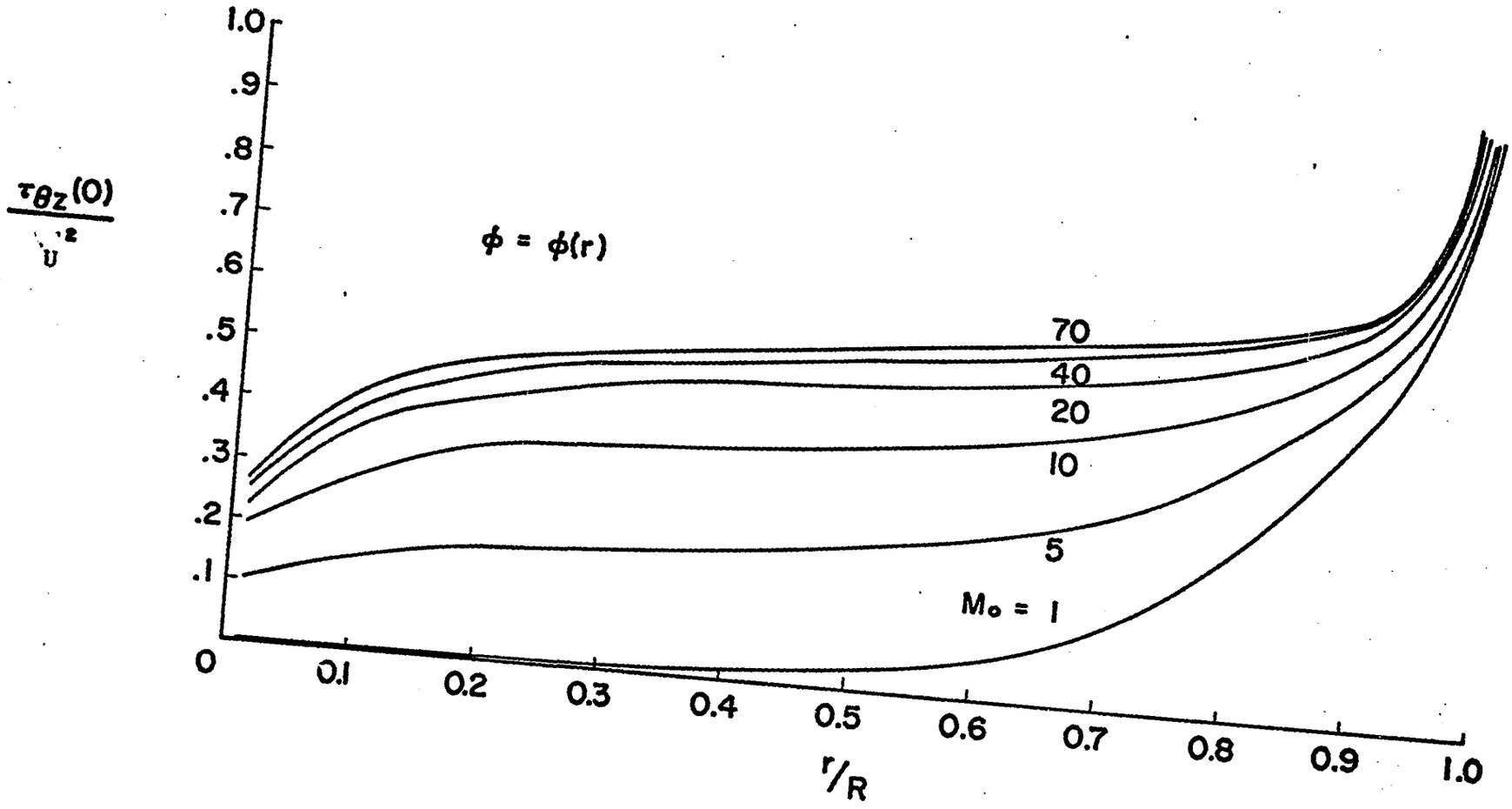

Figure 3.15 Variation of the Tangential Shear Stress Component at the Ground with Radius (Case ii)

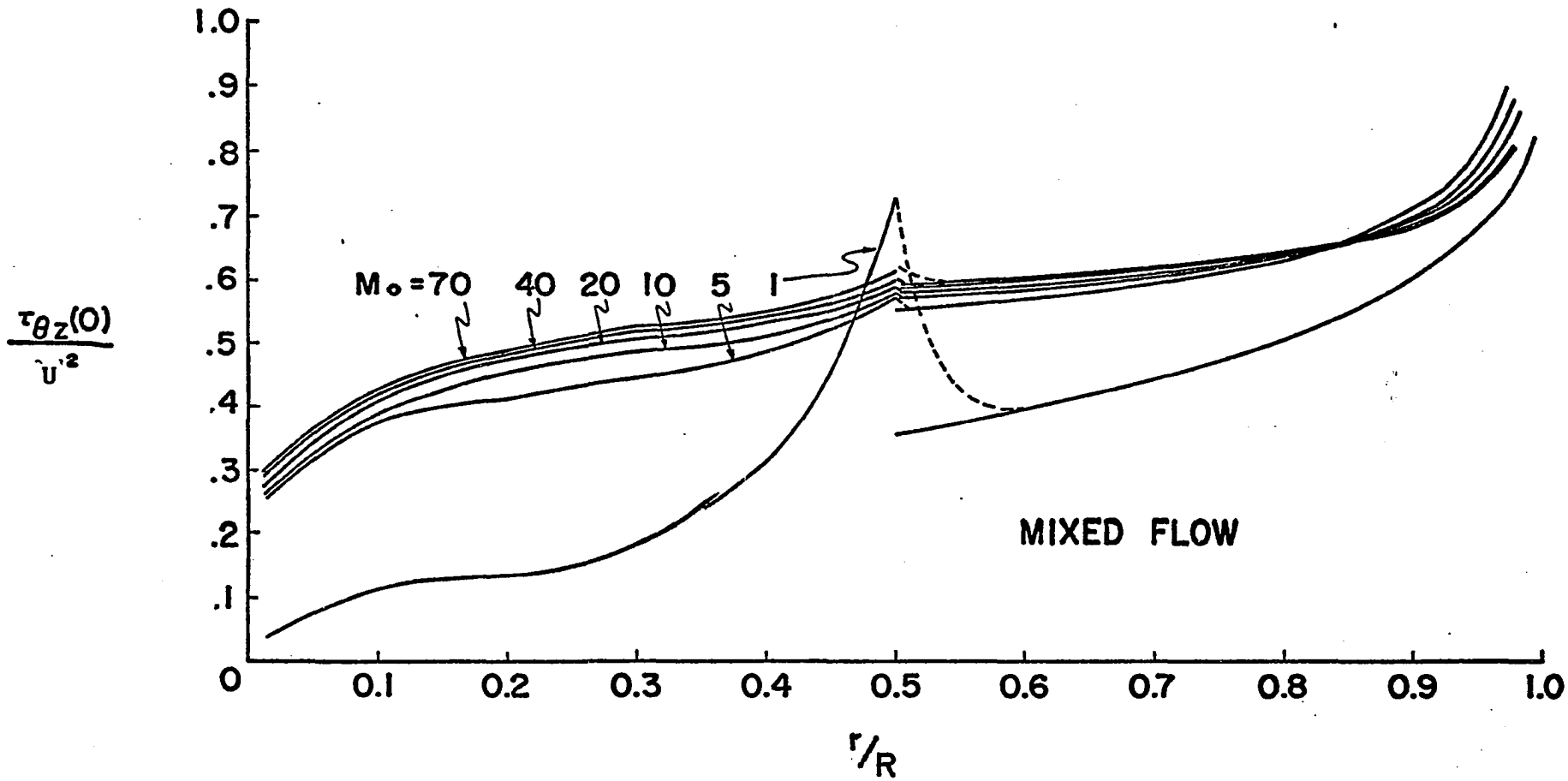

Figure 3.16 Variation of Tangential Shear Stress Component at the Ground with Radius (Mixed Case)

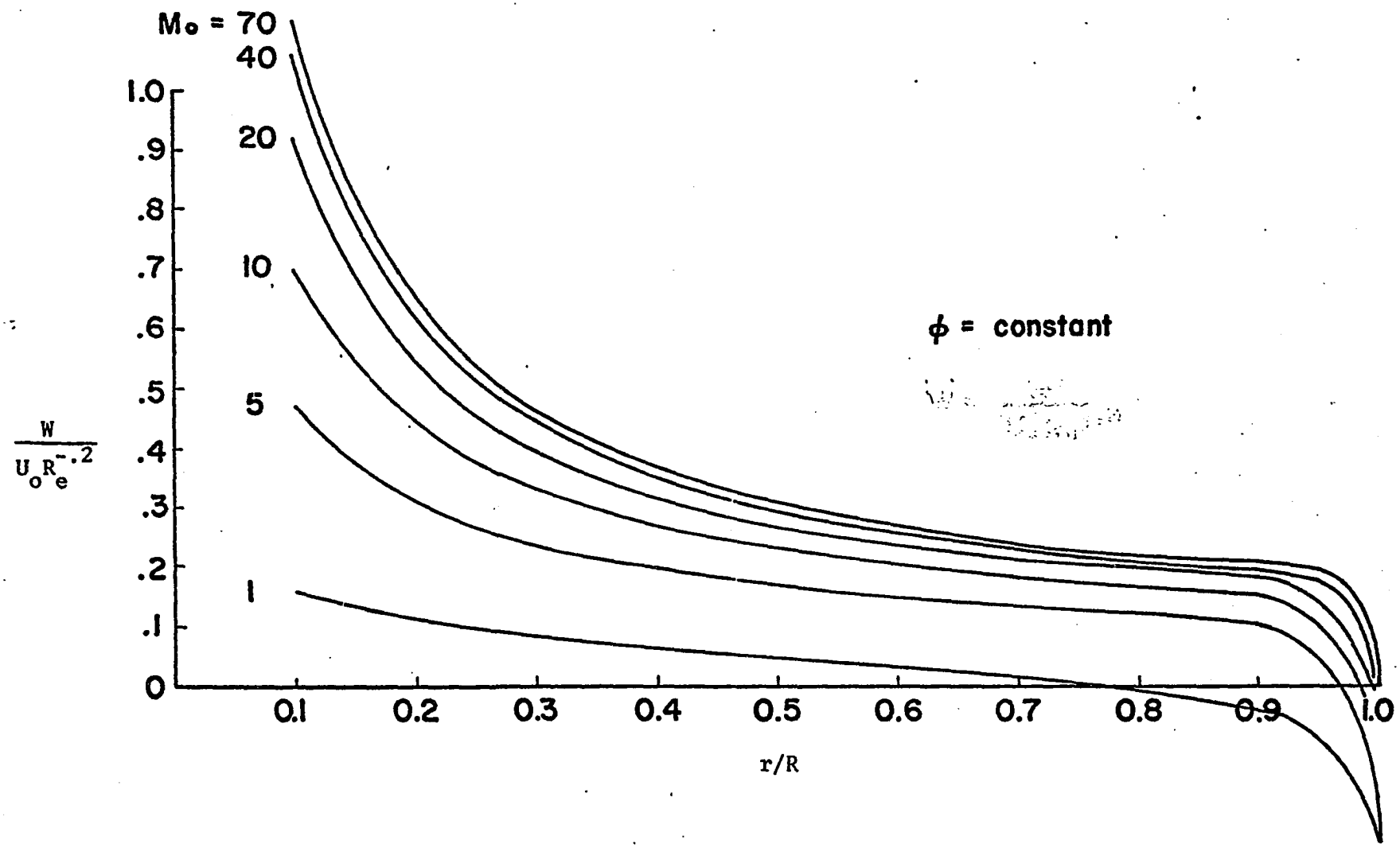

Figure 3.17 Variation of the Negative Axial Velocity Component at the Edge of the Boundary Layer with Radius (Case i)

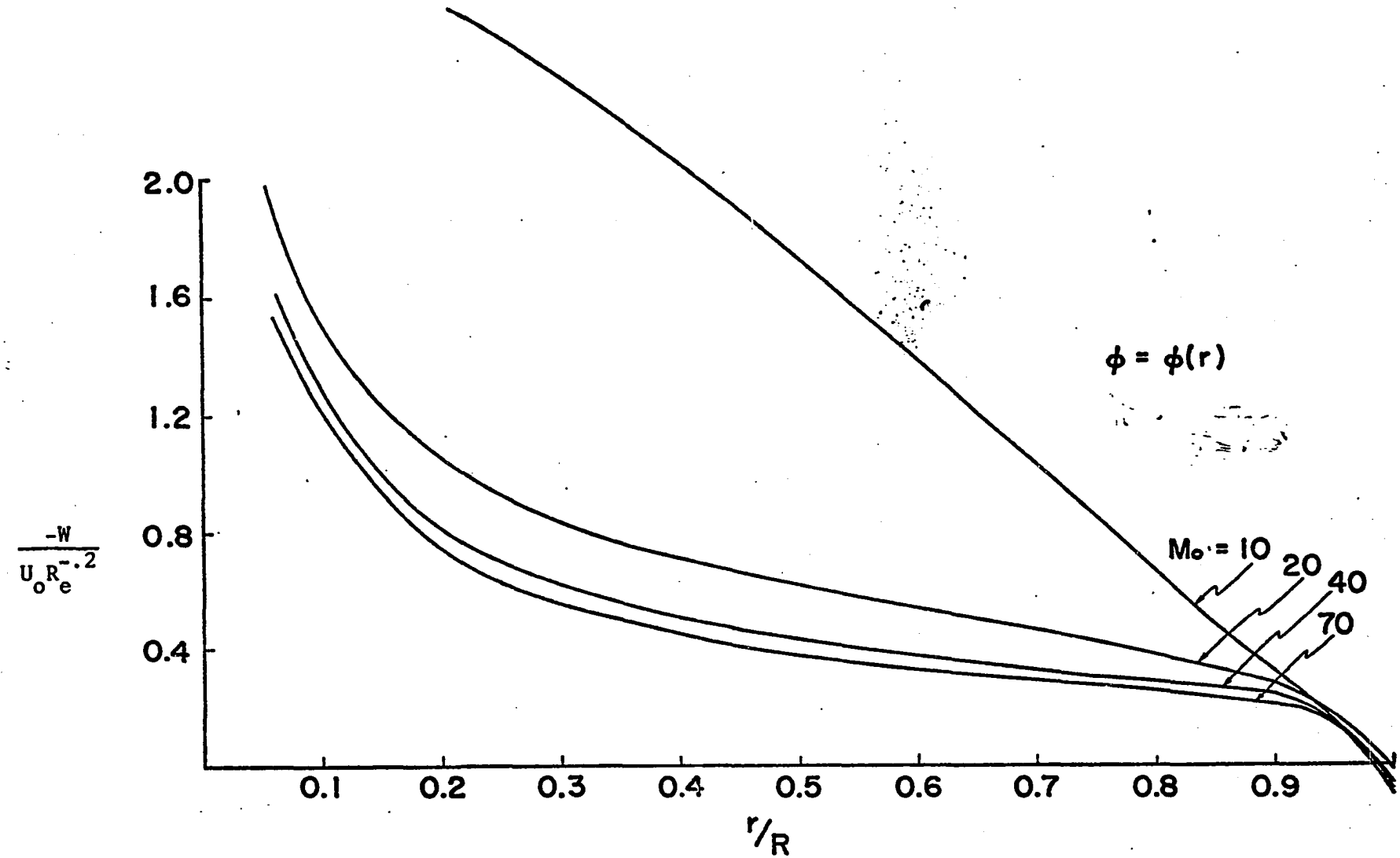

Figure 3.18 Variation of the Negative Axial Velocity Component at the Edge of the Boundary Layer with Radius (Case ii)

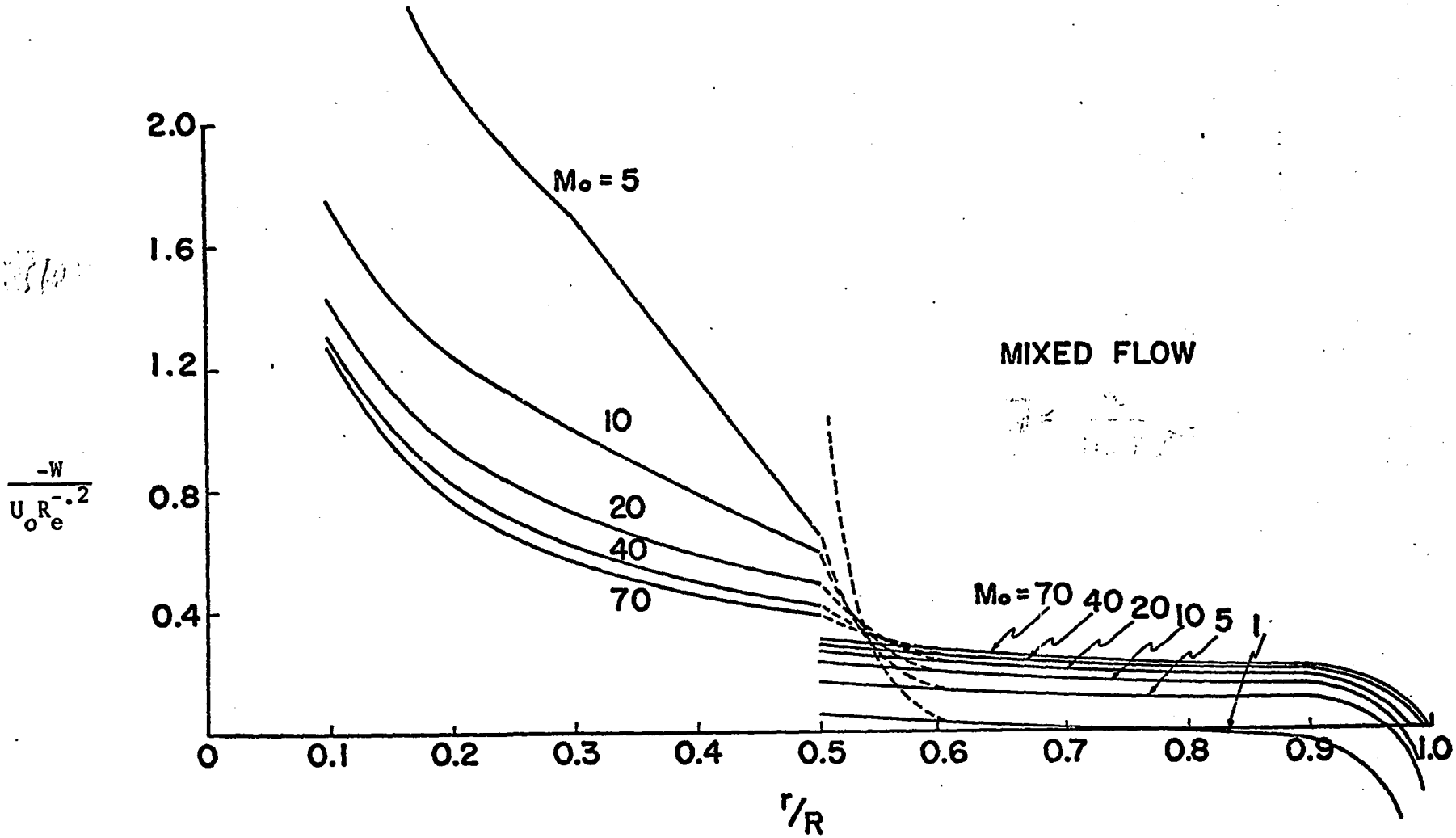

Figure 3.19 Variation of the Negative Axial Velocity Component at the Edge of the Boundary Layer with Radius (Mixed Case)

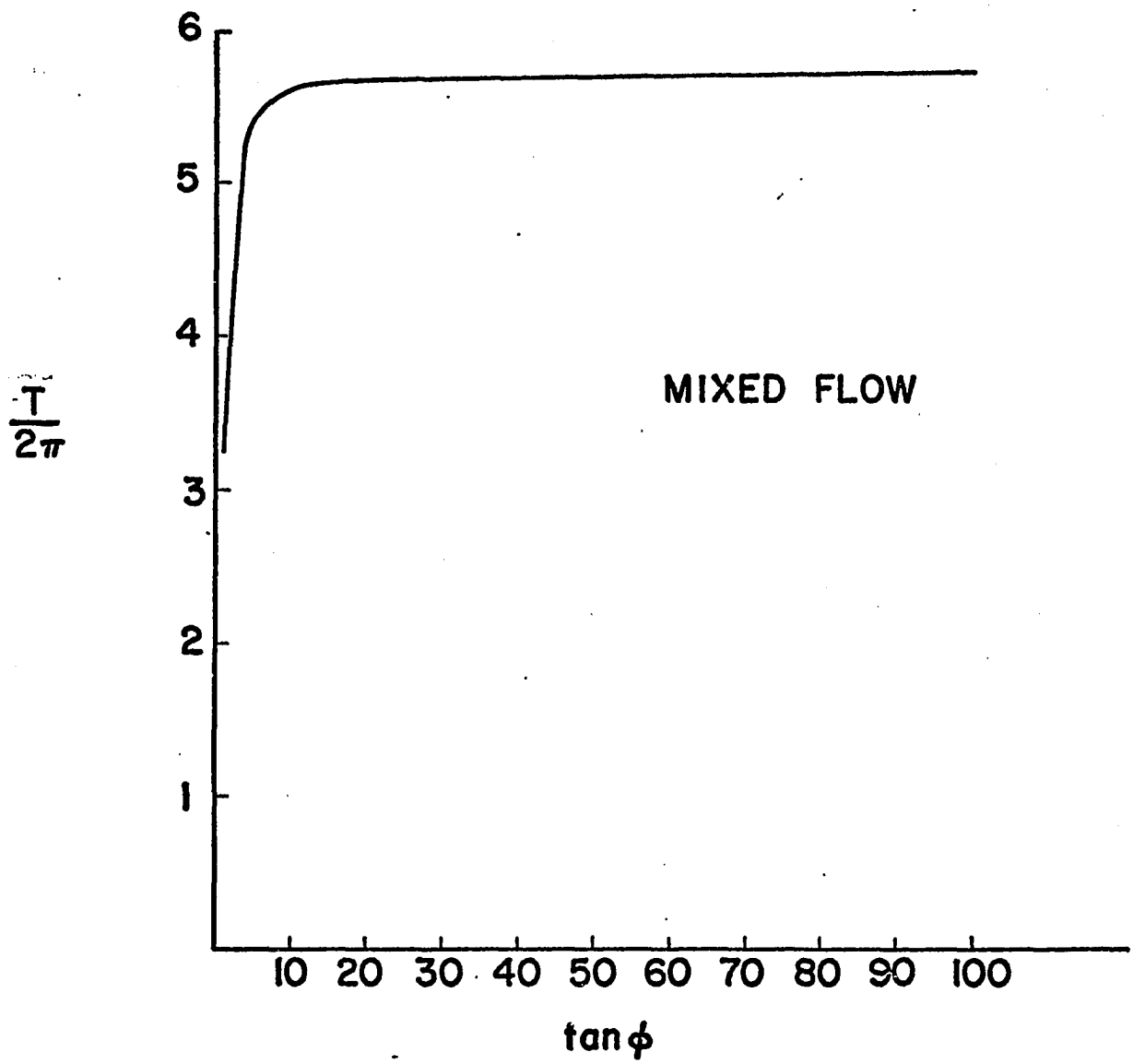

Figure 3.20 Variation of the Nondimensional Torque Exerted by the Ground with Initial Swirl Parameters (Mixed Case)

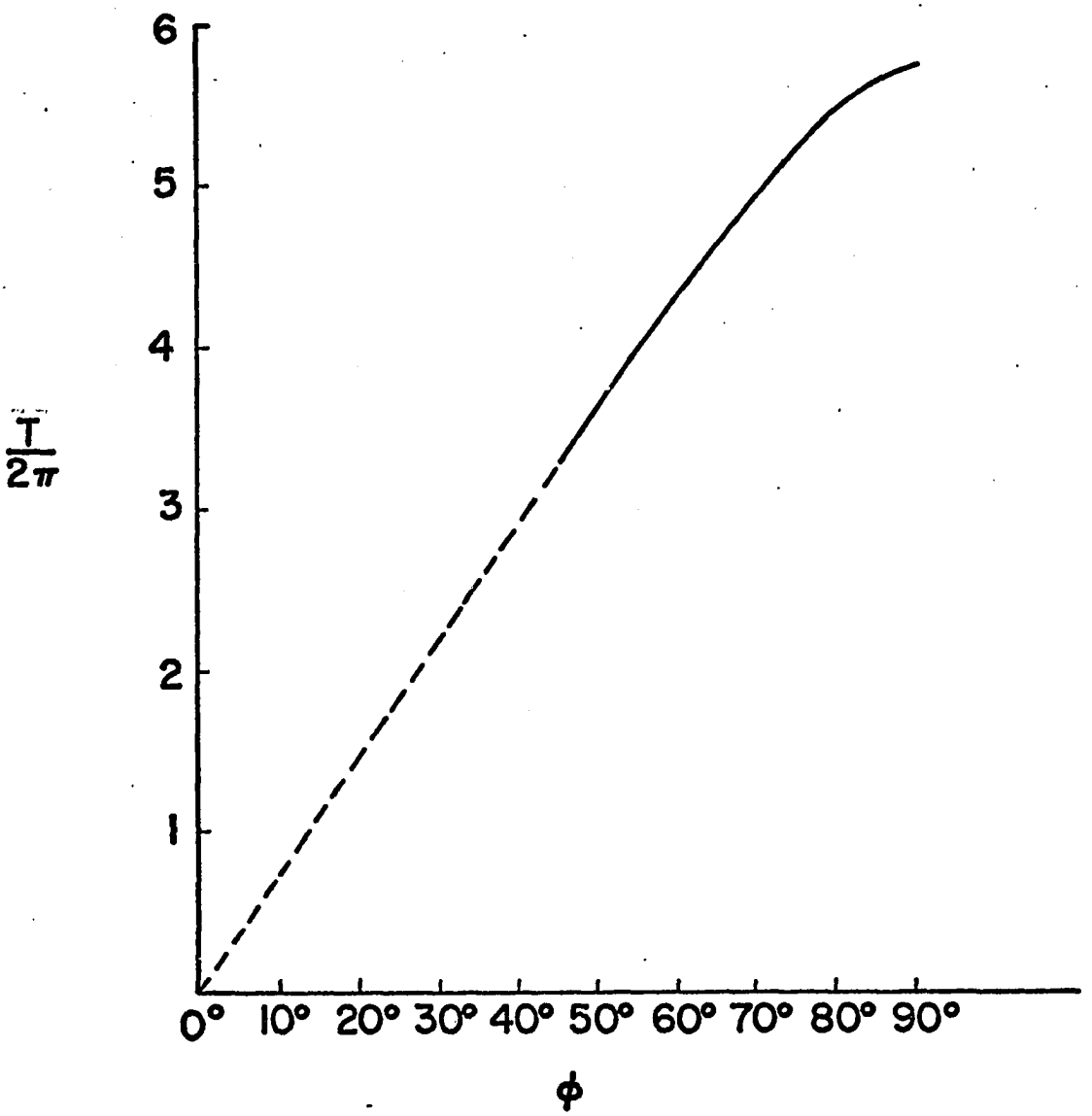

Figure3.21 Variation of the Nondimensional Torque Exerted on the Ground with the Initial Swirl Parameter in Degrees (Mixed Flow)

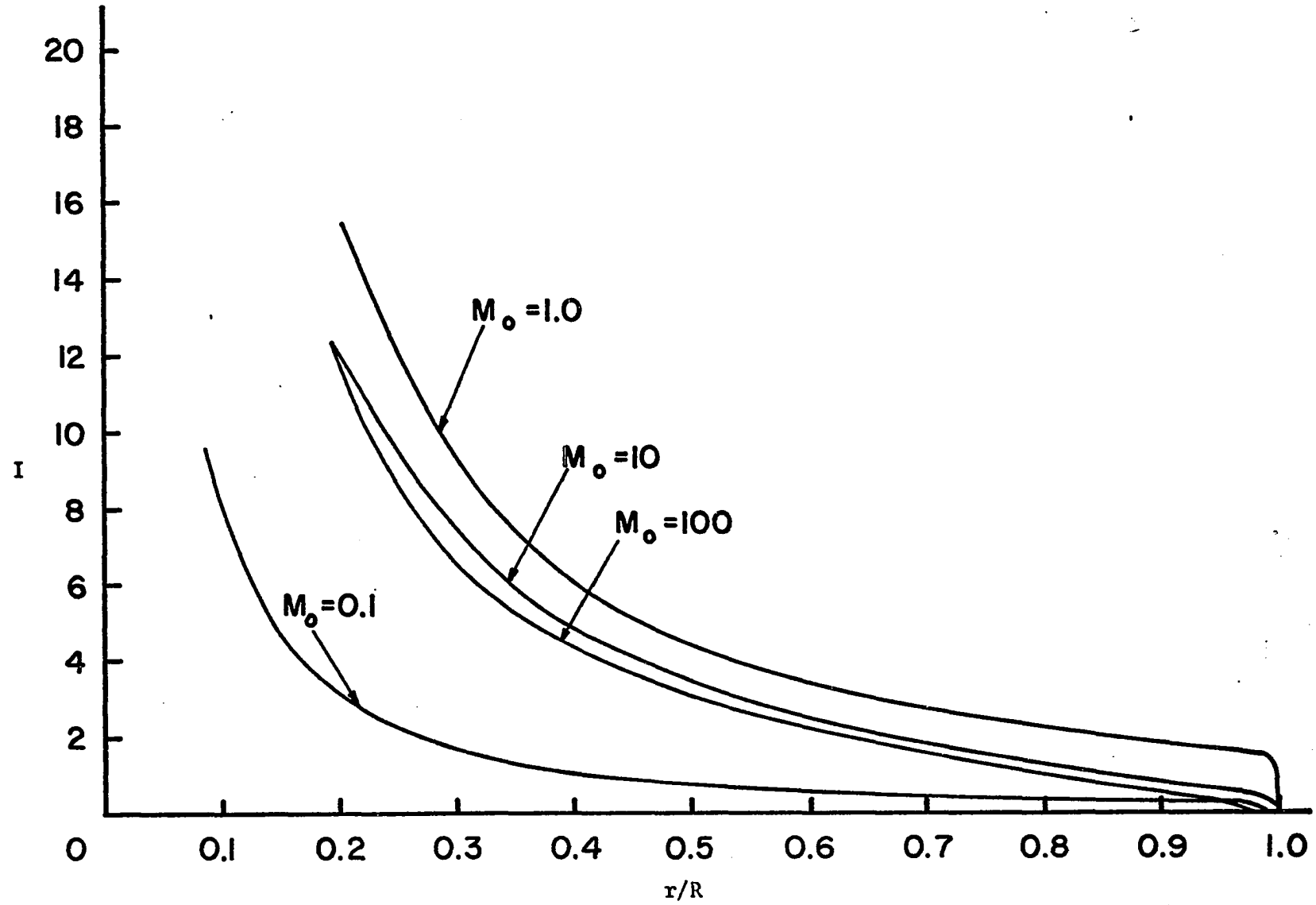

Figure 3.22 Variation of the Radial Vorticity Inflow Rate with Radius (Case i).

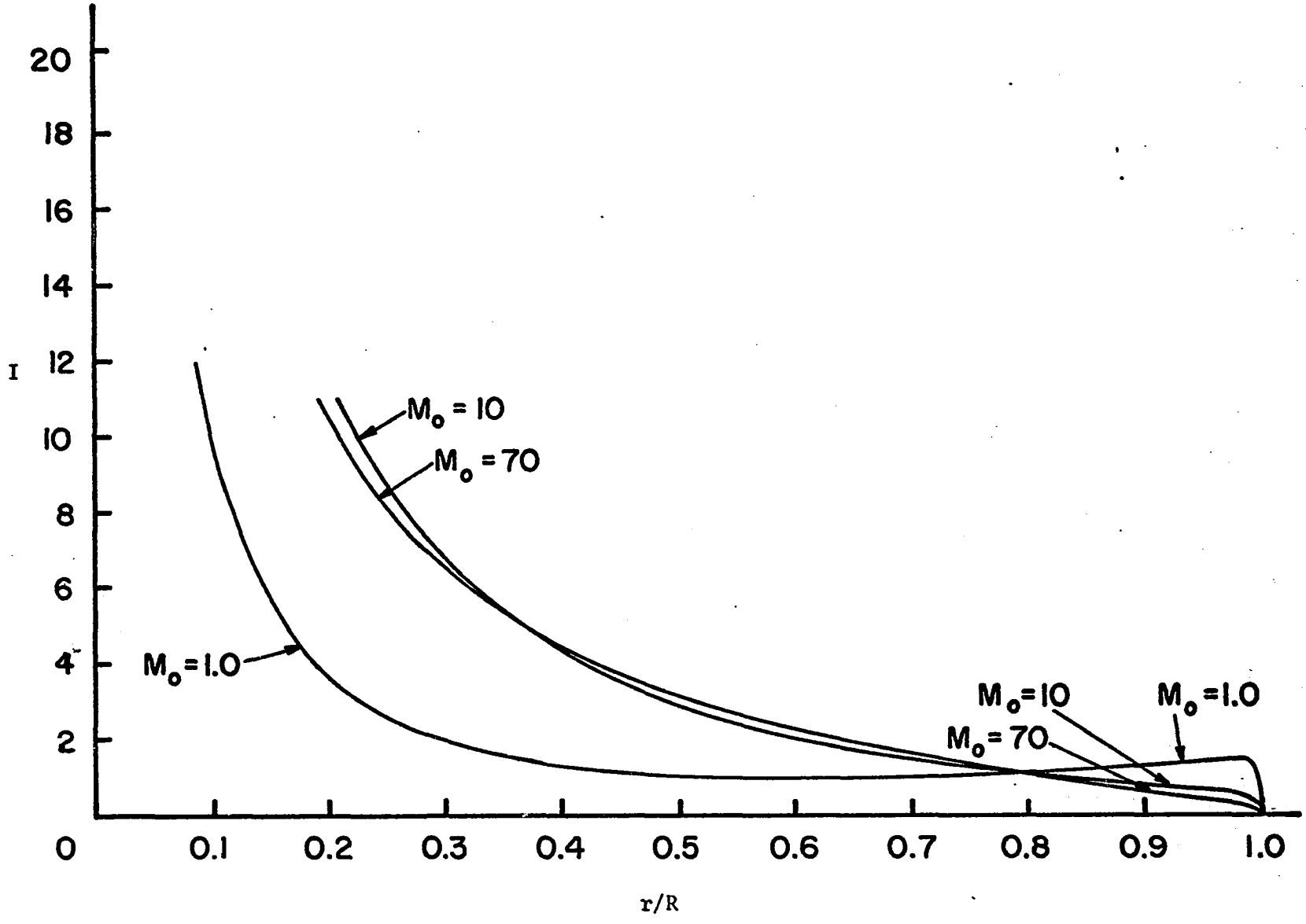

Figure 3.23 Variation of the Radial Vorticity Inflow Rate with Radius (Case ii)

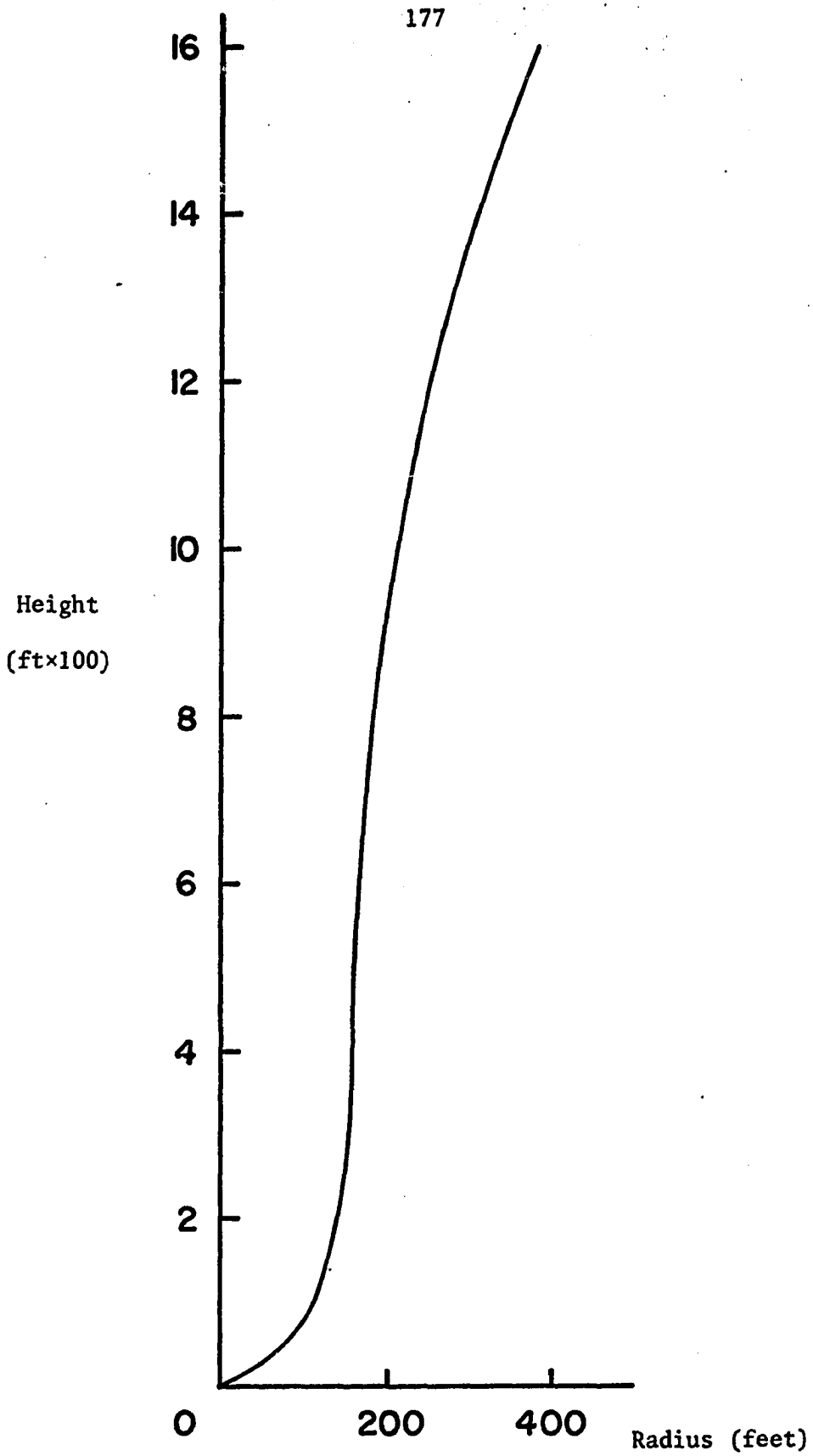

Figure 4.1 Variation of the Radius of Maximum Tangential Velocity (r_m) with Height in Dallas Tornado of April 2, 1957

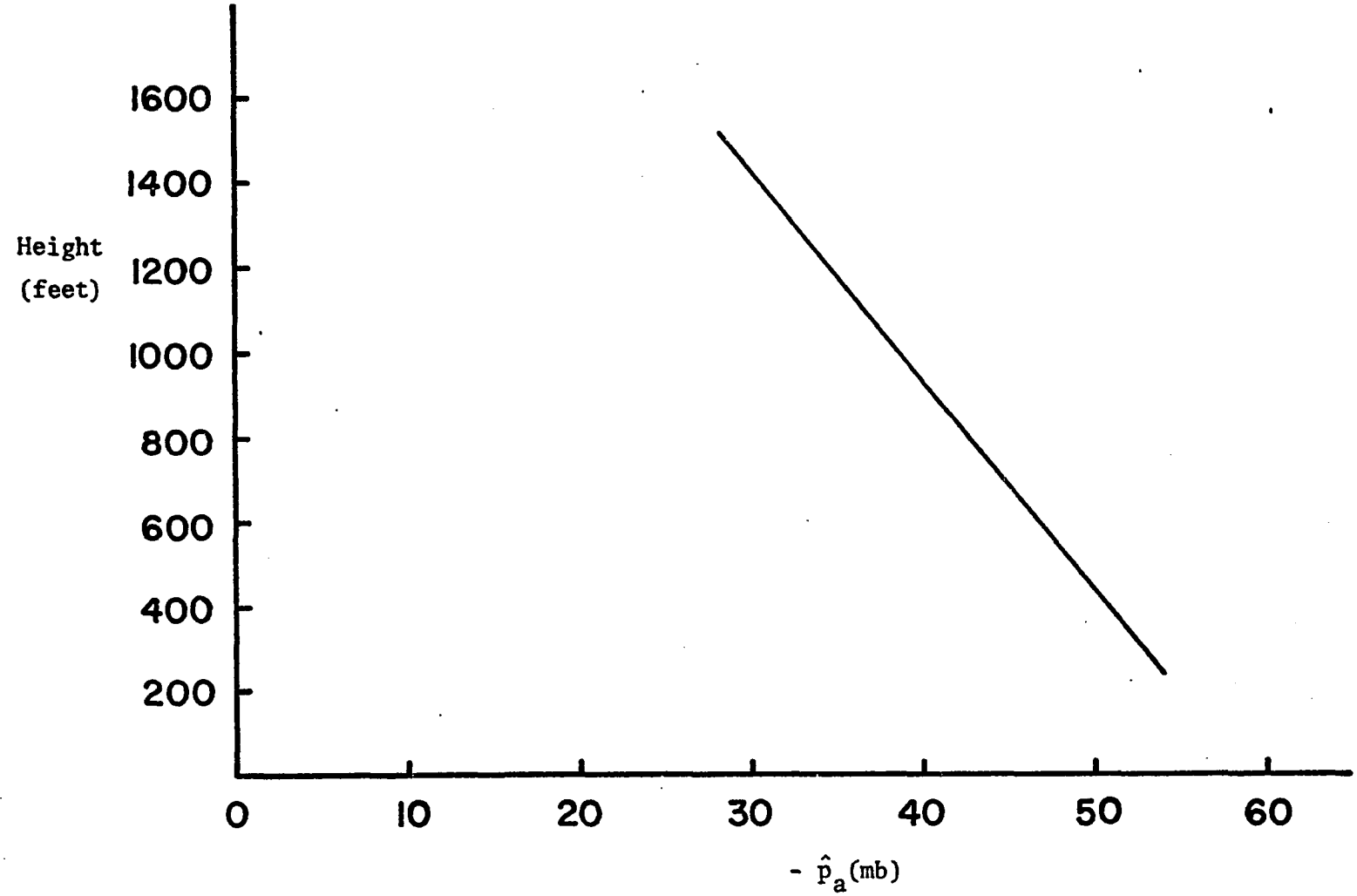

Figure 4.2 Variation of the Disturbed ($\hat{p}$) Axial Pressure with Height in Dallas Tornado of April 2, 1957.

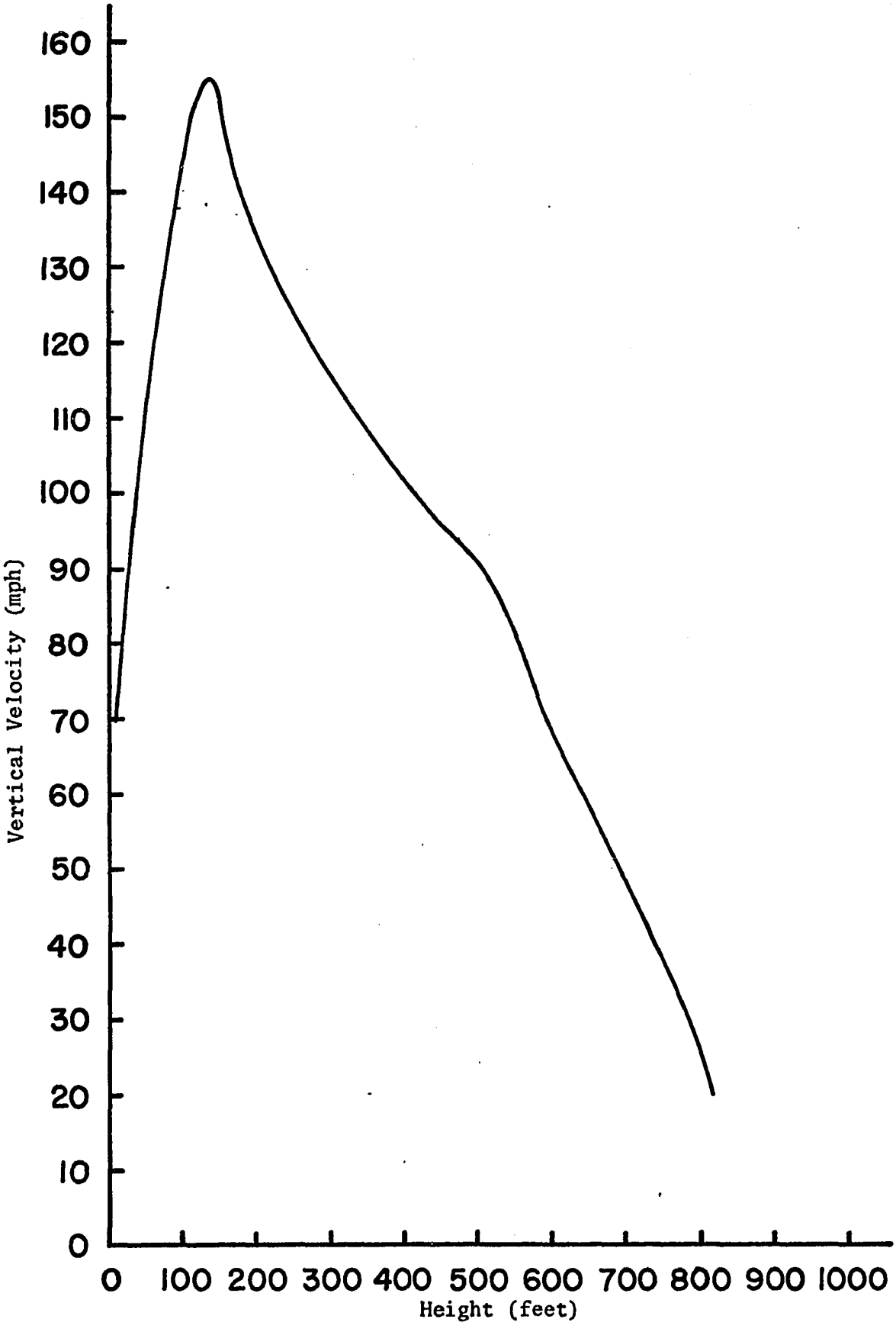

Figure 4.3 Variation of the Axial Velocity with Height in Dallas Tornado of April 2, 1957.

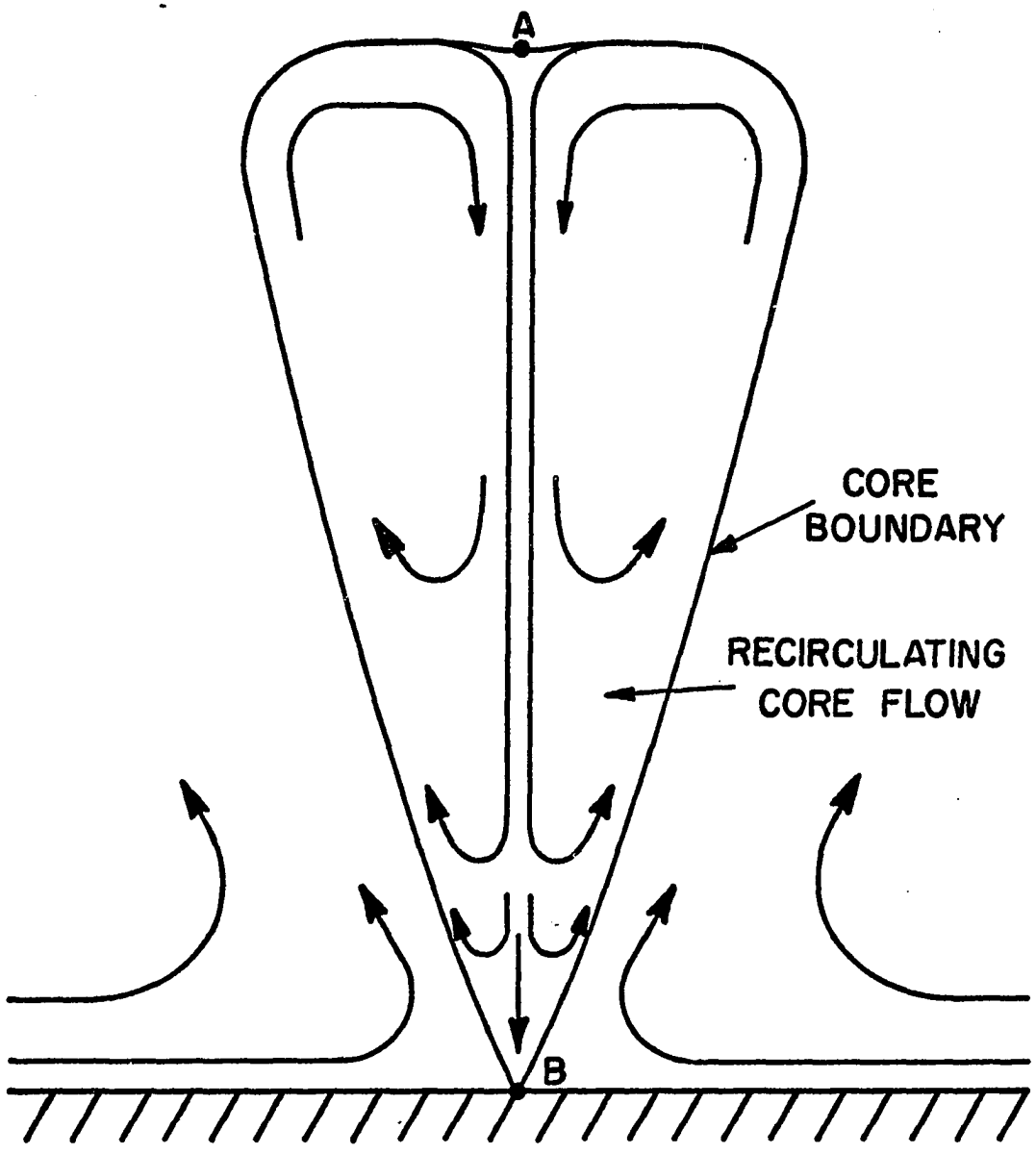

Figure 4.4 Schematic of a Two-Cell Recirculating Vortex Structure on the Ground.

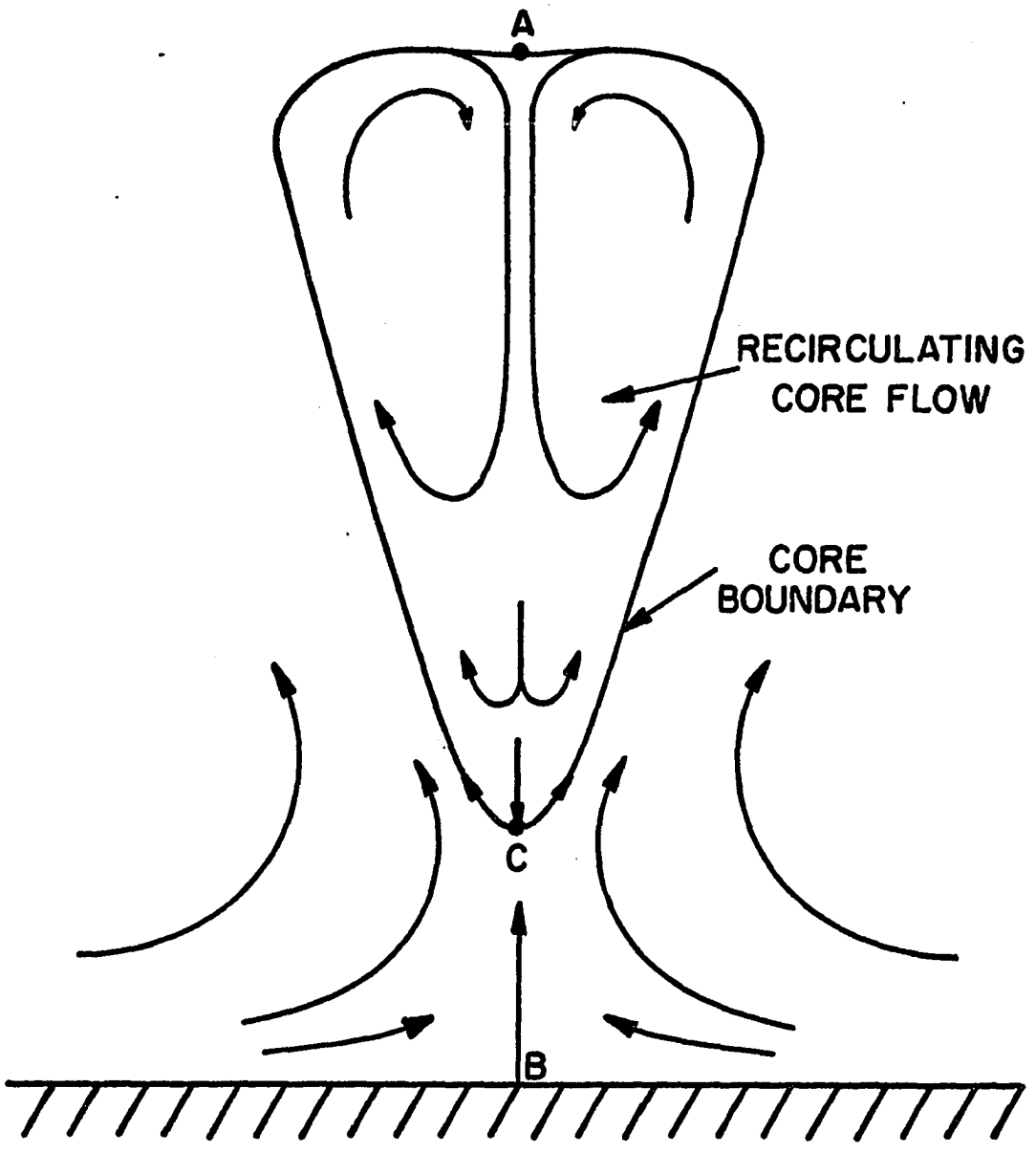

Figure 4.5 Schematic of a Combination of One-Cell Vortex on the Gound and Two-Cell Recirculating Vortex Structure Aloft.

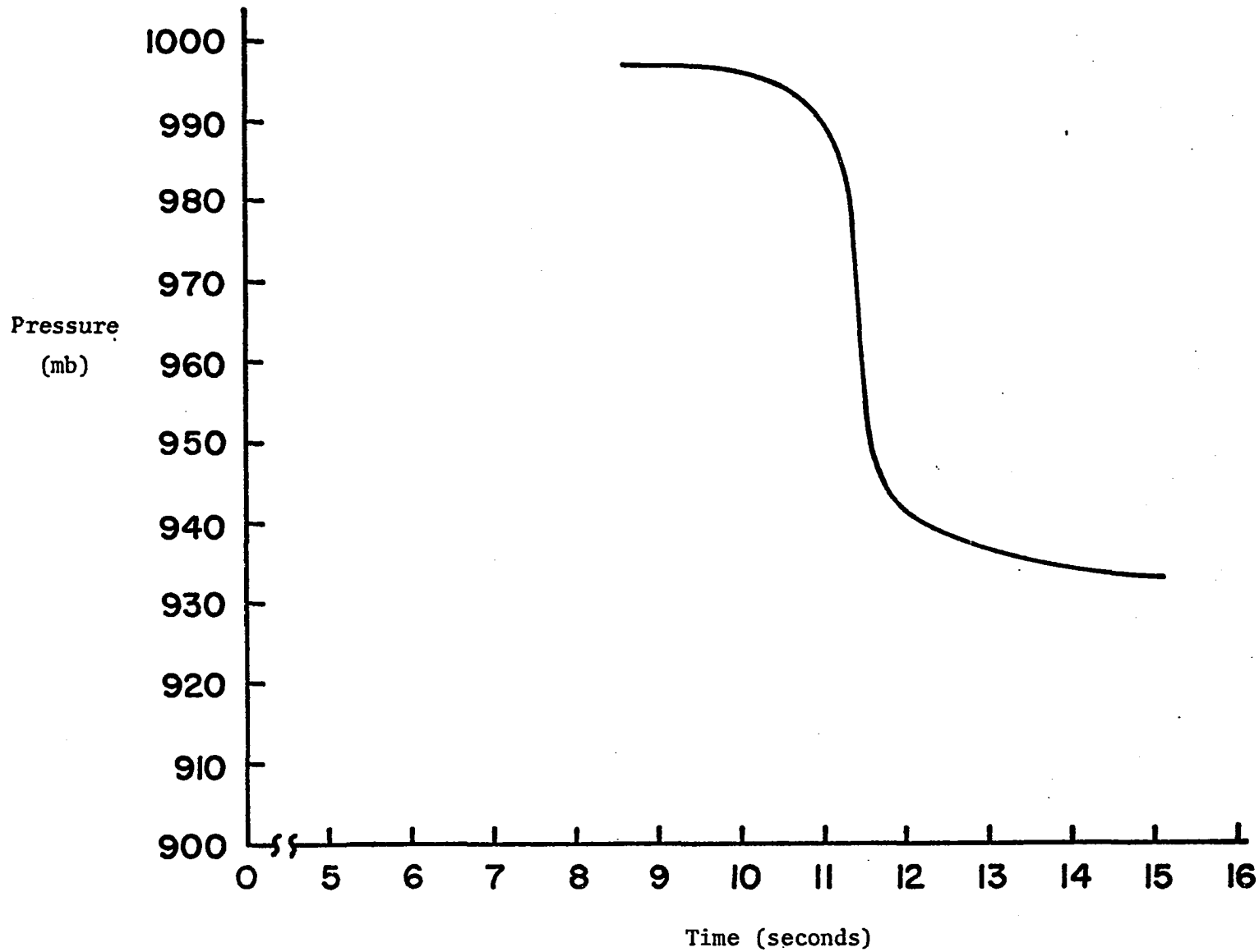

Figure 4.6 Time Variation of the Static Pressure on a Converging Streamline in the Dallas Tornado of April 2, 1957

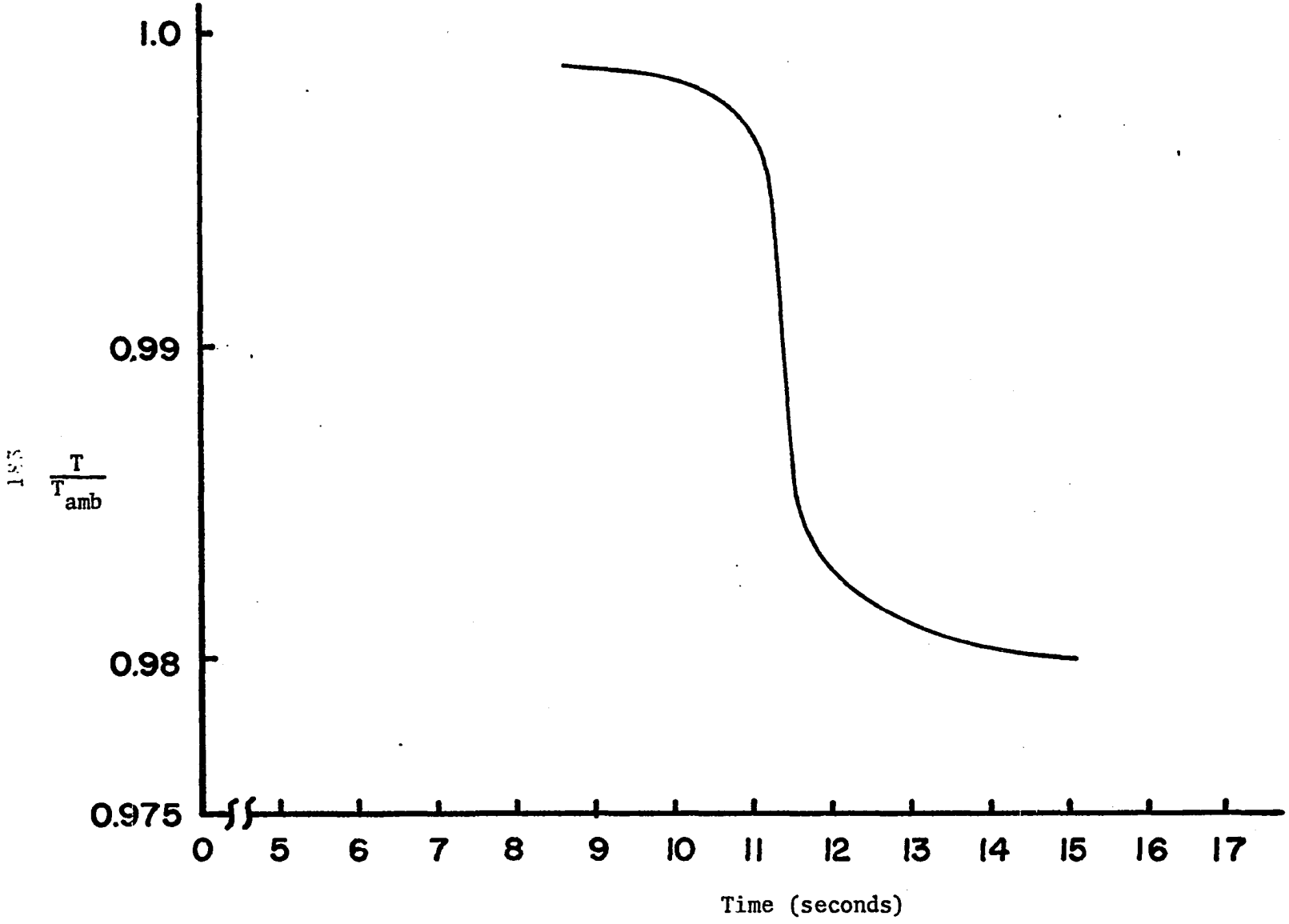

Figure 4.7 Time Variation of the Nondimensional Temperature on a Converging Streamline in Dallas Tornado of April 2, 1957

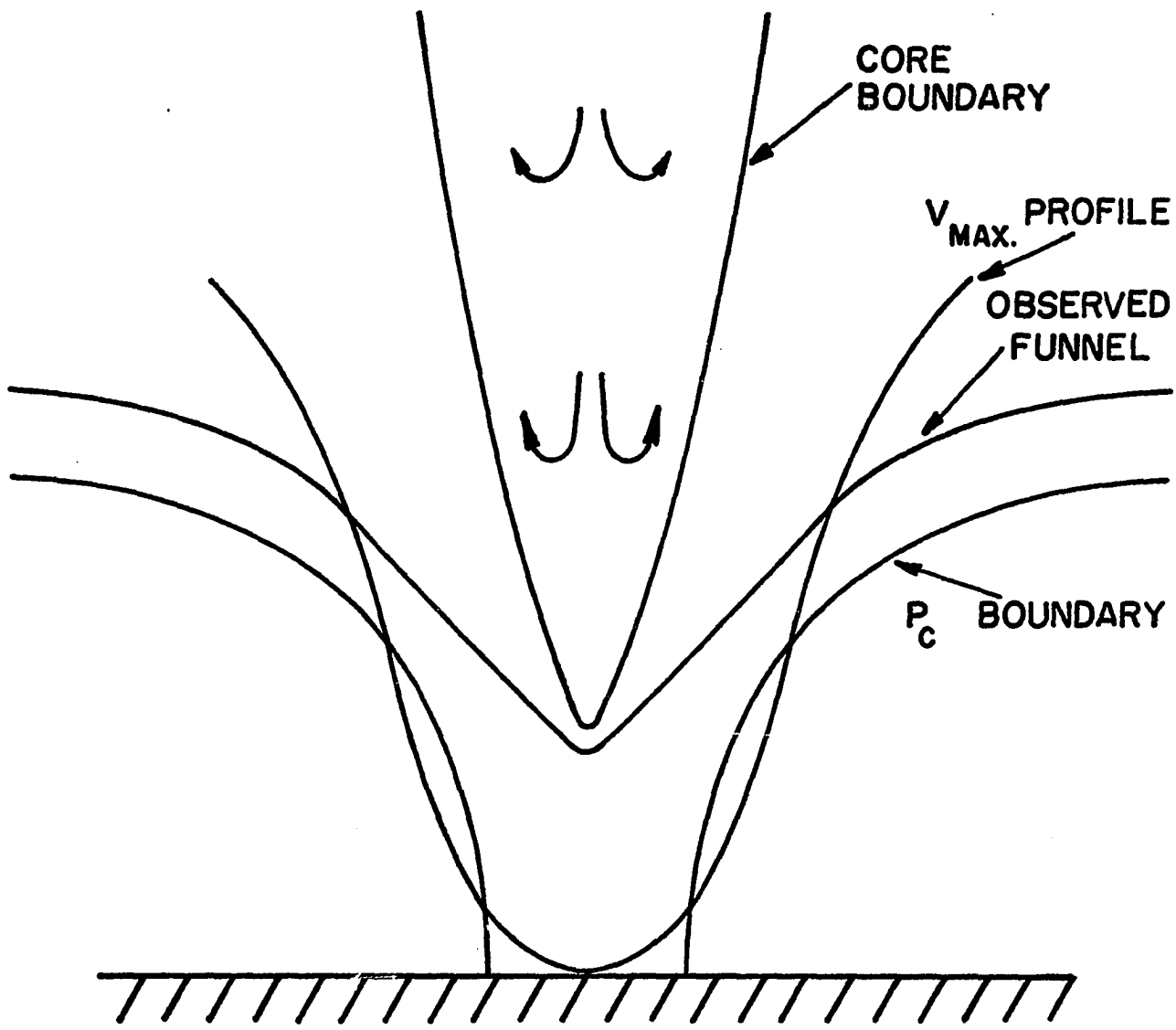

Figure 4.8 Schematic of the Relative Position of Various Tornado "Funnel" Profiles

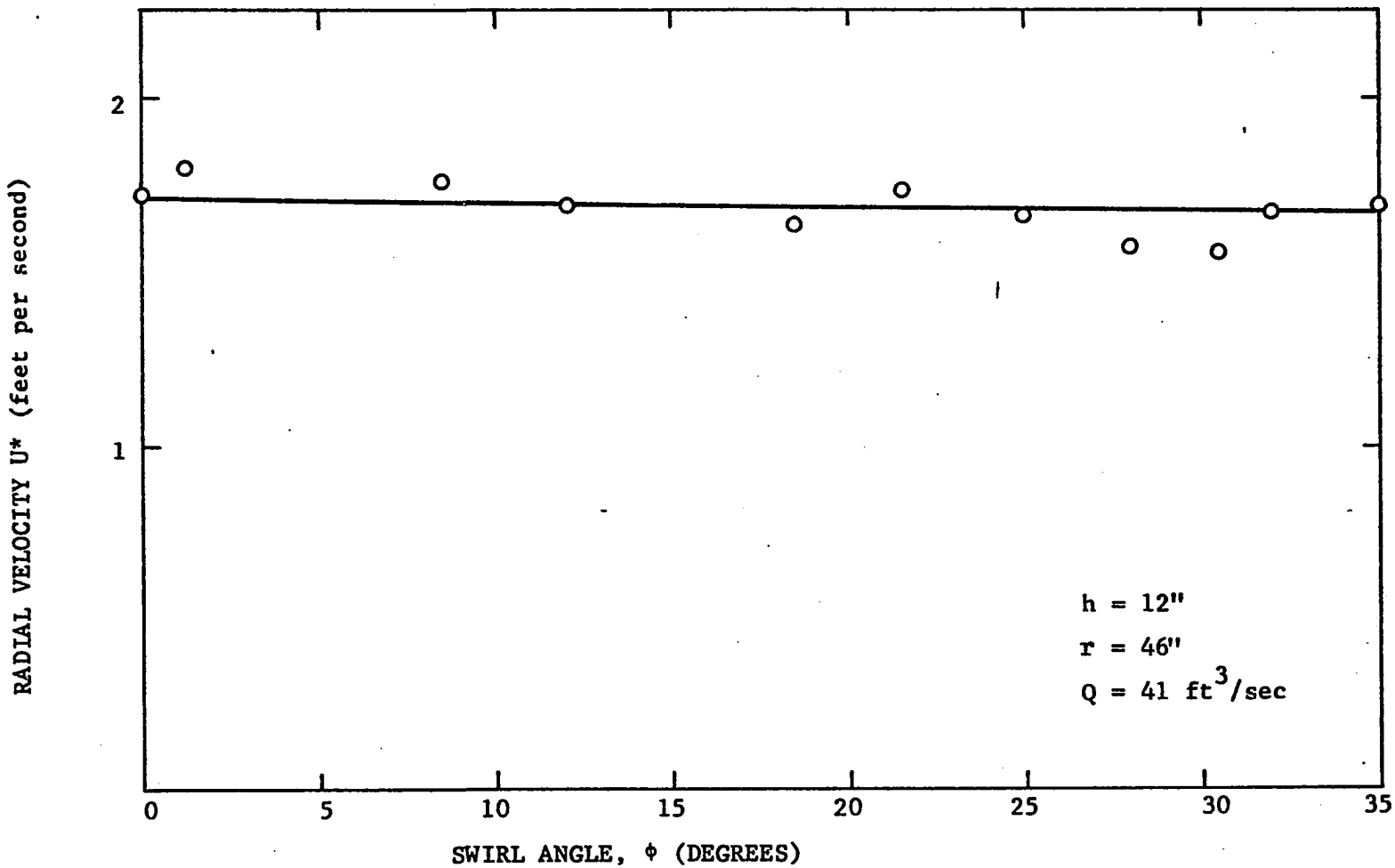

Fig. A-1 Variation of the Radial Velocity with Swirl Angle at the Screen

Plate 1.1. The Palm Sunday Tornado of 1965, Elkhart, Indiana..

Plate 1.2 Fredrick, Oklahoma Tornado of June 18, 1973.

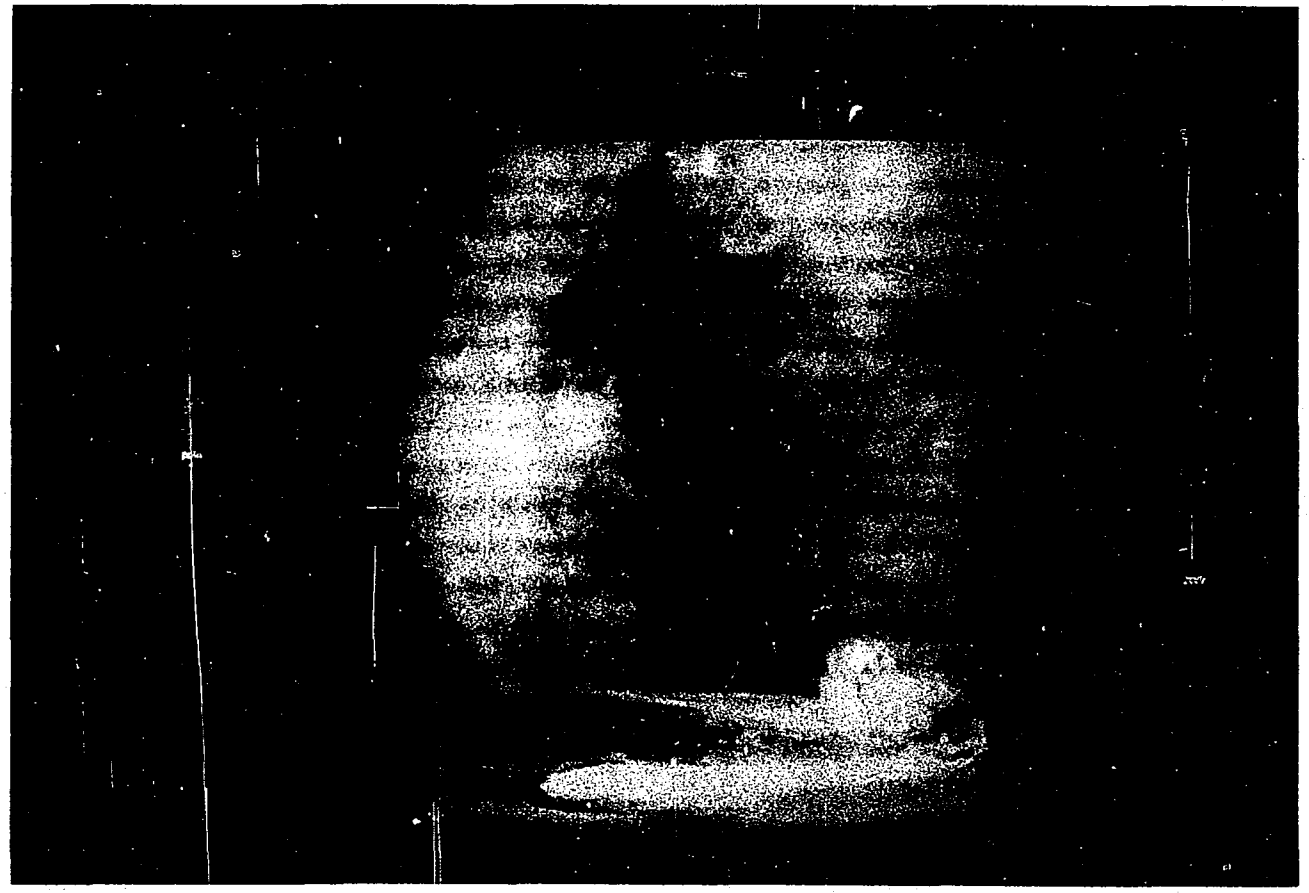

Plate 1.3 "Core-Splitting" in Ward's Apparatus.

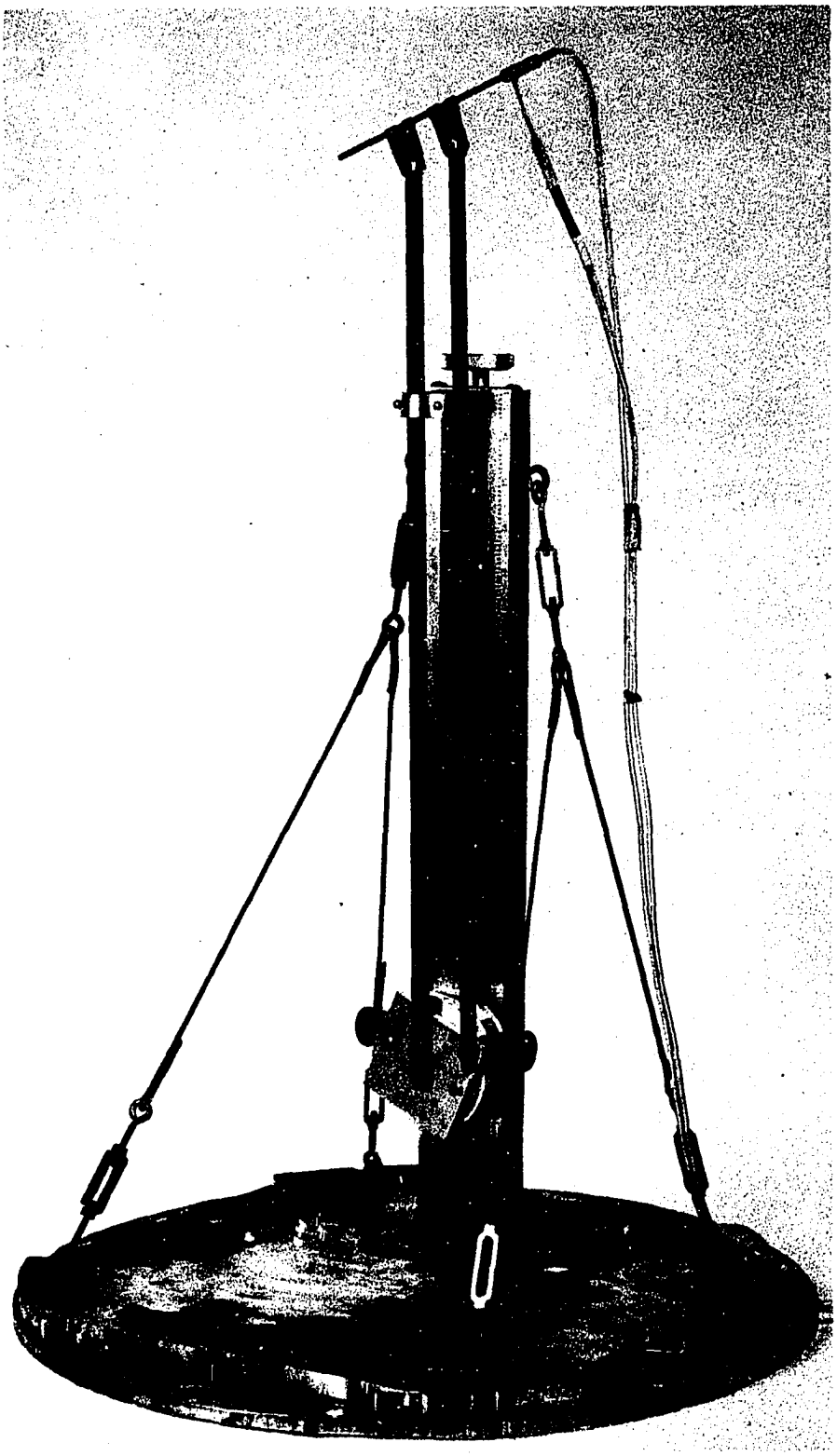

Plate 2.1. The Traverse Mechanism used in Flowfield Measurements.

APPENDIX A

INDEPENDENCE OF SWIRL AND EXHAUST CONTROLS

It is important for the purposes of these experiments to show that the imposed swirl and volumetric flow rate Q can be independently controlled and that there is no effect of increasing swirl on the radial velocity at the screen (e.g. there is no "choking" phenomenon in which there is a decrease of radial velocity with increasing swirl). This was done by measuring the radial velocity at the screen with the pitot tube. Velocities were measured for different imposed swirls at constant power setting on the exhaust fan. The results are shown in Fig. A.1.

The data shows no significant variation of the radial velocity (and hence no variation of volumetric flow rate) with swirl angle ϕ. Hence it can be concluded that there does not exist a "choking" phenomenon and that the volumetric flow rate Q and imposed swirl are indeed independently controlled by the two separate power transformers.

APPENDIX B

BOUNDARY-LAYER EQUATIONS IN CYLINDRICAL POLAR COORDINATE SYSTEM

The boundary-layer equations for a swirling, converging flow corresponding to an inviscid flow given by

$$U^* = U^*(r,z), \qquad V^* = \frac{\Gamma}{2\pi r}, \qquad W^* = W^*(r,z) \quad ,$$

[which contain cases (i) and (ii) as special cases] can be written in cylindrical polar coordinates (r,θ,z) as

$$\text{continuity} \qquad \frac{\partial}{\partial r}(ru^*) + \frac{\partial}{\partial z}(rw^*) = 0 \tag{B.1}$$

$$\text{r-momentum} \qquad u^* \frac{\partial u^*}{\partial r} + w^* \frac{\partial u^*}{\partial z} - \frac{v^{*2}}{r} = -\frac{1}{\rho}\frac{\partial p^*}{\partial r} + \frac{1}{\rho}\frac{\partial \tau_{rz}}{\partial z} \tag{B.2}$$

$$\theta\text{-momentum} \qquad u^* \frac{\partial v^*}{\partial r} + w^* \frac{\partial v^*}{\partial z} + \frac{u^* v^*}{r} = \frac{1}{\rho}\frac{\partial \tau_{\theta z}}{\partial z} \tag{B.3}$$

$$\text{z-momentum} \qquad p^* = P^*(r) \tag{B.4}$$

Combination of the continuity equation, Eq. (B.1) with the radial and tangential components of momentum equation, Eqs. (B.2) and (B.3) and their subsequent integration with respect to z can be shown to yield

$$\text{continuity} \qquad rw^*(\delta) = -\frac{d}{dr}\int_0^\delta ru^* dz + r\,U^*\frac{d\delta}{dr} \tag{B.5}$$

Radial momentum

$$\int_o^\delta (V^{*2}-v^{*2})dz - \frac{d}{dr}\int_o^\delta r(U^{*2}-u^{*2})dz + U^* \frac{d}{dr}\left[r\int_o^\delta (U^*-u^*)dz\right]$$

$$= -\frac{r}{\rho}\tau_{rz}(0) \qquad \text{(B.6)}$$

Tangential momentum

$$rV^* \frac{d}{dr}\left[r\int_o^\delta (U^*-u^*)dz\right] - \frac{d}{dr}\left[r^2\int_o^\delta (UV-u^*v^*)dz\right]$$

$$= -\frac{r^2}{\rho}\tau_{\theta z}(0) - rU^*\delta \frac{d}{dr}(rV^*) \; . \qquad \text{(B.7)}$$

We now assume the following profiles of velocity and ground shear stress law with V_∞ = total inviscid velocity,

$$u^* = U^*h(\eta) + V^*f(\eta)E(r) \qquad \text{(B.8a)}$$

$$v^* = V^*g(\eta) \qquad \text{(B.8b)}$$

$$\tau_{rz}(0) = c\rho V_\infty^2(1+E^2)^{3/8}\left(\frac{\nu}{V_\infty \delta}\right)^{1/4}$$

$$= c\rho[m^2V^{*2}(1+m^2)]^{7/8}(1+E^2)^{3/8}\left(\frac{\nu}{\delta}\right)^{1/4} \qquad \text{(B.8c)}$$

$$\tau_{\theta z}(0) = c\rho V_\infty^2 E(1+E^2)^{3/8}\left(\frac{\nu}{V_\infty \delta}\right)^{1/4}$$

$$= c\rho[m^2V^{*2}(1+m^2)]^{7/8}E(1+E^2)^{3/8}\left(\frac{\nu}{\delta}\right)^{1/4} \qquad \text{(B.8d)}$$

where $\eta = \frac{z}{\delta}$, and c is a constant equal to 0.0225. Furthermore, functions $h(\eta)$, $f(\eta)$ and $g(\eta)$ are assumed to be

$$h(\eta) = g(\eta) = \eta^{1/7}$$

$$f(\eta) = \eta^{1/7} - \eta \; .$$

We substitute Eqs. (B.8a-d) in Eqs. (B.6) and (B.7) and non-dimensionalize the variables as follows

$$r_{\text{nondim.}} = \frac{r}{R}\,, \qquad \bar{v}^* = \frac{v^*}{v_o}\,, \qquad \bar{u}^* = \frac{u^*}{u_o}\,, \qquad \bar{\delta} = \frac{\delta_{\text{dim}}}{\delta_o}$$

where $v_o = V^*(r=R)$, $u_o = U^*(r=R)$, $\delta_o = (v_o R^4 c^4/\nu)^{1/5}$ with R as the radius of the disk. The two momentum equations can be shown to give, *with the bar signs dropped,*

Radial momentum

$$\frac{2}{9} m_o^2 \delta V^{*2} + \frac{d}{dr}\left[m^2 \delta V^{*2}\left(\frac{28}{45} mrE - \frac{2}{9} r + \frac{8}{45} m^2 r E^2\right) - mV^* \frac{d}{dr}\left[mr\delta V^*\left(\frac{3}{8} mE - \frac{1}{8}\right)\right]\right.$$

$$= - r[m^2 V^{*2}(1+m^2)]^{7/8}(1+E^2)^{3/8}\delta^{-\frac{1}{4}} \qquad \text{(B.9a)}$$

Tangential momentum

$$-\frac{d}{dr}\left[\delta V^* m\left(\frac{35}{23} r + mrE\right)\right] + \left[\frac{280}{23} + \frac{112}{23} mE\right]\frac{\delta}{m}\frac{d}{dr}(rV^*)$$

$$= - \frac{360}{23} r[m^2 V^{*2}(1+m^2)]^{7/8} E(1+E^2)^{3/8}\delta^{-\frac{1}{4}} \qquad \text{(B.9b)}$$

where

$$m = \tan\phi_{\text{inviscid}} = \frac{\bar{V}^*}{\bar{U}^*} \quad \text{with } m(r=1) = m_o \ .$$

The above equations are to be solved for the two unknown $\delta(r)$ and $E(r)$ by numerical methods. To be able to proceed in the integration process, the initial solution for δ and E at the edge of the disk have to be obtained analytically. However, the above equations do not yield a consistent solution at the edge of the disk as can be seen in the following manner.

Assume that as $r \sim 1$,

$$\delta \sim (1-r)^{\alpha}\,, \qquad E \sim (1-r)^{\beta} \qquad \text{(B.10)}$$

where since δ and E are to be zero at the edge of the disk, α and β have to be positive and nonzero. The momentum equations, however, imply that a balance of the inertial and viscous forces at the edge of the disk for any m_o requires

$$-\frac{2}{9} m_o \frac{d\delta}{dr} + \frac{1}{8} \frac{d\delta}{dr} \sim m_o^2(1+m_o^2)^{7/8}\delta^{-\frac{1}{4}} - \frac{35}{23} \frac{d\delta}{dr} - \frac{360}{23} m_o^2(1+m_o^2)^{7/8}E\delta^{-\frac{1}{4}} \quad . \qquad (B.11)$$

Substitution of Eqs. (B.10) in above, results in the following two equations for α and β

$$\alpha - 1 = -\frac{\alpha}{4}$$

$$\alpha - 1 = \beta - \frac{\alpha}{4} \quad .$$

The above equations yield the results $\alpha = \frac{4}{5}$, $\beta = 0$ that contradict the assumptions that δ and $E \to 0$ as $r \to 0$ as expected from physical considerations. In general, for arbitrary nonzero m_o, $\delta \sim (1-r)^{4/5}$ where as for $m_o = 0$, which corresponds to a purely potential vortex inviscid flow, $\delta \sim (1-r)^{2/5}$. Only in the case m_o equal to zero can one obtain a physically acceptable result for $\beta(=\frac{1}{2})$ in the cylindrical polar coordinate system. For nonzero m_o, no acceptable solution for β can be obtained.

An attempt to overcome this difficulty can be made by introducing two length scales for boundary-layer thickness δ_u, δ_v corresponding to the radial and tangential components of inviscid velocity. It might then be expected from earlier results that

$$\delta_u \sim (1-r)^{4/5}, \quad \delta_v \sim (1-r)^{2/5} \quad \text{as } r \to 1 \quad . \qquad (B.12)$$

If the equations of the flow are reformulated with the above length

scales included, the boundary-layer equations become

$$\text{continuity} \quad rw^*(\delta_{max.}) = -\frac{d}{dr}\int_o^{\delta max} ru^*dz + rU^*\frac{d}{dr}(\delta_{max.}) \tag{B.13}$$

Radial momentum

$$\int_o^{\delta_v}(V^{*2}-v^{*2})dz - \frac{d}{dr}\int_o^{\delta_u} r(U^{*2}-u^{*2})dz + U^*\frac{d}{dr}\left[r\int_o^{\delta max.}(U^*-u^*)dz\right]$$

$$= -\frac{r}{\rho}\tau_{rz}(0) + U^*\delta_{max.}\frac{d}{dr}(rU^*) \tag{B.14a}$$

Tangential momentum

$$rv^*\frac{d}{dr}\left[r\int_o^{\delta max.}(U^*-u^*)dz\right] - \frac{d}{dr}\left[r^2\int_o^{\delta max.}(U^*V^*-u^*v^*)dz\right]$$

$$= -rU^*\delta_{max.}\frac{d}{dr}(rV^*) - \frac{r}{\rho}\tau_{\theta z}(0) \tag{B.14b}$$

where $\delta_{max.}$ is the maximum of δ_u and δ_v.

The above equations can be integrated and nondimensionalized in a similar fashion as before with the following exception

$$\bar{\delta}_u = \frac{\delta_u}{\delta_o m_o^{-1/5}}, \qquad \bar{\delta}_v = \frac{\delta_v}{\delta_o}.$$

It can be shown, then, that the radial and tangential momentum equation become, with $v^* = \frac{1}{r}$, respectively

$$\frac{2}{9}\frac{\delta_v}{r^2} + \frac{8}{45}\frac{d}{dr}\left(\frac{E^2\delta_v}{r}\right) + 2m_o\frac{d}{dr}(U^*EJ_1) - \frac{3}{8}m_oU^*\frac{d}{dr}(E\delta_v) - \frac{2}{9}m_o^{9/5}\frac{d}{dr}(rU^{*2}\delta_u)$$

$$+ \frac{1}{8}m_o^{9/5}U^*\frac{d}{dr}(rU^*\delta_u) = cr^{-3/4}E(1+E)^{3/8}\delta_v^{-1/4} + crU^{7/4}\delta_u^{-1/4}m_o^{9/5} \tag{B.15a}$$

$$\frac{23}{360}\frac{d}{dr}(E\delta_v) + \frac{1}{8}m_o\frac{d}{dr}(rU^*\delta_v) - m_o\frac{d}{dr}(J_2) = -cr^{1/4}(1+E^2)^{3/8}\delta_v^{-1/4}. \tag{B.15b}$$

where

$$J_1 = \begin{cases} \frac{14}{45}\,\delta_v\left(\frac{\delta_v}{\delta_u}\right)^{1/7} m_o^{1/35}, & \frac{\delta_u}{\delta_v} \geq m_o^{1/5} \\ \delta_v\left[\frac{3}{8}+\frac{1}{30}\,m_o^{-2/5}\left(\frac{\delta_u}{\delta_v}\right)^2-\frac{7}{72}\,m_o^{-8/35}\left(\frac{\delta_u}{\delta_v}\right)^{8/7}\right], & \frac{\delta_u}{\delta_v} \leq m_o^{1/5} \end{cases} \qquad \text{(B.16a)}$$

and

$$J_2 = \begin{cases} \delta_v\left[\frac{1}{8}\left(\frac{\delta_u}{\delta_v}\right)m_o^{-1/5}-\frac{7}{72}\left(\frac{\delta_u}{\delta_v}\right)^{8/7}-m_o^{-8/35}\right], & \frac{\delta_u}{\delta_v} \leq m_o^{1/5} \\ \delta_v\left[\frac{1}{8}-\frac{7}{72}\left(\frac{\delta_v}{\delta_u}\right)^{1/7}m_o^{1/35}\right], & \frac{\delta_u}{\delta_v} \geq m_o^{1/5} \end{cases} \qquad \text{(B.16b)}$$

The ground shear stress components substituted in Eqs. (B.14a-b) are [Serrin, 1972] in dimensional form,

$$\tau_{rz}(0) = -\left[c\rho E(1+E^2)^{3/8}r^{-7/4}\delta_v^{-1/4} + c\rho\left(m_o|U^*|\right)^{7/4}m_o^{1/20}\delta_u^{-1/4}\right] \qquad \text{(B.17a)}$$

$$\tau_{\theta z}(0) = c\rho r^{-7/4}(1+E^2)^{3/8}\delta_v^{-1/4} \; . \qquad \text{(B.17b)}$$

where the appropriate sign is included in the radial stress component for the converging flow. The two equations, Eqs.(B.14a) and (B.14b) involve three unknowns δ_u, δ_v and E. A unique solution can be obtained only if a third equation is developed. We could chose, for example, the third equation to be the mechanical energy equation

$$\vec{V}\cdot(\rho\vec{v}\cdot\nabla\vec{v}+\nabla p-\nabla\cdot\vec{\vec{\tau}}) = 0 \; . \qquad \text{(B.18)}$$

Integration of the above scalar equation with respect to z and further algebraic manipulation and substitution of Eqs. (B.8a-d) would result in the following nondimensional equation

$$\frac{d}{dr}\left[-\frac{7}{80}\,rU^{*3}\delta_u+\frac{33}{160}\,V^{*2}U^{*}\delta_u E+\frac{189}{880}\,U^{*}V^{*2}E^{2}\delta_u+\frac{81}{1760}\,V^{*3}E^{3}\delta_u-\frac{7}{144}\,rU^{*}V^{*2}\delta_{max}\right.$$

$$\left.-\frac{9}{160}\,EV^{*3}\delta_{max.}\right]=-\frac{r}{\delta}\left[\left(\frac{7}{8}\,U^{*}+\frac{3}{8}\,V^{*}E\right)\tau_{zr}(0)\,\frac{\delta_u}{\delta_{max.}}+\frac{7}{8}\,V^{*}\tau_{\theta z}(0)\right]. \quad (B.19)$$

The Eqs. (B.15a-b) and (B.19) are to be integrated numerically for the three unknowns δ_u, δ_v and E. However, integration of the above equations require an analytic solution of the unknowns at the edge of the disk r = 1. Assuming that as $r \to 1$,

$$\delta_u \sim (1-r)^{4/5} \quad , \qquad \delta_v \sim (1-r)^{2/5} \quad , \qquad E \sim (1-r)^{\beta} \quad .$$

Equations (B.15a-b) imply a balance of the following nature, respectively,

$$\frac{d\delta_u}{dr} \sim \delta_u^{-\frac{1}{4}} \quad (B.20)$$

$$\frac{d(E\delta_v)}{dr} \sim \frac{d\delta_v}{dr} \quad (B.21)$$

$$\frac{d\delta_u}{dr} \sim \delta_u^{-\frac{1}{4}} \quad (B.22)$$

We note that the resulting equations do not yield a nonzero positive β and indeed do not possess a consistent solution. In fact, it can be shown that any independent equation chosen to replace the mechanical energy equation (e.g. the moment of momentum equation, etc.) would never result in a consistent solution for E(r) at the edge of the disk.

The lack of a consistent and acceptable initial solution for E(r) in both systems of Eqs. (B.9a-b) and (B.10) and the three Eqs.

(B.15a-b) and (B.19) are due to the nature of the expressions of the shear stress law in cylindrical coordinate system. The components of the radial shear stress induced by the radial velocity would always be present in the radial momentum equation for all values of nonzero m_o resulting in a fundamentally different balance from that of the case $m_o = 0$, at the edge of the disk. This is true regardless of the different formulations of the problem and the number of unknowns as long as the momemtum equations are expressed in cylindrical coordinate system (r,θ,z). In other words, the turbulent shear stress law is a fundamentally empirical law with the inherent limitation that the components of the shear stress can be represented in the functional form of Eqs. (B.8a-d) and (B.17a-b) if and only if they are expressed in the appropriate coordinate system -- namely that of the inviscid flow direction and the direction normal to it. Since for a nonzero m_o, the (r,θ,z) coordinate system do not coincide with the direction of the flow and the normal to it, the expressions of the turbulent shear stress law as formulated empirically by the functional form of Eqs. (B.8a-b) and (B.17a-b) are not appropriate for arbitrary non-zero values of m_o. It can be seen now that only for the limiting cases of $m_o = 0$ and $m_o = \infty$ where the inviscid streamline direction happens to coincide with the cylindrical coordinate system, i.e, pure potential vortex and pure radial flow, do the expressions for ground shear stresses in the form of Eqs. (B.8a-b) and (B.17a-b) yield a consistent and unique solution for E and δ everywhere. For the general case of arbitrary values of m_o, then, the boundary-layer momentum equations must be expressed in the inviscid streamline coordinate system (s,n,z) with the ground shear

stress components formulated in the functional form of Eqs. (B.18a-b) as discussed in the main text. A unique solution at the edge can then be found [Eqs. (51) and (52) of the text for cases (i) and (ii), respectively] and the integration of the momentum equations can be carried out.